The magmatic evolution, eruptive history and geothermal reservoir assessment of the Paka volcanic complex, Northern Kenya rift

Geoffrey Kiptoo Mibei

Faculty of Earth Science
University of Iceland
2021

The magmatic evolution, eruptive history and geothermal reservoir assessment of the Paka volcanic complex, Northern Kenya rift

Geoffrey Kiptoo Mibei

Dissertation submitted in partial fulfillment of a
Philosophiae Doctor degree in Geology

PhD Committee
E. Bali
G. H. Guðfinnsson
H.Geirsson
H.Franzson
B. S. Harðarson

Opponents
Karen Fontjin
Agnes Reyes

Faculty of Earth Science
School of Engineering and Natural Sciences
University of Iceland
Reykjavík, October 2021

The magmatic evolution, eruptive history and geothermal reservoir assessment of the Paka volcanic complex, Northern Kenya rift
Dissertation submitted in partial fulfillment of a *Philosophiae Doctor* degree in Geology

Faculty of Earth Sciences
School of Engineering and Natural Sciences
University of Iceland
Öskju, Sturlugötu 7
101, Reykjavik
Iceland

Telephone: 525 4000

Bibliographic information:
Geoffrey K. Mibei, 2021, *The magmatic evolution, eruptive history and geothermal reservoir assessment of the Paka volcanic complex, Northern Kenya rift*, PhD dissertation, Faculty of Earth Science, University of Iceland, 200 pp.

Author ORCID: https://orcid.org/0000-0002-7866-4873

Printing: Háskólaprent
Reykjavik, Iceland, October 2021

Abstract

In this study, the magmatic evolution and the eruptive history of the Paka volcanic complex are investigated and its geothermal reservoir is assessed. The study comprises two parts. The first part deals with the eruptive history, magma evolution, and magma reservoir storage conditions. The second part focuses on an assessment of the geothermal reservoir. I propose a revised stratigraphic framework for Paka volcanism where five eruptive sequences have been identified, spanning ~582 to 8 ka. The Paka edifice growth comprises four main eruptive sequences commencing at 390 ka with the main caldera collapse occurring at ~36 ka. The volcanic products in the area include alkaline basalt-trachyte lava and tephra deposits. A minimum bulk volume for the erupted products between 390 and 8 ka is estimated to be ~50 km^3. This translates to a magma supply rate of 1.2 x10-4 km^3/yr, this is associated with a heat flux between 110-138 mW/m^2. Trace element modelling using La and Y indicates that Paka primary magma was generated by partial melting of garnet peridotite mantle (60-80 km depth) by 5-10% partial melting. The magma differentiation processes invoked encompass 70% fractionational crystallization and 10-20% assimilation of syenite in the mid to shallow crustal depths to generate the Paka trachyte. Geothermobarometric models indicate magma reservoirs of basaltic and intermediate composition located diversely at depths of 5-20 km and 15-20 km respectively. A shallow trachyte magma reservoir is estimated to occur at 3.7-5 km depth. Based on an evaluation of the temporarily diverse magma series, the established basalt and trachyte magma reservoir depths within the deep to mid and shallow crustal zones are long-lived and have not changed significantly since ~580 ka. The estimated storage temperature for the basalt and intermediate(s) magma is between 1032-1206 °C, whereas for the trachyte it ranges between 900-938°C under relatively oxidized conditions (ΔFMQ +1). The underlying geothermal reservoir within the Paka complex is manifested on the surface by fumaroles, altered surface rocks, and fossil hot springs. Detailed analysis of PK-01 borehole data indicates that the geothermal system is characterized by three hydrothermal alteration zones, namely smectite -mordenite, chlorite-illite, and epidote-actinolite. Evidence suggests notable temperature fluctuations within the deeper levels of the hydrothermal system over time, perhaps associated with faults channelling cold water deep into the system. The reservoir system is liquid-dominated with a boiling zone at ~900 m depth. It is characterized by Na-bicarbonate fluids and has been such over the lifetime of the system.

Útdráttur

Í þessu verkefni er kvikuþróun og gossaga Paka-eldstöðvarinnar rannsökuð og jarðhitageymir hennar metinn. Rannsóknin er í tveimur hlutum. Í fyrri hlutanum er fjallað um gossöguna, kvikuþróun og eiginleika kvikugeymisins. Seinni hlutinn fjallar um mat á jarðhitageyminum. Ég legg til endurskoðaða jarðlagaskipan í Paka þar sem greindar eru fimm gossyrpur sem spanna tímabilið frá um 582 til 8 ka. Paka-eldkeilan óx í fjórum megin gossyrpum sem byrjuðu fyrir 390 ka en öskjusig varð fyrir um 36 ka. Meðal gosmyndana á svæðinu eru alkalíbasalt- til trakýthraun og gjóskulög. Áætlað lágmarks-rúmmál gosefna frá 390 til 8 ka er um 50 km^3. Það þýðir að kvikuframleiðsla er 1,2 $x10^{-4}$ km^3/ári og varmastreymi af völdum innskota á bilinu 110-138 mW/m^2. Reiknilíkan sem byggir á magni La og Y bendir til að frumkvika Paka hafi myndast við 5-10% hlutbráðnun á granatperidótítmöttulefni (á 60-80 km dýpi). Gert er ráð fyrir þróunarferli kviku sem felur í sér yfir 70% hlutkristöllun og 10-20% meltingu á syeníti í mið- til grunnskorpunni til að mynda trakýtið í Paka. Bergfræðilegir hita- og þrýstingsmælar benda til kvikugeyma með samsetningu basalts og ísúrs bergs sem staðsettir eru víða á 5-20 km og 15-20 km dýpi. Áætlað er að grunnstæður trakýtkvikugeymir sé á 3,7-5 km dýpi. Mat á þessari fjölbreyttu bergsyrpu í tímans rás sýnir að ætlaðir basalt- og trakýtgeymar í djúp-, mið- og grunnskorpunni hafa verið langlífir og ekki breyst verulega frá því fyrir um 580 ka. Áætlað hitastig geyma með basaltkviku og ísúrri kviku er á bilinu 1032-1206 °C, en með trakýtkviku á bilinu 900-938 °C við tiltölulega oxaðar aðstæður (ΔFMQ +1). Ummerki jarðhitageymisins undir Paka-eldstöðinni eru á yfirborði sem gufuhverir, jarðhitaummyndun og kulnaðir hverir. Ítarleg greining á borholugögnum frá PK-01 bendir til að jarðhitakerfið einkennist af þremur ummyndunarbeltum, þ.e. smektít-mordenít-, klórít-illít- og epidót-aktínólítbelti. Vísbendingar eru einnig um að áberandi hitasveiflur hafi orðið í jarðhitakerfinu, á bilinu 245-280 °C. Kerfið er vatnsríkt með suðusvæði á um 900 m dýpi. Vökvinn er af bíkarbónatgerð og hefur verið svo meðan kerfið hefur verið virkt.

Dedication

I dedicate this work to my entire Family, and in particular my wife Elizabeth Kiptoo, my daughter Precious Kiptoo and my son Ryan Too.

Preface

This research project is supported by the Government of Iceland through the Geothermal Training Programme (GRÓ-GTP) and the Government of Kenya through the Geothermal Development Company (GDC). It is divided into two sections. Section I focuses on the eruptive history, magma evolution and magma reservoir conditions of the Paka volcanic complex. Section II focuses on assessing the Paka geothermal reservoir. In section I develop a new stratigraphic framework to understand the Paka eruptive history. I use petrology and geochemical numerical modelling techniques to understand magmatic evolution and storage conditions during the growth of Paka volcano. Section I improves the understanding of the volcanic complex and provides a background for the geothermal reservoir assessment in Section II. Section II contains the geothermal assessment, geared towards the characterisation and determination of temperatures and provides insight into fluid chemistry and temporal changes in the hydrothermal reservoir. The results of this work are detailed in three scientific papers, two of which have been published or accepted for publication in peer reviewed journals, i.e., Journal of African Earth Sciences and Lithos, while the third is submitted to Geothermics. The papers are:

Paper I
Eruptive history and volcano-tectonic evolution of Paka volcanic complex in the northern Kenya rift: Insights into the geothermal heat source.

Paper II
Partial melt generation and evolution of magma reservoir conditions at the Paka volcanic complex in Kenya: constraints from geochemistry, petrology and geophysics.

Paper III
Geothermal reservoir characterization of Paka geothermal field in Kenya based on detailed analyses of well PK-01 and a review of surface exploration data.

Table of Contents

List of Figures

List of Tables

Abbreviations

ASAR	Advanced Synthetic Aperture Radar
AMI	After master valve installation
Ab	Albite
An	Anorthite
AFC	Assimilation and fractional crystallization
BSE	Backscattered eloctrons
CaTsch	Ca-Tschermak
CITZAF	Carnegie Institution, atomic number, absorption, fluorescence
CT	Cellar top
η	Conversion efficiency
km^3/yr	Cubic kilometer per year
°C	Degree Celsius
DiHD	Diopside-hedenbergite
EMPA	Electron microprobe analysis
E_{res}	Energy content of the resevoir
EnFs	Enstatite-ferrosillite
Envisat	Enviromental satellite
Kd	Equilibrium constant
Fa	Fayalite
FMQ	Fayalite-Magnetite-Quartz
Fo	Forsterite
FC	Fractional crystallization
ICP-OES	Inductively coupled plasma-optical emission spectroscopy

InSAR	Interferometric Synthetic Aperture Radar
J	Joules
K	Kelvin
KDE	Kernel density plot
kg	Kilogram
Kbar	Kilobars
MT	Magnetotelluric
Mg#	Magnesium number
MWe	Megawatts electric
M a.s.l	Meters above sea level
NCG	Non condensable gases
PK-01	Paka well one
PK-02	Paka well two
PK-03	Paka well three
PM	Partial melting
ppm	Parts per million
P.I	Peralkalinity index
POOH	Pull out of hole
Ωm	Ohm meter (unit of electric resistivity)
QGIS	Quantum geographic information system
RKB	Rotary kelly bushing
Rf	Recovery factor
SEM	Scanning electron microscope
SRTM	Shuttle Radar Topography Mission
m^2	Square meter
SEE	Standard error estimate

SFTT	Static formation temperature test
Terra Sar-X	Terra synthetic apparture radar band X
VEI	Volcanic explosivity index
mW/m^2	Milliwatts per meter square
W/m^2	Watts per meter square
WCARS	West and Central African Rift System
XRD	X-ray diffraction
yr	Year
ZAF	Z-atomic number, A - absorption of X-rays in the specimen, F - fluorescence caused by other X-rays generated

Acknowledgements

Although this research is attributed to me alone, it is in reality a collective effort of persons and institutions whose intellectual input and financial contributions has resulted in its successful completion, after three and half years of my doctoral research programme at the Faculty of Earth Sciences, University of Iceland.

The Government of Iceland through the Geothermal Training Programme (GRÓ-GTP) and the Government of Kenya through the Geothermal Development Company (GDC) funded this research. My sincere gratitude to my employer GDC for granting me leave of absence to pursue this study and facilitating all field work programme. I am grateful to the government of Iceland that through UNU-GTP, now GRÓ-GTP, awarded me this scholarship and support over the study period.

I take this early opportunity to specially mention Dr. Björn S. Harðarson (Iceland GeoSurvey) who first cultivated in me the idea of a PhD in 2012 after the six months UNU-GTP course. This idea led to the application for the UNU-GTP scholarship in 2013, which materialized in 2017. In this regard I am most grateful to Lúðvík Georgsson (Retired Director of the UNU-GTP) who played a major role in me being accepted as a PhD candidate.

My Supervisors and the PhD committee: Dr. Hjalti Franzson (Iceland GeoSurvey), Dr. Enikő Bali (University of Iceland), Dr. Björn S. Harðarson (Iceland GeoSurvey), Dr. Halldór Geirsson (University of Iceland) and Dr. Guðmundur Heiðar Guðfinnson (University of Iceland). You have been my pillars of support in this academic journey. I highly appreciate your ever-present guidance, ideas, and knowledge from the conception to the end of this study. You have greatly contributed to the scientist that I am today.

In a special way, I want to mention the staff of the GRÓ-GTP and express my heartfelt gratitude for their extra dedication in supporting me during this academic journey in Iceland; Lúðvík Georgsson (Retired Director), Guðni Axelsson (Director), Ingimar Haraldsson (Deputy Director), Málfríður Ómarsdóttir, Þórhildur Ísberg, Vigdís Harðardóttir and Markús Wilde. To all the GRÓ-GTP fellows in Iceland: You created a homely environment for me. Thank you very much. To Orkustofnun staff, special thanks to Rósa S. Jónsdóttir, thank you for your assistance.

To all resource persons, I humbly appreciate your efforts and help. Particularly, Prof. Þorvaldur Þórðarson, Dr. Ármann Höskuldsson and Dr. Sæmundur Ari Halldórsson for fruitful discussions in the course of my study. Thank you Sæmundur and Jóhann Gunnarsson Robin for assistance during the laboratory analyses. To my student colleagues and classmates Diego, Dario, Maria and others, thank you very much.

To all the assistance I have received from my GDC colleagues and the management: Cornel Ofwona, John Lagat, the success of this work is directly attributable to you. I am greatly

indebted to the late Dr. Charles Muturia for his invaluable contribution to this work. He sadly passed on before the completion of this thesis. I am grateful for the assistance received during fieldwork from Zablon Mlawasi who prepared the field maps. I would also like to mention Joseph Chege, my field driver, and Gerald Njiru; the samples couldn't have arrived in Iceland without your help.

I couldn't have done it without the love and support from my family. To my wife Elizabeth Kiptoo, my daughter Precious Kiptoo and my son Ryan Too: You have been the source of my greatest inspiration and strength and I do not have enough words to thank you for enduring my absence all this time. To my parents, my dad who has a particular passion for academics and always encouraged me throughout my academic life. Thank you all for cheering me on.

Above all, I thank God for the innumerable mercies. I am grateful for the fortunes that I have and those that continue to be bestowed upon me!!!

1 Introduction

In zones of continental rifting, thinning of crust and rifting has been attributed to stresses linked to plate tectonics and asthenospheric magma upwelling and convection (Ebinger, 2005). It is not clear, however, which stress regime is predominant, but it is undeniable that magmatism plays a fundamental role in alteration of the thermal, chemical and mechanical properties of the crust leading to lithosphere break-up (Buck, 2006). The East African Rift System (EARS) is a good example of such a continental rift where magmatism and tectonism are intimately related, resulting in zones rich in geothermal resources. The EARS therefore provides opportunities and case study areas for understanding the interplay of geological processes, such as magmatic processes and magma-crustal interactions during rift evolution on a regional scale and on a volcano scale.

Geothermal systems benefit from magmatic processes and accompanying intrusives as their heat source. The intrusive activity also induces crustal fractures and faults, enhancing permeability and hydrothermal fluid flow (Sibson, 1994, 1996; Zhang et al., 2003). This simplified model explicitly shows the strong link between the occurrence of high-temperature geothermal resources, magmatism, intrusive activity and tectonic processes. The investigation of these geological processes on a volcano scale is therefore vital for improving conceptual models for geothermal exploration and exploitation in an area, in addition to helping with geohazard risk evaluation and elucidating the underlying crustal structure. In this study, I look into the specific aspects of these processes, focussing on eruptive history, magma generation, magma storage conditions and characterization of the hydrothermal system in the Paka volcanic complex.

1.1 The East African Rift System

The East African Rift System (EARS) is a mega scale classical continental rift structure traversing a total distance of 4000 km from Afar in the north to Mozambique in the south. The evolution of the EARS is structurally controlled whereby Miocene-Quaternary magmatism and rifting exploited the weak collision zone within Proterozoic mobile belts (Smith & Mosley, 1993). Three sources of stress have been modelled and attributed to rifting. According to Ebinger, (2012a) the continental break up such as experienced in the EARS can occur through tensional forces generated by (i) far field plate motions, (ii) pressure and stress gradients induced by asthenospheric upwelling (iii) or traction forces at the base of lithosphere produced by convecting mantle sufficient to thin the 100-250 km lithospheric plates. It is not clear which force is the predominant force but those related to far field as expected to be on a regional scale and possibly bigger.

The EARS is composed of two major arms/rift segments: the western (Albertine) and eastern (Ethiopia and Gregory rift). The eastern arm and the western arm are connected by the Aswa shear zone is 1000 km NW-SE trending structure with NE dipping plunge (Saalmann et al., 2016). The shear zone has affected the basement fabric of the Kenya rift which is thought to have influenced the orientation of some calderas in the northern Kenya rift. The eastern arm is the most volcanically active with high heat flow and voluminous volcanic material >

400000 km^3 over the last ~35 Ma. The spreading rate along the EARS varies along its segments: in the Main Ethiopian Rift it is 6.5 mm/yr. However, because of the rotation of the Victorian microplate, the spreading rate decreases from 4.1 to 1.6 mm/yr from south to north along the western arm, while it increases from 1 to 4.3 mm/yr along the eastern arm (Stamps et al., 2008).

Volcanism preceded rifting and was marked by flood basaltic eruptions occurring southwest Ethiopia and northern Kenya between 45 and 37 Ma based on Ar^{40}/Ar^{39} dating (Ebinger, 2012a; Knight et al., 2003). Rifting in the EARS was initiated at the Gulf of Aden at ~35 Ma, followed by period of uplift and volcanism. At 25 Ma rifting activity shifted to Turkana area and then progressed into southern Ethiopia. At 23-25 Ma the activity again shifted to Red sea and the Gulf of Aden. During 18-20 Ma activity begins at Suguta in Kenya and western rift initiates at this period.

The Kenya rift is denoted by numerous volcanic centres broadly classified as axial centres and off axis centres. They can further be classified as caldera centres and those with no visible calderas. Kenya volcanism is predominantly trachytic compared to Ethiopian rift where rhyolites dominates. Kenyan volcanoes south of the equator e.g. Menengai are larger and produced voluminous pyroclastic deposits that can be traced up to 100 km across. Those in the north e.g., Paka are smaller and dominated by basalt flows.

1.2 The study area

The Paka volcanic complex is located south of Silali in the northern segment of the Kenya rift (Figure 1.1). The Paka volcano is characterized by a small 1.5 by 1.6 km caldera (Dunkley et al., 1993) with a maximum subsidence of 200 m. The main fault structures in the area strike NNE-SSW and N-S (Mibei et al., 2021a). The rocks in the area are alkaline and include basalt, trachyte, mugearite lavas and pyroclastic deposits.

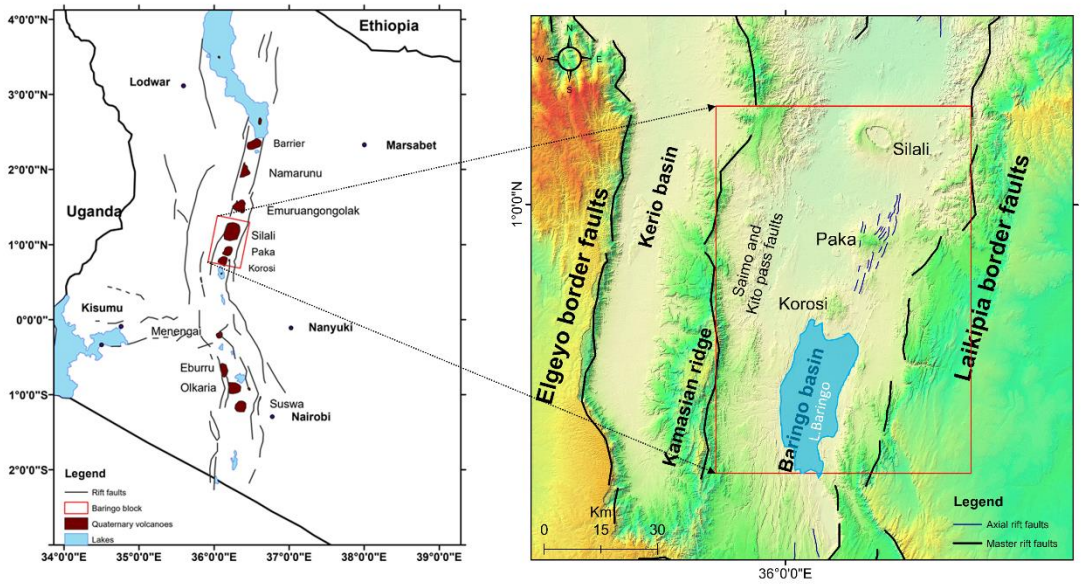

Fig. 1

Figure 1.1 The location of Paka volcanic complex within the Northern Kenya rift.

1.2 Previous work in Paka

Previous work on the geology of Paka volcano was carried out by Sceal in the 1960s as part of a PhD under the auspices of the East African Geological Research Unit (EAGRU). The EAGRU framework resulted in a geological report on Paka volcano and Laikipia (Sceal, 1974). This work formed the first detailed account of Paka geology, showing the main rock types in the area as basalt, intermediates (mugearite and benmoreite) and trachyte. It provided the first description of the stratigraphy and geological history, however hampered by the lack of radiometrically dated rock samples. The general geology of the area outlined by Sceal (1974) has since then been revised by Dunkley et al. (1993) and Mibei et al. (2021a). The latest work was centred around providing an improved stratigraphic framework and geological history of the area.

The geochemical study conducted by Sceal and Weaver (1971) described major and trace element compositions of the rocks. It indicated that main rocks in the area were alkaline and proposed that fractional crystallization was the main magma differentiation process in Paka. The findings also indicated that eruptions from the multivents were cogenetic based on geochemical trend in major elements. A broad description of a range of volcanoes in the Kenya Rift, including Paka, is contained in Williams et al. (1984), which is largely built upon Sceal's work. A later review of the early geological work was done by Hackman (1988) in his geological study of the Baringo-Laikipia area, which provided an overview of the regional volcanic setting.

Geothermal energy exploration in the area was carried out by the British Geological Survey (Dunkley et al., 1993), giving rise to an extensive report on "geothermal activity and the geology of the northern sector of the Kenya Rift". The findings provided detailed geological description of the geothermal prospects north of Lake Baringo, which included Korosi, Chepchuk, Paka, Silali, Emuruangogolak, Namarunu and the Barrier volcano. The report identified these centres as possible sites for geothermal energy exploitation, warranting further detailed work, especially geophysical and hydrogeological studies. The study improved the resolution of the Paka stratigraphic history by providing four radiometric dates.

Fluid and gas geochemical studies in Paka (Darling et al., 1995) indicated that thegeothermal fluids are of meteoric origin and consititute a mantle-degassed fluid componentas evidenced by 3He/4He values of 6 RA. The most recent geothermal review work, focussing mainly on geology and geochemistry, was carried out in 2007 and 2010 by KenGen and GDC and resulted in several conference papers (e.g., Kipngok & Nyamongo, 2013; Mulusa, 2015; Mutonga, 2013). Geophysical studies by Mwakirani (2011) indicated a 400 m thick resistive body (100 Ωm) from the surface, followed by an 800 m thick conductive layer (10 Ω. m) within the Paka summit area, suggesting a possible geothermal reservoir zone below 1200 m depth from the surface. A more recent study (Lichoro et al., 2017) largely confirms the results of Mwakirani (2011) that the geothermal reservoir is located below ~1000 m depth. A review by WJEC & MMTEC (2017), as part of technical assistance to GDC, showed pronounced vertical conductive bodies from surface to larger depths on the western and eastern sides of the Paka Volcano, which display linear patterns inferred to be sediments. A geothermal reservoir was delineated by resistivity of 30-50 Ω.m (900-2000 m), while a deeper resistive body of >200 Ωm at >2000 m depth was modelled as an intrusion. Gravity data, on the other hand, show dense bodies within the central area and low-density bodies in the west and east; indicating the volcanic axis and possible sediment deposits, respectively.

InSAR studies by Biggs et al. (2009) gave interesting results showing that the Paka complex experienced periods of inflation from 2006-2008, while no deformation was observerd 1997-2000. Recent InSAR studies (Using Envisat ASAR and TerraSAR –X) (Friese, 2015; Friese et al., 2014; Sudo et al., 2017) corroborated the findings of Biggs et al. (2009). The results of Envisat ASAR demonstrated ground uplift of 35 mm per year from 2006-2008 and a stable period from 2008-2010. The Terra SAR-X showed 20 mm ground subsidence in March to July 2013 followed by a stable period. The movements appear episodic with source depths estimated between 1.3-5 km (Biggs et al., 2016). These inflation/deflation events were possibly associated with magma injections and build-up/release of volatiles and gases in the hydrothermal system. The movements occurred in the east, northeast and southern parts of the Paka caldera.

1.3 Research background

Previous efforts at outlining the geological history of Paka volcanic complex (Dunkley et al., 1993; Sceal, 1974) were much constrained by scarce radiometric dates. Their detailed sequence of volcanic events and stratigraphic framework, therefore, has inherent inconsistencies leading to uncertainities in the volcanic evolution history of Paka volcano. Moreover, geochemical studies (Sceal & Weaver, 1971) are limited in detail and, therefore, magma genesis, magmatic evolution and storage conditions of Paka magma are poorly

constrained. Recent studies in Paka complex have mainly focused on geothermal exploration, albeit largely as surface studies. This means that knowledge of buried lava formations and hydrothermal alteration mineralogy is lacking. The consequences of the aforementioned knowledge gaps are four key issues which I aim to address with this project:

1. Accurate eruptive history and evolution model: the collapse and age of the Paka caldera
2. Knowledge of the buried volcanic sequence and hydrothermal alteration, and geothermal system characterization
3. Magma storage conditions beneath Paka volcano
4. Magma generation and evolution in the mantle and crust

This will generate vital information contributing to the understanding of the volcanic complex, including the underlying crustal structure, geological history and evaluation of geohazards, especially after recent periods of unrests. The study is also aimed at improving the geothermal conceptual model for exploration and exploitation of the geothermal resource.

The four issues above have been allocated to the first and second subsections of this research study. They are:

i. Magma evolution and eruptive history
ii. Assessment of the geothermal system

The first subsection of this study aims at addressing three questions:

1. What is the source depth(s) and degree of partial melting for Paka eruptive parental magma(s)?
2. What are the magma temperatures and storage depths?
3. What are the eruptive sequences, volumes and associated heat flux for Paka magmatic activity?

While the second subsection addresses the three questions of:

1. What hydrothermal alteration minerals characterize the Paka system?
2. What are the possible temperatures of the geothermal reservoir?
3. What temporal changes have occurred in the Paka reservoir?

1.4 Aims and objectives

The overall aim of the research is to establish the magmatic evolution, eruptive history of Paka volcano and the nature of the Paka geothermal reservoir. The specific objectives as labelled in Figure 1.2 are:

1. To carry out detailed geological mapping and build a new stratigraphic framework combining the mapping data with radiometric dates from recent work (Friese, 2015; Friese et al., 2014; Sudo et al., 2017), including earlier published work of Dunkley et al. (1993).
2. To determine the eruptive history, bulk volumes and the associated heat flux for the Paka volcanic complex.
3. To carry out geochemical numerical and thermobarometric models to determine magma genesis, magmatic processes, magma temperature and storage conditions in the Paka volcanic complex.

4. To characterize the Paka geothermal reservoir in terms of hydrothermal alteration and reservoir temperatures

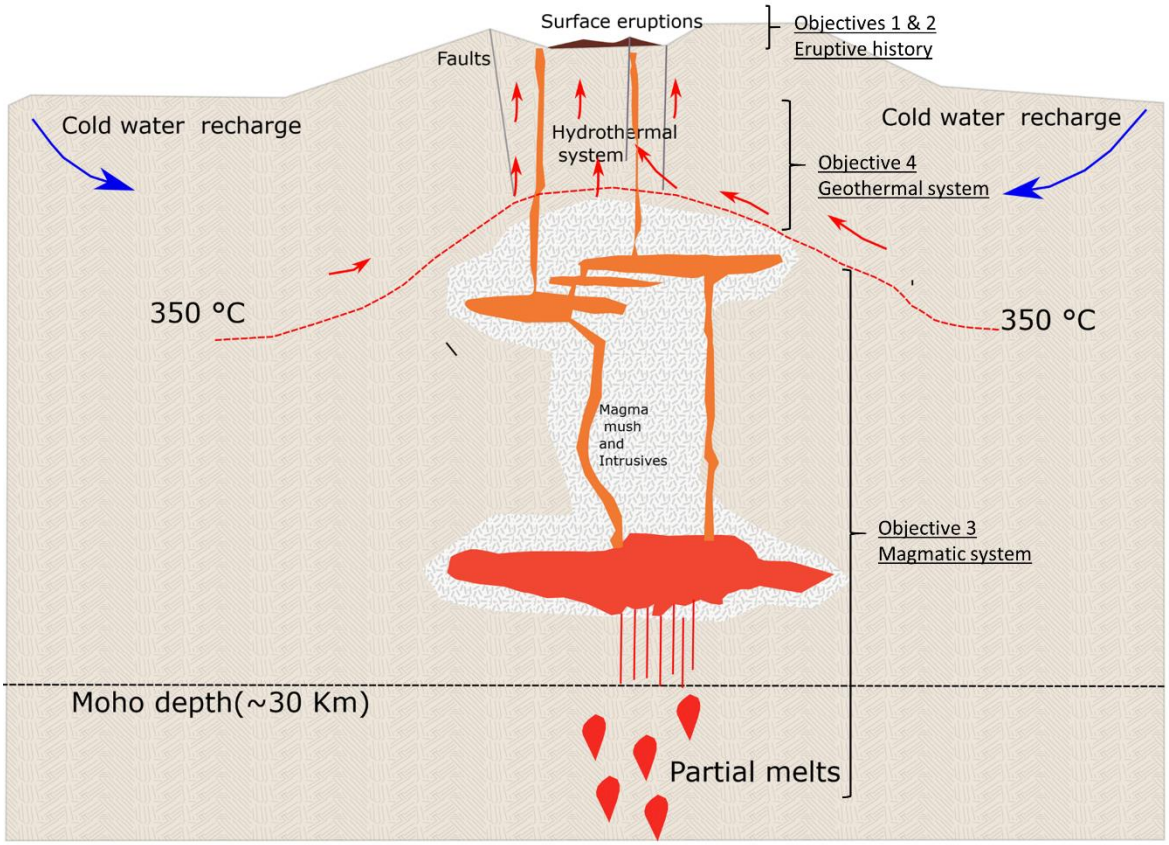

Figure 1.2 Conceptual model of a volcanic system (modified from Ranta et al., 2021), showing the main research objectives.

2 Approach and methodology

The project was partly carried out following the surface mapping and geochemical modelling approach of (Hutchison, Pyle, et al., 2016; Jung et al., 1998; Ngongang et al., 2015). Surface mapping, which led to a new stratigraphic framework, was used to generate a series of time-reconstructed eruptive maps of the Paka caldera. The purpose was to illustrate the progress of volcanism starting with the plateau period followed by the pre-caldera, syn-caldera and post-caldera periods, and explicate eruptive dynamics. Major and selected trace element concentrations from bulk rock analysis were used to model petrogenesis and magma processes in Paka, where the most primitive Paka basalt was used as the parental/source composition. The elemental trends were used to shed light on whether the multivent lava eruptions in the area are co-genetic or otherwise. Mineral-melt pairing was used in geothermobarometry and hydrometry modelling. Olivine, plagioclase and clinopyroxene geothermometers were applied with bulk rock compositions as the liquid composition. In clinopyroxene geothermobarometry, however, melt inclusions were also used as the liquid composition.

In carrying out this study, 36 samples were analysed (Tables 1 and 2). For data completeness and interpretation, additional major element data from seven samples and selected trace

elements from 50 samples were adopted from Sceal and Weaver (1971). A further 22 samples from borehole drill cuttings (Table 3), sampled at 2 m interval from a ~2550 m deep well (PK-01), were used to establish and characterise the underlying rocks of Paka, correlate lithologies at the surface and in the subsurface, and to determine the thickness of Paka edifice formations. Detailed analyses of hydrothermal alteration minerals from the well were used in establishing the hydrothermal alteration zonations, reservoir temperatures and temporal changes in the geothermal system.

2.1 Data review and Fieldwork

Field mapping was carried out between June-August 2018 with the aim of collecting samples and doing field observations and measurements. Digital geological mapping and data integration were undertaken with the use of ArcGIS and QGIS. This involved the analysis of Google Earth images and Hillshade DEM maps developed from 30 m resolution Shuttle Radar Topography Mission data (SRTM GL1). A total of 36 rock samples were collected (Figure 2.1) (Appendix A) from previously sampled locations, which had published radiometric dates (Dunkley et al., 1993; Friese, 2015; Friese et al., 2014; Sudo et al., 2017). The approach was to integrate all published $^{40}Ar/^{39}Ar$ radiometric dates from these previous works with our field observations and the chemical analyses of surface rock samples.

We reviewed and reinterpreted key surface data sets, including MT resistivity data, soil gas (CO_2 concentrations) and shallow temperature measurements, as well as spatial distribution of geothermal manifestations (Kipngok & Nyamongo, 2013; Lichoro et al., 2017; Mwawasi, 2012). Furthermore, detailed analysis of drill cuttings from well PK-01 (marked red in Figure 2.1) was also carried out. The well was drilled to a total depth of 2552 m and logged at 2 m interval (Lopeyok, 2019). The well analysis was carried out to assess the hydrothermal alteration mineralogy and provide some insights into the reservoir temperatures. There were, however, some limitations to well lithological data as significant losses of cuttings were experienced in the well column (Mibei et al., 2021a).

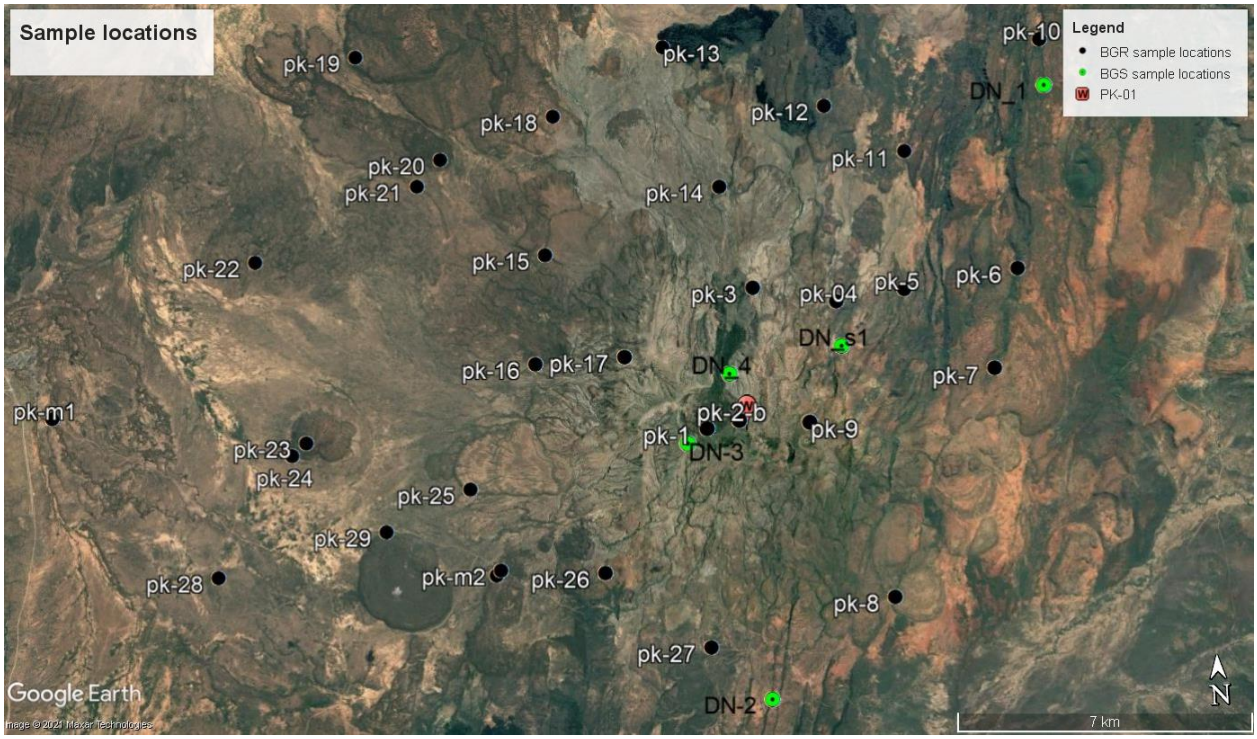

*Figure 2.1 Sample locations. The red point shows the location of well PK-01. Locations labelled DN were previously sampled by Dunkley et al. (1993), while those labelled pk were sampled by Friese (2015).*BGS-British geological survey, BGR-German Federal Institute for Geosciences and Natural Resources.*

2.2 Sample Preparation

The field samples were transported from the field and packaged in a metal box at GDC offices in Nakuru, while the well cutting samples were packaged in small plastic containers and exported to Iceland. Prior to the in-depth chemical analyses, hand specimen of samples were physically examined and selection of samples for further analyses was carried out. Cuttings samples for thin sections were selected from geothermal reservoir depths, i.e., below 400 m, based on the degree of alteration as noted from binocular analysis. In total 10 samples were selected for thin sections, 11 samples for XRD analysis and 3 samples for electron microprobe analysis (EMPA) analysis. In addition, quartz and calcite crystals were selected from 1388-1390m and 2550-2552 m depths for microthermometry and Raman spectroscopic fluid inclusion analysis. From the surface samples, 13 samples were selected for EMPA. Whole rock chemical analysis was carried out on all the samples from the surface and from well PK-01.

2.3 Analytical methods

2.3.1 Binocular microscope analysis

The initial assessment of sample cuttings was carried out using a stereo-microscope and the rock type and hydrothermal alteration minerals were recorded. Binocular analysis of borehole cuttings was done with an Olympus SZX12 stereo microscope at the Iceland GeoSurvey (ÍSOR). It involved washing the samples thoroughly with tap water to remove dust and impurities to enhance visibility. Small sample holder boxes containing the cleaned samples were then observed under the binocular microscope, one at a time. The physical properties of the rock cuttings, which include the colour, texture and grain size, rock fabric, primary mineralogy, secondary/alteration mineralogy and rock type, were then recorded. Other features like oxidation, intensity of alteration, vein fillings, intrusions and various litho-stratigraphic boundaries were also identified. Selected samples were then processed and prepared for further analysis using additional analytical techniques.

2.3.2 Petrographic microscope analysis

A total of 35 thin sections from both the surface samples (26) and borehole samples (9) were prepared and analysed at the University of Iceland and at ÍSOR. Thin sections were prepared by mounting a freshly cut piece of rock onto a glass slide of 27 x 46 mm with epoxy. In the case of the borehole cuttings, the samples were first impregnated with epoxy prior to cutting and glass slide mounting. The sections were then ground down to a thickness of 30 μm and then polished with aluminium oxide powder, followed by diamond paste in two steps, an initial Kemet Diamond Compound 3-KD-C2 of 3 microns followed by Kemet Diamond Compound 1-KD-C2 of 1 micron. Petrographic microscope analysis of thin sections was performed using a polarizing microscope fitted with a camera. The microscope included both transmitted and reflected light and is equipped with objective lenses of 2x, 4x, 10x and 20x magnification. This analysis was done to further determine physical and alteration properties of the rocks noted in the binocular analysis. In addition, the analysis helped to identify additional alteration minerals not observed by the binocular microscope and clearly identify the possible depositional sequence of the alteration minerals.

2.3.3 Inductively Coupled Plasma Optical Emission Spectroscopy (ICP-OES)

Whole-rock chemical analysis was carried out at the Institute of Earth Sciences, University of Iceland using an ICP-OES (SPECTRO CIROS VISION). A total of 36 surface samples and 22 borehole sample cuttings were analysed (Tables 1-3). Fresh surface samples were broken into smaller pieces with a hammer, paying close attention to avoid any contamination, and weighed. Fifty grams of broken rock pieces were further crushed in a Retsch BB100 Mangan jaw-crusher. The crushed mixture was then sieved and about 2 grams of 1 mm grains were collected and ground to a powder in an agate mortar. The borehole sample cuttings went directly for the agate mortar grinding stage. The rock powder was then mixed with $LiBO_2$ flux in a carbon crucible with a sample to flux mass ratio of 2:1. The

reference samples A-THO, B-THO and B-ALK, which have previously been calibrated relative to USGS standards, were used for instrumental calibration. A-THO is an obsidian from Hrafntinnuhryggur. More or less pure glass. B-THO is from the same source as BIR-1 (USGS standard), it is an interglacial lava flows often referred to as the Reykjavik dolerites. B-ALK is some basalt from Eldgjárhraun. For the reference samples, 500 mg of LiBO2 and 250 mg of sample were weighed in a crucible. A selection of in-house international standards (K-1919, BIR-1, JA-2 and RGM-1) were treated the same way as the unknown samples. The weighed samples and standards in the crucibles were placed in a Lindberg/Blue oven at 1000°C for approximately 30 minutes. The resulting glass beads were dissolved overnight in small plastic bottles containing 5 vol% HNO_3 (nitric acid), 1.33 vol.% HCl (hydrochloric acid) and 1.33 vol.% saturated $H_2C_2O_4$ (oxalic acid). Accuracy (2σ) was systematically calculated for each major and trace element based on repeated measurements of the standards. The largest 2σ values for each element were chosen to represent the largest instrumental error. Accuracy was generally better than ± 0.70% for major elements and < 4.62 ppm for trace elements. The detection limit of the ICP-OES instrument for trace elements is close to 20 ppm. Results were reported on a volatile-free basis and normalized to 100 wt.%, expressing the total iron as FeO^t.

2.3.4 Petrography and Electron Micro-Probe Analysis (EMPA)

From the 36 surface samples collected, 12 fresh lava and tuff samples were selected for EMPA of which three were from the summit area, four from the southwest, three from the northeast and three from the northwest of the volcano. The samples include basalt, hawaiite, mugearite, benmorite and trachyte of varying ages spanning 582-11 ka. In addition, three borehole cutting samples were selected from different depths (910, 1180 and 2254 m) for EMPA. Selected thin sections were coated with a fine 25 nm thick carbon film. The carbon film acts as a conductive media to deplete excess charge produced by the electron beam during electron microprobe analysis. The sections were always kept in a dust-free cabinet with a constant humidity of <20% in order to avoid the deposition of impurities.

The instrument used for the EPMA is a JEOL JXA-8230 Super Probe equipped with five wavelength dispersive spectrometers (WDS), each with two different analytical crystals, except one spectrometer which has four. The instrument also has an energy dispersive spectrometer with a silicon drift detector (SDD-EDS). This instrument is at the Institute of Earth Sciences, University of Iceland. An acceleration voltage of 15 kV and a current of 5 nA for silicic glass, 10 nA for basaltic glass and feldspars, and 20 nA for olivine, pyroxene and Fe-Ti oxides was employed. The secondary standards used to monitor the quality of the analyses were Basalt Glass A-99 (NMNH 113498-1 from the Smithsonian Institution) for glass analysis, Plagioclase (Astimex Standards Ltd) for plagioclase, Olivine Springwater meteorite (USNM 2566, Smithsonian Institution) for olivine and Augite (Cr) (NMNH 164905, Smithsonian Institution) for clinopyroxene. The CITZAF program (Armstrong, 1991) was used for corrections, except the ZAF correction program was used for oxides. The mineral compositional data set includes 164 spot analyses of olivine grains, 445 spot analyses of plagioclase grains, 456 spot analyses of clinopyroxene, 18 spot analyses of melt inclusions and 10 spot analyses of groundmass glasses and 136 of Fe-Ti oxides from surface samples. Of the boreholes samples, 20 spot analyses of pyrite, 17 spot analyses of epidote and 5 spot analyses for chlorite clay were acquired. The complete raw analytical data are provided in Appendices C and D (Tables 4-6).

2.3.5 X-Ray powder diffractometry analysis

Clay sample preparation and analysis were carried out at the Iceland GeoSurvey (ÍSOR) laboratories. The sample preparation involved washing of each selected sample in distilled water. Eleven samples were selected at different depth ranges from the well strata. About 4 grams from each selected depth range was placed in a glass test-tube nearly filled with distilled water and agitated in a mechanical shaker for about 6 hours. The slurry was left to settle for about 10 minutes and then suspended clay fraction transferred onto a glass-slide. The samples were left overnight to dry at ambient temperature and humidity.

The analysis was undertaken using a Bruker AXS D8 XRD machine. The equipment parameters were set at Cu Kα radiation with a wavelength of 1.54 Å at 40 kV and 40 mA. The detector used was a NaI scintillation counter. Each sample was measured from $2\Theta = 2–14°$ in 0.02° increments (steps) and measured for 1 second in each step, each measurement taking about 20 minutes. Analyses were in triplets for each sample as; airdried, glycolated and heated sample (550 ºC for 1hr). The results in Table 3.1 are a summary of identified clay types. Identification of various types of clays in well PK-01´s lithological column was important in characterizing the shallow and deeper sections of the geothermal system.

2.3.6 Microthermometry and Raman spectroscopy

Fluid inclusions provide information about physicochemical conditions from the time when the fluid was trapped in mineral grains. This information is obtained through microthermometry and Raman spectroscopy. Microthermometry was carried out to obtain the homogenization temperatures (T_h) and ice-melting temperatures (T_m) of fluid inclusions, while Raman was used to identify chemical species within the fluid inclusions. Sample preparation for both microthermometry and Raman spectroscopy involved a careful selection and polishing of secondary quartz and calcite crystal grains, selected from 1388-1390 m and 2550-2552 m depths of well PK-01. The samples were then double polished using 1200 and 4000 grit sand paper.

Upon confirmation of the presence of clear fluid inclusions by using a petrographic microscope, the crystals, one at a time, were slowly heated on a Linkam THSMG 94 freezing and heating stage fitted on the stage of a Leitz Laborlux microscope at Iceland GeoSurvey (ÍSOR) laboratory. During the initial stage, the heating rate was 20 °C per min up to 200 °C and 10 °C per min at later stages where heating progressed slowly until homogenisation temperature (T_h) was achieved (i.e. bubble disappears) and the T_h was measured. The quartz and calcite T_h data were recorded and presented as kernel density estimate plots. The ice-melting temperature (T_m) measurements, on the other hand, were carried out at the Institute of Earth Sciences, University of Iceland with the same instrument. The transport of the instrument was necessary because of the availability of liquid N_2 for cooling of the stage. The T_m was obtained in four steps. First, freezing was done by cooling the inclusions to -40 °C and held for 2 min (at rate of -10 °C/min) at these conditions until the observed inclusions were frozen. The heating was then done slowly at 10 °C/min to -10°C and held at that point for 1 min. The sample was then heated further at a slower rate (5°C/min) to -2° C and held for 1 min. The last step was the progressive slow heating (2°C/min) towards 0° C, during which melting was observed and recorded.

Raman spectroscopy was used to identify the chemical components of the fluid inclusions. This is a vibrational spectroscopic method that relies on the inelastic scattering of photons on molecules. Molecular vibrations related to covalent bonds give a characteristic spectrum for each phase present (Bodnar & Frezzotti, 2020; Frezzotti et al., 2012). Raman spectroscopy was carried out with the use of a HORIBA LabRAM HR Evolution spectrometer at the Innovation Centre in Iceland. A total of seven fluid inclusions were analysed, four inclusions from the 1388-1390 m depth range and three inclusions from 2552-2554 m depth. The measurement conditions were: a laser power of 100%, acquisition time of 60s, accumulation 3 times to avoid electric spikes in the spectra and Real Time Display (RTD) of 1s with grating of 600 mm and a magnification 50x. The liquid part of the inclusions was analysed at 2800-3000 cm^{-1} spectral range to determine the nature of the liquid. Gas bubbles were analysed at spectral range of between 1000-2400 cm^{-1} to determine whether CO_2 (1200-2000 cm^{-1}) and H_2S (2200-2400 cm^{-1}) were present. Solid phases were analysed within a spectral range of 1000-1500 cm^{-1} in order to determine if they were sulphates (1020 cm^{-1}) or calcite (700-1500). Mineral mapping was also carried out in one of the inclusions from 1388-1390 m. Peak positions were determined by polynomial fitting and saved as text for plotting and presentation.

2.4 Data analysis

2.4.1 Numerical modelling of magma generation and magma processes

Quantitative modelling of different magma processes by use of trace element concentrations was carried out using suitable numerical models. The models are used to assess partial melting, fractional crystallization and assismilation process in Paka magma. The trace elements La and Y were selected for these models due to the fact that they are incompatible and also immobile in the geothermal fluid. Thus, their concentrations are not affected by geothermal or surface alteration in this volcanic system. The degree of partial melting (non modal) during magma generation was evaluated by employing the Rayleigh equation (1)(Shaw, 1985):

$$\frac{C_l}{C_o} = \frac{1}{D_o + F(1-P)} \quad (1)$$

where C_l is the concentration of an element in melt, C_o is concentration in primitive melt, D_o is the bulk partitioning coefficient in the crystallizing phases, F is melt fraction and P is the mode of melting.

The effect of fractional crystallization, on the other hand, was modelled using equation 2 (Neumann et al., 1954).

$$\frac{C_l}{C_o} = F^{D-1} \quad (2)$$

where the parameters are the same as described above.

To simulate coupled assimilation and fractionation (AFC) scenarios, the AFC equation 3 (DePaolo, 1981) was used.

$$C_l^{AFC} = C_o \left[F^{-z} + \left({}^{r}/_{r-1}\right) {}^{C_a}/_{zC_o} \left(1 - F^{-z}\right)\right] \quad (3)$$

The coupled assimilation and fractionation (AFC) equation 3 is similar to the fractional crystallization equation 2 with parameters as explained earlier for equation 1. The additional component $r = m\_a/m\_c$ is the ratio of the concentrations of a selected trace element in the assimilated material (m_a) and in the crystallizing magma (m_c). The value $z = (r + D - 1)/(r - 1)$ is related to the relative ratio and the partition coefficient (D) described above.

2.4.2 Geothermobarometry and hygrometry models

Post-entrapment data *correction of melt inclusions (MIs)*

The chemistry of melt inclusions can undergo major re-equilibration by crystallization and diffusion of elements after being trapped in a macrocryst (e.g.,Cottrell et al., 2002; Danyushevsky et al., 2000). This is due to changing physicochemical conditions, i.e., temperature and pressure. In olivine-hosted inclusions there are commonly concentration changes in FeO and MgO. In clinopyroxene-hosted melt inclusions modifications mostly affect FeO, Al_2O_3 and CaO, while in plagioclase the modification is mainly in the Al_2O_3 content, which requires simultaneous changes in SiO_2, CaO and Na_2O because of coupled substitution and charge balance considerations. These post-entrapment modifications can, in the most extreme cases, totally obscure the original melt chemistry (Lynn et al., 2017; Thomson & Maclennan, 2012) and affect the mineral geothermobarometry. To correct for these changes post-entrapement corrections (PEC) are carried out on the raw melt inclusion data. To correct the clinopyroxene-hosted inclusions, major elements in the mineral phase were added to the glass composition iteratively at a rate of 1% until equilibrium is achieved (Neave et al., 2019), e.g., the Fe-Mg exchange equilibrium constant (Kd) value of 0.27 ± 0.03 is attained. The new values for FeO, Al_2O_3 and CaO obtained were considered to be the original values prior to the modification. Post-entrapment corrections for 80% of the samples required adjustments in the major element chemistry between 1-4%, the rest required adjustments of between 21-37%.

Geothermobarometry

The assumption that crystals grow at or near equilibrium conditions within a magma reservoir is the foundation of mineral-melt thermobarometry calculations. Our modelling followed the approach presented by Putirka (2008). Mineral compositions (both cores and

rims) were paired to putative equilibrium liquid compositions to fully understand the evolution of magma storage conditions (P–T) within the crust (e.g.,Halldórsson et al., 2018). We used mineral core and rim compositions with the intent of capturing both the last equilibrium state of the system before eruption and earlier stages to obtain the complete evolution of the crystal cargo. The selection of groundmass glass and whole rock samples depended on whether they followed the rock compositional trend/liquid line of descent (LLD) for Paka rocks. The whole rock compositions satisfied this criterion (Mibei et al., 2021). The groundmass glass, however, did not. This can be attributed to the almost holocrystalline nature of our samples, and finding large enough groundmass glass pockets for the EMPA beam was not possible without contamination by the nearby crystals. Although some groundmass glass compositions followed the LLD, they were not considered for modelling, because none of the crystal compositions showed chemical equilibrium with them. To implement our models, samples were divided into three groups, i.e., basalts (basalt, hawaiite), intermediates (mugearite, benmorite) and trachyte.

Basalts and intermediates thermobarometry

For basalts and intermediate rock samples, I used the clinopyroxene thermobarometer, plagioclase thermobarometer and hygrometer and the olivine thermometer. In the clinopyroxene geothermobarometer of Putirka (2008) and Neave and Putirka (2017) equation 33 is renamed here as equation 4, the terms $[X_C^{\phi}]$ represent the mole fraction of component C in phase ϕ. The calculations are pressure-dependent where the input pressure is in kbar and utilizes the jadeite-diopside/hedenbergite exchange (Mollo et al., 2010; Putirka et al., 1996) (equation 4). The equilibrium criteria is determined by the difference between predicted versus observed clinopyroxene components EnFs, CaTs and DiHd which should be <0.05, <0.03 and <0.06, respectively, and the Kd value for Fe-Mg exchange should be 0.27 ± 0.03 (Mollo et al., 2010; Neave et al., 2019; Putirka, 2008). The SEE for pressure and temperature is ±1.6 kbar and ±45 °C, respectively.

eq.33

$$\frac{10^4}{T(K)} = 7.53 - 0.14\ln\left[\frac{X_{jd}^{cpx} X_{CaO}^{liq} X_{Fm}^{liq}}{X_{Cao}^{liq}\left(X_{AlO_{1.5}}^{liq}\right)^2\left(X_{SiO_2}^{liq}\right)^2}\right] + 0.07\left(H_2O^{liq}\right) - 14\left(X_{CaO}^{liq} X_{SiO_2}^{liq}\right) - 0.08\ln\left(X_{TiO_2}^{liq}\right) - 3.62\left(X_{NaO_{0.5}}^{liq} + X_{KO_{0.5}}^{liq}\right) - 1.1\left(Mg\#^{liq}\right) - 0.18\ln\left(X_{EnFs}^{cpx}\right) - 0.27P(kbar) \quad (4)$$

The plagioclase–melt thermometer, barometer and hygrometer equations 24a, 25a and 25b, of Putirka (2008) are renamed here as equations 5, 6 and 7, respectively The equation is pressure-dependent, and is solved by setting input pressures adopted from the clinopyroxene thermobarometer for each pair. The equilibrium condition for this model is Kd (An–Ab) value of 0.28 ±0.11. The SEE for temperature is ±36°C, and for H_2O content, the uncertainty is ±1.1 wt.%.

eq.24a

$$\frac{10^4}{T(K)} = 6.4706 + 0.3128\ln\left[\frac{X_{An}^{pl}}{X_{CaO}^{liq}\left(X_{AlO_{1.5}}^{liq}\right)^2\left(X_{SiO_2}^{liq}\right)^2}\right] - 8.103\left(X_{SiO_2}^{liq}\right) + 4.872\left(X_{KO_{0.5}}^{liq}\right) + 1.5346\left(X_{Ab}^{pl}\right)^2 + 8.661\left(X_{SiO_2}^{liq}\right)^2 - 3.341x10^{-2}\left(P(kbar)\right) + 0.18047\left(H_2O^{liq}\right) \quad (5)$$

eq.25a

$$P(kbar) = -42.2 + 4.94x10^{-2}T(K) + 1.16x10^{-2}T(K)ln\left[\frac{X_{Ab}^{pl}X_{AlO_{1.5}}^{liq}X_{CaO}^{liq}}{X_{An}^{pl}X_{NaO_{0.5}}^{liq}X_{SiO_2}^{liq}}\right] - 382.3\left(X_{SiO_2}^{liq}\right)^2 + 514.2\left(X_{SiO_2}^{liq}\right)^3 - 19.6ln\left(X_{Ab}^{pl}\right) - 139.8\left(X_{CaO}^{liq}\right) + 287.2\left(X_{NaO_{0.5}}^{liq}\right) + 163.9\left(X_{KO_{0.5}}^{liq}\right) \quad (6)$$

eq.25b

$$H_2O(wt\%) = 25.95 - 0.0032T(°C)ln\left[\frac{X_{An}^{pl}}{X_{CaO}^{liq}\left(X_{AlO_{1.5}}^{liq}\right)^2\left(X_{SiO_2}^{liq}\right)^2}\right] - 18.9\left(X_{KO_{0.5}}^{liq}\right) + 14.5\left(X_{MgO}^{liq}\right) - 40.3\left(X_{CaO}^{liq}\right) + 5.7\left(X_{SiO_2}^{liq}\right)^2 + 0.108P(kbar) \quad (7)$$

The olivine thermometer relies on equation 16 of Putirka (2008), which is renamed here as equation 8. Equilibrium was achieved when the Kd value (Fe–Mg exchange) became 0.3 ±0.03. The SEE of the thermometer is ±26 °C.

eg.16

$$T(°C) = -583 + 3141\left[X_{SiO_2}^{liq}\right] + 15779\left[X_{Al_2O_3}^{liq}\right] + 1338.6\left[X_{MgO}^{liq}\right] - 31440\left[X_{SiO_2}^{liq} \cdot X_{Al_2O_3}^{liq}\right] + 77.67[\mathrm{P(GPa)}] \quad (8)$$

Trachyte thermobarometry

Geothermobarometry and hygrometry of trachyte samples were retrieved from models specifically calibrated for evolved alkaline rocks, i.e., trachyte and phonolite (Masotta et al., 2013). The clinopyroxene temperatures and pressures were iteratively obtained using equation Talk 2012 and Palk 2012 renamed here as equations 9 and 10 below. To test for equilibrium, the Kd for Fe-Mg exchange and the Na# proposed by Masotta et al. (2013) were adopted. The SEE for this model is ±18.2 °C and ±1.15 kbar for temperature and pressure, respectively. Finally, the trachyte water content was calculated using an alkaline hygrometer (Mollo et al., 2015) shown in equation 11 below and has an uncertainty of ±0.7% wt. %.

eq.*Talk 2012*

$$\frac{10^4}{T(K)} = 2.91 - 0.4\ln\left(\frac{X_{jd}^{cpx} X_{Ca}^{liq} X_{Fm}^{liq}}{X_{DiHd}^{cpx} X_{Na}^{liq} X_{Al}^{liq}}\right) + 0.038(H_2O) - 1.64\left(\frac{\frac{X_{Mg}^{liq}}{X_{Mg}^{liq} + X_{Fe}^{liq}}}{X_{DiHd}^{cpx}}\right) + 1.01\frac{X_{Na}^{liq}}{X_{Na}^{liq} + X_{K}^{liq}} - 0.22ln\left(X_{Ti}^{liq}\right) + 0.47ln\left(\frac{X_{jd}^{cpx}}{X_{Na}^{liq} + X_{Al}^{liq} + \left(X_{Si}^{liq}\right)^2}\right) + 1.62\left(K_{D(Fe-Mg)}^{cpx-liq}\right) + 23.39\left(X_{Ca}^{liq} X_{Si}^{liq}\right) \quad (9)$$

eg.Palk 2012

$$P(kbar) = -3.89 + 0.28\left[\frac{X_{jd}^{cpx}}{X_{Na}^{liq} X_{Al}^{liq}\left(X_{Si}^{liq}\right)^2}\right] + 0.074(H_2O) + 5.01\left(\frac{X_{Na}^{liq}}{X_{Na}^{liq} + X_{K}^{liq}}\right) + 6.39\left(K_D(Fe-Mg)^{cpx-liq}\right) \quad (10)$$

$$H_2O(wt.\%) = -\mathrm{a} + \mathrm{b}\frac{10^4}{T(K)} - \mathrm{cln}\left[Si(Ti+Mg)^{liq}\right] + \mathrm{dln}\left[\frac{(Or^2)^{kfs}}{(CaK)^{liq}}\right] + \mathrm{eln}\left[\frac{(SiCa)}{(Fe+Ca)^2}\right]^{kfs} \quad (11)$$

3 Summary of results

3.1 Paper 1

In this paper we integrated all available 40Ar/39Ar radiometric dates along with field observations, remote sensing data, and the analysis of surface and cutting samples from a 2552 m deep borehole (PK-01). In aim to understand the geology and evolution of the Paka volcanic complex in a revised stratigraphic framework in setting a stage for further studies on its magma plumbing architecture and the geothermal system. Chemical analyses distinguish basalt, hawaiite, mugearite, benmorite, and trachyte rock type in Paka. It also indicates that the eruptive products are genetically related by fractional crystallization. Major element mass balance and Rhyolite-MELTS models are consistent with the trachyte being generated by 74-83% fractional crystallization of Paka basalt. Before the growth of the volcano, volcanic activity was characterised by plateau fissure eruptions at 582-405 ka. Eruptions directly related to the Paka edifice are divided into four different volcanic phase sequences. Sequences 1- 4 span the periods 390-278 ka, 247-205 ka, 160-36 ka, and 36-8 ka. The Pre-Paka plateau eruption products outcrop at the base of the volcano flanks and are overlain by edifice-forming trachyte. Initial caldera-related subsidence is expressed by arcuate structures to the west and southeast parts of the volcano. These initial collapses are associated with tuff and pyroclastic eruptions estimated to have occurred at ~38 ka. Following these explosive eruptions, a ~1.5 by ~1.6 km main caldera developed. The lithological information from the drilled geothermal exploration borehole PK-01 indicates a minimum thickness of ~2200 m for the extrusive lava sequences, with the uppermost 1050 m of the strata being directly related to eruptions from the Paka volcano (Phases 1-4). We estimate a minimum total bulk volume of ~50 km3 for the volcanic material erupted from Paka during the last ~390 ka. This translates to an average eruption rate of ~1.2 x 10-4 km3/yr. The associated advected magmatic heat supported an ‘excess’ heat flux ranging between 110-138 mW/m2 or about twice present day average continental flux (57 mW/m2) and about 1.3 times the background values (90 mW/m2) in geothermal areas. The apparent high heat flux implies a magma-driven geothermal system, where convection of the hydrothermal fluid is occurring above the heat source. Structural mapping revealed normal faults, strike-slip faults, lineaments, and an array of eruptive vents and domes as the main volcano-tectonic structures. We infer at least four faulting and fault reactivation events that have occurred during Paka geological history. The structural orientations in the area are dominated by NNE and NW with subordinate N-S and NNW striking structures. Evidence suggests that the intersection of NNE and NW trending structures may have had a major influence on the volcanism in the area.

3.2 Paper 2

The paper focuses on trace element modelling and mineral-melt geothermobarometry with the aim of determining magma generation source and magma storage conditions. This not only provides insights into shallow crustal structures and volcanic hazards in the wider East African Rift (EARS), but contributes to geothermal conceptual modelling. The magma storage depth is constrained by combining petrological and geochemical data with available geophysical models. Numerical trace element modelling suggests that the primary magma in Paka resulted principally from 5–10 % garnet–peridotite partial melting and possibly 0.1–1.5 % partial melting of spinel-lherzolite. The parental magma was probably held at the Moho (~30 km) and evolved by ~76 % gabbro fractional crystallization to generate a liquid of similar chemistry as that of erupted Paka basalts. We propose that under moderately oxidized conditions (ΔFMQ +1) the primary magma underwent a further ~70 % fractional crystallization and ~20 % assimilation of crustal syenitic material to generate Paka trachyte lavas. Basaltic and intermediate magmas were held at polybaric storage pressure conditions ranging between 1.4–7 kbar (5–25 km), at temperatures between 1086–1204 °C with relatively low water content of <1.8 wt.%. The trachyte magma resided at low pressures, i.e., 0.3–2.5 kbar (1–9 km) at 901–980 °C with water contents of 3.5–5.1 wt.%. Based on our data eruption source depths remained largely the same for a period spanning from 582–11 ka. Geophysical data show correlation with magma depths beneath Paka volcano.

3.3 Paper 3

Here I focus on the Paka geothermal system based on detailed analyses of well PK-01 and a review of surface data. Early geothermal studies carried out in the 1990s (Dunkley et al., 1993) confirmed the existence of a high-enthalpy geothermal resource at Paka. Later studies were done in 2004 by KenGen and in 2010 by GDC, culminating in exploration drilling. In May 2019, the first full exploration well, PK-01, was completed. This was followed by the second well (PK-02) and third well (PK-03) drilled between July-September 2019 and January-June 2020, respectively. Integrated geoscientific data sets, including resistivity anomalies, soil gas (CO_2 concentrations) and shallow temperature measurements, as well as spatial distribution of geothermal manifestations and faults. We suggest that Trachytic and basaltic volcanic material erupted from ~390 ka to Holocene coalesced to form the 136 km2 active volcanic edifice of Paka on top of an older ~580 ka plateau eruptive sequence. The latter constrains the maximum age for the Paka geothermal system manifested mainly as surface fumaroles and hot altered grounds. Analyses of well PK-01 show that the upper part of the well (0-1050 m) is exclusively a trachyte lava sequence while the lower part (1050-2552 m) penetrates sequences of trachyte, intermediate, basaltic and syenite intrusive rocks. Temperature attained in the well based on hydrothermal alteration assemblage vary from ~180 °C at 400 m depth where quartz was first observed in the drill cuttings to >220°C within the chlorite-illite zone at 700m and 280 °C below 1450 m in the actinolite-epidote zone. Fluid inclusion homogenization temperatures (Th) range widely between 211-286°C at 1390 m and 209-271°C at 2550 m. Fluid inclusion indicate that the reservoir fluid from the paleo system was bicarbonate-rich and of very low salinity according to ice-melting temperature, which is comparable to aqueous fluid discharge from the well and therefore has

remained stable in terms of chemistry over time. Stabilised well temperature increases with depth to a maximum of 245 °C at 1800 m depth where a reversal occurs and becomes nearly isothermal at 230 °C, then increases slightly below 2200 m before an inversion to about 220°C. The main high-temperature geothermal system is hosted within the lower part of the well (1050-2552 m). It is probably steam-dominated above 900 m depth where calculated formation temperatures intersect the boiling point curve for pure water, and liquid-dominated below 900 m. Suitability modelling from surface data integration indicates that the most suitable area (P90) for geothermal development is within an area of 12 km2 in the summit area and northeast of the Paka caldera. The up-flow of the Paka system is postulated to be located closer to well PK-03 than the other two wells while the out-flow in the area is mainly northwards largely controlled by NNE and N-S faults

4 General summary and conclusions

The following summary and conclusions can be drawn from this study.

- New and detailed stratigraphic framework suggests four main volcanic sequences within the Paka edifice, in addition to one older pre-Paka or plateau eruptive phase
- The volcano-tectonic evolution of Paka is characterised by progressive faulting from the east during the Pliocene towards the axial rift zone in the Quaternary period
- The Paka geothermal system is younger than ~582 ka based on the oldest dated eruptions in the area. The build-up of the Paka edifice started at ~390 ka, with progressively centralised magma eruptions from deep and shallow magma chambers, with a caldera collapse at ~38 ka
- It is estimated that a minimum total bulk volume of ~50 km^3 was erupted from Paka during the last ~390 ka. This translates to an average eruption rate of ~1.2×10^{-4} km^3/yr, which is five times less than that of the Menengai volcano one of the largest volcanoes in Kenya where Geothermal exploration is ongoing
- Heat flux of 110–138 mW/m^2 is produced by the Paka magmatic activity. This compares favorably with heat flux measurements from boreholes around Paka, indicating 129 mW/m^2, but lower than what was measured in the Menengai area (190 mW/m^2)
- The Paka primary magma is sourced from garnet peridotite by 5-10% partial melting.
- Paka is dominated by trachyte, which is generated by 74–83% fractional crystallization of a basalt parent and 20% crustal assimilation of syenite.
- The crystallization pressures estimated for basaltic magma range between 1.4-7 kbar (5-25 km) at temperatures of 1125 -1204 °C, and for the intermediate rocks ~3-7 kbar and a lower temperature of 1060-1140 °C
- The crystallization pressures estimated for trachyte magma range between 0.3-2.5 kbar (1-9 km) at temperatures of 901-980 °C
- The Paka magma evolved at a moderately oxidized conditions (ΔFMQ +1) and were sourced from a long-lived magma reservoir at deep to shallow crustal depths. The shallow crustal depths were estimated to be between ~3-5 km, which compares well with the magma depths of 2.8-5.2 km modelled from recent geophysical observations
- Based on well PK-01 the geothermal reservoir is below 700 m within the chlorite-illite zone and the actinolite-epidote zone. The reservoir measured temperature range between 245-271 °C, fumarole geothermometry however indicate higher temperatures of 305 °C in Paka
- Three hydrothermal alteration zones are revealed: the zeolite-smectite, chlorite-illite and epidote-actinolite zones.
- The melting temperatures (T_m) of fluid inclusions range between 0 to -0.1°C, indicating low salinity for past geothermal fluids

- The reservoir is water-dominated with low salinity and is of the $NaHCO_3$-type. The chemistry has remained stable over time. The geothermal reservoir temperature has, however, seen fluctuations with time. The current formation temperatures are lower than estimated for the system at some earlier stage.
- The geothermal upflow is located beneath the summit area close to well PK-03 and fumarole PF-02, where fumarole gases and steam condensate have high fluoride and sulphate concentrations. The average estimated reservoir temperature from several gas geothermometers in fumarole PF-02 was higher (305 °C) compared to estimates from other fumaroles.
- The fluid outflow in the area is mainly northwards and controlled by subvertical NNE and N-S trending faults.

References

Baker, B. H., Mohr, P. A., & Williams, L. A. J. (1972). Geology of the Eastern Rift System of Africa. In B. H. Baker, P. A. Mohr, & L. A. J. Williams (Eds.), *Geology of the Eastern Rift System of Africa*: Geological Society of America.

Baker, B. H., Williams, L. A. J., Miller, J. A., & Fitch, F. J. (1971). Sequence and geochronology of the Kenya rift volcanics. Tectonophysics, 11(3), 191-215. doi:https://doi.org/10.1016/0040-1951(71)90030-8

Biggs, J., Anthony, E., & Ebinger, C. (2009). Multiple inflation and deflation events at Kenyan volcanoes, East African Rift. *Geology, 37*, 979-982. doi:10.1130/G30133A.1

Biggs, J., Robertson, E., & Cashman, K. (2016). The lateral extent of volcanic interactions during unrest and eruption. *Nature Geoscience, 9*(4), 308-311.

Buck, W. (2006). The role of magma in the development of the Afro-Arabian Rift System. *Geological Society, London, Special Publications, 259*(1), 43-54.

Chorowicz, J. (2005). The East African rift system. *J. Afr. Earth Sci., 43*.

Cottrell, E., Spiegelman, M., & Langmuir, C. H. (2002). Consequences of diffusive reequilibration for the interpretation of melt inclusions. *Geochemistry, Geophysics, Geosystems, 3*(4), 1-26. doi:10.1029/2001gc000205

Danyushevsky, L., Della-Pasqua, F., & Sokolov, S. (2000). Re-equilibration of melt inclusions trapped by magnesian olivine phenocrysts from subduction-related magmas: petrological implications. *Contributions to Mineralogy and Petrology, 138*(1), 68-83.

Darling, W., Griesshaber, E., Andrews, J., Armannsson, H., & O'nions, R. (1995). The origin of hydrothermal and other gases in the Kenya Rift Valley. *Geochimica et Cosmochimica Acta, 59*(12), 2501-2512.

DePaolo, D. J. (1981). A neodymium and strontium isotopic study of the Mesozoic calc-alkaline granitic batholiths of the Sierra Nevada and Peninsular Ranges, California. *Journal of Geophysical Research: Solid Earth, 86*(B11), 10470-10488. doi:10.1029/JB086iB11p10470

Dunkley, P., Smith, M., Allen, D., & Darling, W. (1993). *The geothermal activity and geology of the northern sector of the Kenya Rift Valley*. Retrieved from Nottingham, UK:

Ebinger, C. (2005). Continental break-up: the East African perspective. *Astronomy & Geophysics, 46*(2), 2.16-12.21.

Ebinger, C. (2012a). 7 - Evolution of the Cenozoic East African rift system: Cratons, plumes, and continental breakup. In D. G. Roberts & A. W. Bally (Eds.), Regional Geology and

Tectonics: Phanerozoic Rift Systems and Sedimentary Basins (pp. 132-162). Boston: Elsevier.

Ebinger, C. (2012b). Evolution of the Cenozoic East Africa rift system: Cratons, plumes, and continental breakup. Phanerozoic Rift Systems and Sedimentary Basins, 133-162.

Friese, A. (2015). InSAR, surface movement and dating of Paka volcanic products, Northern Kenya Rift (report). (BGR 05-2343). Retrieved 16.8.2020, from BGR https://www.bgr.bund.de/DE/Themen/GG_Fernerkundung/Downloads/kenia_paka_final_report.pdf?__blob=publicationFile&v=6

Friese, A., Hahne, K., Mutua, J., Lopeyok, T., & Mibei, G. (2014). *InSAR, surface movement and dating of Paka volcanic products, Northern Kenya Rift*. Paper presented at the GRSG. https://www.bgr.bund.de/EN/Themen/Zusammenarbeit/TechnZusammenarb/Geotherm/Downloads/Publications/Poster%20Paka.pdf?__blob=publicationFile&v=2

Hackman, B. (1988). *Geology of the Baringo-Laikipia area: degree sheet 35 with coloured 1: 250,000 geological map and results of geochemical exploration*: Ministry of Environment and Natural Resources, Mines and Geological Deptartment.

Halldórsson, S., Bali, E., Hartley, M., Neave, D., Peate, D., Guðfinnsson, G., . . . Thordarson, T. (2018). Petrology and geochemistry of the 2014–2015 Holuhraun eruption, central Iceland: compositional and mineralogical characteristics, temporal variability and magma storage. *Contributions to Mineralogy and Petrology, 173*. doi:10.1007/s00410-018-1487-9

Hofmann, C., Courtillot, V., Feraud, G., Rochette, P., Yirgu, G., Ketefo, E., & Pik, R. (1997). Timing of the Ethiopian flood basalt event and implications for plume birth and global change. Nature, 389(6653), 838-841.

Hutchison, W., Pyle, D. M., Mather, T. A., Yirgu, G., Biggs, J., Cohen, B. E., . . . Lewi, E. (2016). The eruptive history and magmatic evolution of Aluto volcano: new insights into silicic peralkaline volcanism in the Ethiopian rift. *Journal of Volcanology and Geothermal Research, 328*, 9-33. doi:https://doi.org/10.1016/j.jvolgeores.2016.09.010

Jung, S., Mezger*, K., Masberg, P., Hoffer, E., & Hoernes, S. (1998). Petrology of an intrusion-related high-grade migmatite: implications for partial melting of metasedimentary rocks and leucosome-forming processes. *Journal of metamorphic Geology, 16*(3), 425-445.

Kipngok, J., & Nyamongo, J. (2013). Fumarole Gas Geochemistry of Paka Geothermal Prospect, North Rift, Kenya. *GRC Transactions,, Vol. 37*.

Knight, K., Furman, T., & Bryce, J. (2003). 40 Million Years of Mafic Volcanism in Turkana, Kenya: Geochemical Insights. Paper presented at the AGU Fall Meeting Abstracts.

Lichoro, C. M., Árnason, K., & Cumming, W. (2017). Resistivity imaging of geothermal resources in northern Kenya rift by joint 1D inversion of MT and TEM data. *Geothermics, 68*, 20-32. doi:https://doi.org/10.1016/j.geothermics.2017.02.006

Lichoro, C. M., Árnason, K., & Cumming, W. (2019). Joint interpretation of gravity and resistivity data from the Northern Kenya volcanic rift zone: Structural and

geothermal significance. *Geothermics, 77*, 139-150. doi:https://doi.org/10.1016/j.geothermics.2018.09.006

Lopeyok, T. (2019). *Draft borehole Geology of well PW-01*. Retrieved from unpublished report:

Lynn, K. J., Shea, T., & Garcia, M. O. (2017). Nickel variability in Hawaiian olivine: Evaluating the relative contributions from mantle and crustal processes. *American Mineralogist, 102*(3), 507-518. doi:10.2138/am-2017-5763

Masotta, M., Mollo, S., Freda, C., Gaeta, M., & Moore, G. (2013). Clinopyroxene–liquid thermometers and barometers specific to alkaline differentiated magmas. *Contributions to Mineralogy and Petrology, 166*. doi:10.1007/s00410-013-0927-9

Mibei, G., Harðarson, B. S., Franzson, H., Bali, E., Geirsson, H., & Guðfinnsson, G. H. (2021). Eruptive history and volcano-tectonic evolution of Paka volcanic complex in the northern Kenya rift: Insights into the geothermal heat source. *Journal of African Earth Sciences, 173*, 103951. doi:https://doi.org/10.1016/j.jafrearsci.2020.103951

Mollo, S., Del Gaudio, P., Ventura, G., Iezzi, G., & Scarlato, P. (2010). Dependence of clinopyroxene composition on cooling rate in basaltic magmas: Implications for thermobarometry. *Lithos, 118*(3), 302-312. doi:https://doi.org/10.1016/j.lithos.2010.05.006

Mollo, S., Masotta, M., Forni, F., Bachmann, O., De Astis, G., Moore, G., & Scarlato, P. (2015). A K-feldspar–liquid hygrometer specific to alkaline differentiated magmas. *Chemical Geology, 392*, 1-8. doi:https://doi.org/10.1016/j.chemgeo.2014.11.010

Mulusa, G. I. (2015). *Geochemical Study of Fumarolic Steam condensates from Paka Volcano, Kenya*. Paper presented at the World Geothermal Congress, Melbourne Australia.

Mutonga, M. (2013). *The geology of Paka volcano, and its implication on geothermal* (Vol. 37).

Mwakirani, R. (2011). Resistivity structure of the Paka Geothermal prospect in Kenya. *Transactions - Geothermal Resources Council, 35*, 1719-1724.

Neave, D. A., Bali, E., Guðfinnsson, G. H., Halldórsson, S. A., Kahl, M., Schmidt, A.-S., & Holtz, F. (2019). Clinopyroxene–liquid equilibria and geothermobarometry in natural and experimental tholeiites: the 2014–2015 Holuhraun eruption, Iceland. *Journal of Petrology, 60*(8), 1653-1680.

Neave, D. A., & Putirka, K. D. (2017). A new clinopyroxene-liquid barometer, and implications for magma storage pressures under Icelandic rift zones. American Mineralogist, 102(4), 777-794.

Neumann, H., Mead, J., & Vitaliano, C. J. (1954). Trace element variation during fractional crystallization as calculated from the distribution law. *Geochimica et Cosmochimica Acta, 6*(2), 90-99. doi:https://doi.org/10.1016/0016-7037(54)90018-6

Ngongang, N. B. T., Kamgang, P., Chazot, G., Agranier, A., Bellon, H., & Nonnotte, P. (2015). Age, geochemical characteristics and petrogenesis of Cenozoic intraplate alkaline volcanic rocks in the Bafang region, West Cameroon. *Journal of African Earth Sciences, 102*, 218-232.

Pik, R., Marty, B., & Hilton, D. (2006). How many mantle plumes in Africa? The geochemical point of view. Chemical Geology, 226(3-4), 100-114.

Putirka, D. K. (2008). Thermometers and Barometers for Volcanic Systems. *Reviews in Mineralogy & Geochemistry - REV MINERAL GEOCHEM, 69*, 61-120. doi:10.2138/rmg.2008.69.3

Putirka, K., Johnson, M., Kinzler, R., Longhi, J., & Walker, D. (1996). Thermobarometry of mafic igneous rocks based on clinopyroxene-liquid equilibria, 0–30 kbar. *Contributions to Mineralogy and Petrology, 123*(1), 92-108.

Ranta, E., Halldórsson, S. A., Barnes, J. D., Jónasson, K., & Stefánsson, A. (2021). Chlorine isotope ratios rec-ord magmatic brine assimilation during rhyolite genesi. *Geochemical Perspective letters*(16), 35-39.

Saalmann, K., Mänttäri, I., Nyakecho, C., & Isabirye, E. (2016). Age, tectonic evolution and origin of the Aswa Shear Zone in Uganda: activation of an oblique ramp during convergence in the East African Orogen. Journal of African Earth Sciences, 117, 303-330.

Sceal, J. (1974). *The Geology of Paka Volcano and the Country to the East, Baringo District, Kenya.* Royal Holloway, University of London,

Sceal, J., & Weaver, S. (1971). Trace element data bearing on the origin of salic rocks from the Quaternary volcano Paka, Gregory Rift, Kenya. *Earth and Planetary Science Letters, 12*(3), 327-331.

Schilling, J. (1973). Afar mantle plume: rare earth evidence. Nature Physical Science, 242(114), 2-5.

Shaw, H. R. (1985). Links between magma-tectonic rate balances, plutonism, and volcanism. *Journal of Geophysical Research: Solid Earth, 90*(B13), 11275-11288. doi:10.1029/JB090iB13p11275

Sibson, R. H. (1994). Crustal stress, faulting and fluid flow. *Geological Society, London, Special Publications, 78*(1), 69-84.

Sibson, R. H. (1996). Structural permeability of fluid-driven fault-fracture meshes. *Journal of Structural Geology, 18*(8), 1031-1042.

Smith, M., & Mosley, P. (1993). Crustal heterogeneity and basement influence on the development of the Kenya Rift, East Africa. *Tectonics, 12*(2), 591-606.

Sudo, M., Strecker, M., Friese, A., Hahne, K., Frei, M., & Riedl, S. (2017). *Temporal change in geochemistry of volcanic rocks along the volcano-tectonic axis of the northern Kenya Rift: Insights from the Ar/Ar geochronology and whole- rock chemistry at Paka*. Paper presented at the IAVCEI 2017 assembly, Portland, USA. http://iavcei2017.org/IAVCEI%202017%20Abstracts.pdf

Stamps, D. S., Calais, E., Saria, E., Hartnady, C., Nocquet, J. M., Ebinger, C. J., & Fernandes, R. M. (2008). A kinematic model for the East African Rift. Geophysical Research Letters, 35(5).

Thomson, A., & Maclennan, J. (2012). The Distribution of Olivine Compositions in Icelandic Basalts and Picrites. Journal of Petrology, 54(4), 745-768. doi:10.1093/petrology/egs083

Williams, L. A. J., MacDonald, R., & Chapman, G. (1984). Late Quaternary caldera volcanoes of the Kenya Rift Valley. *89*(B10), 8553-8570. doi:doi:10.1029/JB089iB10p08553

Paper I

Eruptive history and volcano-tectonic evolution of Paka volcanic complex in the northern Kenya rift: Insights into the geothermal heat source

Geoffrey Mibei, Björn S. Harðarson, Hjalti Franzson, Enikő Bali, Halldór Geirsson, Guðmundur H. Guðfinnsson

Journal of African Earth Science 173(2021) 103951

Eruptive history and volcano-tectonic evolution of Paka volcanic complex in the northern Kenya rift: Insights into the geothermal heat source

Geoffrey Mibei[1,3,4,] Björn S. Harðarson[2], Hjalti Franzson[2], Enikő Bali[3], Halldór Geirsson[3], Guðmundur H. Guðfinnsson[3]

1-Geothermal Development Company, P.O. Box: 17700-20100, Polo House, Nakuru, Kenya
2- Iceland GeoSurvey, Grensásvegur 9, 108 Reykjavík, Iceland
3-Institute of Earth Sciences, University of Iceland, Sturlugata 7,101 Reykjavík, Iceland
4- GRÓ-GTP, Grensásvegur 9, 108 Reykjavík, Iceland

Abstract

In this paper, we provide insights into the eruptive history and volcano-tectonic evolution of the Paka volcanic complex in a revised stratigraphic framework. We integrate all available $^{40}Ar/^{39}Ar$ radiometric dates along with field observations, remote sensing data, and the analysis of surface and cutting samples from a 2552 m deep borehole (PK-01). Chemical analyses distinguish basalt, hawaiite, mugearite, benmoreite, and trachyte rock types in Paka. It also indicates that the eruptive products are genetically related by fractional crystallization. Major element mass balance and Rhyolite-MELTS models are consistent with the trachyte being generated by 74-83% fractional crystallization of Paka basalt. Before the growth of the volcano, volcanic activity was characterised by plateau fissure eruptions at 582-405 ka. Eruptions directly related to the Paka edifice are divided into four different volcanic phase sequences. Sequences 1- 4 span the periods 390-278 ka, 247-205 ka, 160-36 ka, and 36-8 ka. The Pre-Paka plateau eruption products outcrop at the base of the volcano flanks and are overlain by edifice-forming trachyte. Initial caldera-related subsidence is expressed by arcuate structures to the west and southeast parts of the volcano. These initial collapses are associated with pyroclastic eruptions estimated to have occurred at ~38 ka. Following these explosive eruptions, a ~1.5 by ~1.6 km main caldera developed. The lithological information from the drilled geothermal exploration borehole PK-01 indicates a minimum thickness of ~2200 m for the extrusive lava sequences, with the uppermost 1050 m of the strata being directly related to eruptions from the Paka volcano (Phases 1-4). We estimate a minimum total bulk volume of ~50 km^3 for the volcanic material erupted from Paka during the last ~390 ka. This translates to an average eruption rate of ~1.2 x 10^{-4} km^3/yr. The associated advected magmatic heat supported an 'excess' heat flux ranging between 110-138 mW/m^2 or about twice the present day average continental flux (57 mW/m^2) and about 1.3 times the background values (90 mW/m^2) in geothermal areas. The apparent high heat flux implies a magma-driven geothermal system, where convection of the hydrothermal fluid is occurring above the heat source. Structural mapping revealed normal faults, strike-slip faults, lineaments, and an array of eruptive vents and domes as the main volcano-tectonic structures. We infer at least four faulting and fault reactivation events that have occurred during Paka´s geological history. The structural orientations in the area are dominated by NNE and NW with subordinate N-S and NNW striking structures. Evidence suggests that the intersection of NNE and NW trending structures may have had a major influence on the volcanism in the area.

key words; *Paka volcano, volcanic evolution, heat flux, magma supply rate, geothermal heat source*

1.0 Introduction

In zones of continental rifting, volcanism and tectonism are intimately related reflected in the spatial relationships between the faults and the volcanic centres (e.g.,Acocella, 2014; Wright et al., 2006). Tectonic plate motion produces stress fields that create fault structures and crustal weakness. These structures act as pathways for magma intrusions/injections such as dike propagation, sills and the formation and growth of magma reservoirs. The magma injections can trigger changes in crustal stresses, and probably generate seismic events (De Siena et al., 2017; Miller et al., 2010). This way more fault structures are created and older ones reactivated. The heat source in a geothermal system depends directly on volcanism, i.e., eruptive frequency and age, which can be inferred from the eruptive history of an area. The geothermal fluid flow, on the other hand, is enhanced by fault induced crustal permeabilities (Sibson, 1994, 1996; Zhang et al., 2003). This, implies that the occurrence of high-temperature geothermal resources is linked to volcanism and tectonics. It is thus important to evaluate the eruptive history and volcano-tectonic interactions on a regional and in reduced spatial scale in the early stages of geothermal exploration in an area.

The complex relationship between volcanism and tectonism is particularly evident in the eastern arm of the East African Rift System (EARS) (Baker et al., 1972; Chorowicz, 2005; Ebinger, 2012; Macgregor, 2015), where a large volume (>700,000 km^3) of extrusive volcanic material has erupted. Detailed information at the scale of individual volcanic centres in the EARS is, however, rare with noteworthy exceptions from studies of the Ethiopian Rift (Hutchison, Pyle, et al., 2016; Siegburg et al., 2018; Tadesse et al., 2019). This can largely be attributed to the lack of detailed geological mapping, radiometric dating of a complete array of eruptive products and knowledge of buried volcanic sequences.

In the Paka volcanic complex (Fig. 1), early geological studies (Hackman, 1988; Hackman et al., 1990; Sceal & Weaver, 1971; Williams, 1978) resulted in a regional geological map, which provided insight into the geology and volcanic setting. However, no radiometric dates were available and only seven samples had been analysed for major elements and fifty samples for trace elements. Seven samples presented by Sceal & Weaver (1971) are used for comparison in this paper. A later study, focusing on geothermal exploration (Dunkley et al., 1993), provided four radiometric dates but otherwise relied on the previous scarce bulk rock analyses. These limited data provided only partial insights into the evolution of Paka volcano, where volcanism was determined to have commenced at 390 ka and the main caldera collapse at 8 ka (Dunkley et al., 1993).

Currently, geothermal drilling is being conducted in the study area (Fig. 1) and related to these operations we aim to provide insight into some aspects of geothermal heat source and contribute to a geothermal conceptual model for resource assessment through the understanding of the eruptive history and volcano-tectonic evolution of Paka volcanic complex. Here we: *I)* present the results of detailed geological mapping and concurrent sampling of previously dated rocks (Dunkley et al., 1993; Friese et al., 2014b; Sudo et al., 2017b); *II)* outline the eruptive history of the volcano; *III)* discuss the interaction of volcanism and tectonic evolution in the area, including geohazard assessment; *IV)* estimate erupted magma volume, as well as the heat flux. All these are essential information for the on-going geothermal exploration in the area. *V)* finally, we discuss our findings in a regional (East African Rift) and global context, comparing the Paka volcanic complex to other rift-related volcanoes.

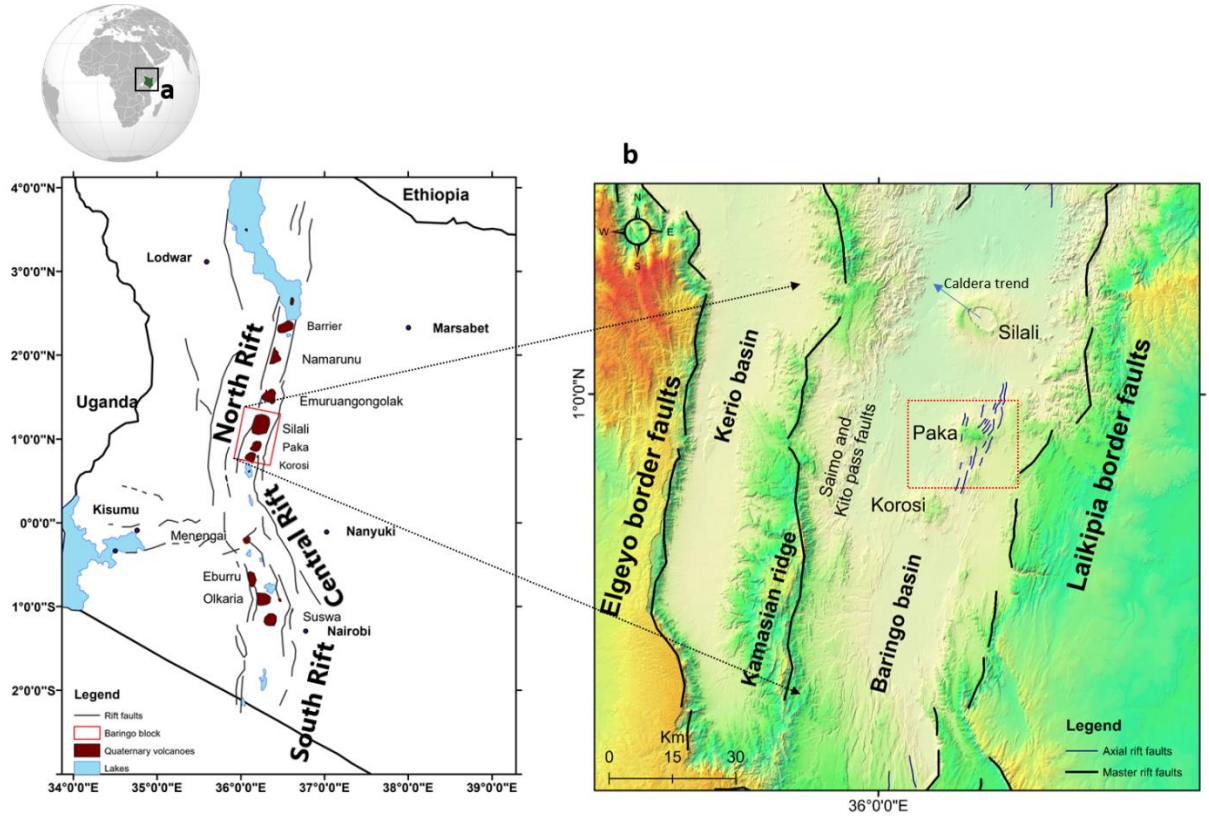

Fig. 1. The location of Paka volcano in the Northern Kenya Rift (b) The northern segment of the Kenya Rift showing Paka volcano south of Silali and north of Korosi.

2.0 Geological background

2.1 Regional setting

Paka volcano is situated south of the Silali volcano and north of the Korosi massif in the northern segment of the Kenya Rift Valley within the EARS (Figs. 1a & 1b). The EARS is an active ~6000 km long continental rift extending from the Gulf of Aden in the north to Mozambique (Beira) in the south, (Baker et al., 1972; Chorowicz, 2005). The Kenya Rift extends over a total of ~900 km (Fig. 1), overprinted on the weak part of a suture zone of the Mozambique belt, resulting from a collision event during the late Neoproterozoic Pan African Orogeny (Cutten, 2002). The Kenya Rift is generally divided into; northern, central and southern rift segments, reflecting spatial variation in the master rift fault architecture. The northern segment extends between latitudes 0.0° to 4°N and trends N10°E, the central segment is between 0.0° and 1.0°S trending N 150°E, while the southern one is bounded by latitudes 1.0°S and 2.1°S trending N10°E (Fig. 1) (Riedl et al., 2020).

. Volcanism associated with the development of the rift began in the Turkana area during the Oligocene period about 40-30 Ma ago (Baker, 1987; Baker et al., 1972; Baker et al., 1971; Smith, 1994). Kenya Rift volcanism is particularly pronounced in a topographic anomaly, 'the Kenya dome', within the central segment, resulting in thick piling of volcanic material. Crustal thinning, however, is evident in the northern segment and to a lesser degree in the southern segment (Simiyu & Keller, 1997). The total volume of eruptive products in the Kenya Rift is estimated to be around 220,000 km^3 (Williams, 1972). Baker et al. (1971) suggested that following the Miocene eruptions the initial regional faulting occurred. This ushered the

Pliocene eruptions within the central segment. A second faulting event followed and formed the Kenya Rift structure as it is known today. It was during the second faulting phase that the border rift faults were formed. Rifting progressively shifted with time to the axial zone in the early Quaternary forming axial faults (Baker et al., 1971; Brotzu et al., 1984; McCall, 1967; Sceal, 1974b). These younger axial rift faults provided conduits for magmatic activity, enabling volcanism manifested by the many Quaternary volcanoes, among them the Paka volcanic complex. In addition to the generally N-S trending axial rift faults, evidence now shows that intersection zones between the N-S and the underlying NW regional structures play an important role, not only in increasing eruption frequency but also by influencing the location and structure of the rift volcanoes (Robertson et al., 2016; Zielke & Strecker, 2009). A good example of a structure related to the NW underlying structure is the Aswa fracture zone (e.g.,Macgregor, 2015). The Aswa intersects the main EARS approximately in the central rift (Kenyan dome) where massive volcanism occurred in the rift´s history. In the northern rift segment, some of the NW underlying structures could be related to the Cretaceous West and Central African Rift System (WCARS) (Bosworth, 1992; Guiraud & Maurin, 1992), forming intersection zones with the main modern rift structures. Most of the volcanoes in this segment occur within these intersections, e.g. the Silali volcano, where the NW trend of the caldera was projected to indicate these underlying NW structures (Robertson et al., 2016).

2.2 Geological setting of the Paka volcanic complex

The northern Kenya rift is composed of two parallel rift basins (Fig. 1b); the Baringo and Kerio basins with a rift floor elevation of ~1000 m a.s.l separated by the Kamasian ridge (~2500 m a.s.l). The Baringo basin is presently volcanically active and has widespread geothermal manifestations. The Kerio Valley is older and displays fossil geothermal activity evidenced by widespread fluorite deposits (e.g.,Nyambok & Gaciri, 1975). The Paka volcano is located in the presently active Baringo basin south of Silali and north of Korosi (Fig.1). The volcano edifice rises from 1000 m a.s.l in the lower plains to around 1680 m a.s.l at the highest point; the edifice, therefore, comprises a minimum of 600 m thick volcanic lava pile. The volcano summit area consists of arcuate collapse structures and the main caldera. Recent magmatic activity in the summit is manifested by the Holocene intra-caldera crater while geothermal manifestations are widespread and include fumaroles, altered ground, etc. (Figs. 2a-f). The structural geology within the Paka area is generally characterized by (i) border rift faults, i.e., the Laikipia border faults ~10 km east of Paka and the Saimo and Kito pass faults ~25 km west of Paka estimated to be of Pliocene age and (ii) axial faults, which are younger Quaternary faults formed by grid faulting (Riaroh & Okoth, 1994; Sceal, 1974b) dissecting the Paka volcanic lavas to form mini graben and horst structures present today.

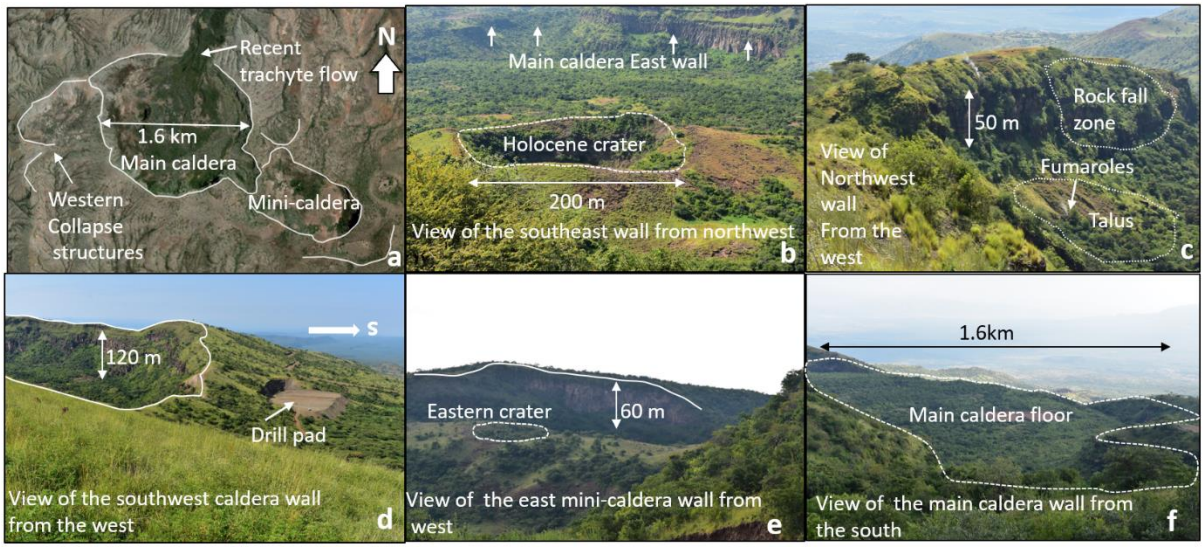

*Fig. 2. Google Earth image of Paka volcano and photographs from the study area. a) The main caldera, arcuate collapse structures on the west, northeast, the southeast mini-caldera. b) Holocene crater in the main caldera. c) Fumaroles, rock falls and talus, northwest of the caldera rim. d) Southwest caldera wall where a drill pad (Pk-03) is located. e) A crater in the southeast mini-caldera where intense geothermal activity is observed. f) The flat topography of the main caldera floor showing the pad with well Pk-02 and Pk-01 just on the right edge. *Refer to (a) for directions annotated on (b-f)*

3.0 Methodology

To elucidate the geological evolution and eruptive history of Paka we established a revised stratigraphic framework (Table 1). The approach used was the integration of all available $^{40}Ar/^{39}Ar$ radiometric dates (Dunkley et al., 1993; Friese, 2015; Friese et al., 2014b; Sudo et al., 2017b) with field observations and chemical analyses of rock samples. Field mapping was carried out between June-August 2018 when field observations, field measurements and collection of surface and borehole samples were done. Digital geological mapping and data integration was undertaken with the use of ArcGIS and involved the analysis of Google Earth images and Hillshade DEM maps developed from a 30 m resolution Shuttle Radar Topography Mission data (SRTM GL1). Drill cuttings from well PK-01 were logged from 0 to 2552 m depth at 2 m interval and plotted using the Strater 4 software. Challenges were experienced in the borehole log due to extensive shortfall of samples, caused by circulation losses during the drilling. However, sufficient information on the nature and the composition of the rocks, as well as the thickness of extrusive volcanic material, were obtained. Surface samples (Table S1) were collected at exact locations where previous samples had been collected for radiometric dating. Therefore, the geochemical results could be linked to the available $^{40}Ar/^{39}Ar$ dates. The whole-rock analysis was carried out at the Institute of Earth Sciences (University of Iceland) using an ICP-OES (SPECTRO CIROS VISION). A total of 36 surface samples and 24 borehole sample cuttings were analysed (Table S1). Fresh surface samples were broken into smaller pieces with a hammer paying close attention to avoid any contamination. Approximately 50 grams of broken rock pieces were further crushed in a Retsch BB100 Mangan jaw-crusher. The crushed mixture was then sieved and about 2 grams of 1mm grains were collected and ground to powder in an agate mortar. The borehole sample cuttings went directly into the agate mortar grinding stage. The rock powder (100 mg) was then mixed with $LiBO_2$ flux (200 mg) in a

carbon crucible. The reference samples A-THO, B-THO, and B-ALK, which have previously been calibrated relative to USGS standards, were used for instrumental calibration. For these reference samples, 500 mg of $LiBO_2$ and 250 mg of sample were weighed in a crucible. A selection of in-house international standards (K-1919, BIR-1, JA-2, and RGM-1) were weighed in the same manner and run as unknown samples. The weighed samples and standards in the crucibles were placed in a Lindberg/Blue oven at 1000°C for approximately 30 minutes. The resulting glass beads were dissolved in small plastic bottles overnight containing 5 vol% HNO_3 (nitric acid), 1.33 vol% HCl (hydrochloric acid) and 1.33 vol% saturated $H_2C_2O_4$ (oxalic acid). Accuracy of 2σ was systematically calculated for each major and trace element, based on repeated measurements of the standards. The largest 2σ values for each element were chosen to represent the largest instrumental error. Accuracy was generally better than ± 0.70% for major elements, ±1.39 ppm for Y and ±4.62 ppm for Zr trace elements. The detection limit of the ICP-OES instrument for trace elements is ~20 ppm. The final results were reported on a volatile-free basis and normalized to 100 wt.%, expressing the total iron as FeO.

4.0 Results

4.1 Bulk rock chemistry

4.1.1 Major elements

Here, we present the major and selected trace element chemistry of the surface samples and borehole cuttings. We rely upon the Total Alkali-Silica classification (Le Bas et al., 1986) in Fig. 3a to distinguish the different rock types from basalts, intermediate rocks to trachyte, all plotting above the alkali-sub alkali division line (Irvine & Baragar, 1971). Intermediate rocks are scarce, while trachyte is the dominant rock type. We employ the Macdonald (1974) plot of Al_2O_3 versus FeOt (Fig. 3b), which shows that the trachytes plot in both the pantellerite and the comendite field. Additional characterization is based on the molar proportions of alkalis, alumina, and calcium in a peralkaline index plot (Fig. 3c), which shows that the trachyte is peralkaline. In all the chemical plots, we superimpose a shaded field corresponding to the chemical composition of borehole samples and we have adopted a colour scheme that differentiates individual eruptive sequences based on the established stratigraphy in section 4.2. Major and trace element data (Figs. 4a-f, Table S1 and Fig. S5) in this study are complemented by those of Sceal (1974). Silica concentration shows a wide range from 47 to 63 wt.% in surface samples and 48 to 65 wt.% in borehole cuttings and is therefore employed as a differentiation index for our plots. MgO, TiO_2, FeO^t, and CaO display a tight negative correlation with SiO_2. MgO content varies between 0-8 wt.% in surface samples and 0-4 wt.% in the borehole cuttings (Fig. 4a). FeO^t ranges between 6 and 13 wt.% in surface samples and 4-8 wt.% in borehole cuttings. CaO has a range of 1-11wt.% in surface samples and ranges from 0 to 5 wt.% in borehole cuttings (Fig. 4b). TiO_2, on the other hand, exhibits large variation and increases with decreasing SiO_2 content from 0.5-3 wt.% in surface samples and 0 to 3 wt. % in borehole cuttings. P_2O_5 has a considerable scatter but generally displays a negative correlation with the SiO_2 content, with values ranging from 0.04-0.46 wt % in surface samples and 0 to 0.4 wt.% in the borehole cuttings, the scatter being particularly pronounced in basalt and benmorite fields. MnO displays very low concentration in both surface and borehole samples (0.1-0.3 wt.%) and correlates positively with silica. Al_2O_3 values range from 14-18 wt.% in surface samples and 13 to 17 wt.% in borehole cuttings (Fig. 4c). Na_2O and K_2O display similar trends and correlate positively with silica. Na_2O varies between 3 to 8 wt.% in surface samples and 4 to 7 wt.% in borehole cuttings whereas, K_2O has lower values of between 0.7 to 5 wt.% in surface samples and 2 to 5 wt. % in borehole cuttings.

The selected trace elements plots in Fig. 4d-f show that Y concentrations vary from 28 to 205 ppm in the surface samples and 53 to 148 ppm in the borehole cuttings. Zr ranges between 119 and 1634 ppm in the surface samples and 342 and 1257 ppm in the borehole cuttings. Y and Zr display a positive correlation both in surface and borehole cuttings (Fig. 4d). They also correlate positively with SiO_2, although there are two outliers in volcanic sequence P.1 with very high Zr and Y contents (Fig. 4e-f). The complete results of major and trace element chemistry and normative mineral calculations for both the surface and borehole cuttings are presented in Table S1.

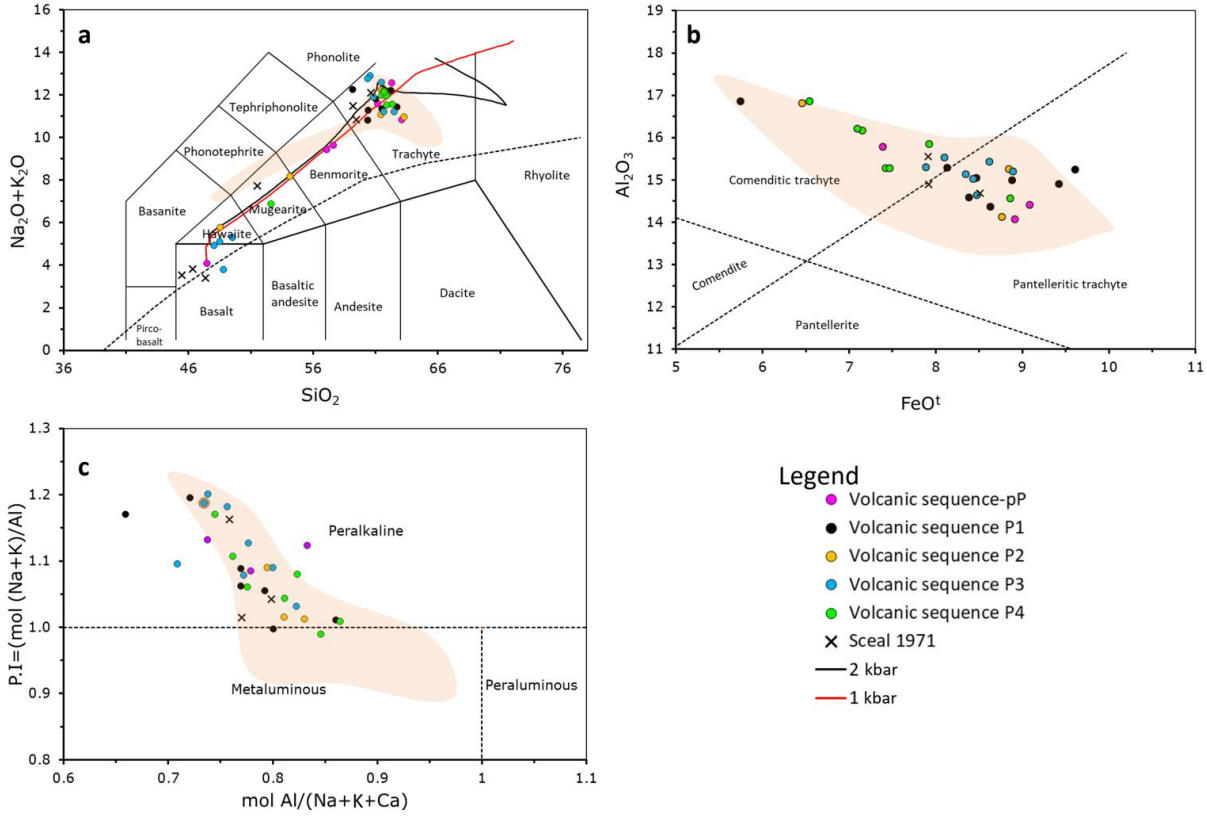

Fig. 3. Rock classification. a) Total Alkali-Silica diagram (Le Bas et al., 1986) showing the rock types in Paka and results of rhyolites MELTS model (Gualda et al., 2012) at 1 and 2 kbar, with initial H_2O content of 1.5 wt% and fO_2 of $\Delta FMQ+1$. b) Al_2O_3-FeO^t classification (Macdonald et al., 2011). c) NK/Al-A/CNK diagram (Maniar & Piccoli, 1989; Shand, 1927). The shaded field in each diagram indicates the composition of sample cuttings from well PK-01.

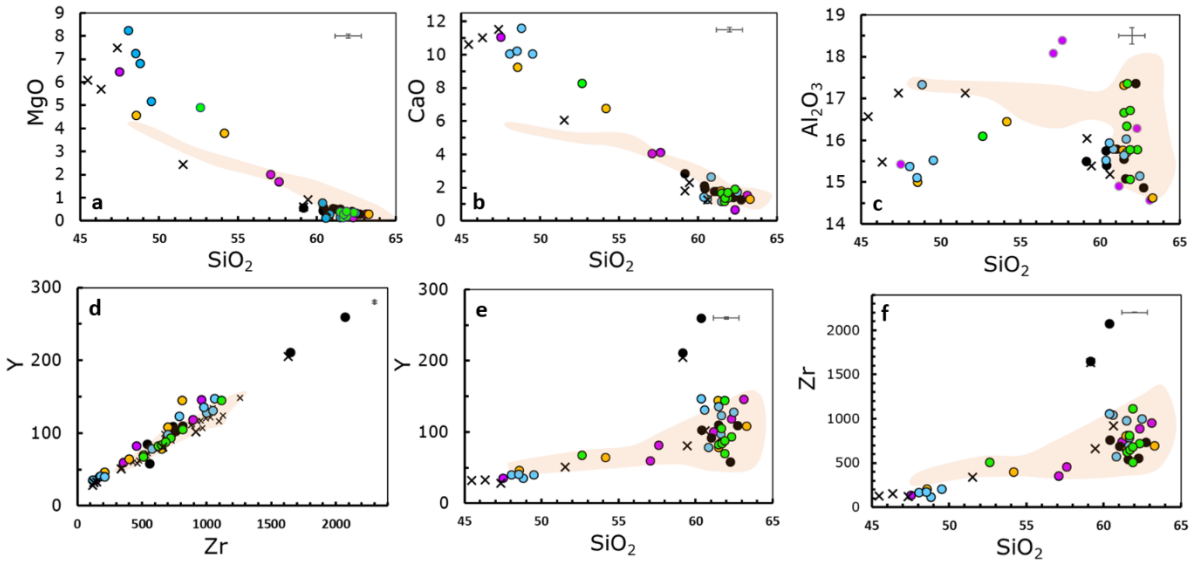

Fig. 4. Harker variation diagrams of major and selected trace elements. Colour code and abbreviations are the same as in Fig. 3. Error bars (±1σ) shown in the right top corner of each diagram (in Y vs. Zr error bar is very small). Note the excellent correlation of Y vs. Zr in the borehole and surface samples.

4.2 Paka lava series

4.2.1 Surface geology and field stratigraphy

Based on the compiled $^{40}Ar/^{39}Ar$ age data and the major element chemistry, a revised stratigraphic framework was developed. It outlines four major Paka volcanic sequences consisting of seventeen subunits, two (12 %) of which are explosive eruptive sequences (Table 1). The spatio-temporal relationship of the distinct units is shown in the geological map (Complete geological map and cross-section in Fig. S1) with inset sampling locations and 4 sites where field stratigraphy was observed (Fig. 5). It is important to note that the petrography of the rock units has been described in previous studies (Sceal, 1974b). Here, we focus mainly on their field relationship in the revised stratigraphic framework, to better understand the eruptive history. We have modified the terminology of the volcanic units from those in Sceal (1974), Dunkley et al. (1993c) and Golden (1978) in light of the new stratigraphy (Table S2) and described below, starting from the oldest.

Table 1. The revised stratigraphic framework for Paka volcanic complex. The error sizes on the age data were evaluated with ±2 σ error (Friese et al., 2014).

Period	$^{40}Ar/^{39}Ar$ (ka)	Reference	Samples	Proposed grouping	Map Code	Volcanic Sequence
Post caldera	<8	Relative date (field observation)	-	P4-alluvial	P4-Al	Phase 4
	8±4	(Dunkley et al., 1993)	PK-U7	P4-air fall	P4-ARf	
	11	Relative date (field observation)		P4-pyroclastic	P4-Py	
	11±3	(Dunkley et al., 1993)	DN-4	P4-trachyte 2	P4-Tr2	
	12±3	(Friese et al., 2014)	PK-12	P4-trachyte 2	P4-Tr2	
	20±5	(Friese et al., 2014)	PK-3	P4-trachyte	P4-Tr1	
	31±17	(Friese et al., 2014)	PK-17	P4-trachyte	P4-Tr1	
	35±10	(Friese et al., 2014)	PK-25	P4-trachyte	P4-Tr1	
	35±5	(Friese et al., 2014)	PK-2	P4-trachyte	P4-Tr1	
	36	Relative date (field observation)	-	P4-mugearite	P4-Mg	
Syn caldera	38-35	Relative date (field observation)	DN-3	P3-pyroclastic flow (PFl),P3-tuff (Tff)	P3-PFl, P3-Tff	Phase 3
	39±6	(Friese et al., 2014)	Pk-29	P3-trachyte	P3-Tr3	
	Fault rejunvination					
Pre caldera	71±13	(Friese et al., 2014)	Pk-27	P3-trachyte	P3-Tr2	
	80±11	(Friese et al., 2014)	PK-14	P3-trachyte	P3-Tr2	
	126±9	(Friese et al., 2014)	PK-30	P3-trachyte	P3-Tr1	
	139±35	(Friese et al., 2014)	PK-15	P3-trachyte	P3-Tr1	
	150±6	(Friese et al., 2014)	PK-26	P3-trachyte	P3-Tr1	
	145±23	(Friese et al., 2014)	PK-13	P3-hawaiite	P3-Ht	
	160±97	(Friese et al., 2014)	PK-M1	P3-basalt	P3-Bt	
	Faulting 3					
	205±6	(Friese et al., 2014)	PK-8	P2-trachyte	P2-Tr	Phase 2
	219±4	(Dunkley et al., 1993)	DN-2	P2-trachyte	P2-Tr	
	234±13	(Friese et al., 2014)	PK-5	P2-trachyte	P2-Tr	
	238±34	(Friese et al., 2014)	PK-4	P2-hawaiite	P2-Ht	
	247±24	(Friese et al., 2014)	PK-M2	P2-mugearite	P2-Mg	
	Faulting 2					
	278±13	(Friese et al., 2014)	PK-7	P1-trachyte 2	P1-Tr3	Phase 1
	321±13	(Friese et al., 2014)	PK-21	P1-trachyte 2	P1-Tr2	
	332±17	(Friese et al., 2014)	PK-9	P1-trachyte 2	P1-Tr2	
	372±5	(Friese et al., 2014)	PK-11	P1-trachyte 1	P1-Tr1	
	382±8	(Friese et al., 2014)	PK-18	P1-trachyte 1	P1-Tr1	
	386±5	(Friese et al., 2014)	PK-16	P1-trachyte1	P1-Tr1	
	389±6	(Friese et al., 2014)	PK-6	P1-trachyte1	P1-Tr1	
	390±6	(Dunkley et al., 1993)	DN-1	P1-trachyte1	P1-Tr1	
	Faulting 1					
Pre-Paka	405±7	(Friese et al., 2014)	PK-10	Pre-Paka trachyte	pPTr	Plateau
	415±28	(Friese et al., 2014)	PK-19	Pre-Paka trachyte	pPTr	
	428±12	(Friese et al., 2014)	PK-23	Pre-Paka trachyte	pPTr	
	464±18	(Friese et al., 2014)	PK-24	Pre-Paka benmorite	pPBr	
	471±13	(Friese et al., 2014)	PK-22	Pre-Paka benmorite	pPBr	
	582±58	(Friese et al., 2014)	PK-20	Pre-Paka basalt	pPBt	

4.2.1.1 Plateau volcanic sequence (Pre-Paka phase)

Pre-Paka basalt (pPBt)

The Pre-Paka basalt is a series of effusive and pyroclastic scoria deposits outcropping northwest, northeast, and southeast of Paka. It is stratigraphically overlain by the Pre-Paka benmorite and the Pre-Paka trachyte. The explosive material is characterised by scoria spatter deposits from cinder cones in the northwest and northeast (Fig. 5). It corresponds to the lower basalt of Dunkley et al. (1993) and older basalt in Sceal (1974), where a relative date was relied upon in their stratigraphic description. The basalt has been dated to be 582±58 ka and is the oldest rock unit sampled in the Paka area. It is faulted, eroded and thickly vegetated. In a hand specimen, it is dark grey, fine-grained and vesicular with up to 4 mm large amygdales. Calculated normative mineralogy suggests that the lava is nepheline-hypersthene normative (Table S1).

Pre-Paka benmorite (pPBr)

The extent of the Pre-Paka benmorite lavas northwest of Paka was determined from the Google Earth image and previous studies (Dunkley et al., 1993). They outcrop northwest of Paka at Tuwei (Figs. 5) and are dated to be between 471±13 and 464±18 ka. The benmorite is dark grey, weathered, aphyric and vesicular lava. It was called the Katalim mugearite by Sceal (1974). This lava is part of the regional plateau Pre-Paka volcanism together with the Pre-Paka trachyte and Pre-Paka basalt. Field observations show that the benmorite is overlain by the P1-trachyte 2 (P1-Tr2) called Kasakat trachyte by Sceal (1974).

Pre-Paka trachyte (pPTr)

The Pre-Paka trachyte (pPTr) lavas were emitted from fissure and vent eruptions outcropping to the northwest (Napokorian and Chepkoghio) and the east of Paka at Orus (Fig. 5). These eruptions were contemporaneous with regional eruptions such as the Baringo trachyte and basalt eruption 20 km south of the Paka area. Following the eruptions that gave rise to this formation, a major episodic faulting event is thought to have occurred east of Paka, resulting in 3° west-dipping faults with a total downthrow of ~300 m (Sceal, 1974). These faults are effectively the boundary between the Pre-Paka volcanic lavas and early Paka volcano eruptions represented by the P1-trachyte1 (P1-Tr1). The highly faulted nature of this lava formation is evident at Orus area, where a 7 m fault escarpment exposes at least two pahoehoe lava flow units of the older trachyte (Section 2.2). According to our revised stratigraphy, a considerable time elapsed (~40 ky) before the eruption of the succeeding P1-trachyte1 (P1-Tr1). This long-time lapse was elucidated by Sceal (1974) as he noted that the older trachyte was overlain by a weathered ~20 cm soil cover, signifying a long eruption hiatus. In the east of Paka the Pre-Paka trachyte outcrop is partly mantled and emerges in the northeast from beneath the P1-trachyte. In the northwest, the Pre-Paka trachyte lava occurs as weathered trachyte blocks of several flows, forming 60 m thick lava piles. In hand specimen, the formation appears fine-grained with feldspar phenocrysts and a trachytic texture. They are dated to be between 428±12 ka and 405±7 ka and underlie the P1-Tr1.

4.2.1.2 Volcanic sequence phase 1

P1-trachyte 1 (*P1-Tr1*)

The P1-trachyte1 (P1-Tr1) is dated to be between 390±6 and 372±5 ka (Table 1). It marks the earliest phase of eruptions directly related to the Paka volcanic centre. The formation outcrops to the northwest, northeast, and east of the volcano (Fig. 5). The northeast outcrop is the most extensive and mantles the Pre-Paka trachyte, burying the main faults east of Paka. It corresponds to the lower and upper trachyte of Dunkley et al. (1993), older trachyte of Sceal (1974) and Orus trachyte of Golden (1978). The northwest lava outcrops in most of the Natan area and is underlain by the Pre-Paka trachyte (pPTr) or the Chemogogoch trachyte (Sceal, 1974). This trachyte flow is characterised by basaltic xenoliths. In hand specimen, the lava is light grey to grey, coarse-grained and porphyritic with phenocrysts of feldspar (6 mm). It has a flow orientation texture with up to 4 mm diameter vesicles, some of which contain amygdales.

***P1-trachyte 2* (P1-Tr2)**

The P1-trachyte 2 (P1-Tr2) west of Paka corresponds to the Kasakat trachyte of Sceal (1974). The lava flow extends 3 km to the northwest between Tuwei and Nakaporian (Fig. 5) overlying the Pre-Paka benmorite. The lava flow originates from a centre buried by P3-Tr_1 and P4-Py northwest of Paka. It is dated at 332±17 to 321±13 ka and displays a trachytic texture with a common occurrence of black fragments, possibly basaltic xenoliths. Most of the formation is weathered and eroded. In hand specimen, it is generally unaltered, light grey, medium-grained and porphyritic with phenocrysts of elongated feldspars (2-3 mm) in a groundmass dominated by feldspar microcrysts.

P1-trachyte 3 1 (P1-Tr3)

P1-trachyte 3 (P1-Tr3) is from parasitic vents to the northeast of Paka, dated at 278±13 ka (Fig. 5). The lava flow is characterised by pressure ridges and tension cracks. In hand specimen, the rock is unaltered, light grey, medium-grained and porphyritic with sparse phenocrysts of elongated feldspars (2-3 mm). It is a fissile rock with a mottled texture and is quartz-bearing.

4.2.1.3 Volcanic sequence phase 2

***P2-mugearite (P2-Mg*)**

This lava erupted on the southwest flank of the volcano through a possible local vent and has a very limited extent (Fig. 5). It covers an area less than 0.5 km^2, coinciding with the location of fossil hydrothermal activity. It has been dated 247±24 ka and is generally dark grey, medium-grained, vesicular and porphyritic lava. The vesicles are stretched and partially filled with secondary silica from hydrothermal alteration.

P2-hawaiite (P2-Ht)

The P2-hawaiite (P2-Ht) is exposed northeast of Paka. The lava flowed into the N-S levee (Fig. 5) for about 3.5 km. Sceal (1974) described this flow as a basalt spatter flow. It is dated at 238±34ka. In hand specimen, it is generally dark grey, medium-grained and vesicular. The

vesicles are partially filled with amygdales formed by hydrothermal activity associated with a fault zone in the area.

P2-trachyte (P2-Tr)

The P2-trachyte lava flow is mapped at Sitoilomeyan east of Paka and southeast of the caldera, as well as scattered outcrops around Gulungui north of Paka (Fig. 5). It was considered to be the upper trachyte by Dunkley et al. (1993) and is dated to be between 234±13 and 205±6 ka. The P2-trachyte (P2-Tr) is heavily faulted southeast of Paka with ~3° west-dipping faults with downthrows up to 7 m. The contemporaneous scattered outcrops in the north erupted from small cone structures surrounded by a hawaiite flow (P3-Ht). The most spectacular flow, however, is the southeast flow which is hydrothermally altered, consisting of high lobate lava fronts (several tongues) and emerges at the base of the Paka ridge. In hand specimen, it is dark grey, fine-grained lava with a streaky appearance and fissile structure, containing micro phenocrysts of feldspars showing trachytic flow textures as well as syenite xenoliths. Chemical analysis indicates that it is slightly quartz normative (Table S1) which contrasts with most of the other trachyte flows from Paka.

4.2.1.4 Volcanic sequence phase 3

The volcanic units in this group include the syn-caldera tuff (P3-Tff), the pyroclastic flow (P3-PFI), P3-hawaiite (P3-YHt) and the P3-basalt (P3-Bt). We believe the Ademayon (ADBs) and the Korosi basalt lavas (KBs) to be of a similar age as rocks of this sequence but originate from the Korosi volcano south of Paka.

P3-basalt (P3-Bt)

The P3-basalt flow (P3-Bt) outcrops west of Paka (Fig. 5) and part of it was called the Nginyang basalt by Sceal (1974). It is an extensive flow that spreads beyond Nginyang and northwest of lake Tilam (outside the mapped area). It has been dated to be between 160±97 and 150±6 ka corresponding to the upper basalt in Sceal (1974). The P3-basalt is associated with the hawaiite (P3-Ht) found north of Paka at Gulungui, which appears to have formed the succeeding eruption after the basalt. On a regional scale, the P3-Bt was contemporaneous with Katemining basalt south of Silali (Dunkley et al., 1993) and the Korosi Ademayon basalt south of Paka. The basalt (P3-Bt) is mostly obscured by the Paka trachyte and the young Korosi volcanic lavas (south of the mapped area). According to Sceal (1974), an 80 m deep borehole drilled in Nyaunyau further west of Paka (outside the map area) intersected only basaltic rocks. We presume, that most of the basalt in the borehole corresponds to the younger basalt (P3-Bt) and partly the underlying Pre-Paka basalt (pPBt) of the Jarota formation. Generally, the formation is faulted but is, however, largely masked by a veneer of pumice and alluvium. In hand specimen, this rock is vesicular, dark grey and fine-grained, plagioclase porphyritic lava. The vesicles have secondary infillings of mostly clays. Chemical analysis shows that it is nepheline-hypersthene normative (Tables S1).

P3-hawaiite (P3-Ht)

The P3-hawaiite (P3-Ht) is closely associated with P3-Bt in terms of age. It outcrops in the northern flanks of Paka within the Cheptomas shield cone at Gulungui (Fig. 5). It is underlying the P3-trachyte (P3-Tr1) and is dated to be 145±23 ka. Sceal (1974) reports this lava as basalt, but it is actually of hawaiite composition. The lava is within an area of geothermal manifestations and has been hydrothermally altered into a reddish coloured formation. In hand specimen, it is dark to reddish grey, fine-grained and vesicular. The mineralogy is characterised by sparse macrocrysts of feldspar, olivine and pyroxene. The vesicles contain in places amygdales linked to hydrothermal activity in the area.

P3-trachyte 1 (P3-Tr1)

The P3-trachyte 1 (P3-Tr1) erupted from several parasitic vents southeast, southwest, and northwest of Paka (Fig. 5). The northwest flow is from the Kasakat hill consisting of several radiating tongues. In the southeast, it originates from a centre buried by tuff (P3-Tff) and was contemporaneous with the southwest flows from another centre also buried by the tuff (P3-Tff). This unit corresponds to the upper trachyte of Dunkley et al. (1993c). The flows are dated to be between 150 ±6 and 126±9 ka. In hand specimen, it is a grey, medium-grained, porphyritic lava with a trachytic texture. Chemical analysis shows that the rock is slightly nepheline normative to slightly quartz normative (Table S1).

P3-trachyte 2 (P3-Tr2)

The P3-trachyte 2 (P3-Tr2) is exposed to the north and south of Paka (Fig. 5). The northern flow is of relatively small volume and came from a buried vent, slightly north of the main caldera. It flowed northwards from the source vent and split into two fronts near Jamokatan. There, one lava front flowed northeast and the other to the northwest, due to a topographic barrier associated with a P2-trachyte vent. South of the volcano the lava emerges from under the tuff (P3-Tff) and extends south, mantling most of the Chebungus area and can be distinguished on Google Earth images by its distinct lobate lava fronts, consisting of several flow branches. It is overlain by the Korosi basalt and is dated to be between 80±11and 71±13 ka corresponding to the upper trachyte of Dunkley et al. (1993c). In hand specimen, the rock is light grey, medium-grained and hydrothermally altered with micro phenocrysts of feldspar (<1 mm). Calculated normative mineralogy suggests that the rock is slightly nepheline normative (Table S1).

P3-trachyte 3 (P3-Tr3)

The P3-trachyte 3 (P3-Tr_3) formed in an effusive eruption from vents to the southwest of Paka (Fig. 5). It corresponds to the upper trachyte of Dunkley et al. (1993c). It marks the last phase of the P3-trachyte eruptions, culminating in events leading to syn-caldera activities. The lava formed the button-shaped monogenetic dome of Muruase in the southwest. Stratigraphic exposures (Site 3) on the southern caldera wall (Fig. 6) show that this lava flow is about 120 m thick in total with basaltic xenoliths and underlies the tuff (P3-Tff). Further stratigraphic evidence confirming the aforementioned stratigraphy is found in the intra-caldera crater wall (Dunkley et al., 1993). In hand specimen, this trachyte is porphyritic, grey with rounded to sub-rounded phenocrysts of white feldspars (1 mm). Calculated normative mineralogy suggests that the rock is slightly nepheline normative (Table S1).

P3-Tuff (P3-Tff)

The P3-tuff (P3-Tff) layer is believed to be from the first explosive eruption in the area. It is most likely contemporaneous with the western, eastern, and southeast arcuate collapse structures nesting the main caldera. The tuff is therefore considered to be a syn-caldera formation with an age of ~38 ka (Table 1). It manifests itself as reddish-yellow tuff horizons with a thickness of 1 m in the west at site 1 (Figs. 5 and 6). It is largely reworked north of Chebungus area. Generally, the tuff is poorly crystalline and slightly welded with fragments of glass (2-5 cm), pumice (3 cm), and micro-syenite. It is exposed south of the caldera and also in the western caldera wall with a thickness of ~10-20 m (Dunkley et al., 1993). The tuff drapes the topography suggesting it is an air-fall. Exposures in the east are, however, poor due to the masking effect of post-caldera pyroclastic (P4-Py). The tuff is underlain by P3-Tr3, based on the stratigraphic profile at site 3 (Fig. 6).

4.2.1.5 Volcanic Sequence phase 4

P4-mugearite (P4-Mg)

The P4-mugearite is the earliest effusive eruption in the main caldera outflowing to the north. It must have been a relatively low-viscosity magma judging from its small volume and the extensive length of the flow (2 km) towards the north (Fig. 5). Exposed wall section of the Holocene intra-caldera crater wall shows that P4-Mg overlies a 10-20 m thick layer of pumice lapilli tuff, which in turn rests on porphyritic trachyte (Dunkley et al., 1993). The lapilli tuff is what we have termed here as the syn-caldera tuff (P3-Tff) and the porphyritic trachyte is the P3-trachyte (P3-Tr3). This stratigraphic evidence is the basis for our relative date of ~36 ka for this formation.

P4-trachyte 1 (P4-Tr1)

The P4-Tr1 filled the caldera floor and was similarly confined by the caldera walls as the succeeding P4-Tr2 (Fig. 5). It outflowed to the north of the caldera for about 3.5 km being lobate with pressure ridges and cooling cracks. This indicates that the volumes involved were larger than those of P4-Tr2 or possibly, that the lava was slightly less viscous. The flow is dated at 35±5 ka. In hand specimen, it is light grey to brownish, fine-grained with microcysts of feldspar showing a trachytic texture.

P4-trachyte 2 (P4-Tr2)

This formation represent the youngest effusive trachyte of the post-caldera eruptions. The eruptions fromed low-lying dome in the southwest and north of Paka and occurred within the main caldera floor. Field observations suggest that the intra-caldera lava may have ponded the area. It then overflowed the north caldera wall into a mini graben structure orientated in the N-S direction, extending for ~2.5 km (Fig. 5). The eruptions are dated to be between 20±5 and 11±3 ka. It is light grey, coarse-grained, massive, porphyritic and altered with elongated phenocrysts of feldspars (5-6 mm).

P4-Pyroclastic deposits (P4-Py)

The Pyroclastic pumice (P4-Py) eruption marked the climactic phase of eruptions in Paka dated at 8±4 ka. It forms an extensive pumice cover over the summit area, the western flanks of Paka (Dunkley et al., 1993) and a thin veneer within the intra-caldera area. The P4-Py volcanic deposits overlie the syn-caldera explosive deposits (P3-Tff) and the trachyte lava (P3-Tr3). They erupted from multiple pumice cones northeast of the volcano and possibly from the Holocene intra-caldera craters. The eruptive products extend less than 2 km towards the east and more than 7 km towards the northwest of the main caldera based on mapped outcrops. This indicates a deposition aided by an easterly prevailing wind. The deposits drape Mundi Hill and partly cover the Nginyang basalts (Dunkley et al., 1993). They are generally characterised by brown pumice fragments of about 3 cm in diameter with micro-syenite xenoliths. They are also hydrothermally altered, especially in the northeast within the pumice cones. A stratigraphic profile sequence at site 2 (Fig. 6) indicates that the P4-Py overlies the P3-Tff, which in turn is underlain by P3-Tr3.

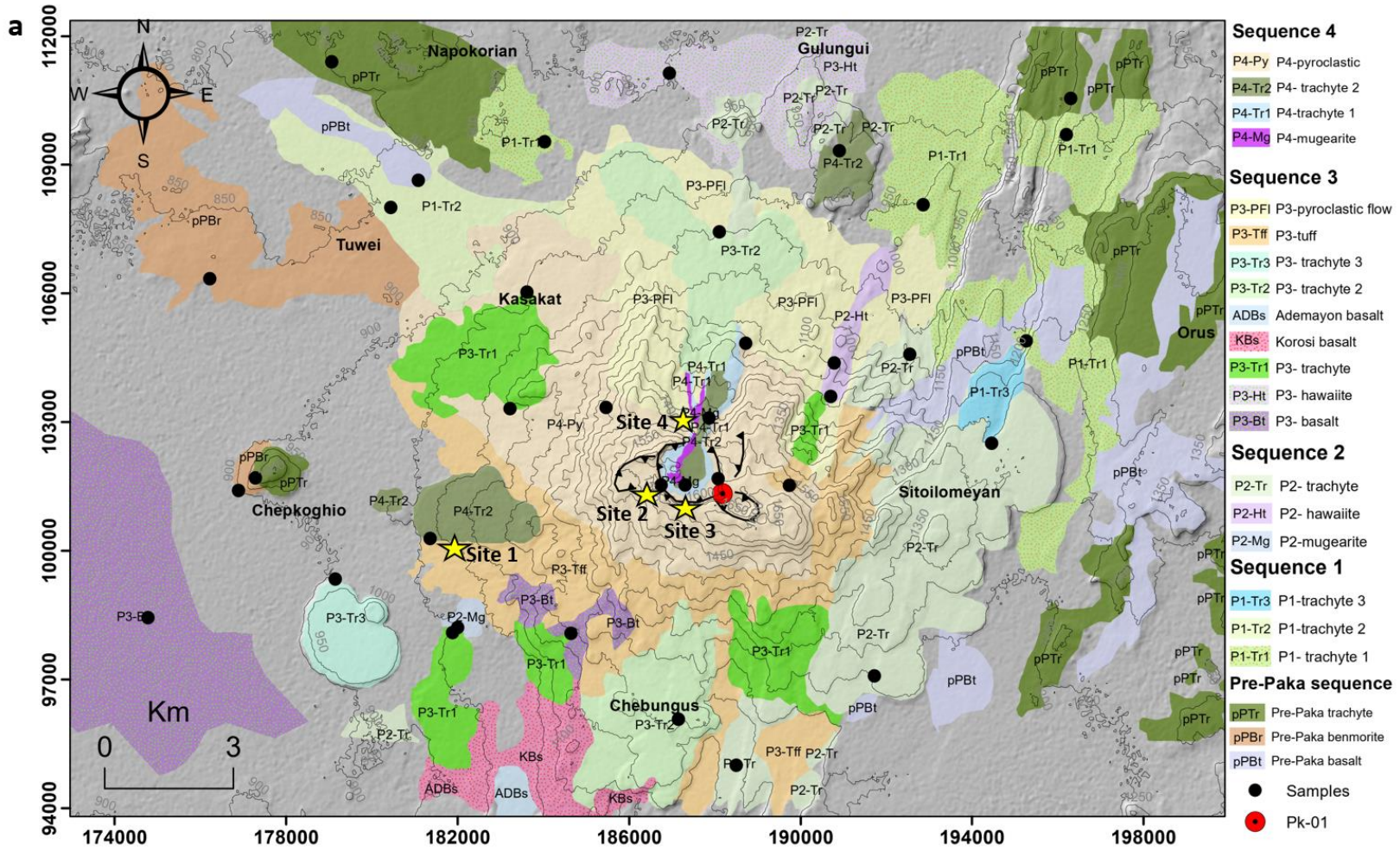

Fig. 5. Geological map of Paka volcano based on the interpretation of remote sensing imagery, field mapping, and previous work. The new map is an updated version of previous work (Dunkley et al., 1993; Sceal, 1974) . The areas with a grey shade correspond to a veneer of alluvium cover. The black spots are sample locations and the yellow stars are sites 1-4 shown in Fig. 6. For the sample names refer to table 1.

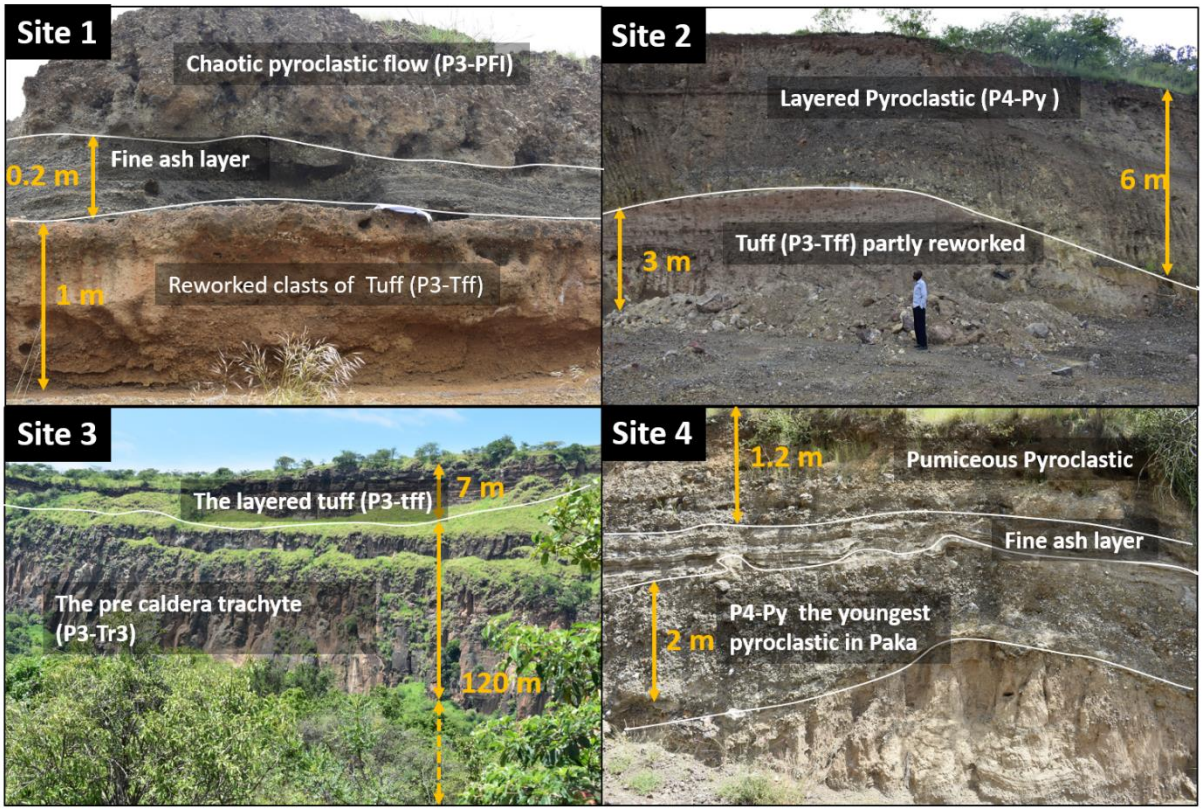

Fig. 6. Field stratigraphic observations with photos corresponding to field stratigraphic log sites in the geological map at Site 1, Site 2, Site 3 and Site 4.

4.3 Borehole stratigraphy

The borehole stratigraphy is based on the first well (PK-01) drilled at Paka. The well was drilled between December 2018 and May 2019 and was undergoing discharge tests in December 2019. It is located at an intersection between the main caldera and the southeast mini-caldera at coordinate location 188155.88°E, 101353.792°N (Fig. 5). The well encountered huge circulation losses and only 60% of cutting samples were recovered (Fig. 7). Nevertheless, careful binocular, hand specimen, thin section, and surface elevation data analyses provided some constraints on the buried stratigraphy at Paka. Results indicate that the drilled hole intersected at least nine units akin to those mapped on the surface, i.e. from the youngest to the oldest; P3-Tr3, P3-Tr2, P3-Tr1 from Phase 3 volcanic sequence. The P2-Tr, from Phase 2 volcanic sequence, P1-Tr3, P1-Tr2, P1-Tr1, from Phase 1 volcanic sequence and pPTr and pPBr from Pre-Paka plateau eruptions. Several formations which were mapped on the surface were not intercepted by the well, among these are; P4-Py, P4-Tr2, P4-Tr1, P4-Mg, P3-Tff, P3-Bt, P3-Ht, P2-Ht, P2-Mg, and pPBt. This is mainly due to the location of the well. It is also possible that some of these formations are formed by fissure or flank eruptions and hence not radially extensive. The total thickness of the drilled lava formations directly associated with the Paka magma system (P1 to P4 excluding Pre-Paka) is ~1050 m. The deepest Paka lava formation in the well was the P1-trachyte 1 (P1-Tr1), which was intercepted at 928-1048 m depth. Below is the description of the established borehole lithological stratigraphy from the oldest to the youngest.

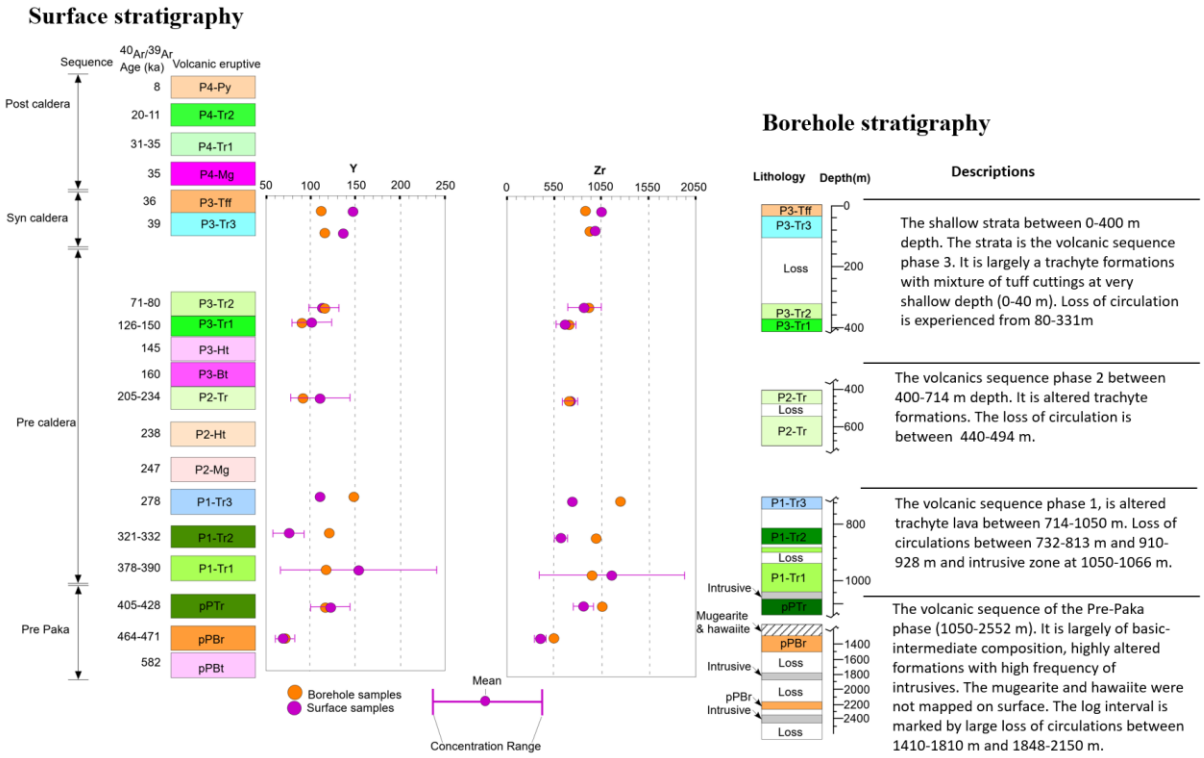

Fig. 7. Correlation of surface and borehole sequence using Y and Zr presented in Table S1. The insert error bars represent the concentration range (Lowest and highest values) of Y and Zr in surface samples as illustrated by the legend at the bottom of the Fig.

4.3.1 Pre-Paka volcanic sequence

Benmorite (pPBr)

This is the oldest extrusive volcanic rock encountered between 1314 and 2290 m. The deepest depth marks the interface between the extrusive and intrusive volcanic material found in the well. The benmorite formation is, dark grey, aphyric, and has extensive thickness. It is linked to the Pre-Paka benmorite mapped on the surface, which has been dated at 464-471 ka. It is underlain by a syenite intrusion.

Mugearite and hawaiite

The mugearite and hawaiite cutting samples have no equivalents among the units mapped on the surface. The mugearite is encountered between 1122 and 1204 m, while the hawaiite is encountered between 1204 and 1314 m, and therefore each about 80 m thick. They are associated with the early regional plateau eruptions. The binocular analysis shows that they are dark grey, fine-grained and altered, suggesting intense hydrothermal alteration.

Pre-Paka trachyte (pPTr)

This is a porphyritic, fine-grained lava encountered between 1066 and 1112 m depth. It is at a greater depth than estimated from the elevation difference (~700 m). This can be explained either by faulting or that at the time of this eruption, a graben structure was present. Considering the present graben and horst structures in the area, this is a distinct possibility. The formation is altered and forms part of the geothermal reservoir rocks.

4.3.2 Volcanic Sequence Phase 1

P1-trachyte

This is medium-grained porphyritic lava encountered between 704 and 1048 m depth. It is composed of several flows named P1-Tr1, P1-Tr2, and P1-Tr3 and underlies the P2-trachyte (P2-Tr). The flows are hydrothermally altered as shown by their mottled texture. It occurs at an elevation of ~ 900 m a.s.l at the surface. Based on the elevation difference, the estimated burial depth would be ~700 m depth. This agrees with the shallowest logged depth of 704 m.

4.3.3 Volcanic Sequence phase 2

P2-trachyte (P2-Tr)

This is a 240 m thick, fine-grained, altered formation encountered between 420 and 666 m depth and probably consists of several flows. It is mapped at an elevation of 1300 m on the surface east of the caldera, an area considered to be the raised footwall of the faulted area. The drilled depth, therefore, is greater than the calculated elevation difference, as a consequence of a fault downthrow. Major element analysis shows the formation is quartz normative (Table S1), which matches the P2-Tr mapped at the surface.

4.3.4 Volcanic Sequence phase 3

P3-trachyte 1 (P3-Tr1)

The P3-Tr1 is a ~20 m thick, medium-grained, sanidine porphyritic lava encountered between 372 and 392 m. This is consistent with a depth of ~400 m, calculated from elevation difference (Fig. 5).

P3-trachyte 2 (P3-Tr2)

The P3-trachyte 2 lava was penetrated at 331-372 m depth and is overlain by P3-Tr3. It is a light grey to brownish grey, sanidine-rich, medium-grained lava. It correlates with P3-Tr2 mapped at an elevation of between 1200-1360 m a.s.l (Fig. 5). The surface elevation difference indicates, that the lava should be encountered at ~ 320 m depth. This depth matches very closely with the drilled depth of 331-372 m. Major element chemistry suggests that the formation is slightly nepheline normative (Table S1), and resembles the P3-Tr2 mapped at the surface.

P3-trachyte 3 (P3-Tr3)

This is a 64 m thick lava unit associated with the syn-caldera lava effusive event penetrated between 16 and 80 m. The binocular analysis suggests that it is porphyritic and oxidised due to surface water interaction. It is related to the sanidine porphyritic trachyte lava at the surface

dated at 39±6 ka. Calculated normative mineralogy from major element analysis indicates that the lavas are slightly nepheline normative (Table S1), which compares well with the mapped P3-Tr3 at the surface.

4.3.5 Volcanic Sequence phase 4

Pyroclastic and tuff (P4-Py and P3-Tff)

Pyroclastic material is encountered at shallow depths (0-16 m) where mixed cuttings of a pyroclastic and trachyte lava formation were logged. According to our evaluation, the pyroclastic formation is related to the pumice eruption of 8 ka and partly to the syn-caldera tuff.

4.3.6 Intrusions

The well intersects intrusive rocks at several depth intervals. Based on thin section and binocular analyses, the intrusives are whitish-grey and porphyritic syenite. The shallowest is encountered between 666-704 m depth as the upper unit while the lower units are between 904-910 m depth. The deeper layers are encountered between 1048 and 1066 m, 1818-1848 m and at 2382-2402 m depth. The apparent total thickness of the syenite intrusives is estimated to be ~113 m, this is derived from by adding all the thicknesses of the intersected intrusions. This is, however, the minimum thickness as major circulation losses were experienced in the intrusive zones.

4.4 Tectonics and volcanic structures

4.4.1 Tectonic structures

Tectonic structures in Paka are characterised as normal faults, strike-slip faults and lineaments. The normal faults in Paka are the structures with clear near vertical displacements while the transform faults are structures that occur as oblique displacement zones between two related normal faults and therefore act as stress transfer or accommodation zones. The lineaments on the other hand are the sum of linear features with no apparent displacement and indistinct features including the inferred faults in the area. Eastern Paka shows intense faulting within the older Pre-Paka volcanic sequence dated at 582-405 ka, P1 (390-278 ka) and the P2 (247-205 Ka) volcanic sequences (Fig. 8a and 8b). This prominent faulting is embodied within a ~5 km wide fault zone which stretches towards the northeast in a right stepping manner for 10 km from Chebungus to Sitoilomeyan. There is a distinct curving in one of the normal faults at Sitoilomeyan perhaps indicating a more complex underlying tectonic environment. The fault intensity diminishes from the rift margins towards the axis of the Paka caldera on the younger lava sequences P3 (160-71 ka) and P4 (<71 ka). The P2-trachyte southeast of the Paka caldera displays the most intense faulting (Fig. 8a). It is also within this lava that we see a clear association of eruption centres and the NNE trending faults (Fig. 8b). In the northeast, a major fault (7 m downthrow) was mapped cutting through the 405 ka Pre-Paka trachyte (Fig. 8c). This lava sequence is towards the margin compared to the P2 sequence. Overall, the fault structures can be divided into two sets (i) the N40°W trending (ii) The N0°-40° E. The dominating faults strike N20°E and covers the whole field area as seen in the length weighted rose diagram (Fig. 9a) based on a total number of 473 faults and displayed in terms of population (%) grouped in 10° class interval The N40°W, are strike-slip structures causing intervening displacements on the N0-40°E trending fault structures within the central axial zone surrounding the main caldera (Fig. 9a).

The northwest-trending strike-slip faults are shorter and oblique to the normal faults. Evidence for the strike-slip fault with the sinistral motion through the main caldera was pointed out by Friese et al. (2014). Lineaments were classified as structures with no visible displacements and indistinct structures identified from the DEM (Fig. 9b). These lineaments have more variable directions and can be grouped into four sets i.e. E-W, N10-20°W, N40-60°W, and N20-40°E. The dominant trends are N60°W and N20°E as seen in the length weighted rose diagram (Fig. 9b) based on a total number of 166 lineaments and displayed in terms of population (%) in a class interval of 10°. The majority of the NW trending lineaments were proposed by Friese et al. (2014) based on a remote sensing study, they are mainly related to regional tectonic shear zones. The NNE trend on the other hand most likely represents buried faults as they appear to follow the predominant fault trend in the area. The lineaments are mostly mapped within the P3 and P4 volcanic sequences (Fig. 9b).

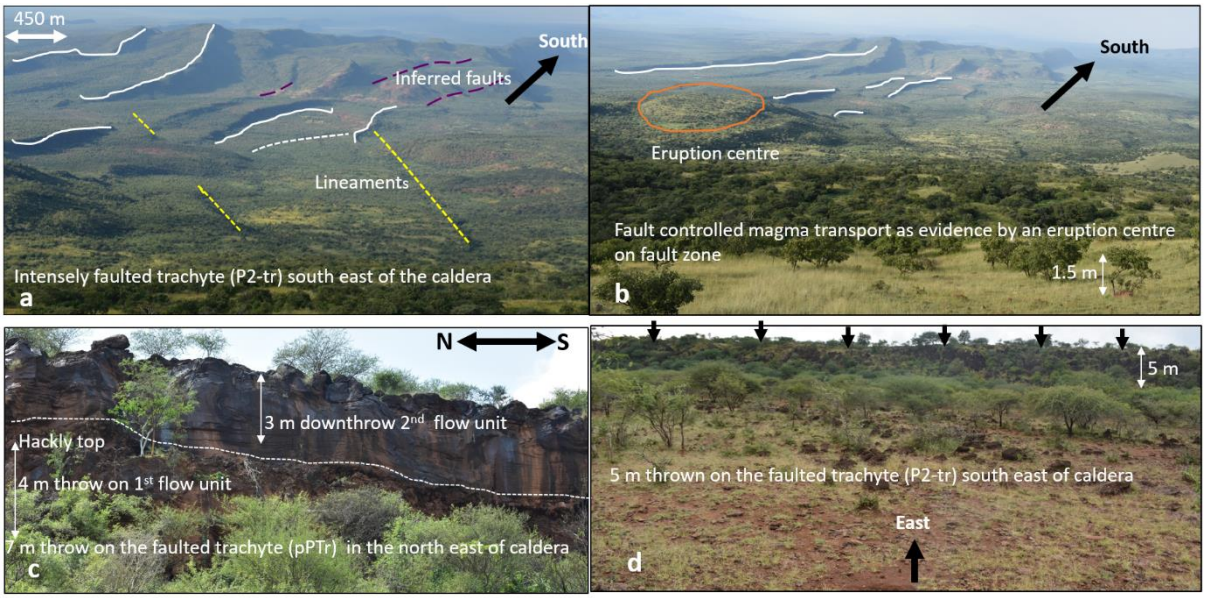

Fig. 8. General tectonic field observations. a) Intense faulting southeast of the Paka caldera. b) An eruption centre within the faulted zone. c) A large fault northeast of the Paka caldera. d) The N-S fault south of the Paka caldera.

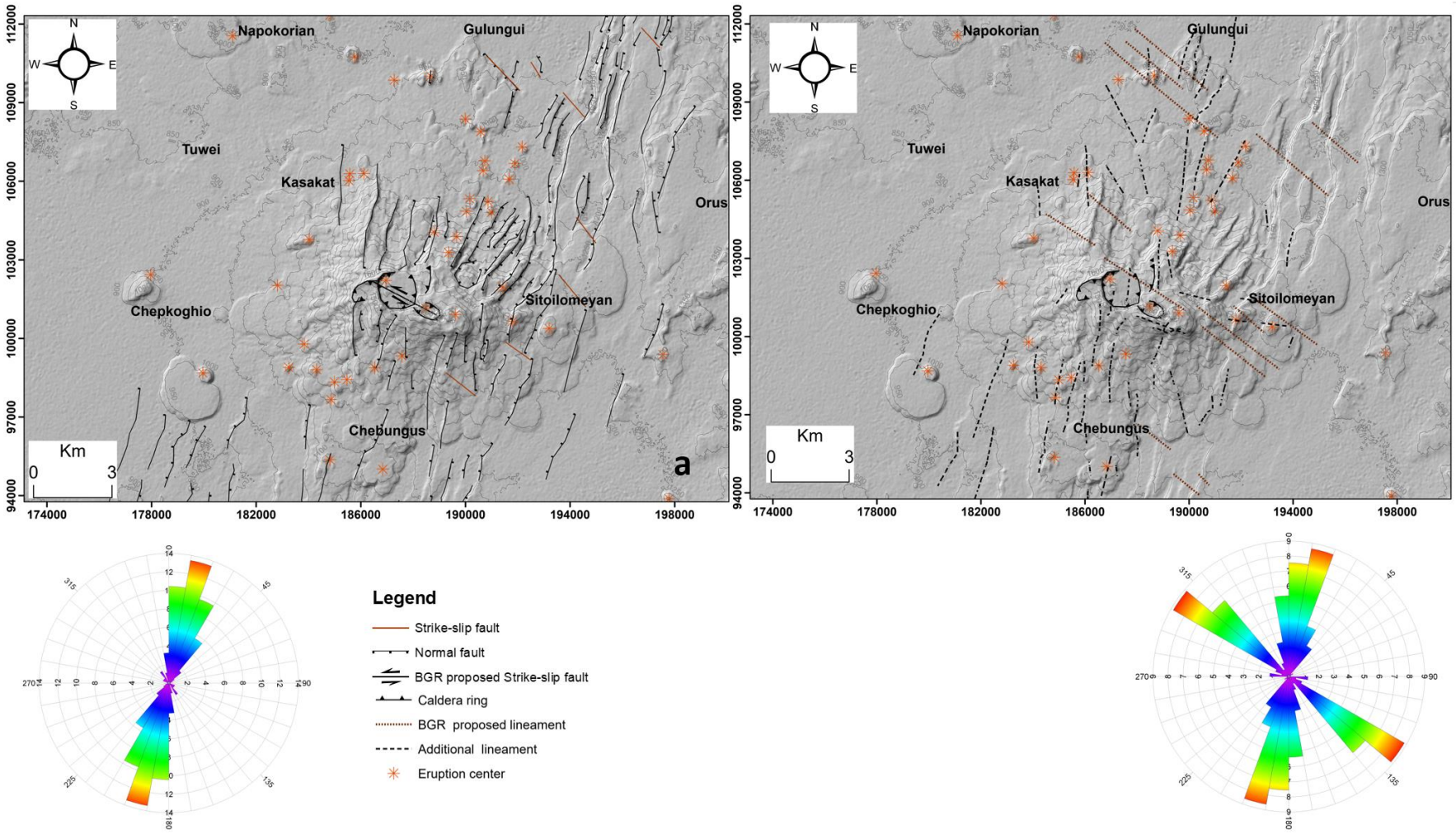

Fig. 9. Structural characterization based on the interpretation of DEM from SRTM data, field validation and previous work (Dunkley et al., 1993; Friese et al., 2014b; Sceal, 1974b). a) The NNE normal faults and NW faults on the left panel b) The lineaments and their structure trends on the right panel. Note the overall structural trends in the rose diagrams.

4.4.2 Eruption centres and the Paka caldera

Eruption centres are denoted by the orange stars in Fig. 9 and include trachyte domes, volcanic cones, tuff rings, craters, and subsidence structures in the summit area. The domes are prominent to the west of Paka, while cones, tuff rings, and craters dominate the northeast, east, and southeast part of the volcano. The alignment and trend pattern of the volcanic structures (volcanic cones, domes, tuff rings, craters) is not clear compared to the orientations of tectonic structures. However, a group of eruption centres aligned in NNE fashion is observed northeast of Paka (Fig. 9). The NNE trend parallels the overall trend of tectonic structures in the area indicating some relationship.

The summit area of Paka is structurally complex (Figs. 2a). It contains the main caldera structure extending 1.6 km in the E-W long axis and 1.5 km N-S short axis (eccentricity ~0.96). The caldera wall is 150 m high in the south, where distinct stratigraphic layers of slightly welded tuff (P3-Tff) and P3-trachyte 3 (P3-Tr3) are observed. To the north, however, the post-caldera lavas have filled the caldera upto the rim and hence no wall structure is exposed. The sub-circular main caldera is nested with arcuate collapse structures to the west and east in addition to an adjacent southeast mini-caldera. Both the main caldera and the southeast mini-caldera have Holocene (< 10 ka) craters, this is based on the dated pumice deposits (8 ka) assumed to have erupted from these craters (Dunkley et al., 1993). The latter appears to be underlain by a more active geothermal system as evidenced by intense fumarolic activity. The arcuate collapse structures are older than the main caldera structure and include a 1.5 km long structure west of the main caldera with an adjacent 0.5 km appendage, a 1.2 km structure to the southeast and a 0.6 km arcuate structure east of the main caldera. The arcuate fault structures are highly degraded by erosion and talus. We postulate that the explosive eruptions associated with the tuff (P3-Tff) caused these arcuate collapses and were a precursor to the main caldera piston collapse event. All the mapped subsidence structures in the summit area, including the main caldera and the mini-caldera, are enclosed in an inferred 3 by 2 km area with the NW-SE orientation.

5.0. Discussion

5.1 Eruptive history of the Paka volcanic complex

Regional lava flows of Miocene age were mapped in the Laikipia escarpment east of Paka by Sceal (1974). These rocks include a succession of basalt, trachyte, and phonolite. The formations were faulted in major successive faulting events estimated to have occurred until the Pleistocene. The later phases of faulting were followed by the plateau volcanic deposition, of which the ~500 ka lava sequence in Paka is most prominent and include the Orus, Secuminus, and Kokwabanga east of Paka. These lava flows were contemporaneous with the Jarota and hill of Mundi formations in the western flanks of Paka (Sceal, 1974). They were also concurrent with widespread regional eruptions, e.g., Baringo trachyte and basalt lava 25 km south of Paka volcano. The Miocene and early Pleistocene rocks make up the buried regional plateau lava formations predating the Silali, Paka, and Korosi volcanic centres as seen today.

In our new geological map (Fig. 5) the plateau lava formations within the Paka area are called the Pre-Paka basalt (pPBt) and the Pre-Paka trachyte (pPTr). They outcrop in the east (Orus area), west (Mundi hill area) and northwest of Paka. In the west, these formations might be much more extensive but are largely buried by the widespread P3- basalt (P3-Bt) associated with the Paka volcanic centre. Sceal (1974) mentions an eighty metre (80 m) deep borehole drilled west of Paka at Nyaunyau close to Nginyang area. This borehole intersects basalt formations exclusively. We postulate this logged formation to be the P3- basalts (P3-Bt) and the underlying plateau Pre-Paka basalts (pPBt). The Pre-Paka basalt (pPBt) was termed as Jarota formation by Sceal (1974). To the east and northeast, the Pre-Paka basalt spreads in an NNE-SSW and N-S manner suggesting a possible fissure-related source. The basalt overlies the Pre-Paka trachyte (pPTr) and is mostly buried below the P1-trachyte (P1-Tr1) in the Orus area, and only emerges at Secumia to the north. The Pre-Paka trachyte and basalt (plateau formations) have been dated at 582 to 405 ka. Following these plateau eruptions, an episode of faulting (Faulting 1) occurred in the Paka area around ~405 ka (Table 1) and is particularly evident in the east. The total downthrow from the faulting episode is approximately 300 m and west-dipping. The faulting resulted in a younger rift floor where the younger eruptions occurred. These younger eruptions marked the beginning of volcanism directly linked to the Paka centre, commencing with the P1-trachyte at ~390 ka. The P1-Tr1 outcrops in the east, northeast, and northwest of Paka and overlie the Pre-Paka trachyte (pPTr). It consists of three units, namely P1-Tr1, P1-Tr2, and P1-Tr3, which construct the base of the 6.6 km diameter Paka edifice.

Overall, volcanism directly liked to Paka centre spans a period between 390 ka and Holocene with the youngest eruption dated at 8±4 ka. This timeline suggests a magmatic history that is closely matched by that of Silali (400 to 7 ka) and Longonot (400 to 0.2 ka) but differs from that of Menengai (200 ka to 85 ka), and the 240-1 ka in Suswa (Clarke et al., 1990; Johnson, 1969; Leat, 1984; Smith et al., 1995). Globally, the Paka eruptions may have begun at similar timescales e.g., with Mount Mazama and Crater Lake caldera (Bacon, 1983) but much older than Iceland volcanoes e.g. Askja (Hartley et al., 2016).The Paka stratigraphy (Section 4.2) is summarised by four volcanic sequences in terms of age. The volcanic products in the sequences show a variation in chemical composition, and clearly point to evolution in the Paka magma over time. Volcanic sequence Phase 1 occurred between 390-278 ka and lasted for about ~120 ky, during which eruptions of the P1-trachyte formation (P1-Tr1, P1-Tr2, and P1-Tr3) occurred (Fig. 10b). After a faulting episode (Faulting 2), volcanic sequence Phase 2 erupted between 247-205 ka, where eruptions ocurred over a period of 35 ky and included the P2-mugearite,

P2-hawaiite and P2-trachyte formations (Fig. 10c). Volcanic sequence Phase 3 erupted between 160-36 ka after a faulting episode (Faulting 3). This eruptive phase lasted ~120 ky, a similar timespan as that of volcanic sequence 1. During this phase P3-basalt, P3-hawaiite, and P3-trachyte erupted (Fig. 10d). The end of Phase 3 volcanism, marks the beginning of an interesting phase in Paka. A phase where fault reactivation occurred between 71-39 ka. The sector collapses at 38 ka are assumed to indicate the early caldera formation phase. The volcanic sequence Phase 4 occurred between 35 to 8 ka and is the shortest volcanic phase during which both effusive and explosive eruptions occurred (Fig. 10e). Associated with this phase is the P4- mugearite (P4-Mg), P4-trachyte (P4-Tr1) and the P4-trachyte 2 (P4-Tr_2) These intra-caldera lava flows are related in terms of chemical composition suggesting periodic eruptions, mixing and finally spilling over from the caldera towards the north.

Based on the spatio-temporal relation of lava flows, the main Paka caldera is estimated to have formed at 37 ka, while the western mini-caldera and eastern collapse formed slightly earlier. This is an older age for the main caldera than the previous estimate of 8 ka (Dunkley et al., 1993). The eruptive volcanic products are further constrained by the results of well PK-01. The top of the borehole to about 1050 m depth is postulated to be the Paka volcanic lava pile (P1-P4), while the bottom part of the well, below 1050 m depth, is the plateau volcanic products (Pre-Paka). The borehole stratigraphy has been used to develop the geological cross-sections (Fig. S1 and S4).

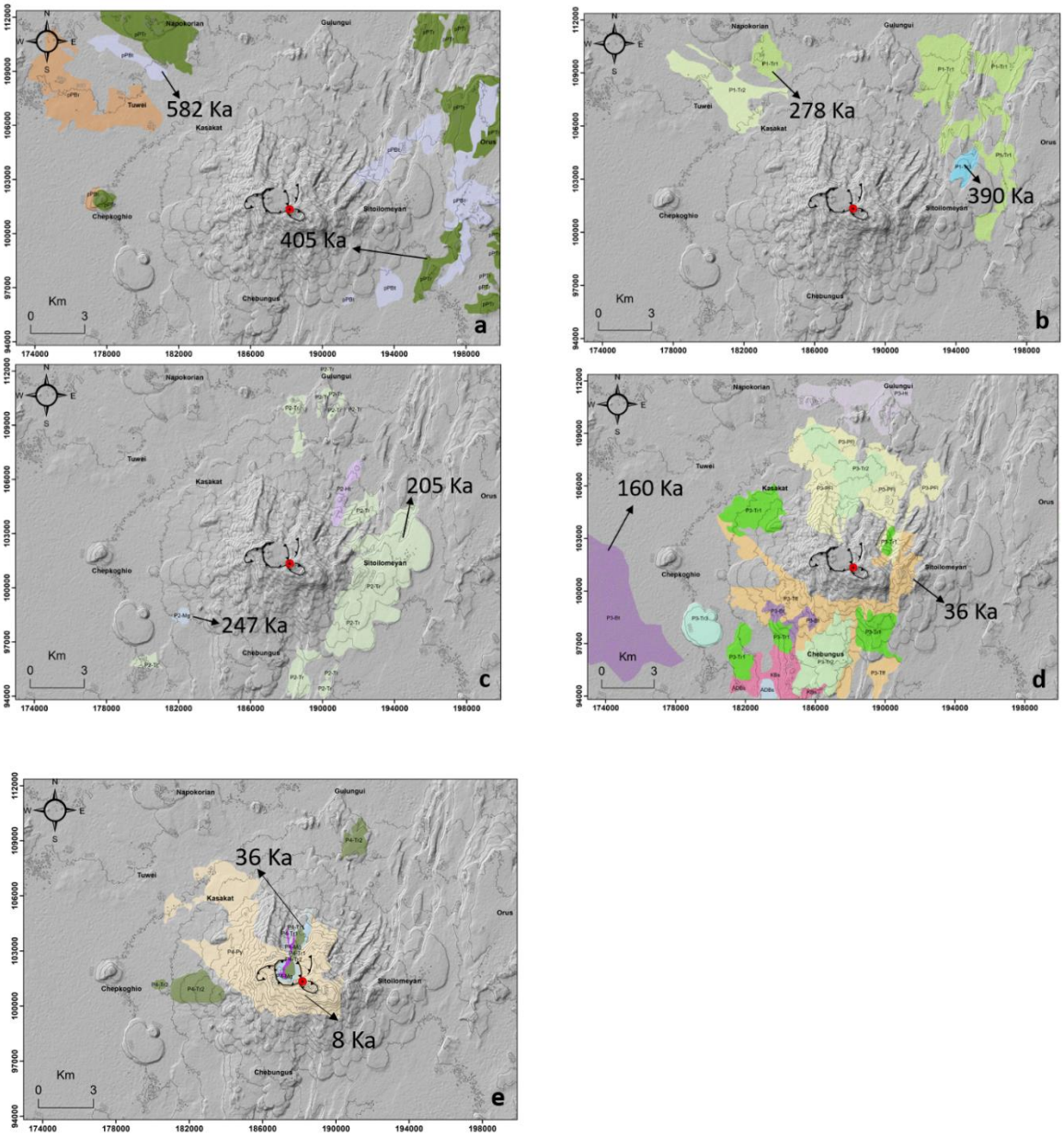

Fig. 10. a) Pre-Paka regional plateau sequence. b) Sequence 1 lava series, the early eruptions linked directly to Paka volcanic centre. c) Sequence 2, short-lived edifice forming lava series. d) Sequence 3, caldera related effusive and explosive sequence. e) Sequence 4, climactic phase intra-caldera effusive and explosive post-caldera products. The ages shown are the youngest and oldest lava eruption in each volcanic phase.

5.2 Paka caldera collapses

The evolution of the Paka caldera is much more complex than previously thought (Dunkley et al., 1993). This is due to the seemingly intricate sector collapses. The main caldera is the most prominent feature in the summit area. It is a 1.5 by 1.6 km sub-circular feature with a caldera wall of ~150 m at the deepest end in the south. The shallowest end is in the north where the caldera is filled by intra-caldera lava flows outflowing to the north. The limited accumulations of talus and erosional features around the main caldera walls, and the fact that it cuts through the ~38ka tuff (P3-Tff), indeed confirms the relatively young age (~37 ka) of the main caldera. There are additional arcuate subsidence structures associated with P3-Tff explosive event in the summit area predating the main caldera as has been pointed out in Section 4.4. The faults associated with these subsidence structures (except the mini-caldera) are highly degraded by erosion, with huge portions of talus accumulation. This indicates that they are older compared to the main caldera and therefore preceded the main caldera formation.

Based on this analysis, then Paka summit area appears to have undergone piecemeal collapse, making it very complex. Piecemeal collapse of similar patterns are prominent in other caldera settings within the Kenya rift, e.g., Menengai, where a number of sectors collapse preceded the latest caldera structure (Leat, 1984b). This is also true for other calderas around the world, e.g.,Krafla and Askja in Iceland, and Las Cañadas caldera in Tenerife (Ármannsson et al., 1987; Hartley & Thordarson, 2012; Martí, 2019). They all have a larger caldera formed from several sectors collapsing over time. If we examine the chronology of events in the Paka summit in detail, we find that the summit collapses began with the outer rim arcuate structures both in the west, east and southeast of the main caldera. This was followed by the southeast mini-caldera subsidence and finally the main caldera event. The main caldera event has no clear corresponding explosive eruption. This is not unique as previous research has shown that not all calderas form by explosive events (Hartley & Thordarson, 2012). As such it could be postulated that the main Paka caldera collapse may have been largely due to the drainage of magma by dyke injection, as Dunkley et al. (1993c) proposed for the nearby Silali Volcano.

5.3 Correlation of surface and borehole volcanic sequence using Y and Zr

Borehole stratigraphy of well (Pk-01) presented in Section 4.3 is largely determined through evidence from the mapped formation thicknesses on the surface and petrographic observations. We explore further whether the proposed volcanic sequences (Phase 3, Phase 2, Phase 1 and Pre-Paka) within the borehole can be correlated with the mapped surface formations by using Y and Zr trace element compositions. We use these elements, because: a) they span a large concentration range i.e 58-260 ppm for Y and 355-2072 ppm for Zr (Table S1), b) borehole samples and surface samples cover the same compositional fields (Fig. 4) and c) the two elements show excellent correlations both among surface and borehole samples (Fig. 4d).

The good correlation (r^2>0.9) between Y and Zr suggests that the studied samples retain their compositions inherited from magmatic differentiation. Both Y and Zr are incompatible during fractional crystallization, therefore in a genetically related volcanic sequence, they should show a good positive correlation. When the samples suffer hydrothermal alteration, this correlation might be disturbed as shown by (e.g.,Pandarinath et al., 2008; Parsapoor et al., 2009; van Dongen et al., 2010). This, however, is not the case in our borehole samples, where Y and Zr seem to be largely immobile similar to the findings of Franzson (2008). This is expected in high-temperature aqueous fluids with a nearly neutral pH (Ayers et al., 2012; Bernini et al., 2013; Tropper et al., 2013)

Fig. 7 shows the mean concentrations and the concentration ranges of Y and Zr for both surface and corresponding borehole samples. The youngest volcanic sequence Phase 4 is excluded since we have no corresponding samples from the borehole. This is because the borehole was drilled outside the main-caldera floor where post-caldera sequence (Phase 4) deposits. Furthermore, during the drilling, several circulation losses occurred as indicated in the borehole log of Fig. 10. The concentration range of Y from the surface and the corresponding borehole samples overlap for volcanic units P3-Tr2, P3-Tr1, P2-Tr, Pi-Tr1, pPTr, and pPBr but discrepancies were evident for P3-Tff, P3-Tr3, P1-Tr3 and P1-Tr2 (Fig. 10). In the few formations where, large differences between the borehole and surface samples are observed, we suggest that the main factor could be the mixing of cuttings. We also note that in three out of four of these formations only one analysis was carried out from the surface formations and possibly that does not fully represent the compositional variation within the unit. On a larger scale view, the trace element data suggests that each unit of the volcanic sequence is a distinct geochemical unit.

5.4 Pace of volcanism and geohazard assessment

A well-constrained stratigraphic framework cannot be overemphasised in the reconstruction of past eruptive patterns, providing insights for future eruptions in a volcano (e.g.,Mattsson & Höskuldsson, 2011; Wolff et al., 2011). The availability of radiometric data for a large number of volcanic products in Paka volcano has provided an opportunity to reassess the stratigraphic framework. The revised stratigraphy highlights the eruptive history (Fig. 11) associated with the lava series corresponding to the four identified volcanic sequences. The mafic/intermediate rocks represent intermittent episodes of fresh magma injections in each volcanic sequence. The trachyte, on the other hand, represents the last phase, in the lifecycle of each magma injection for each sequence. This conclusion is drawn from the fact that each volcanic sequence begins with a less evolved mafic unit and ends with more evolved trachytic unit (Fig. 11). Based on the reconstructed eruptive record (Figs. 11), with the assumption that the record is free from sampling biases and other errors, it is evident that the repose periods of volcanism were between 40-1ka. It seems that the latest phase of volcanism was characterised by a higher frequency compared to earlier phases with a frequency of <1 ka. It was during the final eruptive phase within the summit area that the only known explosive eruption occurred (8 ka) coinciding with the African humid period (deMenocal et al., 2000; Shanahan et al., 2015); a period characterised by high precipitation and wet climate. It is difficult to predict if these latest high-frequency rates of eruptions (<1 ka repose) will be maintained, meaning an eruption in Paka could be impending, or longer repose periods (40 ka) will re-emerge like in the early phases. Generally, in the case of an eruption in Paka we are most likely to experience small to moderate effusive or explosive eruptions (VEI of 1-2). The eruptions will most likely be of trachytic or intermediate rock composition within the summit area. This is because all eruptions in the last 10 ky occurred in the summit area. Additionally, an InSAR study (Biggs et al., 2009; Friese et al., 2014b) shows inflation and deflation events occurring periodically within Paka summit area, which appear to be of magmatic origin.

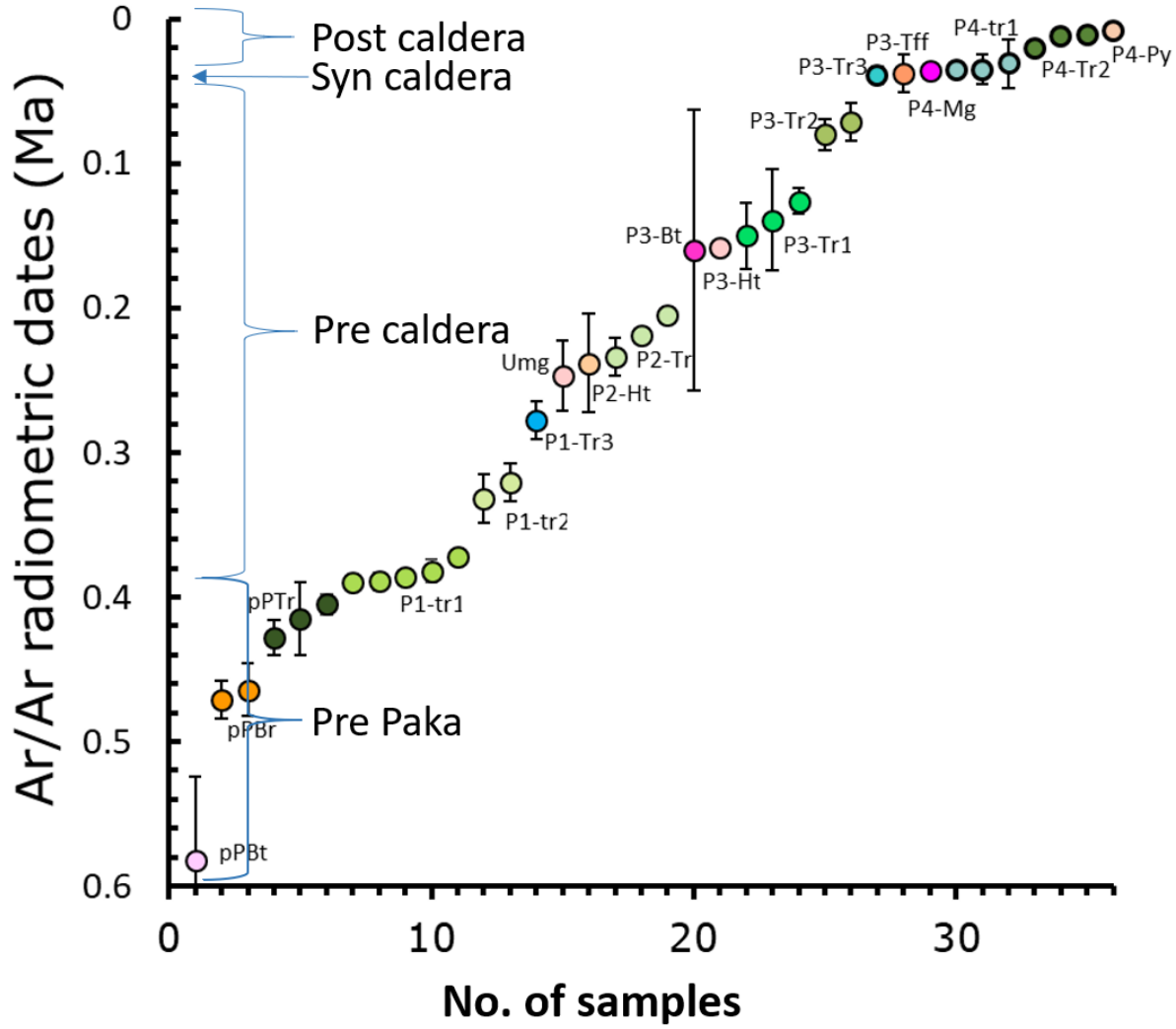

Fig. 11. The eruptive history and evolution of Paka volcanic complex based on $^{40}Ar/^{39}Ar$ age constrain (Dunkley et al., 1993; Friese et al., 2014b; Sudo et al., 2017b). A total of 35 distinct lava eruptions are recorded between 500 ka and 8 ka (The colours are similar to those in Fig. 5).

5.5 Tectonics and structural links to volcanism

Regional faults encompassing Paka area have previously been mapped (Dunkley et al., 1993; Sceal, 1974b; Strecker & Bosworth, 1991). Their findings suggest that faulting progressively shifted from the rift margins towards the central axis of the rift zones (Fig. 12). This means that older structures in Paka are towards the rift margins while the younger ones are towards the axis of the main Paka caldera. We see a similar variation pattern in our eruptive sequences, such that the older lava sequences are on the margin i.e. Pre-Paka, P1, and P2 sequences while the younger eruptives P3 and P4 are within the central axial zone surrounding the main caldera. Further scrutiny of the faulting in Paka indicates that there is a right stepping pattern from the central caldera area towards the margins with intervening displacements suggested as possible strike-slip faulting (Fig. 8a). This right stepping of faults in the area could be the main reason why the structures are most prominent to the east and towards the northeast of the volcano (Section 4.4) and more diffuse in the summit area and west of Paka. Another contributing factor

to the spatial variability in the fault density could be the masking effect of the younger volcanic lava, sediments and alluvium material (Muia, 2015). The general trend overall for all the faults in the area is NNE indicating that the fault extension regime in this small scale, has probably remained the same over time. The NW trending strike-slip faults (Fig. 9a) forms oblique intersections between the NNE trending faults compensating for intermittent movements and stress transfer along the main faults. Such oblique stress transfer faults are common in rifting environments (Dunkelman et al., 1989; Kuria et al., 2010). Some of these transfer structures could be evidence of the pre-existing underlying NW basement structures as proposed by Robertson et al. (2016).

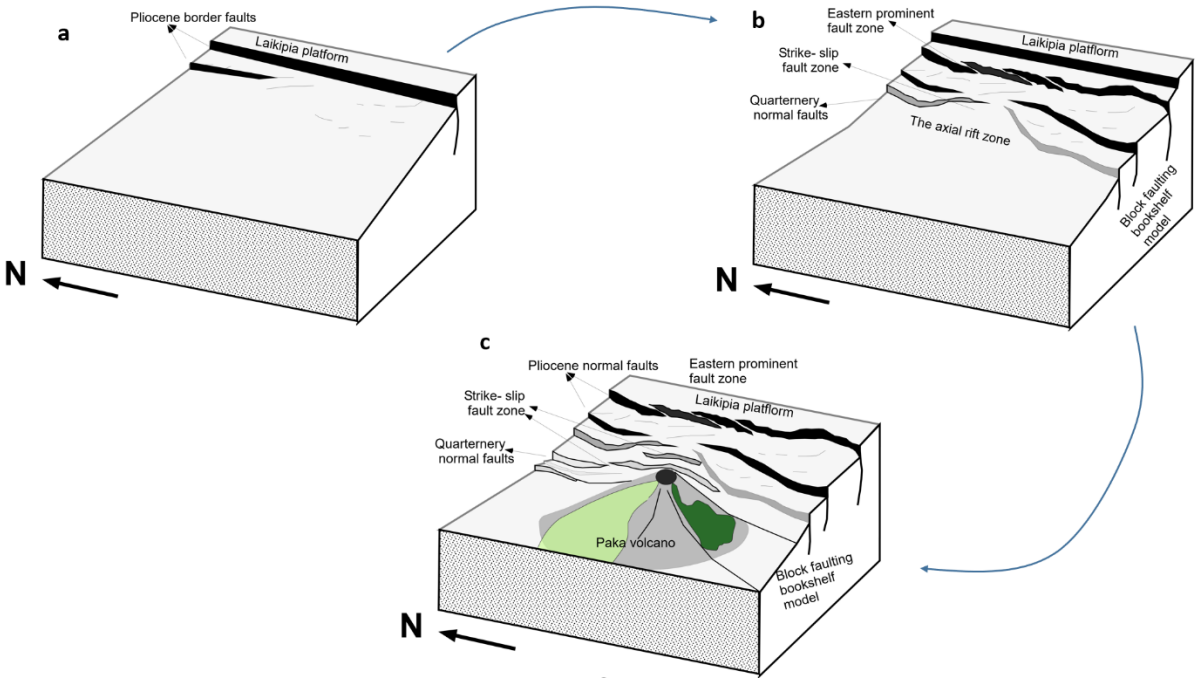

Fig. 12. Schematic diagrams of the evolution of Paka tectonic setting. a) Early faulting is marked by the Pliocene faults forming the border faults in the Laikipia platform. b) Faulting progressively shifted with time to the west and into the Paka axial zone in the Quaternary forming the young Paka faults. c) The intensely faulted Eastern Paka, showing fault jumps within strike-slip zones and intersection facilitating the growth of Paka volcano.

Based on the mapped formations we postulate possible fault ages such that the older faults are those mapped on the Pre-Paka, P1, P2 and the younger faults within P3 and P4 volcanic lavas. The Pre-Paka lava sequences are dated at 582-405 ka and the faults in this sequence can be constrained as being younger than these ages. As one moves from the Pre-Paka lava sequence, faults become more prominent and intense faulting is evident in P1 (390-278 ka) and P2 (247-205 ka) lava sequences (Section 4.4). These faults are of smaller scale and are considered generally younger than the regional faults similar to the Wonji faults in the main Ethiopian Rift (Abdulkadir & Eritro, 2017; Agostini et al., 2011; Corti, 2009; Polun et al., 2018; Wilks et al., 2017).

The prominent structural trends in the area, as noted in Section 4.4, are the NNE and NW crosscutting at intersection zones. The NW striking structures are evidenced by the NW-SE elongated ellipsoidal caldera (Friese et al., 2014b), and indeed, the two adjacent subsidence structures forming an overall NW-SE alignment. Additionally, a ridge trending NW-SE is

evident from the DEM at the summit area. This suggests a preferred volcanic accumulation and a relatively shallow intrusions, confirmed by the cauldron subsidence. This implies that the location and the build-up of the Paka volcano are highly influenced by the interaction of NNE and NW structural features, which form a perfect setting for relatively large shallow magma intrusions and associated volcanism. It is also inferred that the numerous smaller eruption centres northeast of the area, including the lava dome, cones and tuff rings, are influenced by similar tectonic features. Tectonic and magmatic associations are also evident in the southeast of Paka, where a lave dome was mapped within a fault as mentioned earlier (Fig. 8b).

To underpin our findings on the significance of tectonics on volcanism, research in other areas has also revealed an identical trend of structures providing magma passage to the surface. Examples of this are e.g. Mt Etna (Acocella & Neri, 2003), and Volcan Huaynaputina in southern Peru where its location is influenced by N–S trending normal faults and NW–SE strike-slip faults (Lavallée et al., 2009). A further example is the Colima volcanic complex of the western Mexican volcanic belt, where its location is influenced by an interplay of active N-S faults and E-W basement structures (Norini et al., 2010). In the EARS, the Menengai caldera in Kenya has been proposed to be at the intersection zone between NE and NW faults. The NE constitutes the Solai graben structures and the NW is associated with the Molo tectonic-volcanic structures (Mibei & Lagat, 2011). Paka volcano, therefore, should be included as another area where volcanic-tectonic interactions are well expressed.

5.6 Evolution of trachyte magma from a basalt parent

The differentiation from basalt through benmorite to trachyte in the Paka central volcano is reflected by the TAS diagram (Section 4.1.1). The plot shows a differentiation line straddling the alkali/sub-alkali line (Irvine & Baragar, 1971) suggesting a possible relationship of the rock types by fractional crystallization process, as suggested by Sceal & Weaver (1971). To quantitatively examine the fractional crystallization process we carried out a major element mass balance model (e.g.,Bryan et al., 1969), which was further tested through a Rhyolite-MELTS model (Gualda et al., 2012). In the mass balance model, we employed equation 1,

$$C_0 = C_l F + (1\text{-}F)C_s \quad \ldots\ldots 1$$

Where C_0 is the parent composition, C_l is the final composition, F is the fraction of the remaining melt and C_s is the residual component of the melt. The model was simulated by varying F and the ratio of mineral phases until the calculated results (C_l) closely matched the observed chemistry of the selected end members from the Paka samples. The mineral chemistry used as inputs in the model are based on unpublished microprobe analyses of mineral phases for a range of Paka rock samples which showed similar mineral phase chemistry to samples from the nearby Silali volcano lava flows (Macdonald et al., 1995a). Modelling was carried out in a two-step process by Excel. Stage 1 simulated the magma evolution from basalt to benmorite while stage 2 considered trachyte generation from benmorite. We selected the Pre-Paka basalt (Pk-20) as our initial parent composition as it is the oldest and the most primitive Paka basalt based on the low concentrations of incompatible elements, e.g., Y and La (Table S1). The daughter magma from stage 1 model closely matched the benmorite (Pk-22). The benmorite (Stage 1) was used as a parent composition for stage 2, where calculations done intended to achieve a liquid composition closely matching trachyte (Pk-18). The selected end members (Pk-20, Pk-22 and pk18) belongs to the Pre-Paka volcanic sequence, i.e., pPBt, pPBr, and pPTr in the stratigraphy (Table 1). Our results (Table 2) show that in stage 1, a magma liquid similar to benmorite (Pk-22) is achieved after 80% fractional crystallization (F=20) with the removal of 26% clinopyroxene, 21% olivine, 51% plagioclase and 1% K-feldspar. The sum

of squared residual ($\sum r^2$) for this calculation is 0.18. To generate a liquid magma with similar composition as the trachyte (Pk-18), a further 36% fractional crystallization (F=64) was required with the removal of 5% clinopyroxene, 11% olivine, 45% plagioclase, 32% feldspar and 6% magnetite. The $\sum r^2$ for this calculation is 0.19 which is an acceptable fit. Results of both stage 1 and 2 indicates that an overall fractional crystallization of ~72% is required for the Paka basalt to generate a trachytic magma with similar chemistry as the PK-18. The result was further tested through Rhyolite-MELTS (Gualda et al., 2012). The Rhyolites-MELTS approach determines phase equilibrium relations by minimizing Gibbs free energy for given input of intensive variables, i.e., temperature, pressure and oxygen fugacity (fO_2). The model variables tested included two oxidation states (ΔFMQ +1 and -1, four starting water contents (0.1, 0.5, 1.0, and 1.5 wt.%), and three pressures of crystallization (1, 2, and 4 kbar). To determine these initial conditions (Input variables) for our model we were guided by similar works done within the Kenya rift (e.g.,Macdonald et al., 2011; White et al., 2012). Furthermore, constrains on the pressures and water contents were obtained from geothermobarometry and hygrometry calculations from studied Paka volcanic products (Mibei et al., In prep). In carrying out rhyolite-MELTS modelling, the temperature is decreased incrementally from 1280 °C assumed to be sub-liquidus for the basalt to 715 °C the trachyte sub-solidus. The results of twenty-two out of the possible twenty-four (two models were unsuccessful due to a convergence error) attempted models are presented in bivariate plots of CaO vs SiO_2 (Fig. 12). From the results we conclude that best fit models to the chemical variations of the Paka rock samples are obtained when starting H_2O content is 1.5 wt%, oxygen fugacity (ΔFMQ +1) and two pressures conditions (1 and 2 kbar). These two models indicate that fractional crystallization of between 74-83% is required to produce the Paka trachyte compositions. The fractionation amount closely matches the 72% calculated by the mass balance modelling. The two best fit models are highlighted as plots of Na_2O, K_2O, MgO TiO_2 (Fig. S3) and in the TAS plot (Fig. 3a). The apparent poor fit in TiO_2 is possibly due to Fe-Ti oxides cumulates in our samples.

Table 2. Major element mass balance model for the generation of trachyte. (F is the fraction of melt remaining while residual is the difference between calculated and measured chemistry values).

Stage 1.Fractional crystalization of basalt to benmorite													
	PK-20	PK-22	cpx	olivine	plag	k fsld	mgt	ap	Calc.	residuals	FC model		
SiO_2	47.80	57.07	49.00	36.00	51.79	63.00	0.10	0.00	47.78	0.02	PK-24	F=20	
TiO_2	2.00	1.26	6.23	0.85	0.70	0.90	33.00	0.00	2.02	-0.02	cpx	0.25	26.18%
Al_2O_3	14.67	17.59	1.90	0.05	28.00	21.00	0.60	0.00	15.05	-0.38	olivine	0.20	20.94%
FeO	12.00	7.50	20.30	36.00	1.23	0.80	70.00	0.00	12.03	-0.03	plag	0.49	51.31%
MnO	0.21	0.25	0.50	0.50	0.01	0.00	1.50	0.00	0.24	-0.03	k fsld	0.01	1.05%
MgO	6.60	2.02	9.00	28.00	0.10	0.12	0.50	0.00	6.73	-0.13	mgt	0.00	0.42%
CaO	11.20	4.06	23.00	0.30	14.56	5.00	0.00	50.00	11.25	-0.05	ap	0.00	0.10%
Na_2O	3.00	5.99	1.00	0.00	4.21	7.56	0.00	0.00	3.11	-0.11		0.96	100.00%
K_2O	0.78	3.46	0.00	0.00	0.06	0.60	0.00	0.00	0.72	0.06			
P_2O_5	0.20	0.41	0.00	0.00	0.00	0.00	0.00	47.00	0.12	0.08			
									99.05	0.18=$\sum r^2$			
Stage 2.Fractional crystalization of benmorite to trachyte													
	PK-22	PK-18	cpx	olivine	plag	k fsld	mgt	ap	Calc.	residuals	FC model		
SiO_2	57.07	60.37	49.00	37.00	52.00	66.00	0.19	0.00	56.92	0.14	PK-18	F=64	
TiO_2	1.26	0.61	0.90	0.20	0.73	0.12	31.00	0.00	1.23	0.03	cpx	0.05	5.00%
Al_2O_3	17.59	15.25	10.00	0.02	29.00	26.00	0.70	0.00	17.72	-0.13	olivine	0.11	10.99%
FeO	7.50	9.61	25.00	27.00	0.80	0.40	0.00	0.00	7.79	-0.30	plag	0.45	44.96%
MnO	0.25	0.36	0.90	0.30	0.00	0.00	0.70	0.00	0.27	-0.02	k fsld	0.32	31.97%
MgO	2.02	0.45	4.80	36.33	0.65	0.10	0.80	0.00	1.99	0.03	mgt	0.06	5.99%
CaO	4.06	2.12	23.00	0.33	12.00	1.80	0.00	54.00	4.20	-0.14	ap	0.01	1.10%
Na_2O	5.99	6.21	1.50	0.00	6.00	7.87	0.00	0.00	5.87	0.13		1.00	100.00%
K_2O	3.46	4.62	0.00	0.00	1.00	4.00	0.00	0.00	3.55	-0.09			
P_2O_5	0.41	0.08	0.00	0.00	0.20	0.00	0.00	45.00	0.26	0.15			
									99.81	0.19=$\sum r^2$			

*PK-Paka, cpx-clinopyroxene, plag-plagioclase, k fsld-K felspar,mgt-magnetite, ap-apaptite, calc.-calculated, FC-Fractional Crystalization, F-fraction of melt, residuals is the variance between calculated chemistry and measured sample used

5.7 Eruptive volumes, large scale advective heat flux and hazard assessment

Volcanic eruption rates (Q_e) have been evaluated for volcanoes in various tectonic settings (e.g., White et al., 2006). The general conclusion is that the average eruption rate for volcanoes in continental settings is about 4.4 x10^{-3} km^3/yr compared to 2.8 x10^{-2} km^3/yr for volcanoes within oceanic settings (White et al., 2006). The output rate (Q_e) is a useful parameter in correlating and understanding volcanic systems. We, therefore, estimate this parameter for the Paka volcanic complex using the following restrictions; 1) the thickness of the extrusive volcanic material associated with the formation of Paka is ~1050 m (as determined from drilling); 2) the areal extent of the base for the Paka edifice is derived from it being a circle with a radius of 6.6 km; 3) The Paka edifice rises to a height of 650 m from the mean surface elevation of 1000 m a.s.l. Thus, to estimate the extrusive volumes making up the Paka edifice, we assume the shape of a cone with a radius of 6.6 km and a height of 650 m. The other component of the buried sequence underlying the edifice (below 1000 m a.s.l), is conceptualised as a buried inverted cone of radius 6.6 km with a height of 400 m. The 400 m height is calculated by subtracting the observed height of the edifice (650 m) from the total thickness of the Paka volcanic products (~1050 m). The conceptual model for the assumptions on the double-cone model in our calculations is highlighted in Fig. S4a and S4b and is based on the constructed cross-section in Fig. S1.

Based on these assumptions, the minimum volume of the erupted volcanic material is calculated to be ~50 km^3. From the calculated volume and considering the total duration of Paka volcanism of ~0.390 Ma, the volcanic eruption rate (Q_e) is estimated to be approximately 1.2 $x10^{-4}$ km^3/yr (0.12 km^3/ka). This value is similar to the 0.12 km^3/ka and the 0.10 km^3/ka calculated for the 500 ka Gedemsa and the 300 ka Badi volcanoes (Ethiopian Rift) respectively (Hutchison et al., 2018). It is also comparable to rates calculated for Soufrière Hills in Saint Vincent (Francis, 2002), but five times less than those calculated for Menengai (Germa et al., 2015; Leat, 1984b; Ownby et al., 2011). The Paka value is lower by an order of magnitude compared to the average values for volcanoes in continental settings and by two orders compared to volcanoes in oceanic settings. This finding is significant and helps visualise the size of the Paka magmatic system. To calculate the advective heat budget from the long-term magmatism in the Paka complex, we employ a previously used model (White et al., 2006). Based on their model, the excess heat flow (H) in J/yr associated with magma transport into the crust is given by;

$$H = ß\rho Q_e \Delta T \left[C_p + L/\left(T_{liquidus}\text{-}T_{solidus}\right)\right] \quad \text{.....2}$$

where; volcanic eruption rate is Q_e, the Intrusive to Extrusive ratio (I:E) is ß, the volumetric rate of magma in the crust is $ßQ_e$, the temperature difference between the magma and local crust is ΔT, the enthalpy of crystallization is L, the magma density is ρ, the isobaric heat capacity of the magma is C_p, and the liquidus to solidus temperature interval is $T_{liquidus} - T_{solidus}$.

The I:E is a valuable parameter in estimating the proportion of hidden intrusives at various tectonic settings (Greeley & Schneid, 1991). A wide range of I: E values have been published (Shaw, 1985; Wadge, 1980) with the most common value of 3:1 and median of 5:1 (White et al., 2006). In section 5.6 the fractional crystallization model suggests a probable I:E ratio of 4:1 for Paka. For our calculations we use these probable values, i.e., 3:1, 4:1 and 5:1. The calculations also assume a minimum and a maximum radius of the Paka volcanic area as being 6.6 and 7 km respectively. The range of values for I:E ratio and radius are used to test how sensitive the model is to these parameters due to the uncertainties involved. Other constants and assumptions are shown in Table 3 (Iacovino & Till, 2018; Oba & Shiraishi, 1993; Sigurdsson et al., 2015; Spera, 2000). The results show that an excess heat flux of 138 mW/m^2 (0.13 W/m^2) was focused under the Paka complex by the magmatic activity lasting 390 ka when an average area of 136 km^2 (radius 6.6 km) is considered. If an area of 154 km^2 (radius 7 km) is considered, a heat flux of 110 mW/m^2 (0.11 W/m^2) is calculated. These results are in excellent agreement with those derived from the borehole data measurements from Paka volcanic area (110-120 mW/m^2) but less than the maximum values measured in Menengai area boreholes (90-190 mW/m^2) or the Aluto volcano in Ethiopia where measured values range between 95- 200 mW/m^2 (Hochstein et al., 2017; Wheildon et al., 1994; Williamson, 1976). The calculated heat flux exceeds the average continental flux of 57 mW/m^2 (Fowler et al., 2004) and the background values in geothermal areas as indicated by the minimum values measured in boreholes at Menengai and Aluto. The results indicate an apparent high heat flux within the Paka volcanic complex. The high heat flux and the Holocene age of the latest eruption favours the existence of a magma-driven geothermal system.

Table 3. Values and assumptions used in the calculation of excess heat flux.

Equation components	Values used	Source
Ratio ß (I:E)	(a) 3/4, (b) 4/5 and (c) 5/6	a and c are estimates from (White et al., 2006) and b is from this study
density (ρ)	2882 Kg/m^3	Calculated from whole rock analysis of PK-20 a basalt sample from Paka (Iacovino & Till (2019)
Magma supply rate (Qe)	0.00013 km^3/yr	This study
Change in temperature(ΔT)	Magma temperatures 1150°C and country rock 650°C	Basalt magma temperature for Paka estimated from geothermobarometry from Paka samples (Mibei et al., In prep).The country rock is assumed to be syenitic, the sub-solidus temperature of <700° C is assumed (Oba & Shiraishi, 1993)
Isobaric heat capacity (C_p)	1484 J/Kg/K	Spera, 2000 as cited by (Sigurdsson et al., 2015)
Latent heat of crystallization(L)	400000J/kg	Spera, 2000 as cited by (Sigurdsson et al., 2015)
T liquidus	1120°C	Spera, 2000 as cited by (Sigurdsson et al., 2015)
T solidus	950°C	Spera, 2000 as cited by (Sigurdsson et al., 2015)

6.0 Conclusion

The revised field mapping of the Paka central volcano in the north Kenya rift has provided new insights into the eruptive history and volcano-tectonic evolution of Paka. Based on our results, a new and updated geological map has been composed. Our results show that the Pre-Paka volcanism commenced with mafic plateau fissure eruptions at about 500 ka, while eruptions directly associated with the Paka edifice began at 390 ka. The caldera collapse occurred between 38 ka and 35 Ka, while the climactic phase of volcanism was an explosive eruption at 8 ka. This timescale suggests that Paka was active at the same time as Silali and Longonot within Kenya rift. We have identified four main extrusive sequences described in the revised stratigraphy. Explosive eruptions have been rare in Paka, resulting in tuff and pyroclastic flows in the youngest volcanic sequence associated with the initial stages of caldera collapses and the youngest eruptions. Tectonics in the area are dominated by NNE and NW orientated structures. These trends are interpreted from mapped faults, lineaments, and trends of volcanic structures, e.g., eruptive cones and lava domes. We have determined that the NNE and the interaction between the NNE and NW structures play a vital role in magma transport and hence the heat source for the Paka hydrothermal system. The estimated total bulk volume for erupted products is about 50 km^3. This translates to an average volcanic eruption rate of 1.2 $x10^{-4}$ km^3/yr and an associated heat flux ranging from 110-138 mW/m^2. The high heat flux implies a magma-driven hydrothermal system exists in the Paka volcanic complex. Overall, the understanding of the eruptive history and evolution of Paka sets a stage for further studies on its magma plumbing architecture and the geothermal system.

Acknowledgement

The authors would like to thank the Geothermal Development Company Ltd (GDC) for allowing the use of their data, and for the assistance during the several field campaigns. We are grateful to Dario Ingi Di Rienzo, Jóhann Gunnarsson, and Sæmundur Ari Halldórsson for their assistance in sample preparation and ICP OES analysis. We appreciate Ármann Höskuldsson, Þorvaldur Þórðarson and Magnús Tumi Guðmundsson for good discussions related to this work. We also appreciate anonymous reviewers who greatly contributed to improving the manuscript for this paper. The project was funded by the Geothermal Development Company Limited of Kenya and the GRÓ-Geothermal Training Programme as part of a Ph.D. fellowship.

References

Abdulkadir, Y. A., & Eritro, T. H. (2017). 2D resistivity imaging and magnetic survey for characterization of thermal springs: A case study of Gergedi thermal springs in the northwest of Wonji, Main Ethiopian Rift, Ethiopia. *Journal of African Earth Sciences, 133*, 95-103. doi: https://doi.org/10.1016/j.jafrearsci.2017.05.001.

Acocella, V. (2014). Structural control on magmatism along divergent and convergent plate boundaries: Overview, model, problems. *Earth-Science Reviews, 136*, 226-288.

Acocella, V., & Neri, M. (2003). What makes flank eruptions? The 2001 Etna eruption and its possible triggering mechanisms. *Bulletin of Volcanology, 65*, 517-529. doi: 10.1007/s00445-003-0280-3.

Agostini, A., Bonini, M., Corti, G., Sani, F., & Mazzarini, F. (2011). Fault architecture in the Main Ethiopian Rift and comparison with experimental models: Implications for rift evolution and Nubia–Somalia kinematics. *Earth and Planetary Science Letters, 301*(3), 479-492. doi: https://doi.org/10.1016/j.epsl.2010.11.024.

Ayers, J. C., Zhang, L., Luo, Y., & Peters, T. (2012). Zircon solubility in alkaline aqueous fluids at upper crustal conditions. *Geochimica et Cosmochimica Acta, 96*, 18-28.

Ármannsson, H., Guðmundsson, Á., & Steingrímsson, B. (1987). Exploration and development of the Krafla geothermal area. *Jökull, 37*, 13-30.

Bacon, C. R. (1983). Eruptive history of Mount Mazama and Crater Lake Caldera, Cascade Range, U.S.A. *Journal of Volcanology and Geothermal Research, 18*(1), 57-115. doi: https://doi.org/10.1016/0377-0273(83)90004-5.

Baker, B. H. (1987). Outline of the petrology of the Kenya rift alkaline province. *30*(1), 293-311.

Baker, B. H., Mohr, P. A., & Williams, L. A. J. (1972). Geology of the Eastern Rift System of Africa. In B. H. Baker, P. A. Mohr, & L. A. J. Williams (Eds.), *Geology of the Eastern Rift System of Africa*: Geological Society of America.

Baker, B. H., Williams, L. A. J., Miller, J. A., & Fitch, F. J. (1971). Sequence and geochronology of the Kenya rift volcanics. *Tectonophysics, 11*(3), 191-215. doi: https://doi.org/10.1016/0040-1951(71)90030-8.

Bernini, D., Audétat, A., Dolejš, D., & Keppler, H. (2013). Zircon solubility in aqueous fluids at high temperatures and pressures. *Geochimica et Cosmochimica Acta, 119*, 178-187.

Biggs, J., Anthony, E., & Ebinger, C. (2009). Multiple inflation and deflation events at Kenyan volcanoes, East African Rift. *Geology, 37*, 979-982.

Bosworth, W. (1992). Mesozoic and early Tertiary rift tectonics in East Africa. *Tectonophysics, 209*(1), 115-137. doi: https://doi.org/10.1016/0040-1951(92)90014-W.

Brotzu, P., Morbidelli, L., Nicoletti, M., Piccirillo, E., & Traversa, G. (1984). Miocene to Quaternary volcanism in eastern Kenya: sequence and geochronology. *Tectonophysics, 101*(1-2), 75-86.

Chorowicz, J. (2005). The East African rift system. *J. Afr. Earth Sci., 43(1-3) 379-410.*

Clarke, M. C. (1990). Geological, Volcanological and Hydrogeological Controls on the Occurrence of Geothermal Activity in the Area Surrounding Lake Naivasha, Kenya: With Coloured 1: 250 000 Geological Maps. Ministry of Energy.

Corti, G. (2009). Continental rift evolution: From rift initiation to incipient break-up in the Main Ethiopian Rift, East Africa. *Earth-Science Reviews, 96*(1), 1-53. doi: https://doi.org/10.1016/j.earscirev.2009.06.005.

Cutten, H. (2002). *The Mozambique Belt, eastern Africa-tectonic evolution of Gondwanaland amalgamation and (?) Rodinia breakup.* In Geological society of Australia abstracts (Vol.67, pp. 109-109). Geological Society of Australia; 1999.

De Siena, L., Chiodini, G., Vilardo, G., Del Pezzo, E., Castellano, M., Colombelli, S., . . . Ventura, G. (2017). Source and dynamics of a volcanic caldera unrest: Campi Flegrei, 1983–84. *Scientific reports, 7*(1), 1-13.

deMenocal, P., Ortiz, J., Guilderson, T., Adkins, J., Sarnthein, M., Baker, L., & Yarusinsky, M. (2000). Abrupt onset and termination of the African Humid Period:: rapid climate responses to gradual insolation forcing. *Quaternary Science Reviews, 19*(1), 347-361. doi: https://doi.org/10.1016/S0277-3791(99)00081-5.

Dunkelman, T. J., Rosendahl, B. R., & Karson, J. A. (1989). Structure and stratigraphy of the Turkana rift from seismic reflection data. *Journal of African Earth Sciences (and the Middle East), 8*(2), 489-510. doi: https://doi.org/10.1016/S0899-5362(89)80041-7.

Dunkley, P. N., Smith, M., Allen, D. J., & Darling, W. G. (1993). The geothermal activity and geology of the northern sector of the Kenya Rift Valley.

Ebinger, C. (2012). Evolution of the Cenozoic East African rift system: Cratons, plumes, and continental breakup. *Regional Geology and Tectonic*. *Phanerozoic Rift Systems and Sedimentary Basins, eds* D. G. Roberts and A. W. Bally (Amsterdam :Elsevier) pp. 133-156.

Fowler, S. J., Bohrson, W. A., & Spera, F. J. (2004). Magmatic evolution of the Skye igneous centre, western Scotland: modelling of assimilation, recharge and fractional crystallization. Journal of Petrology, 45(12), 2481-2505.

Francis, P. (2002). The eruption of Soufrière Hills volcano, Montserrat, from 1995 to 1999. Geological Society of London.

Franzson, H., Zierenberg, R., & Schiffman, P. (2008). Chemical transport in geothermal systems in Iceland: Evidence from hydrothermal alteration. *Journal of Volcanology and Geothermal Research, 173*(3), 217-229. doi:https://doi.org/10.1016/j.jvolgeores.2008.01.027.

Friese, A., Hahne, K., Mutua, J., Lopeyok, T., & Mibei, G. (2014). *InSAR, surface movement and dating of Paka volcanic products, Northern Kenya Rift;*. (BGR 05-2343). Hannover,Germany: Federal Institute for Geoscience and Natural Resources Retrieved from https://www.bgr.bund.de/EN/Themen/Zusammenarbeit/TechnZusammenarb/Geotherm/Downloads/Publications/Poster.

Germa, A., Lahitte, P., & Quidelleur, X. (2015). Construction and destruction of Mont Pelée volcano: Volumes and rates constrained from a geomorphological model of evolution. *Journal of Geophysical Research: Earth Surface, 120*(7), 1206-1226.

Golden, M. (1978). *The Geology of the area east of silale, rift valley province, Kenya (Doctoral dissertation,* Royal Holloway, University of London).

Greeley, R., & Schneid, B. D. (1991). Magma generation on Mars: Amounts, rates, and comparisons with Earth, Moon, and Venus. *Science, 254*(5034), 996-998.

Gualda, G. A. R., Ghiorso, M. S., Lemons, R. V., & Carley, T. L. (2012). Rhyolite-MELTS: a Modified Calibration of MELTS Optimized for Silica-rich, Fluid-bearing Magmatic Systems. *Journal of Petrology, 53*(5), 875-890.

Guiraud, R., & Maurin, J.-C. (1992). Early Cretaceous rifts of Western and Central Africa: an overview. *Tectonophysics, 213*(1), 153-168. doi: https://doi.org/10.1016/0040-1951(92)90256-6.

Hackman, B. (1988). *Geology of the Baringo-Laikipia area: degree sheet 35 with coloured 1: 250,000 geological map and results of geochemical exploration*: Ministry of Environment and Natural Resources, Mines and Geological Deptartment.

Hackman, B., Charsley, T., Key, R., & Wilkinson, A. (1990). The development of the East African Rift system in north-central Kenya. *Tectonophysics, 184*(2), 189-211.

Hartley, M., & Thordarson, T. (2012). Formation of Öskjuvatn caldera at Askja, North Iceland: Mechanism of caldera collapse and implications for the lateral flow hypothesis. *Journal of Volcanology and Geothermal Research, 227-228*, 85-101. doi: https://doi.org/10.1016/j.jvolgeores.2012.02.009.

Hartley, M., Thordarson, T., & de Joux, A. (2016). Postglacial eruptive history of the Askja region, North Iceland. *Bulletin of Volcanology, 78(4), 28*.

Hochstein, M. P., Oluma, B., & Hole, H. (2017). Early exploration of the Aluto geothermal field, Ethiopia (History of discovery well LA-3). Geothermics, 66, 73-84. doi:https://doi.org/10.1016/j.geothermics.2016.11.010.

Hutchison, W., Mather, T. A., Pyle, D. M., Boyce, A. J., Gleeson, M. L., Yirgu, G., . . . Millar, I. L. (2018). The evolution of magma during continental rifting: New constraints from the isotopic and trace element signatures of silicic magmas from Ethiopian volcanoes. *Earth and Planetary Science Letters, 489*, 203-218.

Hutchison, W., Pyle, D. M., Mather, T. A., Yirgu, G., Biggs, J., Cohen, B. E., . . . Lewi, E. (2016). The eruptive history and magmatic evolution of Aluto volcano: new insights into silicic peralkaline volcanism in the Ethiopian rift. *Journal of Volcanology and Geothermal Research, 328*, 9-33. doi: https://doi.org/10.1016/j.jvolgeores.2016.09.010.

Iacovino, K., & Till, C. (2018). DensityX: A program for calculating the densities of hydrous magmatic liquids from 427-1,627 °C and up to 30 kbar. *Volcanica, 2*, 1-10. doi: 10.30909/vol.02.01.0110.

Irvine, T. N., & Baragar, W. R. A. (1971). A Guide to the Chemical Classification of the Common Volcanic Rocks. Canadian Journal of Earth Sciences, 8(5), 523-548.

Johnshon, R. W. (1969). Volcanic geology of Mount Suswa, Kenya. Philosophical Transactions of the Royal Society of London. Series A, Mathematical and Physical Sciences, 265(1164), 383-412.

Kuria, Z. N., Woldai, T., Meer, F. D. v. d., & Barongo, J. O. (2010). Active fault segments as potential earthquake sources: Inferences from integrated geophysical mapping of the Magadi fault system, southern Kenya Rift. Journal of African Earth Sciences, 57(4), 345-359. doi: https://doi.org/10.1016/j.jafrearsci.2009.11.004.

Lavallée, Y., de Silva, S. L., Salas, G., & Byrnes, J. M. (2009). Structural control on volcanism at the Ubinas, Huaynaputina, and Ticsani Volcanic Group (UHTVG), southern Peru. *Journal of Volcanology and Geothermal Research, 186*(3), 253-264. doi: https://doi.org/10.1016/j.jvolgeores.2009.07.003.

Leat, P. T. (1984). Geological evolution of the trachytic caldera volcano Menengai, Kenya Rift Valley. *141*(6), 1057-1069.

Le Bas, M. J., Maitre, R. W. L., Streckeisen, A., Zanettin, B., & IUGS Subcommission on the Systematics of Igneous Rocks. (1986). A chemical classification of volcanic rocks based on the total alkali-silica diagram. *Journal of Petrology, 27*(3), 745-750.

Macdonald, R., Bagiński, B., Leat, P. T., White, J. C., & Dzierżanowski, P. (2011). Mineral stability in peralkaline silicic rocks: Information from trachytes of the Menengai volcano, Kenya. *Lithos, 125*(1), 553-568. doi: https://doi.org/10.1016/j.lithos.2011.03.011.

Macdonald, R., Davies, G., Upton, B., Dunkley, P., Smith, M., & Leat, P. (1995). Petrogenesis of Silali volcano, Gregory Rift, Kenya. *Journal of the Geological Society, 152*(4), 703-720.

Macdonald, R. (1974). Nomenclature and petrochemistry of the peralkaline oversaturated extrusive rocks. Bulletin volcanologique, 38(2), 498-516.

Macgregor, D. (2015). History of the development of the East African Rift System: A series of interpreted maps through time. *Journal of African Earth Sciences, 101*, 232-252. doi: https://doi.org/10.1016/j.jafrearsci.2014.09.016.

Maniar, P. D., & Piccoli, P. M. (1989). Tectonic discrimination of granitoids. *Geological Society of America Bulletin, 101*(5), 635-643.

Martí, J. (2019). Las Cañadas caldera, Tenerife, Canary Islands: A review, or the end of a long volcanological controversy. *Earth-Science Reviews, 196*, 102889. doi: https://doi.org/10.1016/j.earscirev.2019.102889.

Mattsson, H. B., & Höskuldsson, Á. (2011). Contemporaneous phreatomagmatic and effusive activity along the Hverfjall eruptive fissure, north Iceland: Eruption chronology and resulting deposits. *Journal of Volcanology and Geothermal Research, 201*(1), 241-252. doi: https://doi.org/10.1016/j.jvolgeores.2010.05.015.

McCall, G. J. H. (1967). *Geology of the Nakuru-Thomson's Falls-Lake Hannington area. Rep.Geol. Surv. Kenya, 78, 122.*

Mibei, G., & Lagat, J. (2011). Structural controls in Menengai geothermal field. *In Proceedings* (PP.21-21).

Miller, V., Voight, B., Ammon, C. J., Shalev, E., & Thompson, G. (2010). Seismic expression of magma-induced crustal strains and localized fluid pressures during initial eruptive stages, Soufrière Hills Volcano, Montserrat. *Geophysical Research Letters, 37*(19).

Muia, G. (2015). *The " Turkana Grits " : Potential Hydrocarbon Reservoirs of the Northern and Central Kenya Rifts.* Université de Rennes 1, Retrieved from https://hal-insu.archives-ouvertes.fr/tel-01379989.

Norini, G., Capra, L., Groppelli, G., Agliardi, F., Pola, A., & Cortes, A. (2010). Structural architecture of the Colima Volcanic Complex. *Journal of Geophysical Research: Solid Earth, 115*(B12).

Nyambok, I. O., & Gaciri, S. J. (1975). Geology of the fluorite deposits in Kerio Valley, Kenya. *Economic Geology, 70*(2), 299-307.

Oba, T., & Shiraishi, K. (1993). *Experimental studies on syenitic rocks in the Yamato Mountains, East Antarctica.* Paper presented at the Proceedings of the NIPR Symposium on Antarctic Geosciences (Vol. 6, pp. 72-82).

Ownby, S. E., Lange, R. A., Hall, C. M., & Delgado-Granados, H. (2011). Origin of andesite in the deep crust and eruption rates in the Tancítaro–Nueva Italia region of the central Mexican arc. *GSA Bulletin, 123*(1-2), 274-294.

Pandarinath, K., Dulski, P., Torres-Alvarado, I. S., & Verma, S. P. (2008). Element mobility during the hydrothermal alteration of rhyolitic rocks of the Los Azufres geothermal field, Mexico. *Geothermics, 37*(1), 53-72.

Parsapoor, A., Khalili, M., & Mackizadeh, M. A. (2009). The behaviour of trace and rare earth elements (REE) during hydrothermal alteration in the Rangan area (Central Iran). *Journal of Asian Earth Sciences, 34*(2), 123-134. doi: https://doi.org/10.1016/j.jseaes.2008.04.005.

Polun, S. G., Gomez, F., & Tesfaye, S. (2018). Scaling properties of normal faults in the central Afar, Ethiopia and Djibouti: Implications for strain partitioning during the final stages of continental breakup. *Journal of Structural Geology, 115*, 178-189. doi: https://doi.org/10.1016/j.jsg.2018.07.018.

Riaroh, D., & Okoth, W. (1994). The geothermal fields of the Kenya rift. Tectonophysics, 236(1-4), 117-130.

Robertson, E., Biggs, J., Cashman, K., Floyd, M., & Vye-Brown, C. (2016). Influence of regional tectonics and pre-existing structures on the formation of elliptical calderas in the Kenyan Rift. Geological Society, London, Special Publications, 420(1), 43-67.

Sceal, J., & Weaver, S. (1971). Trace element data bearing on the origin of salic rocks from the Quaternary volcano Paka, Gregory Rift, Kenya. *Earth and Planetary Science Letters*, *12*(3), 327-331.

Sceal, J. S. C. (1974). *The Geology of Paka Volcano and the Country to the East, Baringo District, Kenya* (Doctoral dissertation,Royal Holloway, University of London).

Shanahan, T. M., McKay, N. P., Hughen, K. A., Overpeck, J. T., Otto-Bliesner, B., Heil, C. W., . . . Peck, J. (2015). The time-transgressive termination of the African Humid Period. *Nature Geoscience, 8*(2), 140.

Shand, S. (1927). On the relations between silica, alumina, and the bases in eruptive rocks, considered as a means of classification. *Geological Magazine, 64*(10), 446-449.

Shaw, H. R. (1985). Links between magma-tectonic rate balances, plutonism, and volcanism. *Journal of Geophysical Research: Solid Earth*, *90*(B13), 11275-11288.

Sibson, R. H. (1994). Crustal stress, faulting and fluid flow. *Geological Society, London, Special Publications, 78*(1), 69-84.

Sibson, R. H. (1996). Structural permeability of fluid-driven fault-fracture meshes. *Journal of Structural Geology, 18*(8), 1031-1042.

Siegburg, M., Gernon, T. M., Bull, J. M., Keir, D., Barfod, D. N., Taylor, R. N., . . . Ayele, A. (2018). Geological evolution of the Boset-Bericha Volcanic Complex, Main Ethiopian Rift: 40Ar/39Ar evidence for episodic Pleistocene to Holocene volcanism. *Journal of Volcanology and Geothermal Research, 351*, 115-133. doi: https://doi.org/10.1016/j.jvolgeores.2017.12.014.

Sigurdsson, H., Houghton, B., McNutt, S., Rymer, H., & Stix, J. (2015). *The encyclopedia of volcanoes*: Elsevier.

Simiyu, S. M., & Keller, G. R. (1997). An integrated analysis of lithospheric structure across the East African plateau based on gravity anomalies and recent seismic studies. Tectonophysics, 278(1), 291-313. doi: https://doi.org/10.1016/S0040-1951(97)00109-1.

Smith, M., Dunkley, P. N., Deino, A., Williams, L. A. J., & McCall, G. J. H. (1995). Geochronology, stratigraphy and structural evolution of Silali volcano, Gregory Rift, Kenya. Journal of the Geological Society, 152(2), 297-310.

Smith, M. (1994). Stratigraphic and structural constraints on mechanisms of active rifting in the Gregory Rift, Kenya. *Tectonophysics, 236*(1), 3-22. doi: https://doi.org/10.1016/0040-1951(94)90166-X.

Spera, F. J. (2000). Physical properties of magma. *Encyclopedia on Volcanoes*.

Strecker, M., & Bosworth, W. (1991). Quaternary stress-field change in the Gregory Rift, Kenya. *Eos, Transactions of the American Geophysical Union, 72*, 17-22.

Sudo, M., Strecker, M., Friese, A., Hahne, K., Frei, M., & Riedl, S. (2017). *Temporal change in geochemistry of volcanic rocks in northern Kenya Ar geochronology at Paka*. Retrieved from https://confit.atlas.jp/guide/event-img/jpguagu2017/SGL37-05/public/pdf?type=in.

Tadesse, A. Z., Ayalew, D., Pik, R., Yirgu, G., & Fontijn, K. (2019). Magmatic evolution of the Boku Volcanic Complex, Main Ethiopian Rift. *Journal of African Earth Sciences, 149*, 109-130. doi: https://doi.org/10.1016/j.jafrearsci.2018.08.003.

Tropper, P., Manning, C., & Harlov, D. (2013). Experimental determination of CePO 4 and YPO 4 solubilities in H2O–NaF at 800° C and 1 GPa: implications for rare earth element transport in high-grade metamorphic fluids. *Geofluids, 13*(3), 372-380.

van Dongen, M., Weinberg, R. F., & Tomkins, A. G. (2010). REE-Y, Ti, and P Remobilization in Magmatic Rocks by Hydrothermal Alteration during Cu-Au Deposit Formation. *Economic Geology, 105*(4), 763-776.

Wadge, G. (1980). Output rate of magma from active central volcanoes. *Nature, 288*(5788), 253-255.

Wheildon, J., Morgan, P., Williamson, K., Evans, T., & Swanberg, C. (1994). Heat flow in the Kenya rift zone. Tectonophysics, 236(1-4), 131-149.

White, J. C., Espejel-García, V. V., Anthony, E. Y., & Omenda, P. (2012). Open System evolution of peralkaline trachyte and phonolite from the Suswa volcano, Kenya rift. *Lithos, 152*, 84-104. doi: https://doi.org/10.1016/j.lithos.2012.01.023.

White, S. M., Crisp, J. A., & Spera, F. J. (2006). Long-term volumetric eruption rates and magma budgets. *Geochemistry, Geophysics, Geosystems, 7*(3).

Wilks, M., Kendall, J. M., Nowacki, A., Biggs, J., Wookey, J., Birhanu, Y., . . . Bedada, T. (2017). Seismicity associated with magmatism, faulting and hydrothermal circulation at Aluto Volcano, Main Ethiopian Rift. *Journal of Volcanology and Geothermal Research, 340*, 52-67. doi: https://doi.org/10.1016/j.jvolgeores.2017.04.003.

Williams, L. A. J. (1972). The Kenya Rift Volcanics: A Note on Volumes and Chemical Composition. In R. W. Girdler (Ed.), *Developments in Geotectonics* (Vol. 7, pp. 83-96): Elsevier.

Williams, L. A. J. (1978). Character of Quaternary volcanism in the Gregory Rift Valley. *Geological Society, London, Special Publications, 6*(1), 55-69.

Williamson, K. H. (1976). Terrestrial heat flow studies in Kenya.

Wolff, J. A., Brunstad, K. A., & Gardner, J. N. (2011). Reconstruction of the most recent volcanic eruptions from the Valles caldera, New Mexico. *Journal of Volcanology and Geothermal Research, 199*(1), 53-68. doi: https://doi.org/10.1016/j.jvolgeores.2010.10.008.

Wright, T. J., Ebinger, C., Biggs, J., Ayele, A., Yirgu, G., Keir, D., & Stork, A. (2006). Magma-maintained rift segmentation at continental rupture in the 2005 Afar dyking episode. *Nature*, *442*(7100), 291-294.

Zhang, Y., Hobbs, B., Ord, A., Barnicoat, A., Zhao, C., Walshe, J., & Lin, G. (2003). The influence of faulting on host-rock permeability, fluid flow and ore genesis of gold deposits: a theoretical 2D numerical model. *Journal of Geochemical Exploration, 78*, 279-284.

Zielke, O., & Strecker, M. R. (2009). Recurrence of large earthquakes in magmatic continental rifts: insights from a paleoseismic study along the Laikipia–Marmanet Fault, Subukia Valley, Kenya Rift. *Bulletin of the Seismological Society of America*, *99*(1), 61-70.

Supplementary material to paper 1

Supplementary Figures S1–S4 are listed below. The supplementary Tables S1 indicating bulk rock chemistry analyses and Table S2 showing sample location and $^{40}Ar/^{39}Ar$ dating results and stratigraphic classification are included in Appendix A and B of the Thesis.

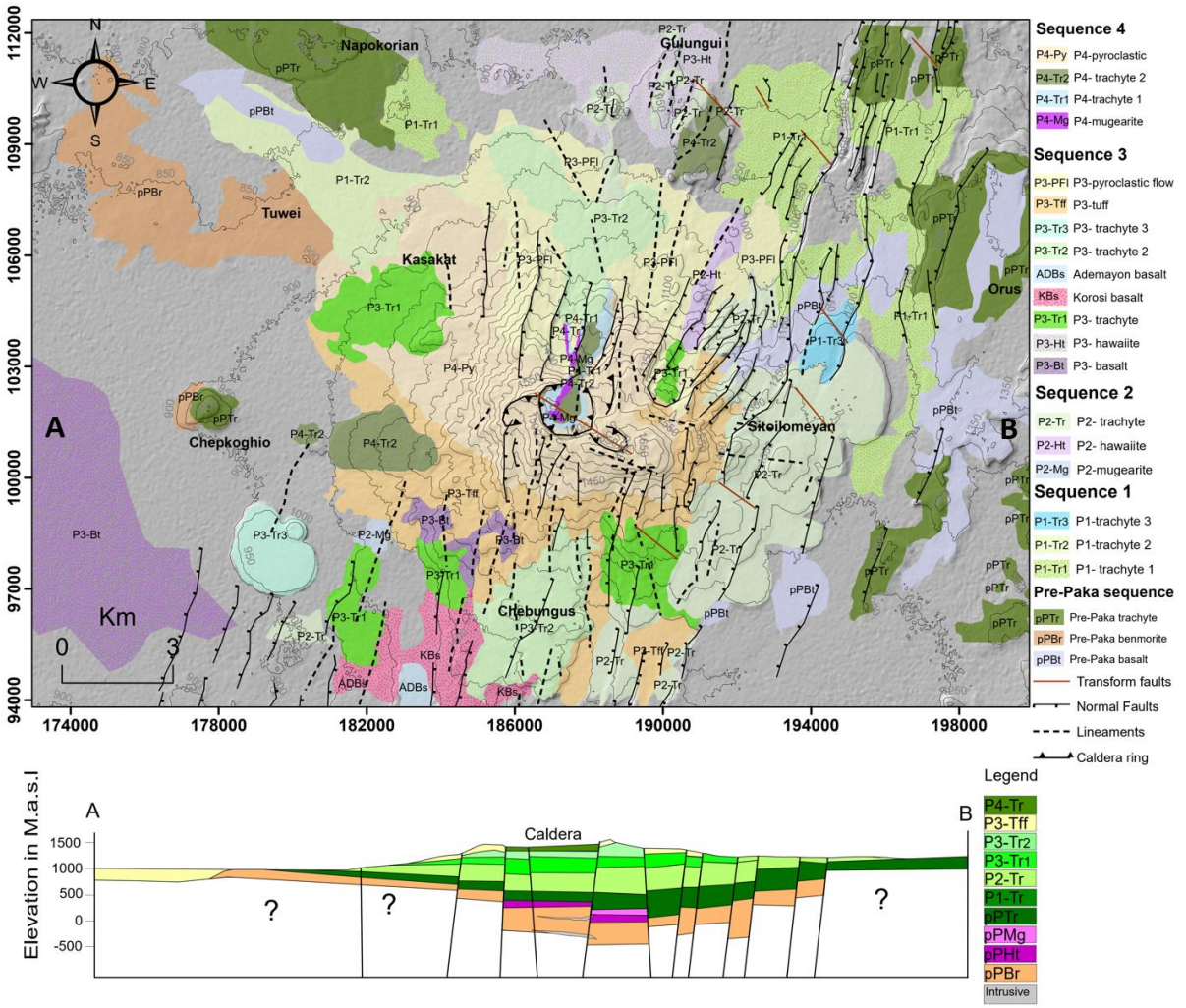

Fig. S1. The new geological map of Paka volcano in a revised stratigraphic framework. The projection is UTM (Universal Transverse Mercator) Zone 37 N, the datum is Arc 1960.

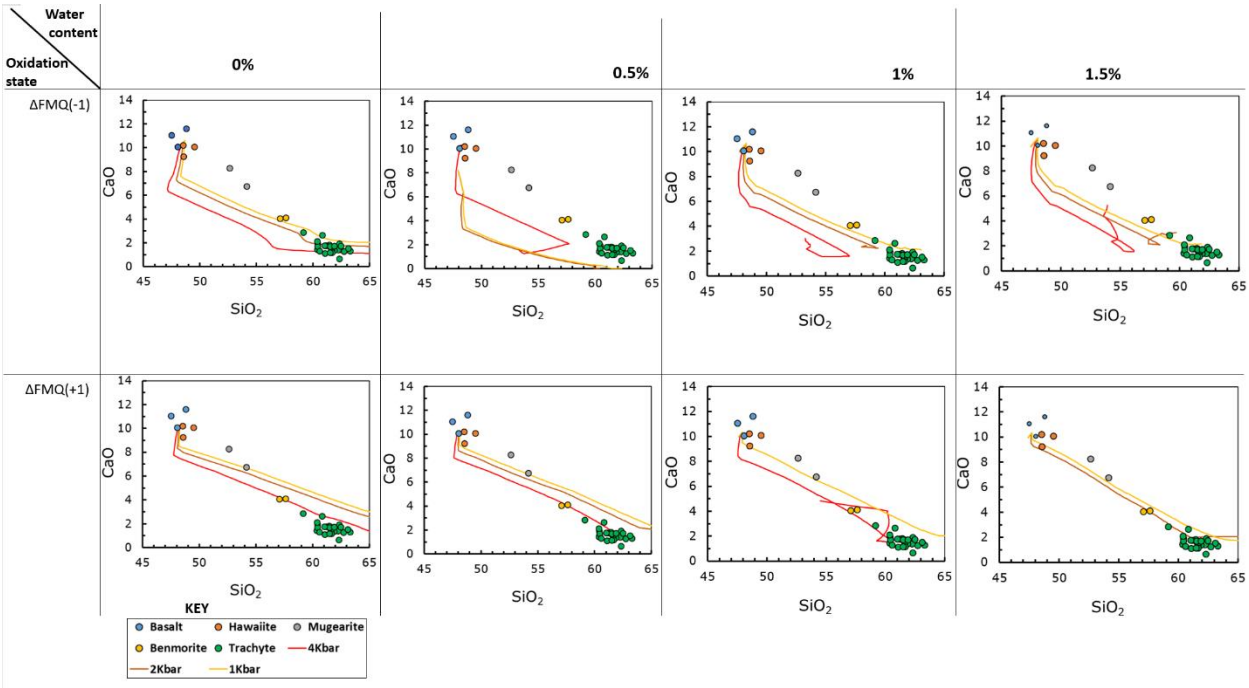

Fig. S2. Rhyolite-MELTS models with different initial water contents, pressures and oxygen fugacities.Two model runs were unsuccessful due to a convergence error, at 2 kbar with H_2O of 1% and at 4 kbar with H_2O of 1.5%.

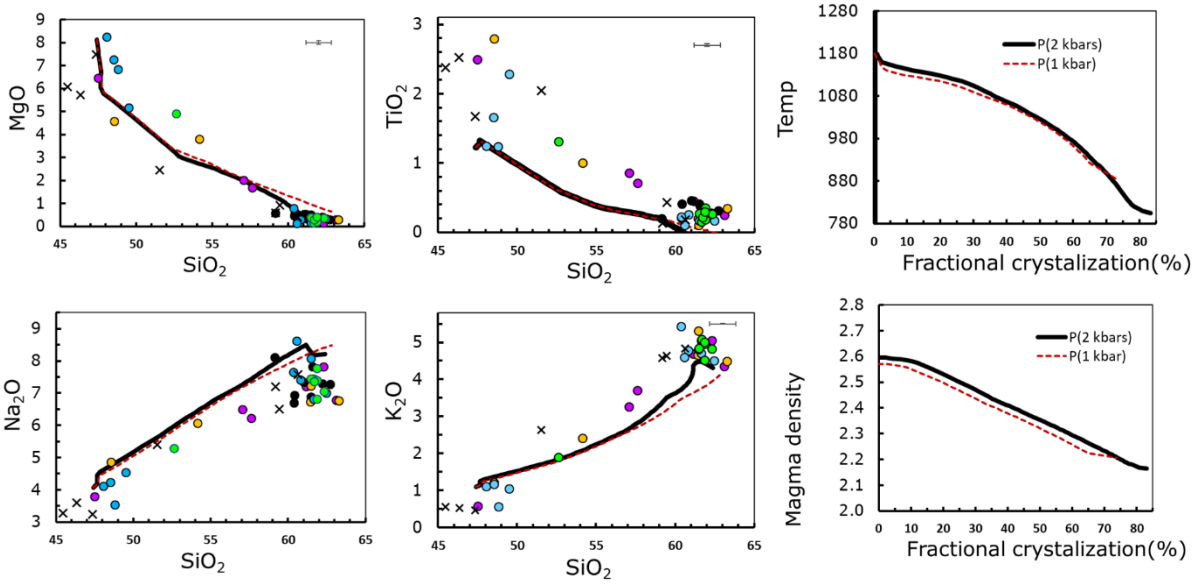

Fig. S3. The selected major elements plots and the best fitting Rhyolite-MELTS models with initial H2O content of 1.5 wt% and fO2 of ΔFMQ+1. Note the 74% fractional crystallization for the 1 kbar model and 83% fractional crystallization for 2 kbar model, also note the density of trachyte magma at the 74-83% fractional crystallization is between 2.16-2.20 gm/cm^3.

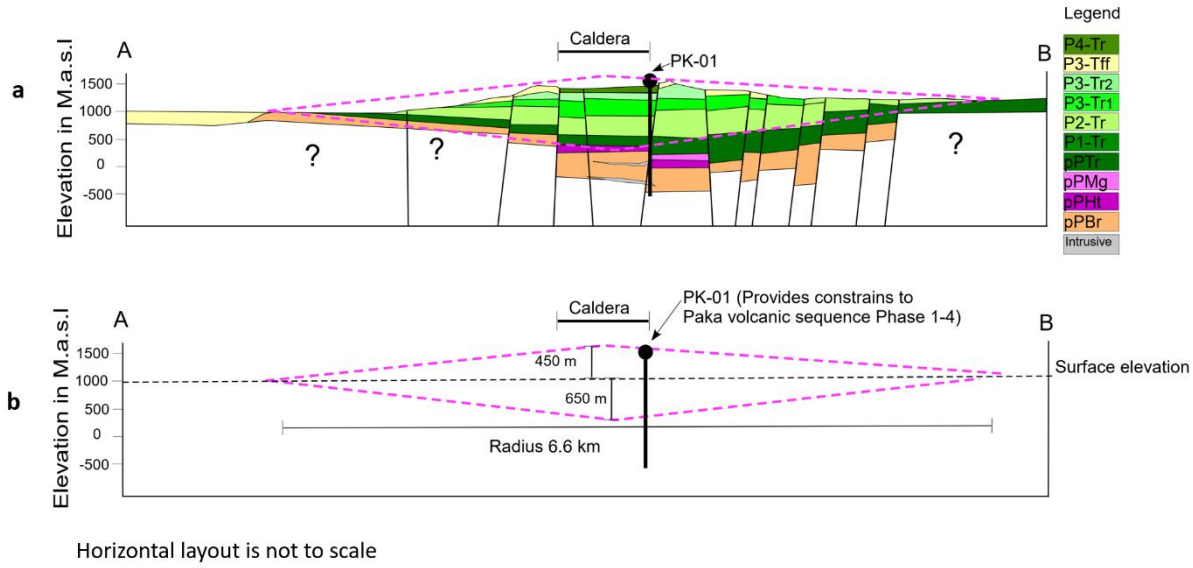

Fig. S4. The geological cross-sections. a) The stratigraphy constraints of well PK-01. b) The double cone concept for volume calculation

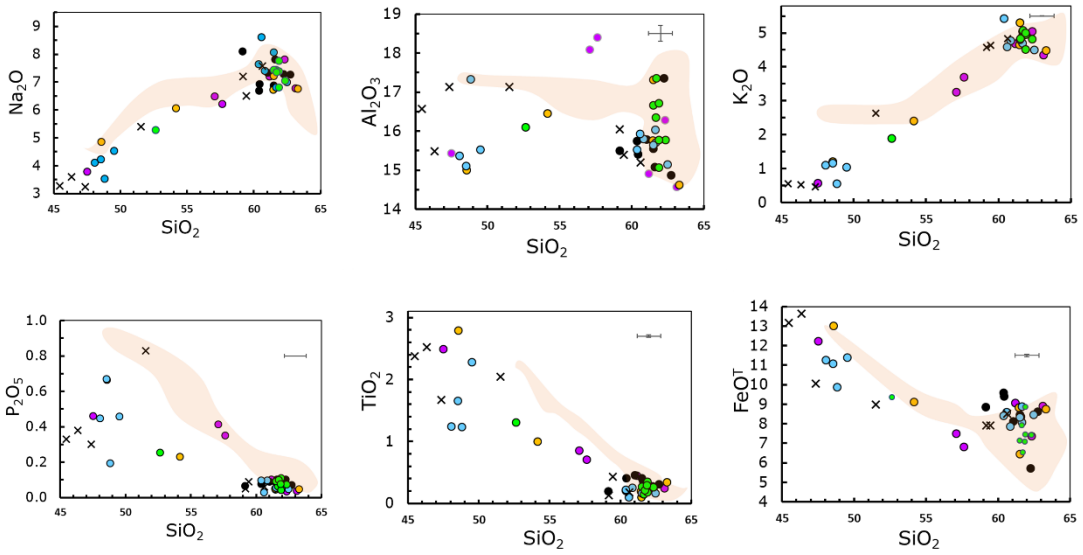

Fig. S5. Major element plots

Paper II

Partial melt generation and evolution of magma reservoir conditions at the Paka volcanic complex in Kenya: constraints from geochemistry, petrology and geophysics

Geoffrey Mibei, Enikő Bali, Halldór Geirsson, Guðmundur H. Guðfinnsson, Björn S. Harðarson, Hjalti Franzson

Lithos, 400-401, 106385. doi:https://doi.org/10.1016/j.lithos.2021.106385

Partial melt generation and evolution of magma reservoir conditions at the Paka volcanic complex in Kenya: constraints from geochemistry, petrology and geophysics

Geoffrey Mibei[1,2,4], Enikő Bali[2], Halldór Geirsson[2], Guðmundur H. Guðfinnsson[2], Björn S. Harðarson[3] and Hjalti Franzson[3]

1–Geothermal Development Company, P.O. Box: 17700–20100, Polo House, Nakuru, Kenya
2–Institute of Earth Sciences, University of Iceland, Sturlugata 7, 101 Reykjavík, Iceland
3–Iceland GeoSurvey, Grensásvegur 9, 108 Reykjavík, Iceland
4–GRÓ–GTP, Grensásvegur 9, 108 Reykjavík, Iceland

Abstract

In this study, we determine magma generation and evolution of magma storage conditions beneath Paka volcano located in the northern segment of the Kenya Rift. The surface geology of the area is characterized by five main sequences including pre-Paka formations and volcanic sequence 1-4, all built up by basalt, intermediate and trachyte rocks spanning 582-8 ka. Numerical trace element modelling suggests that the primary magma in Paka resulted principally from 5–10 % garnet–peridotite partial melting and possibly 0.1–1.5 % partial melting of spinel-lherzolite. The parental magma was probably held at the Moho (~30 km) and evolved by ~76 % gabbro fractional crystallization to generate a liquid of similar chemistry as that of erupted Paka basalts. We propose that under moderately oxidized conditions (ΔFMQ +1) the primary magma underwent a further ~70 % fractional crystallization and ~20 % assimilation of crustal syenitic material to generate Paka trachyte lavas. Basaltic and intermediate magmas were held at polybaric storage pressure conditions ranging between 1.4–7 kbar (5–25 km), at temperatures between 1086–1204 °C with relatively low water content of <1.8 wt.%. The trachyte magma resided at low pressures, i.e., 0.3–2.5 kbar (1–9 km) at 901–980 °C with water contents of 3.5–5.1 wt.%. Based on our data eruption source depths remained largely the same for a period spanning from 582–11 ka. Geophysical data show correlation with magma depths beneath Paka volcano.

key words: *Geothermobarometry; Magma temperatures; Magma depth; Oxygen fugacity; Kenya Rift*

1.0 Introduction

Multiple techniques exist to image shallow magma bodies, each with its advantages and disadvantages. Magneto-tellurics is the main geophysical method used in geothermal exploration but has limitations in resolving shallow magma bodies within caldera-hosted geothermal systems. This has led to unexpected drilling into magma at shallow depths, e.g., in the Krafla and Menengai calderas (Kanda et al., 2019; Masotta et al., 2018). Drilling into a shallow magma body can lead to numerous challenges and increased drilling costs. Additionally, it impacts negatively on the steam quality due to high heat and gas flux, observed, e.g., at the Philippines Pinatubo geothermal system (Kayzar et al., 2009).

Studies have shown that magma reservoirs are liquid–poor crystal mushes as opposed to large liquid–dominated systems (Cashman et al., 2017). This partly explains why geophysical methods, such as the magneto-tellurics have low resolution in imaging relatively small subsurface magma bodies (Eskandari et al., 2018). Geochemistry and the petrological approach can overcome this challenge by utilizing minerals and their carrier melt to provide information about storage temperature and pressure conditions, even of smaller and shallower magma bodies (Caracciolo et al., 2020).

The geochemistry/petrology approach, however, records the past and may not reflect the present state of the system. This limitation may be resolved by combining petrological and geochemical data with geophysical models. To examine this, we focus on the Paka volcanic complex located in the northern rift segment of the Kenya Rift. The volcano is a geothermal field in its early phases of resource assessment. Previous works in Paka have described the general geology, stratigraphy, and aspects of petrogenesis, mainly from major element modelling (Mibei et al., 2021a; Sceal, 1974a; Sceal & Weaver, 1971). However, the conditions of the underlying magmatic system of the volcano have not been explored and hence its geothermal conceptual model is prone to uncertainties.

In this study, we aim to: (i) determine the temporal evolution of magma storage conditions through geothermobarometric calculations combined with geophysical models such as resistivity and geodetic surface deformation, and (ii) provide insights into magma generation through simple trace element-based numerical modelling as a contribution to understanding the magmatic system. These will not only help in updating the geothermal conceptual model for the Paka volcanic complex but also provide insights into the shallow crustal structure and volcanic hazards in the context of the wider East African Rift System (EARS).

2.0 Geological background of Paka

The Kenyan rift valley is part of an active continental rift system extending at a rate of ~0.2–0.5 cm/yr and is characterised by numerous Quaternary volcanoes (Baker et al., 1972). Paka volcanic complex is located in the northern segment of the Kenya rift (Figs. 1a). Here, a thin crust of 20–30 km has been proposed (Mechie et al., 1994). On the basis of $^{40}Ar/^{39}Ar$ dates (Dunkley et al., 1993b; Friese et al., 2014b; Sudo et al., 2017b) and detailed field mapping a new geological map was developed (Fig. 1b) (Mibei et al., 2021a). The map divides the surface geology of the area into five volcanic sequences. These include: 1) the Pre-Paka sequence constituting basalt, intermediate and trachyte rocks on the lower flanks of the volcano, dated 582–405 ka; 2) volcanic sequence 1, which is a trachyte series dated 390–247 ka, forming the volcanic edifice; 3) volcanic sequence 2 consisting of basalt and trachyte and is dated 247–205 ka; 4) volcanic sequence 3 consists also of basalt and trachyte and is dated 160–38 ka; and 5) the post-caldera intermediate and trachyte rocks of volcanic sequence 4 dated 36–8 ka (Fig.1b).

The volcano edifice growth began at 390 ka and a caldera collapse event occurred at ~36 ka. Trachyte is volumetrically dominant and eruptions were characterised by effusive and intermittent explosivity along tectonic fissures, domes and vents. (Mibei et al., 2021a). The long-lived volcanic activity in the area has facilitated high heat flow, manifested by widespread structurally controlled surface geothermal features in a similar fashion as seen in Eburru (Velador et al., 2003). Recent volcanic unrest has been inferred from ground

deformation and seismic activity within the summit area (Biggs et al., 2009; Biggs et al., 2016; Patlan Almeida, 2016).

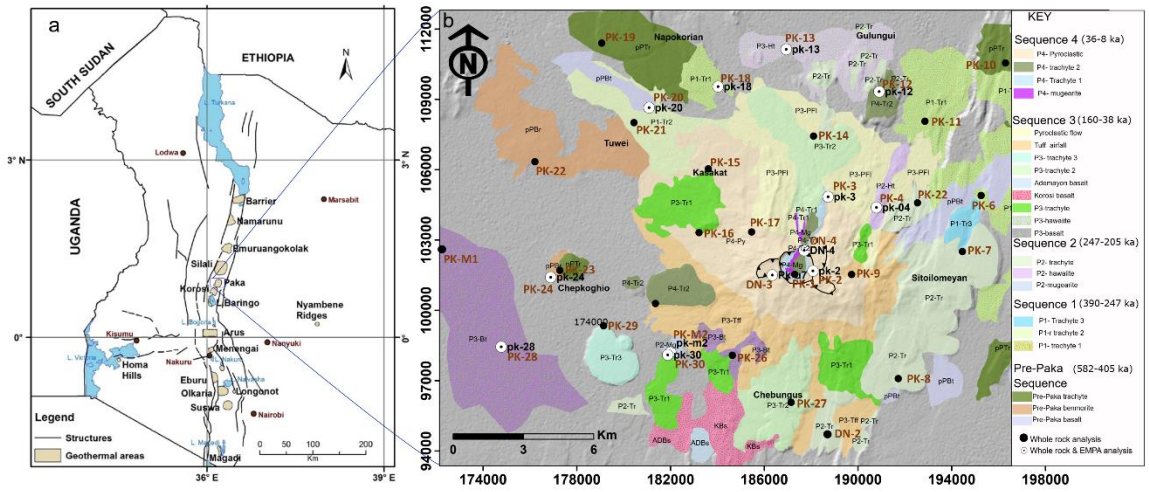

Fig.1. a) Paka volcanic complex within the northern Kenya Rift. b) Geological map of Paka volcanic complex (Mibei et al. 2021) with location of analysed samples. Black dots (PK) show label in brown where samples were analysed by ICP-OES, white dots label in black (pk) show locations of samples analysed by both ICP-OES and EMPA.

3.0 Methodology

3.1 Sampling

Thirty-six samples from basalt and trachyte lavas were collected from the Pre-Paka, Sequence 1, Sequence 2, Sequence 3 and Sequence 4 (Fig.1b, Table S1) and selected trace elements analysed by ICP-OES. Thirteen fresh lava and pyroclastic samples including at least two samples from each volcanic sequence (Table S1) were studied in detail by electron microprobe analysis (EMPA) (Fig. 1b, Table S3–S8). The EMPA samples include three samples from the summit area, four from the southwest, three from the northeast and three from the northwest of the volcano. The samples span the basalt, hawaiite, mugearite, benmorite and trachyte compositional range, and are of ages between 11–582 ka. In this paper, mugearite and benmorite samples are grouped as intermediate rocks, while hawaiite is included as basalt.

3.2 Analytical methods

Petrography, EMPA and ICP-OES were carried out at the Institute of Earth Sciences, University of Iceland. The EPMA used is a JEOL JXA-8230 SuperProbe equipped with five wavelength-dispersive spectrometers (WDS), each with two different analytical crystals, except one spectrometer which has four. The instrument also has an energy dispersive spectrometer with a silicon drift detector (SDD-EDS) used for quick phase identification before quantitative analyses. Acceleration voltage of 15 kV and current of 5 nA was used for silicic glass, 10 nA for basaltic glass and feldspars, and 20 nA for olivine, pyroxene, and Fe–Ti oxides. The mineral chemistry acquisition involved core–rim spot analysis in each mineral analysed. The dataset includes 128 spot analyses of olivine grains, 255 spot analyses of plagioclase grains, 175 K-feldspar grains, 358 spot analyses of clinopyroxene, 47 spot analyses of melt inclusions and 44 spot analyses of groundmass glasses and 126 spots on Fe–Ti oxides. In all the analyses a focused beam was used, except that in the case of feldspars a defocused beam size of 5µm was applied and 10–15 µm for the groundmass glass and glassy melt inclusions. A larger beam size (15µm) in the partially crystalline melt inclusions was used so that it encased the partially crystalline material. In large, partially crystalline melt inclusions, multiple spots were analysed to acquire representative average compositions. Complete chemistry data is provided in Table S3–S8.

Selected trace elements (Ba, Co, Cr, Cu, La, Ni, Rb, Sc, Sr, V, Zn) in whole rock samples (Table S2) were determined by ICP-OES. Accuracy was generally between ± 0.26 to 4.62 ppm for the selected trace elements apart from Rb for which it is ±30 ppm (Mibei et al., 2021). For completeness of data we considered additional major and trace element data from previous work (Mibei et al., 2021a; Sceal & Weaver, 1971).

4.0 Results

4.1 Petrography

We consider mineral grains of <500 µm diameter, but larger than the general groundmass size, as microcrysts, while those of >500 µm diameter are classified as macrocrysts (Fig. 2). This is strictly based on size in relation to groundmass, but by origin these crystals could be antecrysts, xenocrysts and phenocrysts.

4.1.1 Basaltic rocks

Basalt is hypocrystalline, porphyritic and vesicular with euhedral and subhedral macrocrysts of plagioclase and clinopyroxene with microcrysts of olivine (Fig. 2a, d and g). The common minerals are plagioclase (40–42 %) and clinopyroxene (35–40 %) with subordinate olivine (5–10 %) and about 10 % Fe–Ti oxide (Fig. 2a). Plagioclase occurs as glomerocrysts with clinopyroxene or as single crystals. Olivine crystals are <0.3 mm in size, while clinopyroxenes vary in size from 0.3–0.5 mm (Fig. 2d). Silicate melt mostly appears as small (~20 µm) (Fig. 4g), partially cryptocrystalline pockets between groundmass of feldspar and minor clinopyroxene minerals.

4.1.2 Intermediate rocks

The intermediate rocks are hypocrystalline, porphyritic and vesicular with fine grained groundmass of plagioclase and mafic minerals. The feldspars are macrocrysts, while clinopyroxenes are regarded as micro and macrocrysts, the olivines are microcrysts (Figs. 2b, e and h). The main minerals are clinopyroxene (40–42 %), plagioclase (35–40 %) and olivine (<5 %). Fe–Ti oxides occur as accessory minerals. Clinopyroxene contains sporadic glassy or partially glassy melt inclusions (Fig. 2h) and has iron-rich rims. Very small pools of silicate glass (~50 µm) are present between feldspar crystals (Fig. 4h). The groundmass is made principally of fine-grained crystals of feldspars, clinopyroxene and olivine. (Fig. 4b)

4.1.3 Trachyte

The trachyte is hypocrystalline, porphyritic with large sanidine macrocrysts in fine groundmass of feldspar, forming trachytic texture. The feldspars and clinopyroxene are regarded as macrocrysts, while olivine are microcrysts (Figs. 2c, f and i). The main minerals are sanidine (45–50 %), clinopyroxene (20–30 %) and Fe–Ti oxides (10 %). The Fe–Ti oxide minerals are conspicuously larger (>0.5 mm) than those of mafic rocks, as seen in BSE images (Fig. 3f). Sanidine is large (>6mm) (Fig. 2f) and homogeneous but characterised by resorbed disequilibrium textures and formed as single crystals or aggregates with Fe–Ti oxides and clinopyroxene. Clinopyroxene is <0.1 mm in size and shows resorbed disequilibrium textures. Small pools of silicate glass <50 µm (Fig. 4f) are present in the interstitial spaces between feldspars.

4.1.4 Melt inclusions

Silicate melt inclusions are rare in plagioclase and olivine but common in clinopyroxene (Figs. 2e, g and h). They vary in shape from spherical (Figs. 2e–g) to elongated (Fig. 2h), and also range from cryptocrystalline to glassy. Olivine- and plagioclase-hosted melt inclusions are partially crystalline. Clinopyroxene-hosted melt inclusions are commonly trapped as single inclusions in mineral cores. They vary in sizes from 10 µm to 50 µm. The larger ones (50 µm) are commonly partially crystalline and are spherical, while the smaller ones (10 µm) are glassy and elongated.

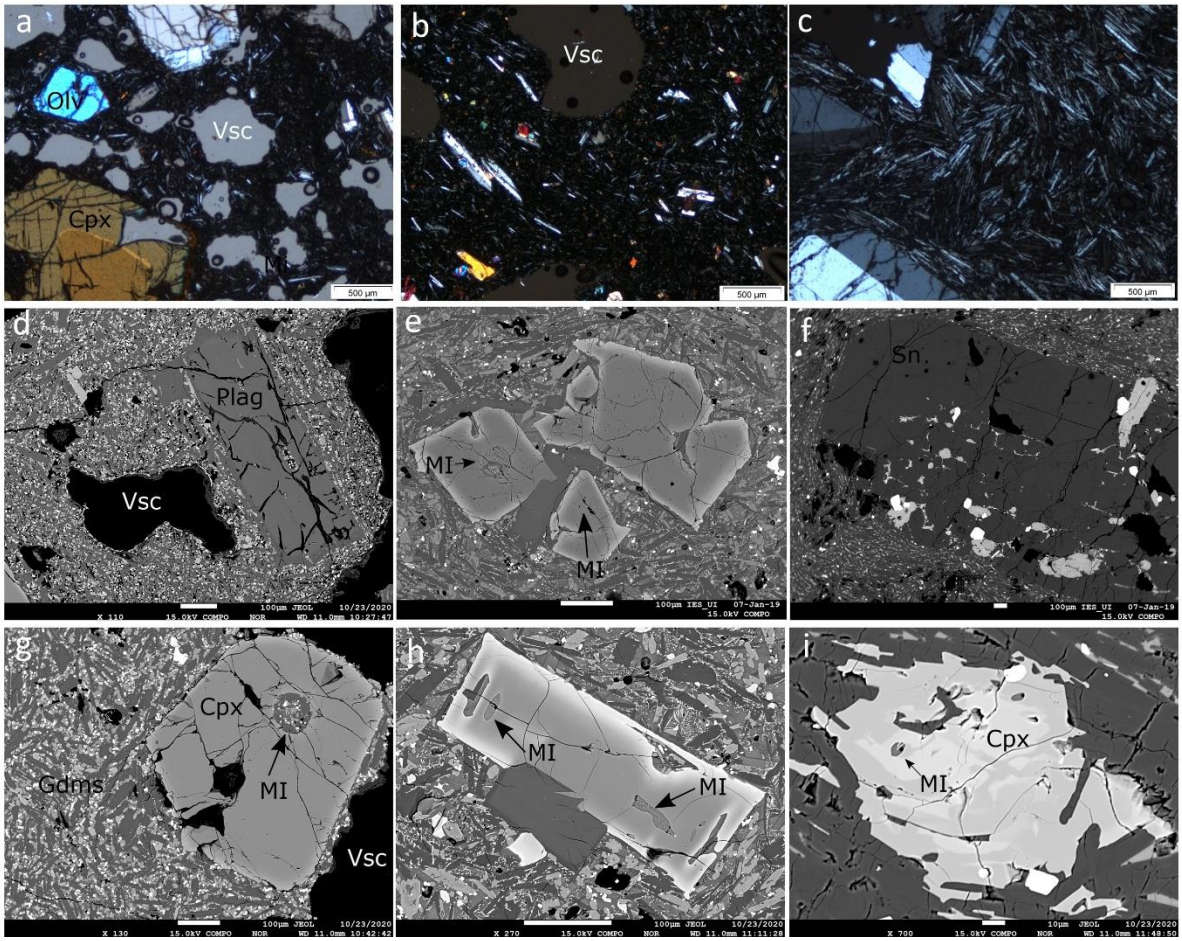

Fig. 2. Thin section and EMPA images a) Vesicular porphyritic basalt with macrocrysts of clinopyroxene and plagioclase. b) Vesicular mugearite with plagioclase macrocrysts and microcrysts of clinopyroxene in a fine-grained groundmass. c) Porphyritic trachyte with feldspar macrocryst in a fine-grained groundmass. d) BSE image of vesicular basalt showing zoned plagioclase. e) Hypocrystalline porphyritic mugearite with clinopyroxene and MI in BSE image. e) BSE image of porphyritic trachyte showing glomerocrysts of oxide, sandine and clinopyroxene. g) BSE image of clinopyroxene macrocrysts in basalt. Note the partially crystalline MI. h) Plagioclase-clinopyroxene glomerocrysts in mugearite with MI and mineral inclusion in BSE image. i) BSE image showing resorbed clinopyroxene in trachyte with glassy MI. The light colour suggests iron-rich composition. Abbreviations: Sanidine-Sn, Plagioclase-Plag, Clinopyroxene-CPX, Olivine-Olv, Groundmass-Gdms, Vesicles-Vsc, Melt Inclusion-MI.

4.2 Mineral chemistry

Ternary chemical classification of olivine, feldspars, clinopyroxene and Fe–Ti oxides are shown in Figs. S1a–d.

4.2.1 Feldspars

Plagioclase crystals occur in basalt and intermediate rocks. They have a wide compositional variation from bytownite to oligoclase ($An_{16–84}$), (Fig. S1a). Core and rim analyses show that 76% are normally zoned while 24% are reversely zoned (Table.S15). The FeO content varies from ~0.3–1.2 wt.%, showing a negative trend with anorthite (An) content, with overlapping composition of plagioclase in basalt and intermediate rocks (Fig. 3a). In basalt, the An content in the cores varies between An_{16} and An_{84}, and between An_{22} and An_{82} in the rims. An content of plagioclase in intermediate rocks, on the other hand, varies between An_{38} and An_{80} in cores and An_{27} to An_{68} in the rims.

K-feldspar occurs in both basalt and trachyte rocks as anorthoclase and sanidine, with composition between $Or_{18–42}$ (Fig S1a). All analysed crystals have normal zoning (Table. S16). The FeO in K-feldspars varies from 0.1–0.7 wt.% (Fig. 3b). Sanidine and anorthoclase coexist in basalt (Fig S1a), with an Or content that varies between $Or_{19–21}$ in the cores and $Or_{22–29}$ in the rims. In trachyte, the K-feldspar is exclusively sanidine with Or content between $Or_{23–42}$ in the cores and $Or_{24–44}$ in the rims.

Kernel density estimates (KDE) (Fig. 4a) show plagioclase core and rim distributions in intermediate rocks, while Fig. 4b is for plagioclase in basalt. The plagioclase in intermediate rocks shows a bimodal An distribution in both the cores and the rims. The main population of the cores has a distribution peak value of $An_{60,}$ while the smaller population has a distribution peak value of An_{77}. The rims are offset to less An-rich compositions compared to core compositions with a peak value of An_{35} for the main population and An_{65} for the minor population. The plagioclase in basalt shows a unimodal distribution with compositions having high An content and with an overlap in the cores (peak value An_{59}) and rims compositions (peak value An_{60}).

The trachytes have K-feldspars with unimodal distribution of Or for both cores (peak Or_{38}) and rims (peak value of Or_{36}), which overlap (Fig. 4c). The cores of K-feldspar in the basalts are unimodally distributed with peak of Or_{20} (Fig. 4d). The rims, however, are bimodal with a peak of Or_{30} for the main population and Or_{22} for the minor population, hence offset to higher Or content in comparison with the core composition. Interestingly, K-feldspar in basalt and trachyte have overlapping compositions.

4.2.2 Olivine

Olivine in basalt and intermediate rocks is relatively forsterite-rich ($Fo_{46–82}$), and fayalite-rich ($Fo_{18–24}$) in trachyte (Fig. S1c). Data show that 61% of the crystals are normally zoned, while 39 % are reversely zoned (Table.S18). NiO and Fo contents are positively correlated, with NiO values between 0–0.18 wt.%. The range in Fo content in trachyte is limited and varies between $Fo_{14–23}$ in the cores and $Fo_{14–21}$ in the rims (Fig. 4e). In the intermediate rocks the Fo content varies between $Fo_{62–82}$ in the cores and $Fo_{60–74}$ in the rims; hence, the rims are offset to lower Fo contents in relation to the cores. In the basalts (Fig. 4f) we see $Fo_{55–84}$ in

the cores and $Fo_{46–87}$ in the rims; the distribution is negatively skewed towards lower Fo contents. There is an overlap of the core and rim compositions with a peak of Fo_{75}.

4.2.3 Clinopyroxene

Clinopyroxenes are characterised by iron-rich rims, as seen on BSE images (Fig. 2b). We recalculated and solved for Fe^{3+} content for our plots (Fig. S1d) using the Excel spreadsheet of Deer et al. (2013). In basalts, clinopyroxene compositions vary from diopside to salite ($Fs_{5–25}$), but are salitic ($Fs_{8–25}$) in intermediate rocks and ferro–salite ($Fs_{28–47}$) in the trachytes (Fig. S1d). 42% are normally zoned, while 58% have reverse zoning (Table. S17). Al_2O_3 concentrations vary between 0.1–9 wt.% in basalt and the evolved samples. There is a positive correlation between the Mg# and Al_2O_3 contents and a perfect overlap of the clinopyroxene compositions in the basalts and intermediate rocks (Fig. 3d). In trachyte the clinopyroxene core and rim compositions have bimodal distributions but are skewed to low Mg# (Fig. 4g); the cores have a peak of Mg# 35, while the rims have a peak value of Mg# 30. In the intermediate rocks, the core and rim compositions are also bimodal and negatively skewed towards low Mg#. The cores have a peak of Mg# 79 while the rims have a distribution peak of Mg# 81. In basalt the distribution is unimodal with a slightly negative skew to lower Mg# values (Fig. 4h). The core and the rim compositions overlap with the distribution peak of Mg# 80. Interestingly, there is slight overlap in trachyte and basalts compositions.

4.2.4 Fe–Ti oxides minerals

The Fe–Ti oxides occur as groundmass minerals in basalt and intermediates rocks. However, in trachyte, they are conspicuous, large macrocrysts, occurring as glomerocrysts with sanidine (Fig. 2f) The TiO_2 content ranges from 18–30 wt.%, while the FeO content ranges from 63–73 wt.% (Table S8). The analysed phases belong to the ulvospinel–magnetite series (Fig. S1b).

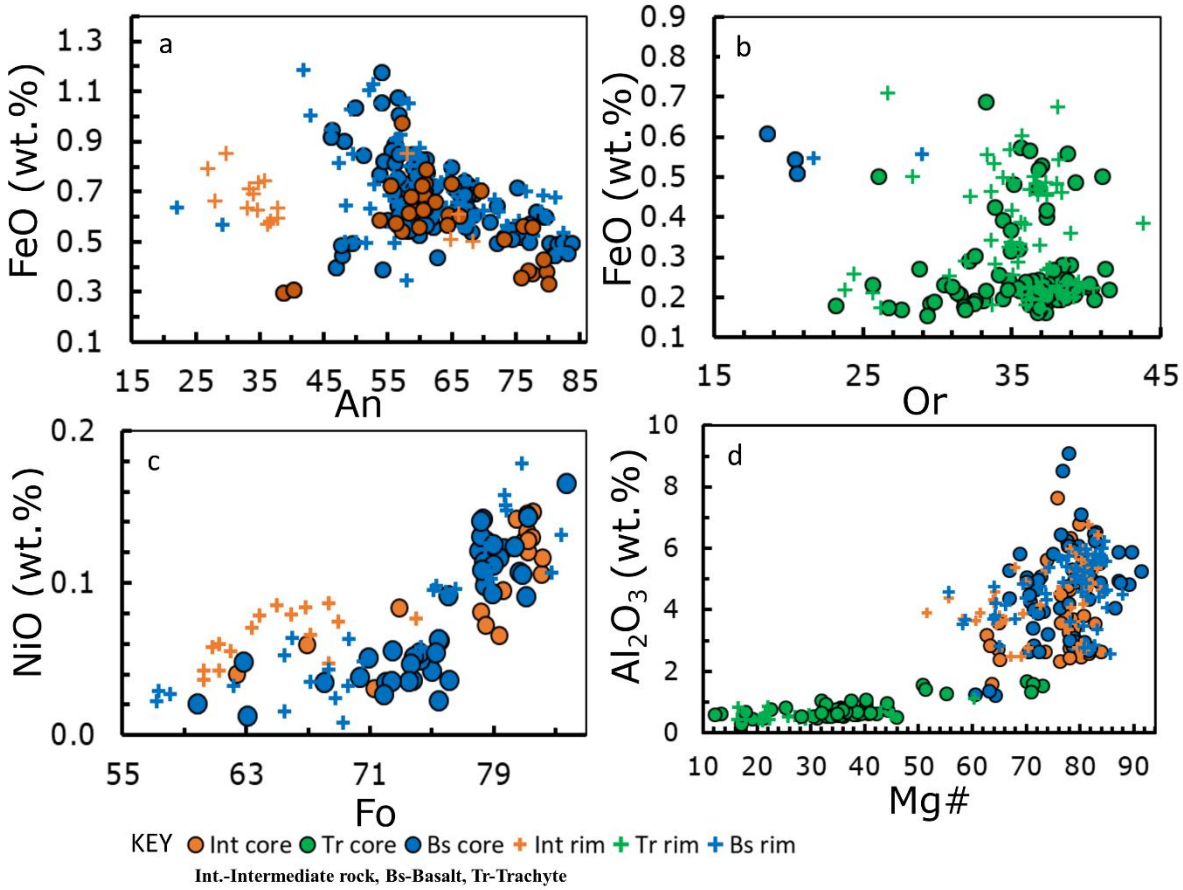

Fig. 3

Fig. 3. Mineral chemistry variation plots a) The FeO variation, as a function of anorthite in the cores and rims of plagioclase suggests similar compositions range. b) The FeO variation as function of orthoclase in the cores and rims of K-feldspar. c) The NiO variation as function of forsterite in the cores and rims of olivine. d) The Al_2O_3 variation as a function of magnesium in the cores and rims of clinopyroxene.

4.2.5. Mineral-melt equilibrium

The inset shaded bars in Fig. 4 show the range of mineral compositions and the equilibrium range of carrier liquid compositions The equilibrium ranges were calculated based on model constraints of the specific geothermobarometers (Putirka, 2008). In basalt the equilibrium range is $An_{78–87}$ for plagioclase, $Fo_{68–80}$ for olivine and $Mg\#_{72–83}$ for clinopyroxene. In the intermediate rocks, on the other hand, the range is $An_{54–76}$ for plagioclase, $Fo_{60–76}$ for olivine and $Mg\#_{61–76}$ for clinopyroxene, while in trachyte the range is Fo_{10-38} for olivine and $Mg\#_{10-41}$ for clinopyroxene.

Fewer of the plagioclase crystals (cores and rims) are primitive and in equilibrium with basaltic carrier liquid. Most of the cargo (rims and cores) is evolved but in disequilibrium with the carrier liquid. In contrast, the intermediate carrier liquid is in equilibrium with most

mineral cores and a few primitive rims. Most of the rims however are evolved and in disequilibrium.

The majority of the olivine crystals (cores and rims) are in equilibrium with the basaltic liquid compositions. The intermediate compositions, however, show that most rims are in equilibrium, while most cores were not. All the olivine in trachyte were found to be in equilibrium with their carrier liquid.

Most clinopyroxene cores and rims were in equilibrium in basaltic liquid compositions. This is in contrast with intermediate liquid compositions where most cores and rims were found to be in disequilibrium. The majority of trachyte clinopyroxene were, however, in equilibrium.

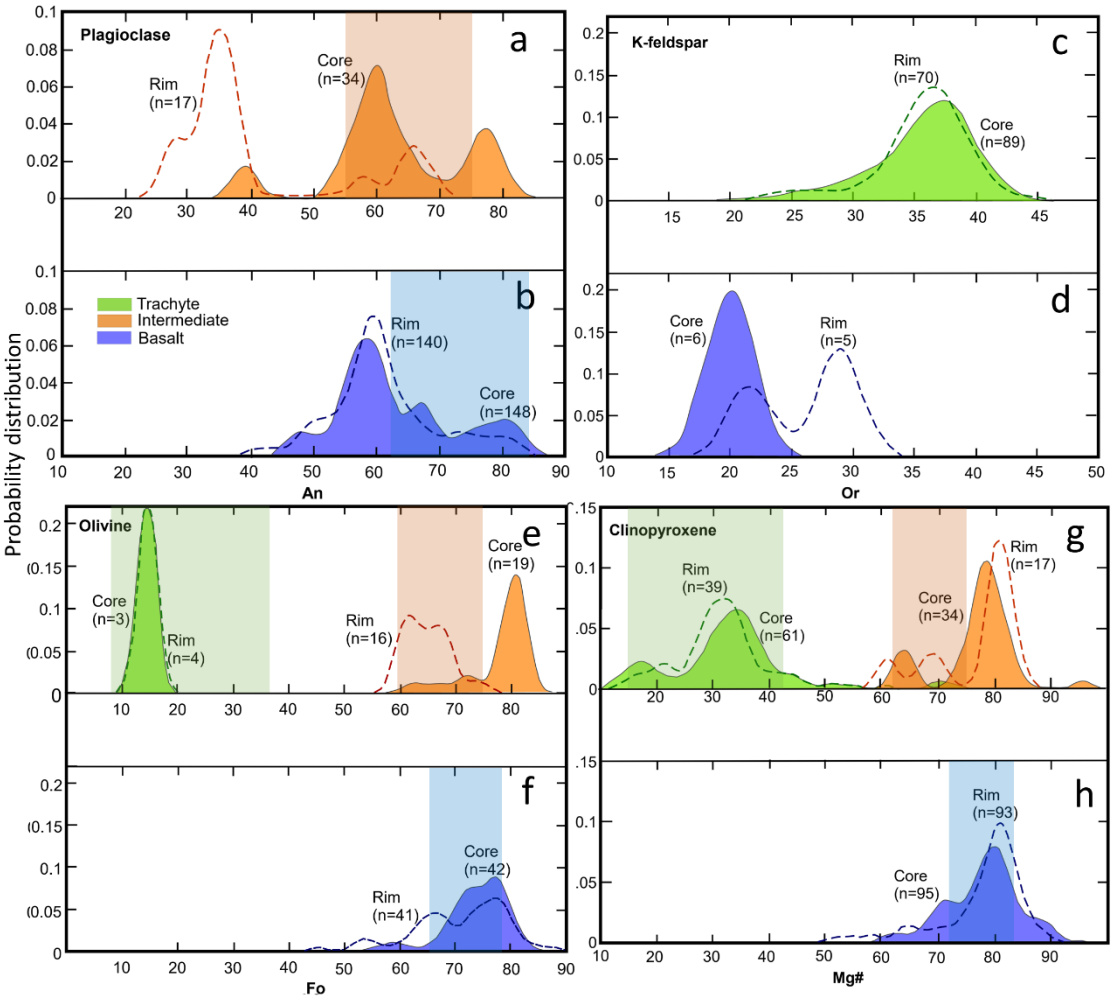

Fig. 4

Fig. 4. KDE plots of a) An content of plagioclase cores and rims in intermediate rocks (bandwidth 1.8), b) An contents of plagioclase cores and rims in basalts (bandwidth 1.8), c) Or contents of K-feldspar cores and rims in trachyte (bandwidth 1), d) Or contents of K-feldspar cores and rims in basalts (bandwidth 1), e) Fo content of olivine cores and rims in trachyte and intermediate rocks (bandwidth 1.8), f) Fo content of olivine cores and rims in basalts (bandwidth 1.8), g) Mg# of clinopyroxene cores and rims in trachyte and intermediate rocks (bandwidth 1.8), and h) Mg# of clinopyroxene cores and rims in basalt (bandwidth 1.8).

4.3 Liquid melt compositions

4.3.1 Melt inclusions and whole rock

The composition of clinopyroxene-hosted melt inclusions shows FeO variations between 7.5–13.4 wt.% in basalt and 1.1–4.7 wt.% in trachyte melts. The whole rock major element data (Mibei et al., 2021a), on the other hand, shows that FeO varies between 9.9–13.6 wt.% in basalt and 5.7–9.6 wt.% in trachyte. In intermediate rocks FeO is 6.8–9.4 wt.%. The Al_2O_3 content, in melt inclusions ranges from 14.4–17.1 wt. % in basalt and 15.4–18.7 wt.% in trachyte, whereas the whole rock Al_2O_3 content ranges from 14.5–16.8 wt. % in basalt and 14.0–16.8 wt.% in trachyte. In intermediate rocks Al_2O_3 is 15.6–17.6 wt.%. Whole rock CaO content ranges between 9.3–11.6 wt.%, 4.1–8.3 wt.% and 0.7–2.9 wt.% in basalt, intermediate rocks and trachyte, respectively, while it is 4.0 -5.6 wt.% in basaltic melt inclusions and 0.1-0.4 wt.% in trachyte melt inclusions. The complete data set is shown in Tables S2 & S3.

The composition of clinopyroxene–hosted melt inclusions shows a larger variability compared to whole rock chemistry as shown also in the TAS diagram (Fig. 5). Furthermore, melt inclusions and their clinopyroxene hosts did not show chemical equilibrium (see criteria in 4.3.2). The variability is due to the effects of element re-equilibration occurring after melt inclusions were trapped in a phenocryst (Cottrell et al., 2002; Danyushevsky et al., 2000). The post-entrapment modifications affect mostly FeO, Al_2O_3, and CaO in clinopyroxene-hosted melt inclusions, and in the most extreme cases obscure the true melt chemistry (e.g.,Lynn et al., 2017; Thomson & Maclennan, 2012). This has a negative effect on mineral-melt geothermobarometry. Therefore, the melt inclusions required recalculations for post-entrapment corrections (PEC) before use in geothermobarometry.

4.3.2 Glass compositions

The selection of liquid melt composition depended on whether they followed the liquid line of descent (LLD) based on the general trend for whole rock compositions. The groundmass glasses did not meet this requirement (see TAS plot) (Fig. 5). This can be attributed to the almost holocrystalline nature of our samples, and finding large enough groundmass glass pockets for the EMPA beam was not possible without contamination by nearby crystals. Although some groundmass glass compositions followed the LLD, they were not considered for modelling, because none of the crystal compositions showed chemical equilibrium with them.

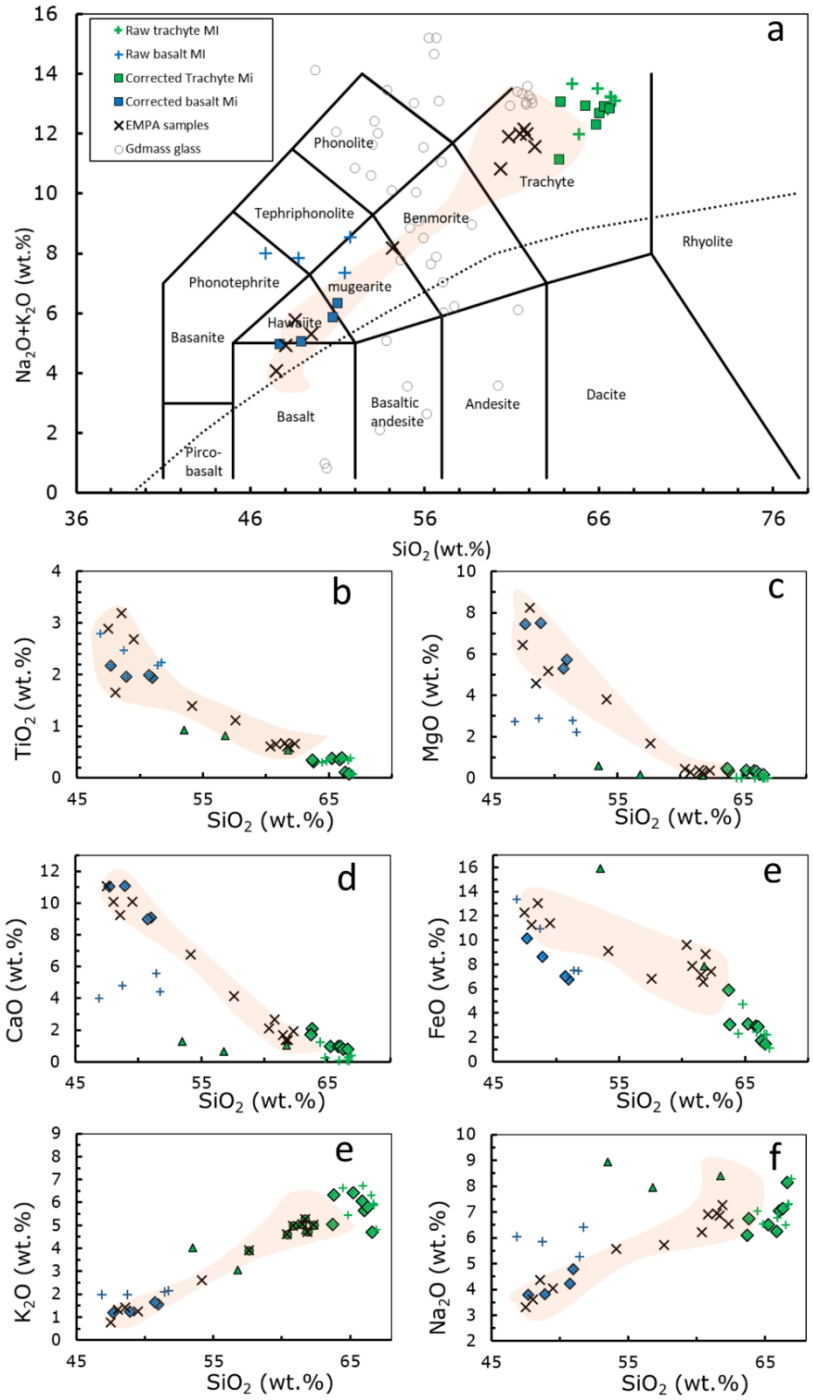

Fig. 5. a) TAS classification diagram (Le Bas et al., 1986) for the Melt inclusions (raw and corrected). The brown shaded field denotes the range of previous whole rock chemistry data (Mibei et al., 2021). Crosses indicate whole rock composition of specific samples selected for EMPA mineral analyses, the faint grey circles are the groundmass glass compositions which were set aside (section 3.5). b-f) Melt inclusions major element variation diagrams for TiO_2, CaO and K_2O (1st column) and MgO, FeO and, Na_2O and (2nd column) versus SiO_2. Shaded area shows the bulk composition of Paka surface samples from Mibei et al. (2021).

4.3.3 Post entrapment corrections (PEC) for melt inclusions

To perform post entrapment corrections (PEC), we first distinguished between clinopyroxene from basalt/intermediate rock compositions and trachyte samples; then treated them separately as different melt–mineral equilibrium criteria had to be applied. The corrections were undertaken by adding the composition of clinopyroxene to the melt inclusions iteratively in 1% increments until the clinopyroxene-melt equilibrium was achieved. In basalts and intermediate rocks, the $Kd^{Fe–Mg}{}_{cpx/melt}$ value had to be 0.27 ± 0.03 (Neave et al., 2019; Putirka, 2008); secondly, we applied further filtering by ensuring the difference between predicted versus observed clinopyroxene components (EnFs, CaTs and DiHd) was <0.05, <0.03 and <0.06, respectively (Mollo et al., 2010; Neave et al., 2019; Putirka, 2008), after which the compositions were used for thermobarometry modelling. According to Masotta et al. (2013), different equilibrium criteria apply for strongly alkaline SiO_2-rich rocks. Therefore, for trachyte samples, we added clinopyroxene compositions to the melt inclusions iteratively, and instantaneously compared the calculated $Kd^{Fe–Mg}{}_{cpx/melt}$ and the Na# values with those predicted (see details in Masotta et al. 2013). When the values were within 0.05, equilibrium was achieved, and melt compositions were used for thermobarometric purposes. PEC for melt inclusions in basalt required adjustments of between 21–37 %, while the trachyte required adjustments between 2–5 % (Table S3). The corrected MI dataset shows FeO variations between 6.8–10.2 wt.% in basalt and 1.4–5.9 wt.% in trachyte. The Al_2O_3 content, on the other hand, ranges from 14.4–17.1 wt.% in basalt and 15.4–18.7 wt.% in trachyte, while CaO content ranges between 9.0–11.1 wt.% and 0.8–2.1 wt.% in basalt and trachyte, respectively. The corrected data displayed in a TAS diagram (Fig.5a) shows a good fit with the whole rock chemistry range.

4.4 Trace elements chemistry

Selected whole rock trace element analyses (Table S2) from this study, which include Sc, Co, V, Cr, Ni, La, Rb, Ba, Sr, and Zn, are plotted with trace element data from previous work (Mibei et al., 2021a; Sceal & Weaver, 1971) to ensure completeness of the data presentation and interpretation (Fig. 6). We selected Zr as a differentiation index in the chemical plots due to its wide compositional range (558–2032 ppm) and continuous concentration increase from basalt to trachyte. Y and La display a clear positive correlation with Zr concentration. In trachyte, Y is enriched and varies from 76–103 ppm, while La ranges from 70–242 ppm. The ratio of La to Y is nearly constant, slightly higher than unity. A positive correlation is displayed between Rb and Zr, but the trend is highly scattered in the trachyte field with Rb values ranging from 1–254 ppm. Neither Ba nor Sr display a clear correlation with Zr. Ba has a wider range of values between 10 and 3179 ppm compared to the Sr range of 12–776 ppm. It is important to note that benmorite has anomalously high concentrations of both Ba and Sr. Vanadium content ranges between 25 and 348 ppm in basalts to benmorite, compared to 0.8–6 ppm in the trachyte. Cr content is high in the basalt and hawaiite with maximum values of up to 253 ppm, but it exhibits a remarkable decline from mugearite to the trachyte series. Sc concentration varies from 0.7–36 ppm from basalt to trachyte. Co content, on the other hand, varies between 2 and 62 ppm, while Cu content ranges from 15–78 ppm.

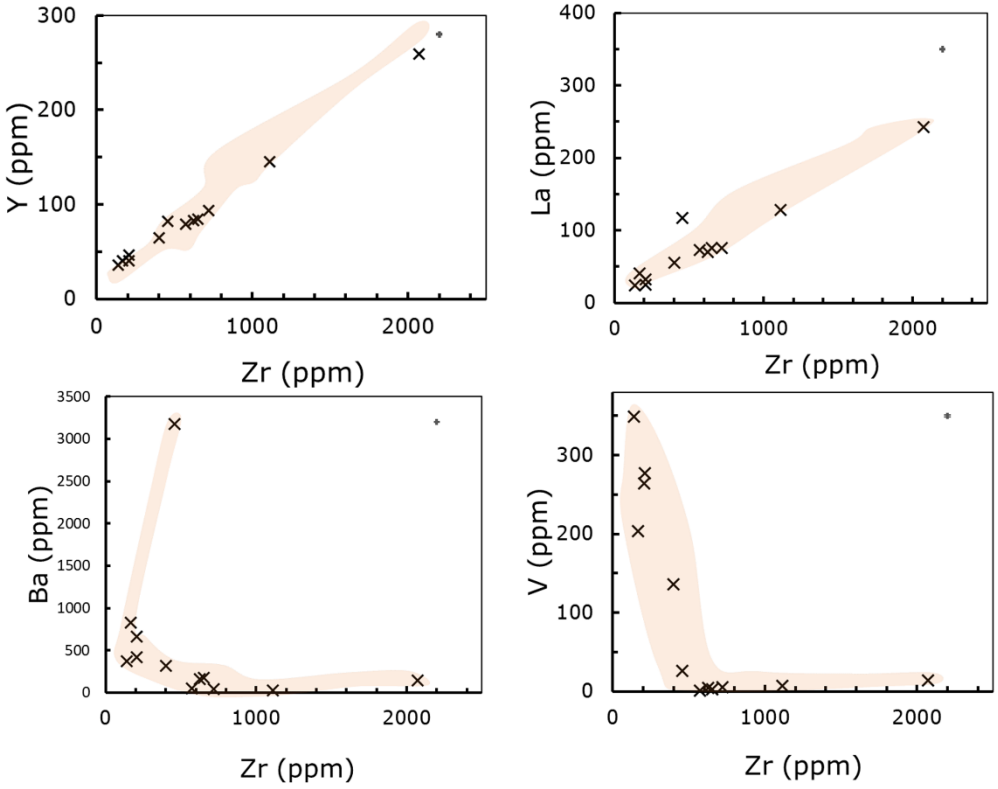

Fig. 6. Trace element plots with Zr as an index of differentiation. Black crosses are the 12 selected samples for which the mineral chemistry was determined by EMPA in this study (Fig. 5). The inset field shows bulk rock chemistry for all the analysed field samples. The 2σ error bars on top right corners.

4.5 Geothermobarometry modelling

Geothermobarometry modelling followed the approach presented by Neave and Putirka (2017). To capture the last equilibrium state of the crystal cargo before eruption and earlier stages in order to fully understand the evolution of magma storage conditions (P–T) within the crust; both mineral cores and rims were paired to putative equilibrium liquid compositions (e.g.,Halldórsson et al., 2018). The liquid compositions used were clinopyroxene-hosted melt inclusions and the whole rock compositions. To check for chemical equilibrium between pairs of minerals and silicate melt in basalts and intermediate rocks, we used the criteria discussed in Putirka (2008), while for trachyte samples we followed the approached of Masotta et al. (2013) (see also section 4.3.2).

In our models, samples were divided into three groups, i.e., basalts (basalt, hawaiite), intermediates (mugearite, benmorite) and trachyte. For basalts and intermediates, the models used include: (i) The clinopyroxene geothermometer of Putirka (2008) (equation 33) and the geobarometer of Neave and Putirka (2017) with a standard error of estimate (SEE) for pressure and temperature of ±1.6 kbar and ±45 °C, respectively (ii) The plagioclase–melt geothermometer and hygrometer based on equations 24a and 25b, respectively (Putirka, 2008); the equilibrium condition for this model was achieved when $Kd^{An–Ab}_{plag/melt}$ was 0.28

±0.11 and the accuracy (SEE) for temperature and H_2O content was ±36°C and ±1.1 wt.% respectively (iii) The olivine thermometer based on equation 16 of Putirka (2008), equilibrium was achieved when $Kd^{Fe–Mg}_{olivine/melt}$ was within 0.3 ±0.03 while the accuracy (SEE) was within ±26 °C. Geothermobarometry and hygrometry of trachyte samples were retrieved from models specifically calibrated for evolved alkaline rocks, i.e., trachyte and phonolite using Talk 2012 and Palk 2012 (Masotta et al., 2013). The trachyte water content was calculated using an alkaline hygrometer (Mollo et al., 2015) with uncertainty of ±0.7% wt. %.

The geothermobarometry results (Table S9-S12) indicate a temperature range of 1101–1204 °C for basalts and very low water content (<0.1 wt.%). However, the uncertainty for estimating H_2O is large (±1.1 wt.%) (Putirka, 2008). The calculated temperatures for the intermediate rocks range from 1016–1117 °C, with estimated water content of 0.8–1.8 (±1.1 wt.%) (Fig. S13). Obtained trachyte temperatures range from 901–980 °C and water content between 3.5–5.1 wt.% (± 0.7 wt.%) (Fig. S14). The relative probability of the thermometry data is highlighted by KDE plots (Figs. 7a–d). The trachyte temperatures (Fig. 7a) have a distribution peak values of 925 °C for the core and 950 °C from the rim data. The intermediate rocks show distribution peak values of 1090 °C at the rim and 1110 °C in the core. The basalts, on the other hand, have a temperature peak value of 1170 °C obtained for both mineral rims and cores (Fig. 7b).

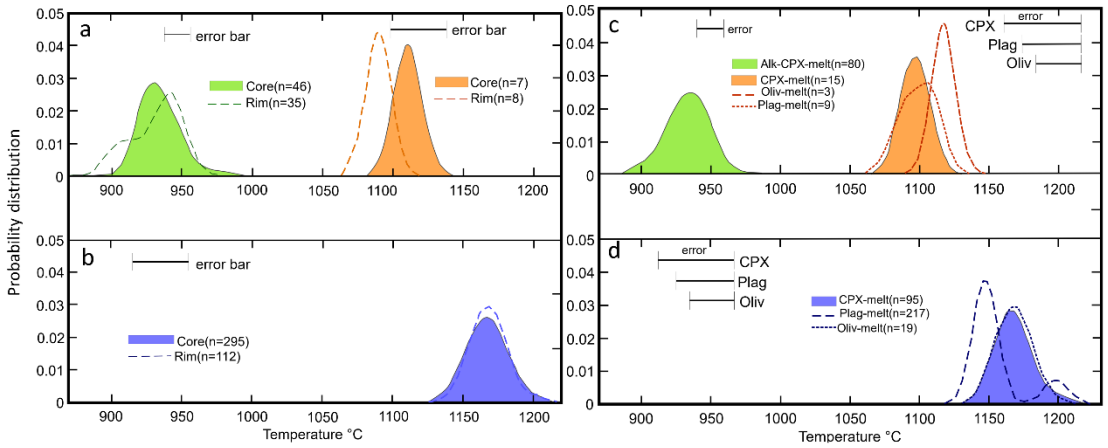

Fig. 7. a) Temperatures (bandwidth 5) from clinopyroxene, plagioclase and olivine core and rim compositions in trachyte (green) and intermediate rocks (orange). b) Temperatures for basalts based on clinopyroxene, plagioclase and olivine core and rim compositions c) Thermometers (bandwidth 5) for trachyte and intermediate rocks. d) Thermometers in basalt show values calculated with the olivine thermometer overlapping those from the clinopyroxene thermometer. The Plagioclase thermometer gives slight offset values.

There is a wide range of storage pressures calculated for basalt (1.4–7 kbar) but limited range for the intermediate rocks (4.8–6.7 kbar). The trachyte storage pressures were low and constrained (0.3–2.5 kbar) (Figs. 8a and b) with most probable pressure at 1 and 1.5 kbar for

the mineral cores and the rims, respectively. The most probable pressures for intermediate magmas are 6.5 kbar and ~6 kbar based cores and rims, respectively. The most probable pressures of basalt crystallization are calculated to be around 5.5 kbar based on the core compositions and 5 kbar based on rim data. These results suggest distinct storage conditions for trachyte, basaltic and intermediate rocks (Fig. 8c).

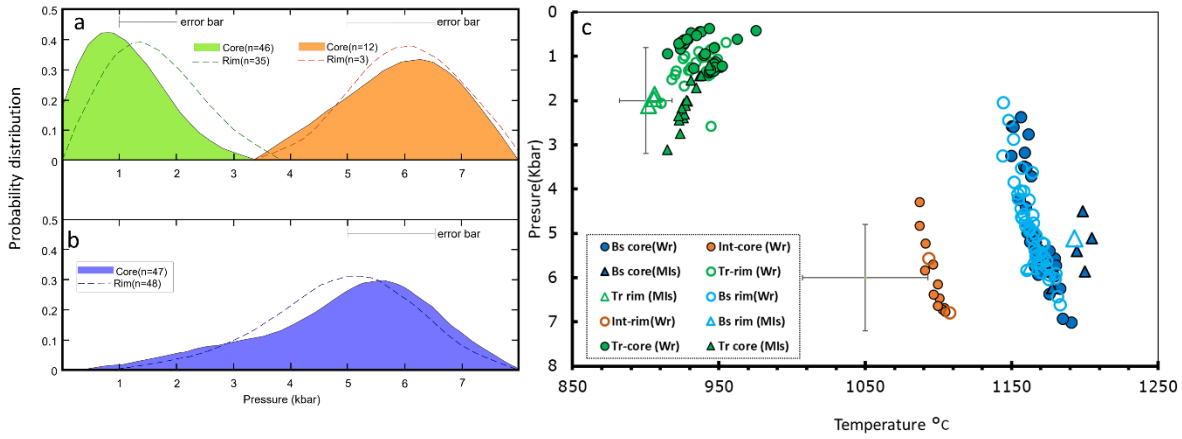

Fig. 8. a) KDE plots for crystallization pressures calculated from core and rim compositions of clinopyroxene, olivine and plagioclase in trachyte and intermediate rocks (bandwidth 0.9). b) Basalt crystallization pressures overlap partly with the estimated range for the trachyte and intermediate rocks. c) Calculated pressures versus temperatures derived only from the clinopyroxene geothermobarometers. Trachyte (green), intermediate rocks (orange) and basalts (blue) plot in distinct fields. Abbreviations: Bs. -Basalt, Tr.-Trachyte, Int.-Intermediate, Wr. -Whole rock, Mi.-Melt inclusion.

5.0 Discussion

5.1 Basaltic magma generation

Insights into the petrogenesis of volcanic complexes can be approached in multiple ways ranging from simple to complex quantitative modelling. Here, we examine the magma generation and partial melting process through a simple model of Y and La trace elements based on the theoretical equation 1 (Shaw, 1970), following the approach by Ersoy (2013).

$$\frac{C_l}{C_o} = \frac{1}{D_o + F(1\text{-}P)} \quad (1)$$

Y and La were selected because they are not affected significantly by fractional crystallisation of olivine, clinopyroxene, and plagioclase, which are the main mineral phases expected to fractionate from primitive mantle melts. The Y and La concentrations of the most primitive sample (PK-20) are assumed to be those of the parental liquid (C_l). The initial primitive mantle concentrations (C_o) of Y and La were assumed to be 4.37 ppm and 0.69 ppm, respectively (Palme & O'Neill, 2003). The bulk partition coefficients (D_o) and the mode (P) are calculated based on the coefficient values of Y and La in different mineral phases, adopted from White (2013) and based on mineral proportions shown in Table 1. The melt fraction (F) was varied incrementally between 0.1–20 %.

Table 1 Partial melt model parameters

Initial concentrations-Co (Palme and O'Neill 2003)								
La	0.686							
Y	4.37							
Mineralogy proportions for (D_o) calculation								
	olivine	clinopyroxene	othopyroxene	spinel	garnet	plagioclase		
Spinel lherzolite	53	17	27	3	0			
Garnet lhezolite	60	10	20	0	10			
Mineral proportions for melting mode (P) calculation								
	olivine	clinopyroxene	othopyroxene	spinel	garnet	plagioclase		
Spinel lherzolite	2	80	15	3	0			
Garnet lhezolite	10	70	0	0	10			
Coefficient values for phases used (White, 2013)								
	olivine	clinopyroxene	othopyroxene	spinel	garnet	plagioclase	D_o	P
La	0.000001	0.07	0.0007	0.001	0.001	0.08	0.0121	0.0561
Y	0.005	0.4	0.01	0.05	3.1	0.008	0.0749	0.3231
*Model parameters used to calculate trace element variation during partial melt modelling								

Our model (Fig. 9a) suggests that a La/Y ratio similar to that of the Paka basalts can be reproduced by between 5–10 % partial melting within the garnet peridotite stability field and a possible contribution of small-degree (0.1–1.5 %) partial melts of spinel peridotite. The general estimated depth to the spinel–garnet peridotite transition is ~80 km (Macdonald et al., 1995b). The model (Fig. 9), however, indicates high Y (35 ppm) in the most primitive basalts (Pk–20) to be a direct product of garnet peridotite partial melting. Furthermore, the most primitive basalt has a MgO content of 7 % (with Mg# 40). Accordingly, these basalts are not near-primary melts but have gone through substantial fractional crystallisation before reaching the surface.

The trace element fractionation model (Equation 2) suggests that the most primitive Paka basalt (PK-20) composition can be achieved after 76 % fractional crystallization of primary magma (5–10% partial melts) with the assumption that 50 % plagioclase, 35 % clinopyroxene and 15 % olivine are removed by gabbro phase assemblage fractionation. The removed modal mineralogy is based on the composition of the massive Bikilal Ghimbi gabbro intrusion (Woldemichael & Kimura, 2008), which is used as a proxy for gabbroic intrusions under the East African Rift. Indeed, if we model 76 % reverse crystallization of Paka basalt (PK-20) at the estimated Moho pressure of 9 kbar (~30 km) using the Petrolog software with 50% plagioclase, 35% clinopyroxene and 15% olivine fractionation at fO_2 equivalent to the FMQ buffer and mineral–melt models of Danyushevsky and Plechov (2011), then the MgO content of the resulting primitive basalt is found to be 10 % (Mg# 72); a possible basaltic magma in equilibrium with mantle olivine mineral assemblage (Fo_{90}) (Roeder & Emslie, 1970). Olivine in mantle xenoliths found in Chyulu volcanic region within the Kenyan rift have forsterite content ranging between $Fo_{90–92}$ (Omenda, 1997). Therefore, we believe our calculations are plausible.

Based on these results, we propose that partial melts ponded below the crust–mantle boundary (Moho 30 km). They underwent 76 % gabbro fractionation and achieved the critical density of 2.61 g/cm^3 (Lange & Carmichael, 1987) confirmed by a reverse fractional crystallization model. The magma then travelled through a complex plumbing system towards the surface.The obtained garnet peridotite melting degree of 5–10 % is higher than the values calculated for Suswa(<5 %) in the central rift (Omenda, 1997). It is also much higher than the 1–2 % values calculated for the rift flank volcanoes of Chyulu and Hurri hills (Omenda, 1997). Geophysical models indicate that the lithosphere–asthenosphere boundary coincides with Moho in the northern rift (Paka) and is between 20–30 km, while in the central rift (Lake Naivasha), the Moho is at more than 35 km depth (Mechie et al., 1994). The variations in partial melting values can therefore be linked to the difference in crustal thickness.

5.2 Evolution of Paka trachyte from a basaltic parent magma

Trace element modelling

Chemical variation plots (Fig. 5) show that the basalt, intermediate and trachyte rock types at Paka volcano might be related by a single liquid line of descent. Bivariant element plots show a decrease of CaO, FeO, MgO and TiO_2 with SiO_2, therefore behaving compatibly, while Na_2O and K_2O increase with SiO_2 and are incompatible. This is consistent with fractional crystallization controlled by the removal of olivine, clinopyroxene, Fe–Ti oxide, plagioclase and alkali feldspars. The idea of a protracted fractional crystallization process is also confirmed by the variation in trace elements, i.e., Y and La, which both show an increase

with Zr content, hence are incompatible (Fig. 6a-b). Magma differentiation processes can include partial melting (PM), fractional crystallization (FC) and assimilation (A) of the surrounding crust. FC and assimilation can occur simultaneously, hence in an AFC process (Taylor, 1980), or be decoupled (Cribb & Barton, 1996). We explore the role of fractional crystallization processes as invoked by previous studies (Sceal & Weaver, 1971) and indeed suggested by the chemical plots (Figs. 5 and 6). To examine quantitatively whether fractional crystallization is the dominant magma differentiation process in Paka basalt, and whether such a process could generate the Paka trachyte, we use the theoretical equation 2 (Neumann et al., 1954):

$$\frac{C_l}{C_o} = F^{D-1} \quad (2)$$

We input the concentrations of La and Y in the parent magma (C_o), assumed to be the most primitive Paka basalt (PK-20), to reach the concentration in trachyte (C_l). The model that best fits the measured concentrations in trachyte is generated by varying the fraction of the remaining melt (F). The assumed fractionating mineral assemblage comprises 5 % olivine, 35 % clinopyroxene and 40 % plagioclase estimated from petrographic analysis (Section 4.1). Our FC model (Figs. 9 b–c) suggests that 60–80 % magma fractionation is needed to generate the Paka trachyte from the Paka basalts, which compares well with previous results from a Rhyolite MELTS model (Mibei et al., 2021a) that indicated 74–83% fractional crystallization under initial H_2O content of 1.0 wt.%, oxygen fugacity at ΔFMQ +1 and two probable pressure conditions of 4 and 2 kbar. However, the results of fractional crystallization (FC) do not fit with the complete compositional variation observed in Paka trachyte, suggesting that an additional process might be at play, most likely assimilation and contamination.

We modelled coupled assimilation and fractionation (DePaolo, 1981) in an attempt to better explain the variation of our samples.

$$C_l^{AFC} = C_o \left[F^{-z} + \left({}^{r}/_{r-1}\right) {}^{C_a}/_{zC_o} \left(1-F^{-z}\right)\right] \quad (3)$$

where; $r = \frac{m_a}{m_c}$ and $z = \frac{r+D-1}{r-1}$

Two AFC models (Figs. 9b–c) were tested with 10 % (r=0.1) and 20 % (r=0.2) assimilation. The assimilated material (m_a) was assumed to be a syenite intrusive with Y and La concentrations of 41 and 102 ppm, respectively. These average values were obtained from syenites of the Kilombe volcano within the northern Kenya rift valley (Ridolfi et al., 2006). Syenite is considered as potential assimilant due to the availability of largely buried syenite intrusions under Paka volcano, as inferred from gravity anomalies (density = 2.7g/cm^3) 2 km below the surface in the area (Mariita & Keller, 2007), and the occurrence of syenite xenoliths in many of the pre and post-caldera lavas, and syenite intrusion from borehole data (Mibei et al., 2021a). The two tested models, accompanied by 70 % fractional crystallization, show good fits for the entire of Paka trachyte data set (Figs. 9b–c). We conclude therefore that 10–20 % assimilation of syenite intrusives and ~70 % fractional crystallization is required to generate a liquid similar to Paka trachyte. This proposed AFC model is consistent with previously published magma differentiation models for the Paka complex, and indeed volcanism in the inner graben of the northern Kenya rift (Macdonald et al., 1995b)

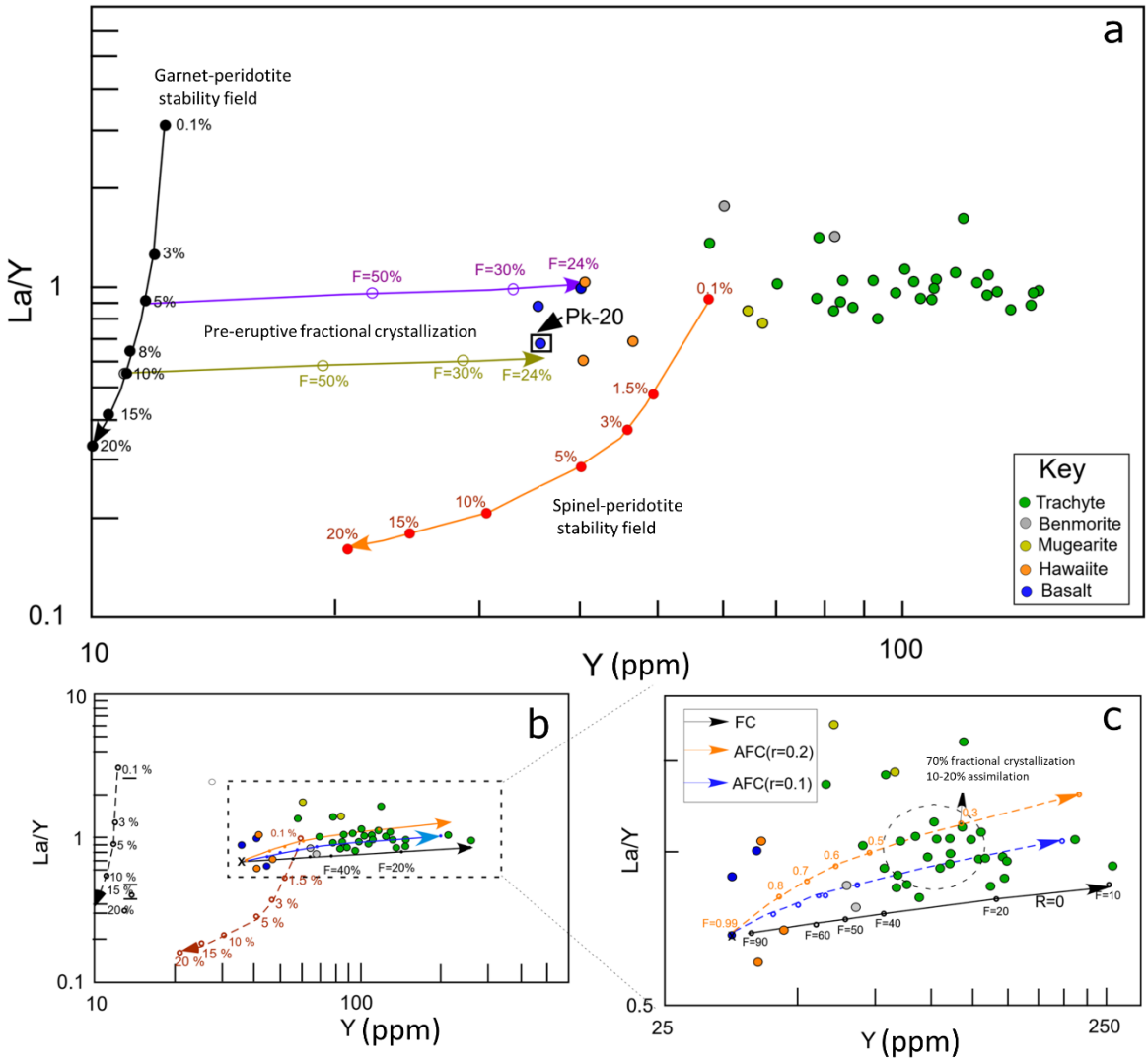

Fig. 9. a) Magma genesis model for basalt generation by 5–10 % partial melting of garnet peridotite with possible addition of a small fraction of low-degree melt (0.1–1.5 %) from spinel peridotite b) Fractional crystallization model (FC) (black arrow) shows that up to 60-80 % crystallization explains Paka samples. Good fits are AFC model entails 70 % FC with 10 % or 20 % assimilation, shown with blue and orange arrows, respectively. c) Enlarged figure of the AFC model.

5.3 Magma temperatures and water contents

The geothermobarometry and hygrometry models employed whole rock and melt inclusion (after PEC correction) compositions as the melt component (Neave et al., 2019). The melt inclusion PEC required adjustments of between 2–37 % (Table S3). The PEC variation is linked to potential differences in the cooling rates of different magma types. The groundmass glass compositions did not meet the criteria for use in the models as melt compositions as they plot outside the 'normal trend' for Paka rock compositions (Fig. 5). This is due to the fact that, on the one hand, the interstitial groundmass glass pools were probably too small for the EMPA beam and, on the other hand, they might be affected by local crystallization of the surrounding minerals in the lava flow. Both cores and rims were used to estimate pressure and temperature conditions for two main reasons: (i) some minerals were homogeneous; hence cores and rims must have crystallised at the same conditions, and (ii) to have a complete range of P–T crystallisation conditions for both cores and rims in normal and reversely zoned crystals.

The temperature range calculated for the complete rock series (trachyte–basalts) is 901–1204 °C, whereas the H_2O contents vary from 0.8–5.1 wt.%. The H_2O contents estimated with the plagioclase and K–feldspar hygrometers (Table S14) are consistent with the rhyolite–MELTS model estimates (Mibei et al., 2021a) within model uncertainties. When the different thermometry models are assessed, the olivine thermometer in the intermediate rocks gives higher temperatures (peak value 1125 °C) compared to the clinopyroxene and plagioclase thermometers (peak value 1100 °C), but this difference is within the model uncertainties (Fig. 7c). For basalts (Fig. 7d), the olivine thermometer gives lower temperature (peak value of 1150 °C) than the clinopyroxene and plagioclase thermometers (peak value of 1170 °C), again within the model uncertainties.

In comparison with the calculated temperature for the Paka trachyte (>900 °C), trachyte temperature at Eburru volcano was calculated to be in the range 709–793 °C (Ren et al., 2006) and is higher than temperatures of Suswa and Menengai trachytes ranging between 858 and 919 °C (Macdonald et al., 2011; White et al., 2012). The highest Suswa and Menengai temperatures closely match the temperatures calculated for the Paka trachyte. Under hydrous conditions, sanidine can coexist with amphibole in trachyte, but at temperatures lower than 815 °C (White et al., 2012). This would therefore explain why Paka trachytes lack amphibole, as suggested by petrographic analysis. The relatively high trachyte temperatures of Paka within the Kenya rift could reflect an open magma system and direct crystal transport between the deep (intermediate–mafic) and shallow (felsic) magma reservoirs as proposed for Suswa. This assumption is supported by the disequilibrium resorption textures of feldspars and clinopyroxene noted earlier (Section 4.1), the presence of crystal reverse zoning and the compositional overlap between trachyte and intermediate and basalt clinopyroxene (Table S15–S18) (Fig. 4). The open system is favourable for geothermal resources within the volcanic complex, as the heat source is periodically renewed by fresh magma injections from the deeper intermediate–mafic magma reservoir.

5.4 Magma storage depths

Storage pressures were converted to depth (km) by assuming a crustal density of 2800 kg/m^3 (1 kbar to 3.6 km). The assumed crustal density is a mean of the estimated crustal density of the area (2.75 g/cm^3) and the intrusive bodies (2.90 g/cm^3) below the area (Mariita & Keller, 2007).

The barometric model (Fig. 11a) suggests variable crystallization pressures for the basaltic and intermediate rocks with a mean value of 5.5-6 kbar (19–21km) and with skewness towards low pressures (Fig. 8). The trachyte on the other hand indicates probable pressure of 1-2 kbar (3.7–7.4 km). The intermediates on average have higher pressures than basalts is surprising and may require further investigations. The trachyte storage at low pressure overlapped with basalts, this may indicate that part of basalt magma equilibrated at lower pressures and may explain basalt xenoliths in trachyte (Mibei et al., 2021a). We propose therefore that Paka volcanic eruptions tapped laterally and vertically stacked sources of interacting mafic and silicic system. The calculated magma storage depths here are comparable to results of a MELTS model in previous work (Mibei et al., 2021a), that proposed crystallization pressures of 2–4 kbar (7–14 km) considering SEE of our models as indicated in section 3.5. The magma storage therefore occurred at variable depths in Paka between 3.6–21 km and therefore within the deep, mid and shallow–crustal levels (Fig. 11a).

5.5 Temporal evolution of Paka magma conditions

We evaluate the temporal aspects for both the temperature and pressure conditions by plotting the geothermobarometry results in relation to age. Samples were evaluated from five stratigraphic sequences (Fig. 1b), i.e., the Pre–Paka plateau basalt (582 ka) (pk-20), Phase 1 trachyte (382 ka) (pk-18), Phase 2 hawaiite (238 ka) (pk-4), Phase 3 basalt (160 ka) (pk-28), Phase 3 hawaiite (145 ka) (pk-13), Phase 3 trachyte (126 ka) (pk-30), Phase 4 trachyte (20 ka) (pk-3) and Phase 4 pyroclastic (11 ka) (DN-4); for these samples, both radiometric ages and geothermobarometry results are available. The results (Fig. 10) indicate that the Pre-Paka basalt (582 ka) had a temperature with peak of ~1180 °C, the Phase 2 hawaiite (238 ka) had temperatures with peak of 1150°C, while the Phase 3 basalt (160 ka) had a temperature peak of 1165 °C and Phase 3 hawaiite (145 ka) had temperature of 1175 °C. This suggests that the mafic lava eruptions spanning between 145–582 ka had a reservoir temperature in the range of 1150–1180 °C. Assuming the SEE of the calibration being ±45 °C, this basically means that the magma storage temperatures remained the same over time. The trachyte data (Fig. 10a) show that the trachyte lavas in Phases 1(382 ka), Phase 3 (126 ka) and Phase 4 (20 ka) had temperature peaks of 950 °C, 940 °C and 930 °C, respectively, while the phase 4 trachytic pyroclastic (11 ka) had a peak of 925°C. If we consider the SEE of ±18 °C for the trachyte thermometer (Masotta et al., 2013),this means that Phase 1 and Phase 3 trachytes were hotter and had similar reservoir temperatures, while the succeeding magmas, i.e., Phase 4 trachyte and Phase 4 trachytic pyroclastic were slightly cooler.

The pressure (Figs. 10c–d) is similarly evaluated and results show that the Pre–Paka plateau basalt (pPBt), dated at 582 ka, came from two magma reservoirs of different depths. The deeper crustal reservoir is indicated by the peak pressure value of 5.5 kbar (19.8 km depth), and a shallower one with a peak pressure value of 2.5 kbar (~ 9km) at mid–crustal level. The Phase 2 hawaiite (P2–Ht), dated at 238 ka, was exclusively stored at a pressure with a peak value of 1.5 kbar (5.4 km), within a mid–level reservoir. Phase 3 basalt (160 ka) and Phase

3 hawaiite (145 ka) were at a similar storage pressure with a peak value 5.5 kbar, similar to the pre–Paka basalt deep crustal reservoir.

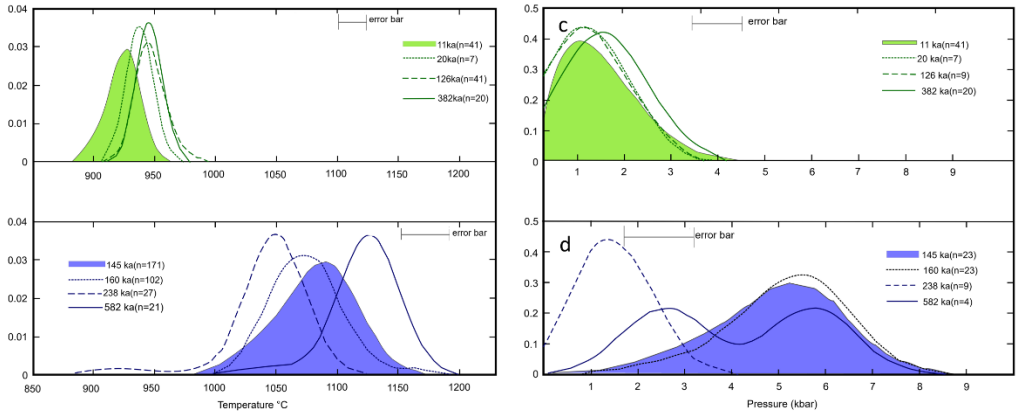

Fig. 10. a) KDE plots (bandwidth 5) for trachyte temperature spanning 11–382 ka. b) KDE plot (bandwidth 5) for temperature for mafic lavas spanning 145-582 ka. c) KDE plots (bandwidth 0.3) for pressure distributions and storage depths of trachyte magma spanning 11–382 ka. d) The KDE plot (bandwidth 0.3) showing crystallization pressure distribution for basaltic magma spanning 145–582 ka, the pressures were around 5.5 kbar, with low pressure centered at 1.2 kbar for the 238 ka samples.

We therefore conclude that the mafic melts were derived mostly from deeper crustal levels throughout the whole lifetime of the Paka volcano, where a stack of magma reservoirs has possibly been supplying melt since volcanism begun 582 ka ago in the area (Figs. 11). The trachytic magma was sourced over time from a similarly stacked shallow magma reservoir. We suggest that there has been a well–established magma pathway under Paka for the last ~0.5 million years, which might be slightly different below the summit area compared to the flanks, as proposed for other systems (Bouvet de Maisonneuve et al., 2012), but no significant change in the Paka magma plumbing system is obvious over time. This is, however, based on a limited number of clinopyroxene–melt data.

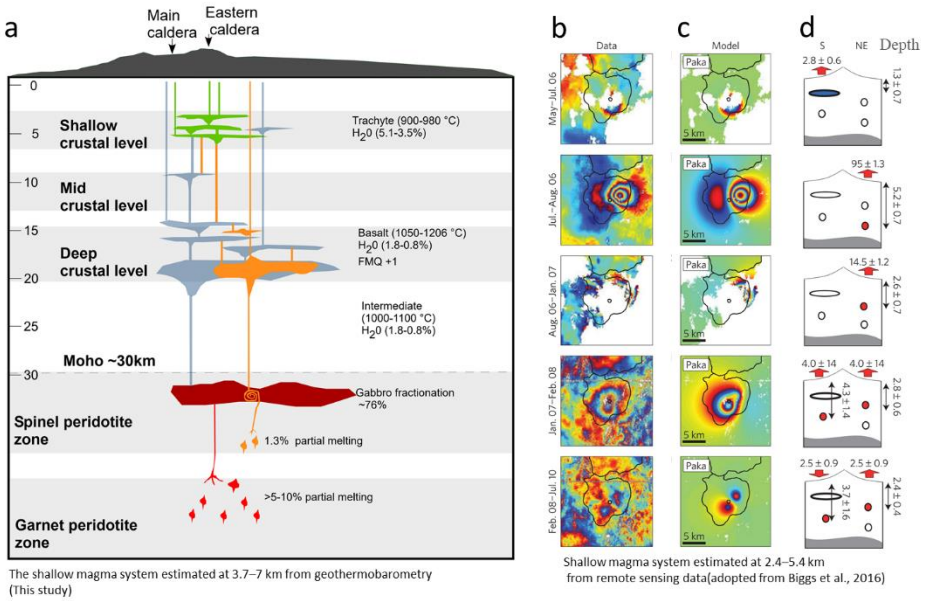

Fig. 11. a) Geochemical/petrology conceptual model for the Paka magma plumbing system indicating variable P–T, and H_2O conditions. b) Remote sensing data used in geodetic modelling from Biggs et al., 2016c) Surface deformation models from Bigg et al., 2016. d) Estimated surface deformation source depths from remotes sensing data.

5.6 Geophysical constraints to the calculated magma depths

The interaction of the magmatism and tectonism in Paka influenced eruption styles involving effusive and minor explosive activity through fissures and eruption centres (Mibei et al., 2021a). This magmatic activity was fed by a system of dikes as proposed in section 5.4 and conceptualised in Fig. 11a. We constrain our geochemical/petrology magma depths with available geophysical data from previous works. This includes MT resistivity (Lichoro et al., 2017, 2019) and InSAR detected surface deformation (Biggs et al., 2009; Biggs et al., 2016),

According to Lichoro et al (2017), the resistivity structure under the Paka volcano (Fig. 12) includes a shallow 1100 m thick heterogenous zone of resistive surface (>500 Ω m) overlying a low resistive layer (30 Ω m). Below this zone is a ~400 m conductor (<20 Ω) suggested to be the top of the Paka hydrothermal system. Below the conductor is a relatively resistive area (>35 Ω m), within a resistive core (100 Ω m), extending from 1.6-3 km and modelled as a geothermal reservoir and intrusive stratum. This interpretation is consistent with other volcanos, e.g., Asama in Japan (Aizawa et al., 2008). The intrusive rocks in Paka have been confirmed to be syenite by geothermal drilling (Mibei et al., 2021). The deep syenite intrusive zone is evidence of cooled or cooling magma mush nearby a magma body estimated by our model to be at between 3.7 to 7 km depth. This is constrained by seismic and magneto-telluric studies indicating a magma body at 2-5 km depth (Biggs et al., 2016).

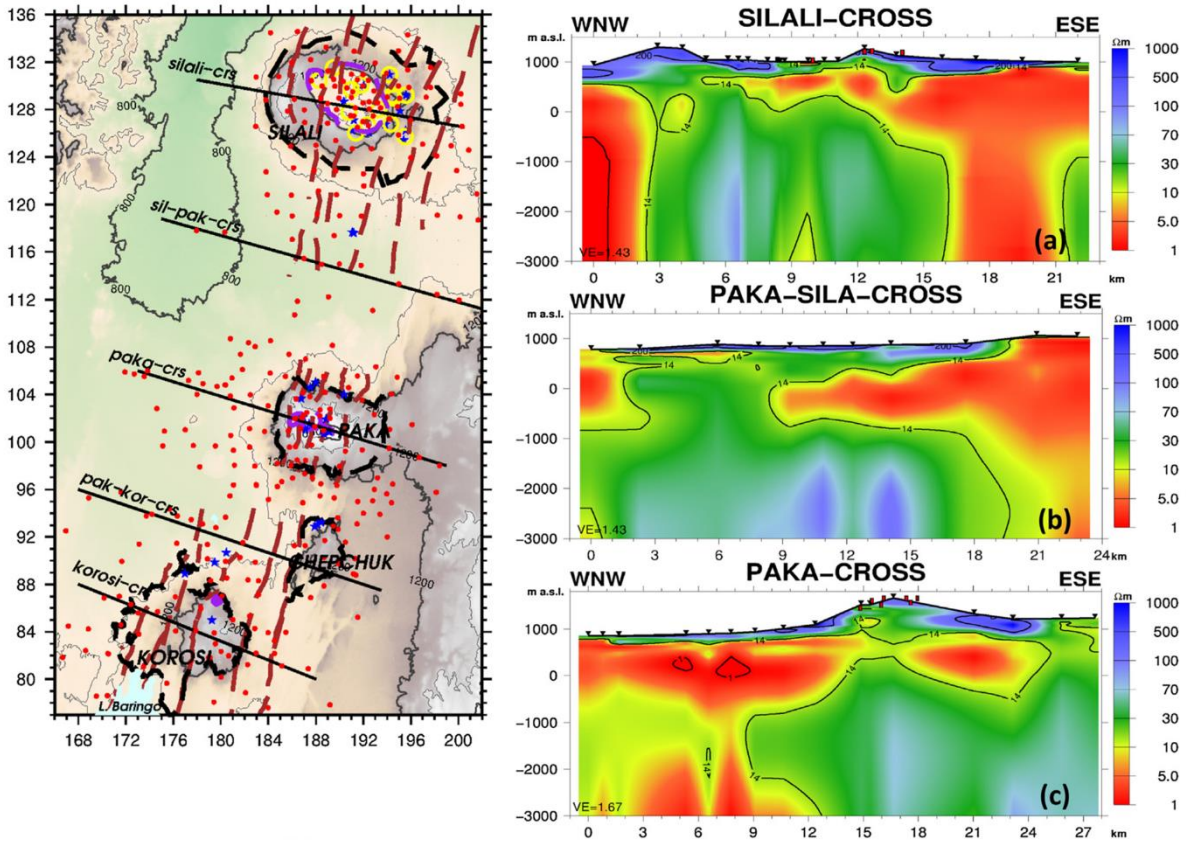

Fig. 12. The electrical resistivity cross-sections Lichoro et al (2017). Paka is located between Silali and Chepchuk while its cross-section in on lower left panel.

Surface inflation and deflation events have also occurred periodically beneath the northeastern and southern flanks of Paka volcano (Biggs et al., 2016). This was linked to magma activity below this area; however, it has also been suggested that inflation-deflation events may relate to the hydrothermal system (Biggs et al., 2016). The source depths for these events were found to be between 1.3–2.4 km and 2.4–5.2 km for the hydrothermal and magma controlled deformations, respectively (Biggs et al., 2016)(Figs. 11b–d). The depth of the magmatic source events (2.4–5.4 km) overlaps within the magma depths of our model (3.7–7 km). The estimated shallow magma reservoir depth (~3 km) is within geothermal drilling range and high or even critical bottom–hole temperatures are expected within Paka volcano. These results are therefore of significant importance for future drilling plans, operations and resource exploration.

6.0 Conclusions

- The primary magma in Paka was most probably generated by 5–10 % partial melting of garnet-peridotite, although low-degree melts (0.1–1.5 % partial melt) from the spinel-peridotite stability field may also have contributed to the primary magma.
- The primary magma experienced extensive fractionation (~76 %) at the Moho before attaining critical density, estimated to be 2.61 g/cm^3, facilitating transportation of basalt magma up to crustal levels. There was a further >70 % fractional crystallization and 10–20 % crustal assimilation of intrusive bodies.
- Paka magma evolved at different pressures, indicating crystallization at deep crustal levels (14–21 km), mid–crustal reservoirs (~ 9 km) and at shallow crustal levels (3.7–7 km). Temperatures varied between 901–1204 °C in the silicic-mafic system
- There are no indications of major changes in the magma storage depths and temperatures over time, and therefore a well–established long–lived plumbing system exists below Paka.
- Textural and chemical observations suggest connection between the deeper and the shallow magma reservoirs. This implies continuous renewal of the geothermal heat source.
- Previous geophysical work supports a shallow magma body at between 2-5 km depth
- The estimated shallow magma reservoir depth (~3 km) is within the geothermal well drilling depth range and related risk factors have to be considered in future drilling plans.

Acknowledgments

We would like to thank the Geothermal Development Company Ltd (GDC) for allowing the use of their data, and for assistance during several field campaigns. We are grateful to Dario Ingi Di Rienzo, Jóhann Gunnarsson-Robin and Sæmundur Ari Halldórsson for their assistance during sample preparation and ICP–OES analysis. We would also want to acknowledge the reviewers; Elizabeth Y. Antony, Nick Rogers, one anonymous reviewer and the Editor-in-Chief Mike Roden who's comments and suggestions have significantly improved this manuscript from the previous version. The project was funded by the Geothermal Development Company Limited of Kenya and the GRÓ–Geothermal Training Programme as part of a Ph.D. fellowship.

References

Aizawa, K., Ogawa, Y., Hashimoto, T., Koyama, T., Kanda, W., Yamaya, Y., . . . Kagiyama, T. (2008). Shallow resistivity structure of Asama Volcano and its implications for magma ascent process in the 2004 eruption. *Journal of Volcanology and Geothermal Research, 173*(3), 165-177. doi:https://doi.org/10.1016/j.jvolgeores.2008.01.016

Baker, B. H., Mohr, P. A., & Williams, L. A. J. (1972). Geology of the Eastern Rift System of Africa. In B. H. Baker, P. A. Mohr, & L. A. J. Williams (Eds.), *Geology of the Eastern Rift System of Africa*: Geological Society of America.

Biggs, J., Anthony, E., & Ebinger, C. (2009). Multiple inflation and deflation events at Kenyan volcanoes, East African Rift. *Geology, 37*, 979-982. doi:10.1130/G30133A.1

Biggs, J., Robertson, E., & Cashman, K. (2016). The lateral extent of volcanic interactions during unrest and eruption. *Nature Geoscience, 9*(4), 308-311.

Bouvet de Maisonneuve, C., Dungan, M. A., Bachmann, O., & Burgisser, A. (2012). Insights into shallow magma storage and crystallization at Volcán Llaima (Andean Southern Volcanic Zone, Chile). *Journal of Volcanology and Geothermal Research, 211-212*, 76-91. doi:https://doi.org/10.1016/j.jvolgeores.2011.09.010

Caracciolo, A., Bali, E., Guðfinnsson, G. H., Kahl, M., Halldórsson, S. A., Hartley, M. E., & Gunnarsson, H. (2020). Temporal evolution of magma and crystal mush storage conditions in the Bárðarbunga-Veiðivötn volcanic system, Iceland. *Lithos, 352-353*, 105234. doi:https://doi.org/10.1016/j.lithos.2019.105234

Cashman, K. V., Sparks, R. S. J., & Blundy, J. D. (2017). Vertically extensive and unstable magmatic systems: A unified view of igneous processes. *Science, 355*(6331), eaag3055. doi:10.1126/science.aag3055

Cottrell, E., Spiegelman, M., & Langmuir, C. H. (2002). Consequences of diffusive reequilibration for the interpretation of melt inclusions. *Geochemistry, Geophysics, Geosystems, 3*(4), 1-26. doi:10.1029/2001gc000205

Cribb, J. W., & Barton, M. (1996). Geochemical effects of decoupled fractional crystallization and crustal assimilation. *Lithos, 37*(4), 293-307. doi:https://doi.org/10.1016/0024-4937(95)00027-5

Danyushevsky, L., Della-Pasqua, F., & Sokolov, S. (2000). Re-equilibration of melt inclusions trapped by magnesian olivine phenocrysts from subduction-related magmas: petrological implications. *Contributions to Mineralogy and Petrology, 138*(1), 68-83.

Danyushevsky, L. V., & Plechov, P. (2011). Petrolog3: Integrated software for modeling crystallization processes. *12*(7). doi:10.1029/2011gc003516

Deer, W., Howie, R., & Zussman, J. (2013). An introduction to the rock-forming minerals (pp. 498). *Mineralogical Society of Great Britain and Ireland, London*.

DePaolo, D. J. (1981). A neodymium and strontium isotopic study of the Mesozoic calc-alkaline granitic batholiths of the Sierra Nevada and Peninsular Ranges, California. *Journal of Geophysical Research: Solid Earth, 86*(B11), 10470-10488. doi:10.1029/JB086iB11p10470

Dunkley, P., Smith, M., Allen, D. J., & Darling, W. G. (1993). The geothermal activity and geology of the northern sector of the Kenya Rift Valley. *Br. Geol. Surv. Res. Rep., SC/93/1*.

Ersoy, E. Y. (2013). PETROMODELER (Petrological Modeler): a Microsoft® Excel© spreadsheet program for modelling melting, mixing, crystallization and assimilation processes in magmatic systems. *Turkish Journal of Earth Sciences, 22*(1), 115-125.

Eskandari, A., Amini, S., De Rosa, R., & Donato, P. (2018). Nature of the magma storage system beneath the Damavand volcano (N. Iran): An integrated study. *Lithos, 300-301*, 154-176. doi:https://doi.org/10.1016/j.lithos.2017.12.002

Friese, A., Hahne, K., Mutua, J., Lopeyok, T., & Mibei, G. (2014). *InSAR, surface movement and dating of Paka volcanic products, Northern Kenya Rift;*. (BGR 05-2343). Hannover,Germany: Federal Institute for Geoscience and Natural Resources Retrieved from https://www.bgr.bund.de/EN/Themen/Zusammenarbeit/TechnZusammenarb/Geotherm/Downloads/Publications/Poster Paka.pdf?__blob=publicationFile&v=2

Halldórsson, S., Bali, E., Hartley, M., Neave, D., Peate, D., Guðfinnsson, G., . . . Thordarson, T. (2018). Petrology and geochemistry of the 2014–2015 Holuhraun eruption, central Iceland: compositional and mineralogical characteristics, temporal variability and magma storage. *Contributions to Mineralogy and Petrology, 173*. doi:10.1007/s00410-018-1487-9

Kanda, I., Fujimitsu, Y., & Nishijima, J. (2019). Geological structures controlling the placement and geometry of heat sources within the Menengai geothermal field, Kenya as evidenced by gravity study. *Geothermics, 79*, 67-81. doi:https://doi.org/10.1016/j.geothermics.2018.12.012

Kayzar, T. M., Cooper, K. M., Reagan, M. K., & Kent, A. J. R. (2009). Gas transport model for the magmatic system at Mount Pinatubo, Philippines: Insights from (210Pb)/(226Ra). *Journal of Volcanology and Geothermal Research, 181*(1), 124-140. doi:https://doi.org/10.1016/j.jvolgeores.2009.01.006

Lange, R. A., & Carmichael, I. S. (1987). Densities of Na2O-K2O-CaO-MgO-FeO-Fe2O3-Al2O3-TiO2-SiO2 liquids: new measurements and derived partial molar properties. *Geochimica et Cosmochimica Acta, 51*(11), 2931-2946.

Le Bas, M. J., Maitre, R. W. L., Streckeisen, A., Zanettin, B., & Rocks, I. S. o. t. S. o. I. (1986). A Chemical Classification of Volcanic Rocks Based on the Total Alkali-Silica Diagram. *Journal of Petrology, 27*(3), 745-750. doi:10.1093/petrology/27.3.745 %J Journal of Petrology

Lichoro, C. M., Árnason, K., & Cumming, W. (2017). Resistivity imaging of geothermal resources in northern Kenya rift by joint 1D inversion of MT and TEM data. *Geothermics, 68*, 20-32. doi:https://doi.org/10.1016/j.geothermics.2017.02.006

Lichoro, C. M., Árnason, K., & Cumming, W. (2019). Joint interpretation of gravity and resistivity data from the Northern Kenya volcanic rift zone: Structural and

geothermal significance. *Geothermics, 77*, 139-150. doi:https://doi.org/10.1016/j.geothermics.2018.09.006

Lynn, K. J., Shea, T., & Garcia, M. O. (2017). Nickel variability in Hawaiian olivine: Evaluating the relative contributions from mantle and crustal processes. *American Mineralogist, 102*(3), 507-518. doi:10.2138/am-2017-5763

Macdonald, R., Bagiński, B., Leat, P. T., White, J. C., & Dzierżanowski, P. (2011). Mineral stability in peralkaline silicic rocks: Information from trachytes of the Menengai volcano, Kenya. *Lithos, 125*(1), 553-568. doi:https://doi.org/10.1016/j.lithos.2011.03.011

Macdonald, R., Davies, G., Upton, B., DUNKLEY, P. N., Smith, M., & Leat, P. T. (1995). *Petrogenesis of Silali volcano, Gregory Rift, Kenya* (Vol. 152).

Mariita, N., & Keller, R. (2007). An integrated geophysical study of the northern Kenya rift. *Journal of African Earth Sciences, 48*, 80-94. doi:10.1016/j.jafrearsci.2006.05.008

Masotta, M., Mollo, S., Freda, C., Gaeta, M., & Moore, G. (2013). Clinopyroxene–liquid thermometers and barometers specific to alkaline differentiated magmas. *Contributions to Mineralogy and Petrology, 166*. doi:10.1007/s00410-013-0927-9

Masotta, M., Mollo, S., Nazzari, M., Tecchiato, V., Scarlato, P., Papale, P., & Bachmann, O. (2018). Crystallization and partial melting of rhyolite and felsite rocks at Krafla volcano: A comparative approach based on mineral and glass chemistry of natural and experimental products. *Chemical Geology, 483*, 603-618. doi:https://doi.org/10.1016/j.chemgeo.2018.03.031

Mechie, J., Keller, G. A., Prodehl, C., Gaciri, S., Braile, L., Mooney, W., . . . Sandmeier, K.-J. (1994). Crustal structure beneath the Kenya Rift from axial profile data. *Tectonophysics, 236*, 179-200. doi:10.1016/0040-1951(94)90176-7

Mibei, G., Harðarson, B. S., Franzson, H., Bali, E., Geirsson, H., & Guðfinnsson, G. H. (2021). Eruptive history and volcano-tectonic evolution of Paka volcanic complex in the northern Kenya rift: Insights into the geothermal heat source. *Journal of African Earth Sciences, 173*, 103951. doi:https://doi.org/10.1016/j.jafrearsci.2020.103951

Mollo, S., Del Gaudio, P., Ventura, G., Iezzi, G., & Scarlato, P. (2010). Dependence of clinopyroxene composition on cooling rate in basaltic magmas: Implications for thermobarometry. *Lithos, 118*(3), 302-312. doi:https://doi.org/10.1016/j.lithos.2010.05.006

Mollo, S., Masotta, M., Forni, F., Bachmann, O., De Astis, G., Moore, G., & Scarlato, P. (2015). A K-feldspar–liquid hygrometer specific to alkaline differentiated magmas. *Chemical Geology, 392*, 1-8. doi:https://doi.org/10.1016/j.chemgeo.2014.11.010

Neave, D. A., Bali, E., Guðfinnsson, G. H., Halldórsson, S. A., Kahl, M., Schmidt, A.-S., & Holtz, F. (2019). Clinopyroxene–liquid equilibria and geothermobarometry in natural and experimental tholeiites: the 2014–2015 Holuhraun eruption, Iceland. *Journal of Petrology, 60*(8), 1653-1680.

Neave, D. A., & Putirka, K. D. (2017). A new clinopyroxene-liquid barometer, and implications for magma storage pressures under Icelandic rift zones. *American Mineralogist, 102*(4), 777-794.

Neumann, H., Mead, J., & Vitaliano, C. J. (1954). Trace element variation during fractional crystallization as calculated from the distribution law. *Geochimica et Cosmochimica Acta, 6*(2), 90-99. doi:https://doi.org/10.1016/0016-7037(54)90018-6

Omenda, P. A. (1997). The geochemical evolution of Quaternary volcanism in the south-central portion of the Kenya Rift.

Palme, H., & O'Neill, H. (2003). Cosmochemical Estimates of Mantle Composition. *Treatise on Geochemistry, 2*, 1-38. doi:10.1016/B0-08-043751-6/02177-0

Patlan Almeida, E. (2016). Insights into volcanic processes using seismic data techniques. *PhDT*.

Putirka, D. K. (2008). Thermometers and Barometers for Volcanic Systems. *Reviews in Mineralogy & Geochemistry - REV MINERAL GEOCHEM, 69*, 61-120. doi:10.2138/rmg.2008.69.3

Ren, M., Omenda, P. A., Anthony, E. Y., White, J. C., Macdonald, R., & Bailey, D. K. (2006). Application of the QUILF thermobarometer to the peralkaline trachytes and pantellerites of the Eburru volcanic complex, East African Rift, Kenya. *Lithos, 91*(1), 109-124. doi:https://doi.org/10.1016/j.lithos.2006.03.011

Ridolfi, F., Renzulli, A., Macdonald, R., & Upton, B. G. J. (2006). Peralkaline syenite autoliths from Kilombe volcano, Kenya Rift Valley: Evidence for subvolcanic interaction with carbonatitic fluids. *Lithos, 91*(1), 373-392. doi:https://doi.org/10.1016/j.lithos.2006.03.026

Roeder, P. L., & Emslie, R. F. (1970). Olivine-liquid equilibrium. *Contributions to Mineralogy and Petrology, 29*(4), 275-289. doi:10.1007/BF00371276

Sceal, J. (1974). *The Geology of Paka Volcano and the Country to the East, Baringo District, Kenya.* Royal Holloway, University of London,

Sceal, J., & Weaver, S. (1971). Trace element data bearing on the origin of salic rocks from the Quaternary volcano Paka, Gregory Rift, Kenya. *Earth and Planetary Science Letters, 12*(3), 327-331.

Shaw, D. M. (1970). Trace element fractionation during anatexis. *Geochimica et Cosmochimica Acta, 34*(2), 237-243.

Sudo, M., Strecker, M., Friese, A., Hahne, K., Frei, M., & Riedl, S. (2017). *Temporal change in geochemistry of volcanic rocks in northern Kenya Ar geochronology at Paka*. Retrieved from https://confit.atlas.jp/guide/event-img/jpguagu2017/SGL37-05/public/pdf?type=in

Taylor, H. P. (1980). The effects of assimilation of country rocks by magmas on 18O/16O and 87Sr/86Sr systematics in igneous rocks. *Earth and Planetary Science Letters, 47*(2), 243-254. doi:https://doi.org/10.1016/0012-821X(80)90040-0

Thomson, A., & Maclennan, J. (2012). The Distribution of Olivine Compositions in Icelandic Basalts and Picrites. *Journal of Petrology, 54*(4), 745-768. doi:10.1093/petrology/egs083

Velador, J., Omenda, P., & Anthony, E. (2003). An integrated mapping and remote sensing investigation of the structural control for fumarole location in the Eburru Volcanic Complex, Kenya Rift. *TRANSACTIONS-GEOTHERMAL RESOURCES COUNCIL*, 639-642.

White, J. C., Espejel-García, V. V., Anthony, E. Y., & Omenda, P. (2012). Open System evolution of peralkaline trachyte and phonolite from the Suswa volcano, Kenya rift. *Lithos, 152*, 84-104. doi:https://doi.org/10.1016/j.lithos.2012.01.023

White, W. M. (2013). *Geochemistry*: John Wiley & Sons.

Woldemichael, B., & Kimura, J.-I. (2008). Petrogenesis of the Neoproterozoic Bikilal-Ghimbi gabbro, Western Ethiopia. *Journal of Mineralogical and Petrological Sciences - J MINER PETROL SCI, 103*, 23-46. doi:10.2465/jmps.070401

Supplementary material to paper 2

Supplementary Figures S1shows the mineral classification of feldspar indicating the range of plagioclases and K-felspars. The olivine is mostly forsterite, the clinopyroxene varies from diopside to hedenbergite while the Fe-Ti oxides range between ulvospinel-magnetite series. The supplementary Tables S1–S8 are mineral chemistry included in Appendix D of the Thesis.

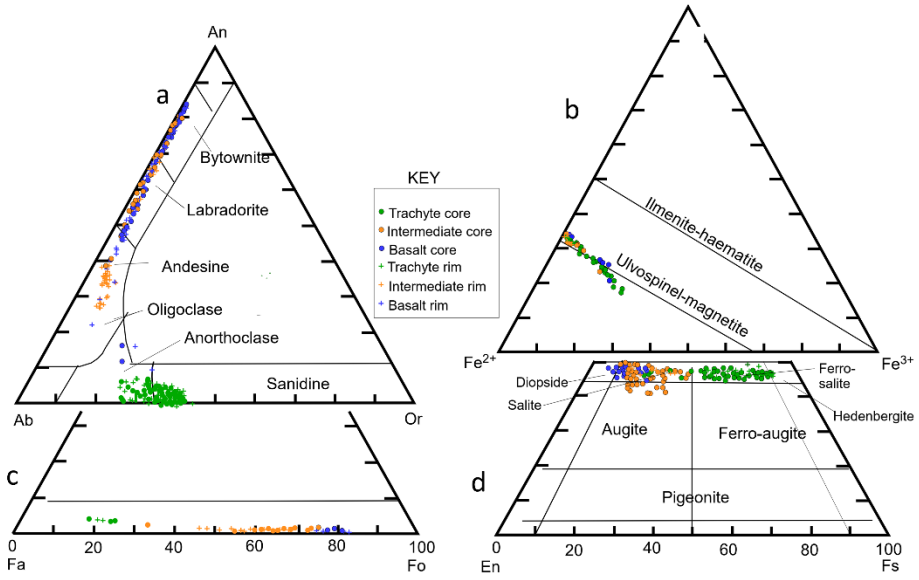

Fig.1. Mineral chemistry classification. a) Plagioclases ranging from bytownite to oligoclase in the intermediates and basalts, orthoclase mainly in trachyte. b) Oxides plotting in the Ulvospinel-magnetite series. c) Olivine are forsterite rich in intermediates and basalts and fayalite rich in trachyte. d) Pyroxenes plotting in the diopside for basalt, intermediates and hedenbergite for trachyte. **colour code: Blue-basalt, Brown-intermediate and Green-trachyte*

Paper III

Geothermal reservoir characterization of Paka geothermal field in Kenya based on detailed analyses of well PK-01 and review of surface exploration data

Geoffrey Mibei, Björn S. Harðarson, Hjalti Franzson, Enikő Bali, Halldór Geirsson, Guðmundur H. Guðfinnsson, Charles Lichoro, John Lagat

Journal of Geothermics (submitted)

Reservoir characterization of the Paka geothermal system in Kenya: insights from borehole PK-01

Geoffrey Mibei[1,3,4,] Björn S. Harðarson[2], Hjalti Franzson[2], Enikő Bali[3], Halldór Geirsson[3], Guðmundur H. Guðfinnsson[3], Charles Lichoro[1], John Lagat[1]

1-Geothermal Development Company, P.O. Box: 17700-20100, Polo House, Nakuru, Kenya
2-Iceland GeoSurvey, Grensásvegur 9, 108 Reykjavík, Iceland
3-NordVulk, Institute of Earth Sciences, University of Iceland, Sturlugata 7,101 Reykjavík, Iceland
4-GRÓ-GTP, Grensásvegur 9, 108 Reykjavík, Iceland

Abstract

Trachytic and basaltic volcanic material erupted from ~390 ka to Holocene coalesced to form the 136 km^2 active volcanic edifice of Paka on top of an older ~580 ka plateau eruptive sequence. The latter constrains the maximum age for the Paka geothermal system manifested mainly as surface fumaroles and hot altered grounds. To date, three exploration wells have been drilled to >2500 m depth. Results from analyses of well PK-01 show that the upper part of the well (0-1050 m) is exclusively a trachyte lava sequence while the lower part (1050-2552 m) penetrates sequences of trachyte, intermediate, basaltic and syenite intrusive rocks. Temperature attained in the well based on hydrothermal alteration assemblage vary from ~180 °C at 400 m depth where quartz was first observed in the drill cuttings to >220°C within the chlorite-illite zone at 700m and 280 °C below 1450 m in the actinolite-epidote zone. Fluid inclusion homogenization temperatures (T_h) range widely between 211-286°C at 1390 m and 209-271°C at 2550 m. Fluid inclusion indicate that the reservoir fluid from the paleo system was bicarbonate-rich and of very low salinity according to ice-melting temperature, which is comparable to aqueous fluid discharge from the well. Stabilised well temperature increases with depth to a maximum of 245 °C at 1800 m depth where a reversal occurs and becomes nearly isothermal at 230 °C, then increases slightly below 2200 m before an inversion to about 220°C. The main high-temperature geothermal system is hosted within the lower part of the well (1050-2552 m). It is probably steam-dominated above 900 m depth where calculated formation temperatures intersect the boiling point curve for pure water, and liquid-dominated below 900 m. Suitability modelling from surface data integration indicates that the most suitable area (P90) for geothermal development is within an area of 12 km^2 in the summit area and northeast of the Paka caldera.

Key words: *Paka geothermal system, hydrothermal, alteration, reservoir temperature, fluid inclusion, Kenya.*

1.0 Introduction

The Paka geothermal system is hosted within a shield volcanic complex located in the northern part of the 900 km long Kenyan rift segment (Fig.1a) of the East African Rift system (EARs). It is ~250 km north of the producing Olkaria geothermal system and 160 km from Nakuru town in Baringo basin adjacent to Silali and Korosi volcanoes (Fig. 1b). Previously,

Dunkley et al. (1993) confirmed the existence of a high-temperature geothermal resource in Paka. Further studies by KenGen and GDC (Lagat et al., 2013; Opondo, 2010) culminated in a preliminary conceptual model and drilling of three exploration wells in 2018-2020, i.e., PK-01, PK-02 and PK-03. Despite extensive progress in the geothermal exploration of Paka, the conceptual model is still in the initial stages. Additionally, the geothermal reservoir conditions, including the hydrothermal alteration mineralogy, evolution of reservoir temperature and fluid chemistry, are gradually unfolding. For this reason, we carried out a detailed study of the reservoir using drill cuttings and other geoscientific data from borehole PK-01 (GDC, 2020; Lopeyok, 2019; Ochieng, 2019). Our focus is on the petrography and characterization of hydrothermal alteration minerals, including fluid inclusions as they often provide information about past and present reservoir temperatures, permeability and fluid chemistry (Browne, 1970). Results from this study are integrated with existing surface exploration data (Section 3) to update the geothermal conceptual model and contribute to a better understanding of the Paka reservoir conditions.

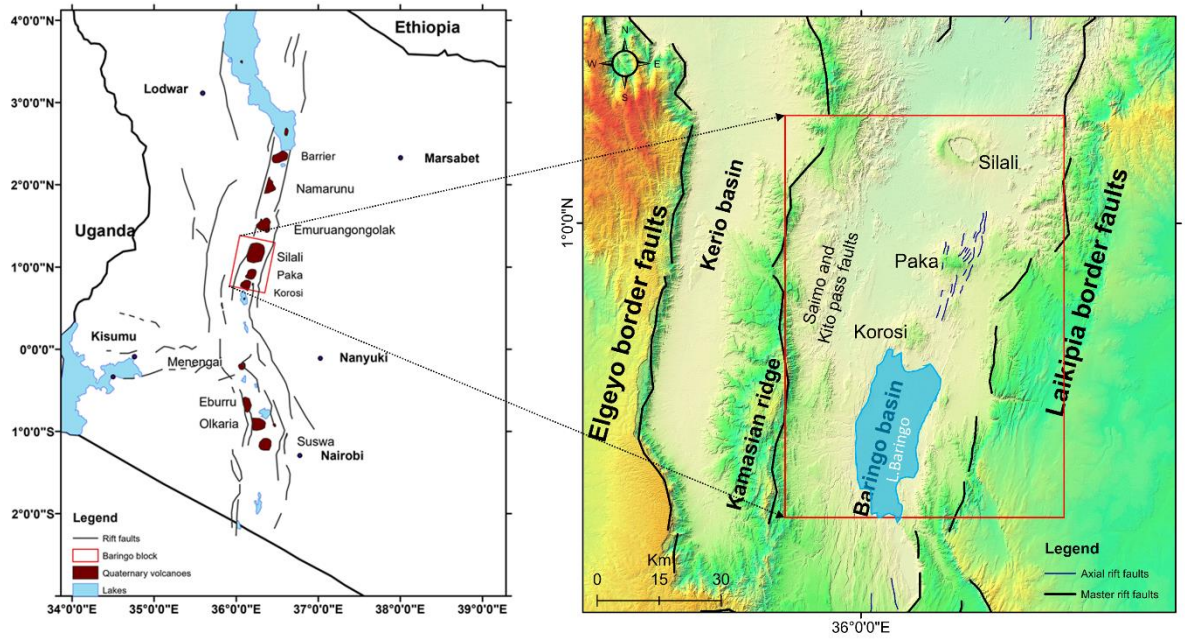

Fig. 1: a) Map showing the location of Paka and other geothermal systems in a regional context within the Kenyan rift system. The left panel is the location of Paka volcano and neighbouring geothermal systems within the northern Kenya rift segment from Mibei et al (2021a).

2.0 Geological background of Paka

The Paka geothermal field is associated with a volcanic complex situated within the Baringo-Silali geothermal block in Kenya. Paka volcano consists of trachytic and basaltic volcanic sequences erupted in the last 390 ka. It is approximately 136 km^2 in area with a caldera 1.5 by 1.6 km in diameter estimated to have formed 35 ka ago (Mibei et al., 2021a). The regional eruptive activity, however, began earlier (>582 ka) with an accumulation of plateau trachyte lavas, which appear to be contemporaneous with the Baringo trachyte erupted further south during widespread rift volcanism. The maximum age limit for the Paka hydrothermal system

is assumed to coincide with the onset of the Paka central volcanic activity which succeeded the plateau eruptive phase (<582 ka) and the accompanying intrusive activity.

According to Mibei et al. (2021a), the surface stratigraphy of the volcano consists of four volcanic sequences succeeding the plateau/Pre-Paka sequence (pP). These are volcanic sequence 1 (P1), volcanic sequence 2 (P2) and volcanic sequence 3 (P3), which are mainly composed of trachytic lavas with intercalations of basalt lava and pyroclastic deposits, while the youngest volcanic sequence 4 (P4) is mainly trachytic lavas with pyroclastic intercalations (Fig. 2). The stratigraphic succession has been further refined by data from the 2.5 km deep exploration well PK-01 (Mibei et al., 2021a). The well stratigraphy indicates that the Pre-Paka sequence first intersected at 1050 m is very thick and continues to the bottom of the borehole. At 1800 m depth within the Pre-Paka formation, the increase in frequency of syenite intrusives implies an associated intrusive heat source for the rock formations and consequently the geothermal system beneath Paka (Mibei et al., 2021a). The total volume of erupted volcanic material in Paka is ~50 km^3 with an estimated average eruption rate of ~1.2 x 10-4 km^3/yr and associated heat flux of ~110-138 mW/m^2 (Mibei et al., 2021a). This in addition to increased eruption frequency in the later stages of volcano growth (volcanic sequence 4) strongly indicates a magma-driven heat source for the geothermal system within the volcanic complex.

The volcano is dominated by normal faulting that shows a right stepping en échelon arrangement across the volcano, correlating with the regional fault pattern recognizable at Korosi and Chepchuk in the south and Silali volcano in the north (Friese, 2015). The faults on the southern flanks of Paka trend N-S. However, the direction changes to NNE to NE in the northern flanks as they converge at the summit area. Eastern Paka is intensely faulted with a distinct ~5 km wide fault zone stretching towards the NE (Fig. 2). Most of geothermal manifestations and eruption centres show a strong association to these NNE trending faults. The few lineaments and NW and E-W strike slip faults appear not to influence the underlying hydrothermal and magmatic systems as much as the NE trending faults (Mibei et al 2021a).

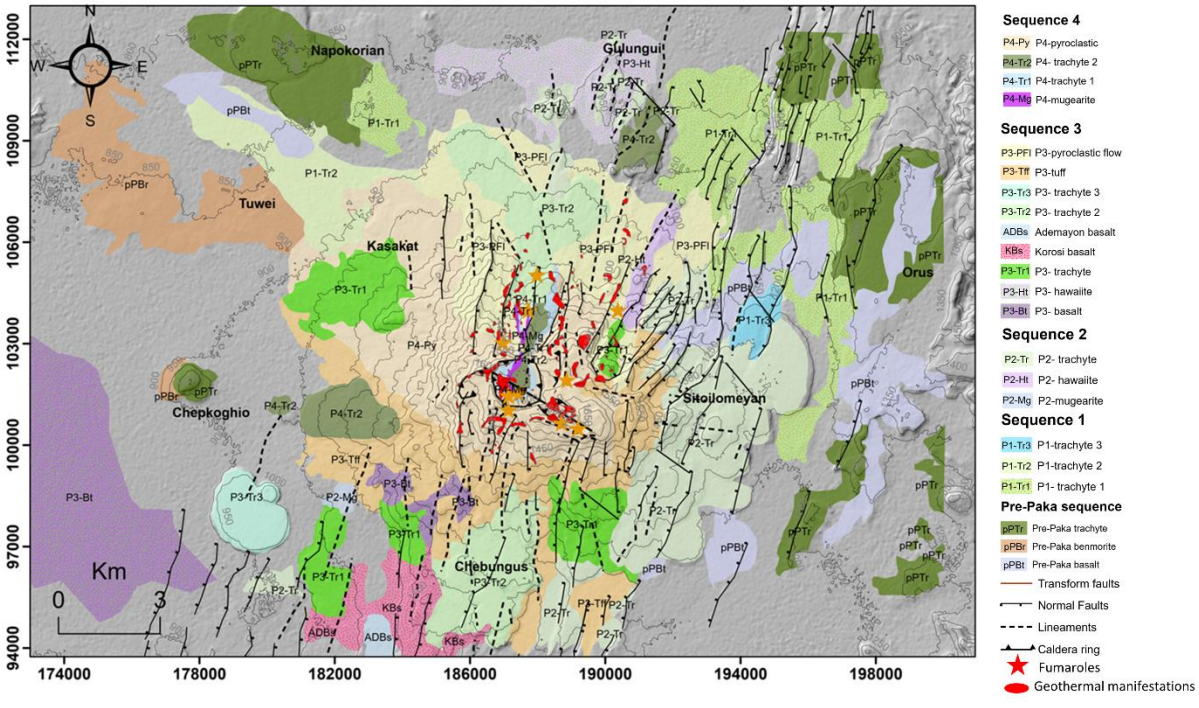

Fig. 2*: Geological map of Paka showing surface lithology, tectonic structures and geothermal manifestations in the area (Mibei et al 2021a).*

2.1 Geothermal manifestations

The term 'Paka' comes from the language of a local tribe and refers to the white clay associated with the surface kaolinite alteration. Surface geothermal features in Paka include fumaroles, paleo hotsprings, altered hot grounds, steaming grounds, sulphur deposits, high CO_2 gas concentration, and Holocene eruption centres (Fig. 3). The manifestations are widespread in the summit area and towards the north but limited southwards, possibly masked by tuff deposits from volcanic sequence 3 (P3-tuff). Fumarole temperatures measured from 2011 to 2014 range between 73.4 and 95.3 °C (Table S1). The hottest fumaroles (> 95 °C) are PF-3 and PF-9 (Fumarole 3 and 9, Fig. 3) located in the north and northeast of the main caldera, respectively. Fumarole PF-2 (Fumarole 2) has the lowest temperature (~73° C) and is within the summit area south of the caldera. The spatial variation in surface temperature remains unexplored but could be related to structural controls.

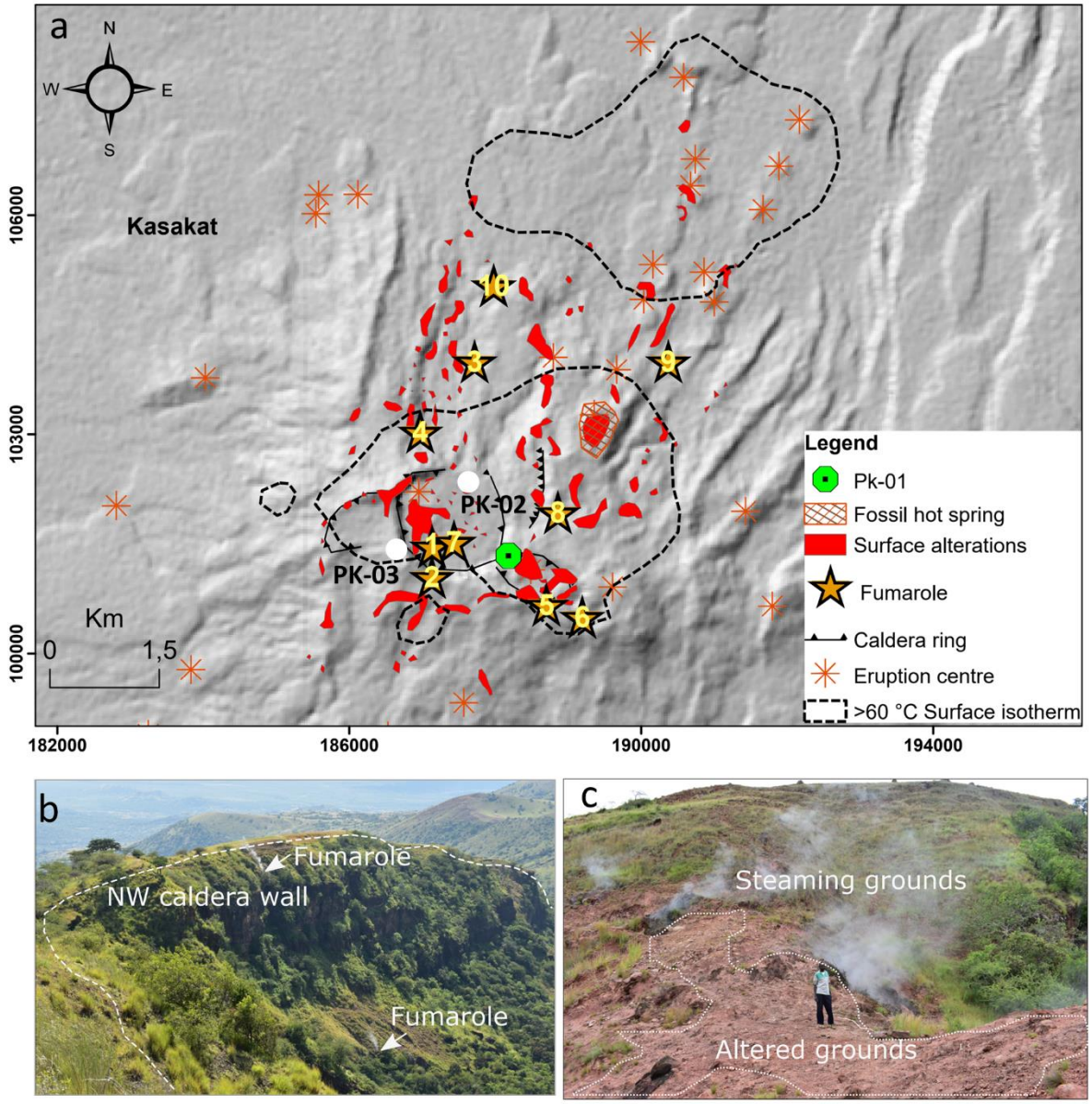

Fig. 3: a) Surface geothermal manifestations in Paka and the location of wells PK-01, PK-02 and PK-03. b) Fumaroles (numbered 1-10) on the northwest caldera wall structure. c) Steaming and altered grounds east of the main caldera

Surface temperature measurements taken at 1 m depth show that Paka has high conductive heat loss (Mwawasi, 2012) within the anomalously high-temperature area outlined by the >60 °C temperature isotherm (black dashed line in Fig. 3). The temperature anomaly and orientation of eruptions centre within the summit area and to the northeast of the caldera confirms the dominating NNE structural trend of the geothermal system, and likely reflect the tectonic control and dyke propagation from the main magmatic system. The most recent eruption centre is a Holocene crater close to fumarole 1 or PF-01 (Fig. 3) west of the main caldera floor with conspicuous surface alteration. A paleo hot spring is inferred from massive silica sinter deposits to the northeast of the caldera indicating past out-flow. An additional

indication for magmatic-hydrothermal activity in Paka are inflation-deflation cycles in the NE, E and SE of the caldera at source depths of 2 and 5 km. (Biggs et al., 2009; Biggs et al., 2016). The existence of a shallow magma reservoir is in accordance with petrological depth estimates of 3.7 to 5 km (Mibei et al., 2021b).

3.0 Literature and data review

Any geoscientific evaluation of a geothermal system requires a multi-disciplinary approach. In the case of Paka, geothermal exploration studies include geological (mapping of manifestations, structures, rock formations), geochemical (soil gas concentration, fumarole gas and steam condensate chemical and isotopic compositions) and geophysical surveys (1m temperature surveys, gravity, MT and TEM resistivity) (Kipngok & Nyamongo, 2013; Lichoro et al., 2017; Mwawasi, 2012). In this study, these surface data are integrated with detailed analyses of subsurface borehole data of well PK-01 and available data on well PK-02 and PK-03 as reported by GDC (2020), Lopeyok (2019) and Ochieng (2019) to further characterise the surface and subsurface of the Paka geothermal system.

3.1 Soil gas survey

Carbon dioxide (CO_2) constitutes one of the main gases discharging from hydrothermal systems. High CO_2 gas concentration at the surface indicates a degassing hydrothermal system associated with a magmatic heat source. The venting of the CO_2 gas can therefore be used to map the spatial extent of a hydrothermal system and its pathways, i.e., vents and faults (Hutchison et al., 2015). The soil gas concentration (CO_2) in the Paka area (Table. S2) was measured at 0.7 m below the surface using an Orsat analyser (Lagat et al., 2013; Opondo, 2010). The geometry and extent of the magmatic-hydrothermal source within the area can be inferred from the distribution of fumaroles, surface alteration and anomalous CO_2 gas concentration (>2%). Fumaroles 8 and 9 (PF-08 and PF-09) associated with NNE trending faults recorded CO_2 gas concentration values between 2-5 % (Fig. 4a). The eastern caldera wall has the highest CO_2 concentration values at 5-30 %, comparable to anomalous values found in the nearby Silali volcano (Lagat et al., 2013). No CO_2 anomaly is evident south and southwest of caldera (Fig. 4a). This is probably due to masking by tuff (P3-tff) also inferred by the lack of geothermal manifestations. The inflation and deflation site in the eastern caldera is particularly correlated to prominent CO_2 concentration anomalies. The deformation events and high CO_2 concentration are associated with changes in crustal stresses due to magma injection episodes and/or degassing hydrothermal fluids (e.g.,Biggs et al., 2016; Hutchison et al., 2016).

3.2 Fumarole chemistry

The main non-condensable gases in the Paka fumarole steam are CO_2 and H_2S (Kipngok & Nyamongo, 2013). Fumaroles located in the northern part of the caldera have higher CO_2/H_2S ratios than in the summit area (Fig. 4b). The spatial variation in CO_2/H_2S ratios can be explained by the hypothesis that efficient H_2S removal occurs in the water column because of slower diffusive rates associated with the outflow zone, but less efficient H_2S removal within the relatively rapidly rising bubbling gas and steam in the upflow (Rouwet et al., 2020) . It is therefore possible that the northern and eastern caldera fumaroles are away from the main up-flow zone located within the caldera summit area. Elevated helium isotopes ratios have been reported in fumarole PF-01 ($7.9R_A$) and PF-04 ($6.2R_A$) and lower

ratios(3.2 R_A) at PF-06 (Darling et al., 1995) suggesting SCLM source for values > 6R_A and crustal source <6 R_A.
The variation of δ^2H and $\delta^{18}O$ isotopic values (Fig. 4c) of the fumarole condensate (Mulusa, 2015), on the other hand, suggest that fluids are steam-heated groundwater. The projected mean reservoir temperatures derived from fumarole gas compositions are: T_{CO2} = 320 °C, T_{H2S} = 252 °C, T_{H2} = 267 °C and $T_{CO2/H2}$ = 251 °C, based on Arnórsson and Gunnlaugsson (1985). These values suggest a geothermal reservoir temperature range of ~250-320 °C.

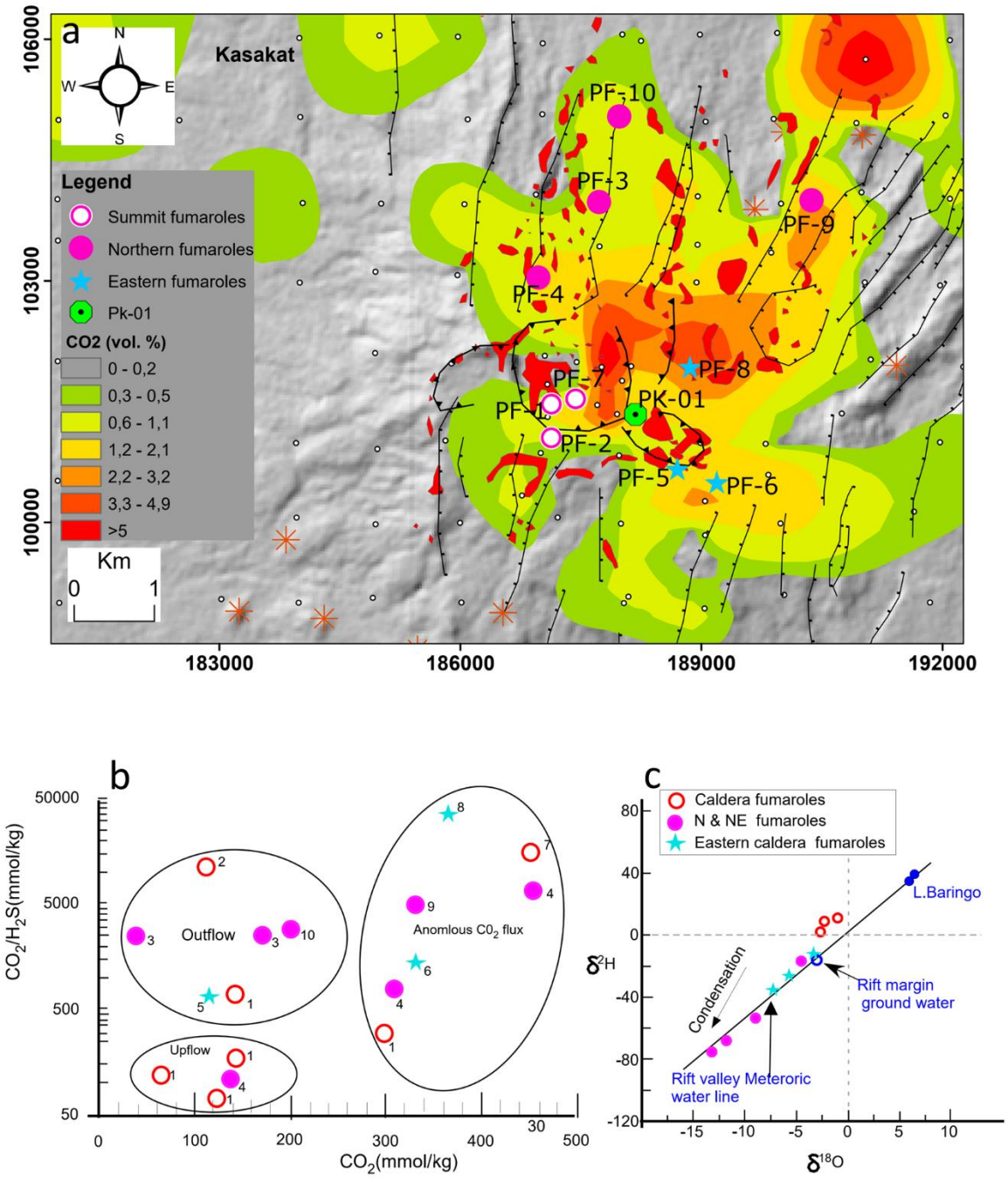

Fig. 4: a) Location of Paka fumaroles and relative intensity of CO_2 gas concentration in volume %. b) CO_2 versus CO_2/H_2S variation plot suggesting up-flow and out-flow areas c) δ^2H versus $\delta^{18}O$ isotopic variation indicating condensation towards the out-flow areas (modified from Mulusa, 2015). The stars, purple filled circles and the red open circles represent classification of fumaroles. The numbers are fumarole labels as in the text. In the CO_2 values comma is used as decimal separator.

3.3 Resistivity

Because of their proven effectivity in delineating subsurface changes in interface conductance and pore fluid conductance, linked indirectly to reservoir temperature, magnetotelluric (MT) and Transient Electromagnetic (TEM) resistivity surveys (e.g., Thanassoulas, 1991; Arnason & Flovenz, 1992; Arnason et al., 2000; Ussher et al., 2000; Uchida & Sasaki, 2006; Cumming & Mackie, 2010; Stimac et al., 2015;) have been conducted in the Paka geothermal field since 2010 to constrain and outline the depth of the geothermal system (Lichoro, 2017; Lichoro et al., 2019). A resistivity map at sea level (~1600 m depth) shows a ~20 km^2 >30 Ωm NNE-trending anomaly (yellow line in Fig. 5a). This is the estimated areal extent of the Paka geothermal resource.

The NE-SW resistivity cross-section (Fig. 5c) shows a ~200 m thick near-surface high-resistivity zone attributed to unaltered lavas underlain by a discontinuous (heterogenous) conductive layer (<30 Ωm) at 200-600 m and 200-1200 m depth in the SW and NE areas, respectively. This conductive layer, forming the cap of the geothermal reservoir, is thinner and discontinuous in the summit area, suggesting an up-flow zone and thicker to the NE possibly depicting the out-flow zone. According to Árnason et al. (2010), the base of the conductive layer coincides with the 230 °C isotherm in Icelandic geothermal systems, hence marking the top of an economically viable reservoir zone. Below the conductive layer is the relatively resistive zone (>30 Ωm), interpreted to be the high-temperature reservoir zone, intercalated by very resistive bodies (>100 Ωm) at the base, possibly syenite intrusions in the form of sills and dikes.

3.4 Gravity

A residual gravity anomaly map (Lichoro et al., 2019) reveals a 10 km long NNE trending high-gravity anomaly (Fig. 5c), concordant with the resistivity anomaly (Fig. 5a) but slightly offset to the west. Low gravity on both sides of this anomaly and extending into the caldera from the east is inferred to be caused by volcanic sediments (Fig. 5c). The NNE trending gravity high is thought to be generated by dense rocks along the main volcanic axis and dike feeders controlling magmatism and emplacement of intrusive rocks (Lichoro et al., 2019). The relatively low gravity below the Paka caldera, on the other hand, is interpreted as hydrothermally altered rock and less dense felsic intrusive magmatic bodies (Lichoro et al., 2019).

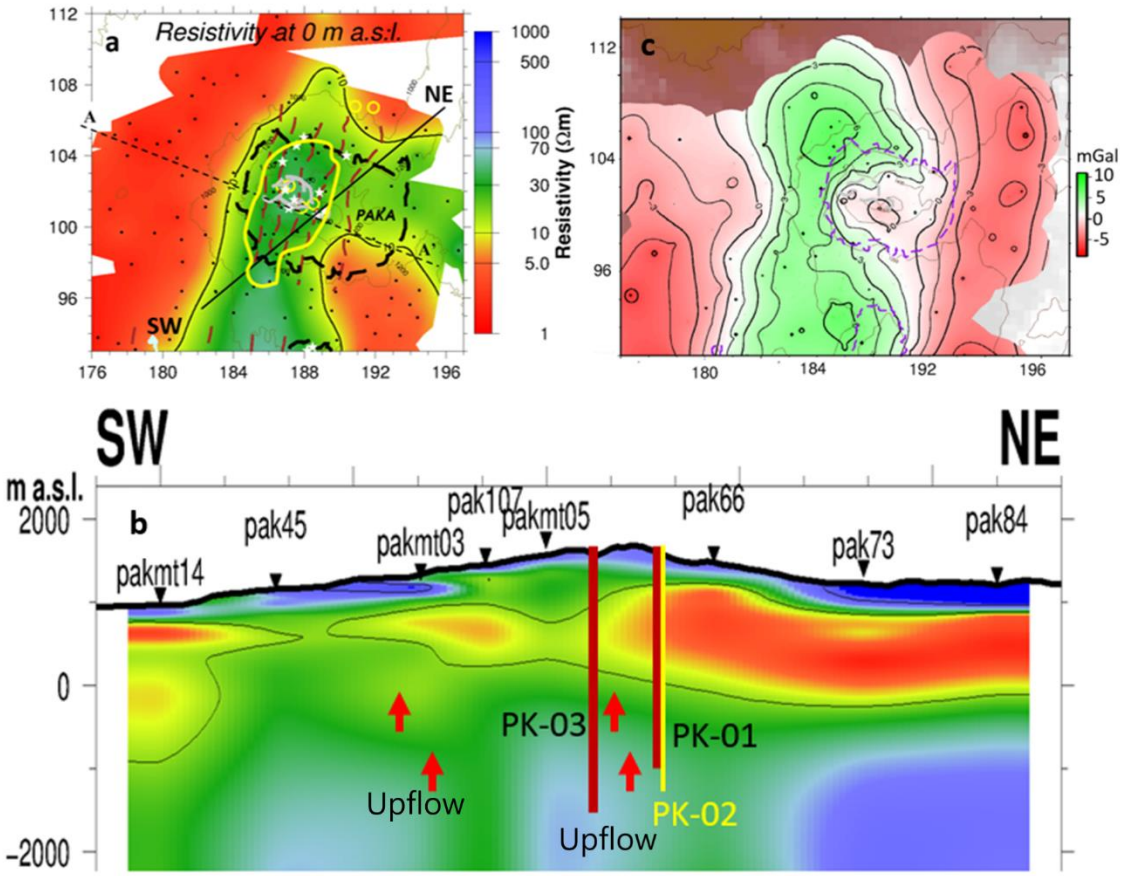

Fig. 5: a) The resistivity section at sea-level, the yellow line is 30 Ω. m area assumed to enclose the reservoir extent. The conductive zone in red are possible sediments (Lichoro, 2017; Lichoro et al., 2017, 2019). The white stars denote fumaroles and the yellow circles are eruption centres. b) Resistivity cross-section with inset drilled wells (PK-01, PK-02 and PK-03) (see text), showing a discontinuous shallow conductive clay cap (thin at the up-flow) and a relatively resistive reservoir (30 Ωm) intersected by very resistive bodies (100 Ωm), inferred to be solidified intrusions (Lichoro unpublished, data). c) The high gravity (10 mGal) indicated volcanic axis while low gravity enclosing the Paka caldera is due to hydrothermal alterations, the low gravity on western flanks could be sediments as also indicated by their conductivity nature (Lichoro et al., 2019)

3.5 Paka exploration well PK-01

PK-01 was spudded on 30th December 2018 and drilled to a total depth of 2552 m from the cellar top (CT) at an elevation of 1619.84 m a.s.l (Fig. S1). Water and mud sweeps were used to drill down to 340 m, after which aerated water and foam were used to the bottom of the well. The 8 1/2" production section of the well was drilled from 704 to 2552 m CT and a 7" slotted liner installed.

Pressure (Fig. S2) and temperature logs during completion tests in the well (Fig. 6a) suggest a maximum measured temperature of 245 °C, with the main feed zones inferred at 780 m, 1050-1150 m, 1450-1500 m, 1800 m and minor ones at 2300 and 2450 m. Based on pressure

log measurements under shut conditions, the water table located at 800 m (GDC, 2020). Resistivity measurements, from a station within the well pad prior to drilling, suggest resistivity of ~100 Ωm between 0-200 m, 5-30 Ωm at 200-800 m depth, >30 Ωm below 800-1300 m and >100 Ωm below 1300 m depth. Fluid discharge data obtained by GDC from well PK-01 between September and December 2019 (Ochieng, 2019) indicate that the well discharges at mass flow rate of 66 t/hr. The discharge fluids are $NaHCO_3$-type with a pH between 9.4 and 10.1 and liquid-dominated with an estimated enthalpy of 1100 kJ/kg (Table S6). The total dissolved solids (TDS) range between 3870-4680 mg/kg. The SiO_2 content ranges between 576-911 mg/kg, while the Cl content is between 706-1139 mg/kg. The CO_2 gas is about 1.6 wt. % of the total non-condensable gases. It is inferred that the temperature of the reservoir fluids entering the well varies from 250 °C to 275 °C based on silica solubility (Fournier & Potter, 1982; Giggenbach et al., 1994) using the SiO_2 content of 576-680mg/kg. These temperatures fall within the range predicted by fumarole gas geothermometry and are slightly higher than the maximum measured temperature of 245 °C. For comparison, PK-02 shows a maximum measured temperature of 260 °C between 1100-1600 m and a temperature reversal at the bottom of the well (Fig. 6b). PK-03 has a maximum of 271 °C between 1600-2100 m, below which a temperature reversal is observed.

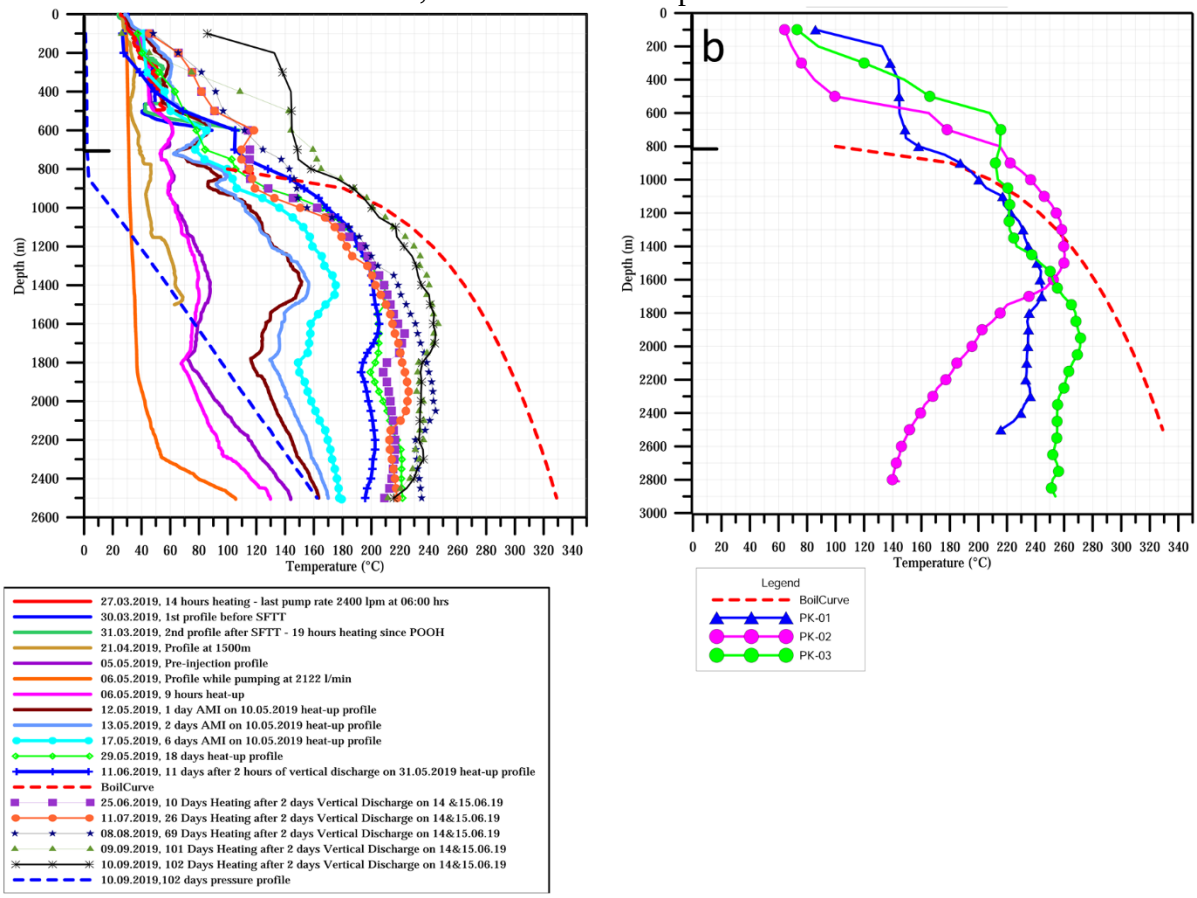

Fig. 6. a) Several measured temperature profiles from PK-01. b) Stabilised measured temperature profiles in wells PK-01, PK-02 and PK-03. The boiling point curve is set at the well water table at 800 m depth (GDC, 2020).

3.5.1 Stratigraphy of well PK-01

The whole rock chemistry of surface and subsurface rock samples from Paka has previously been discussed in detail by Mibei et al. (2021a). In that study, the PK-01 stratigraphy is divided into four volcanic phases, i.e., the Pre-Paka, Phase 1, Phase 2 and Phase 3 volcanic sequences. Volcanic phase 4 was not intersected in the well due to its location away from the post-caldera formation (Phase 4). The strata belonging to the Paka central volcano extends from the surface to 1050 m and include Phase 3 lava (0-428 m), Phase 2 lava (428-720 m) and Phase 1 lava (720-1050 m) cross-cut by a minor syenite intrusion. Pre-Paka lavas from 1050-2552 m depth are of basic-silicic compositions with syenite intrusions prevalent below 1800 m depth.

The analysed borehole samples fall into the hawaiite, mugearite, benmoreite and trachyte fields in the Total Alkali-Silica (TAS) diagram (Fig. 7a). Disparities between the chemical compositions of borehole and surface samples (shaded field in Fig. 7a) are attributed to hydrothermal alteration affecting mobile elements to varying degrees depending on the rock type. Thus, the chemical plots indicate Al, Ti, and Sr enrichment in basaltic and intermediate rocks but depletion in Ca and Mg (Figs. 7a to m). In contrast, most elements in trachyte appear to be immobile during hydrothermal alteration except for depletion in Na, Sr and V.

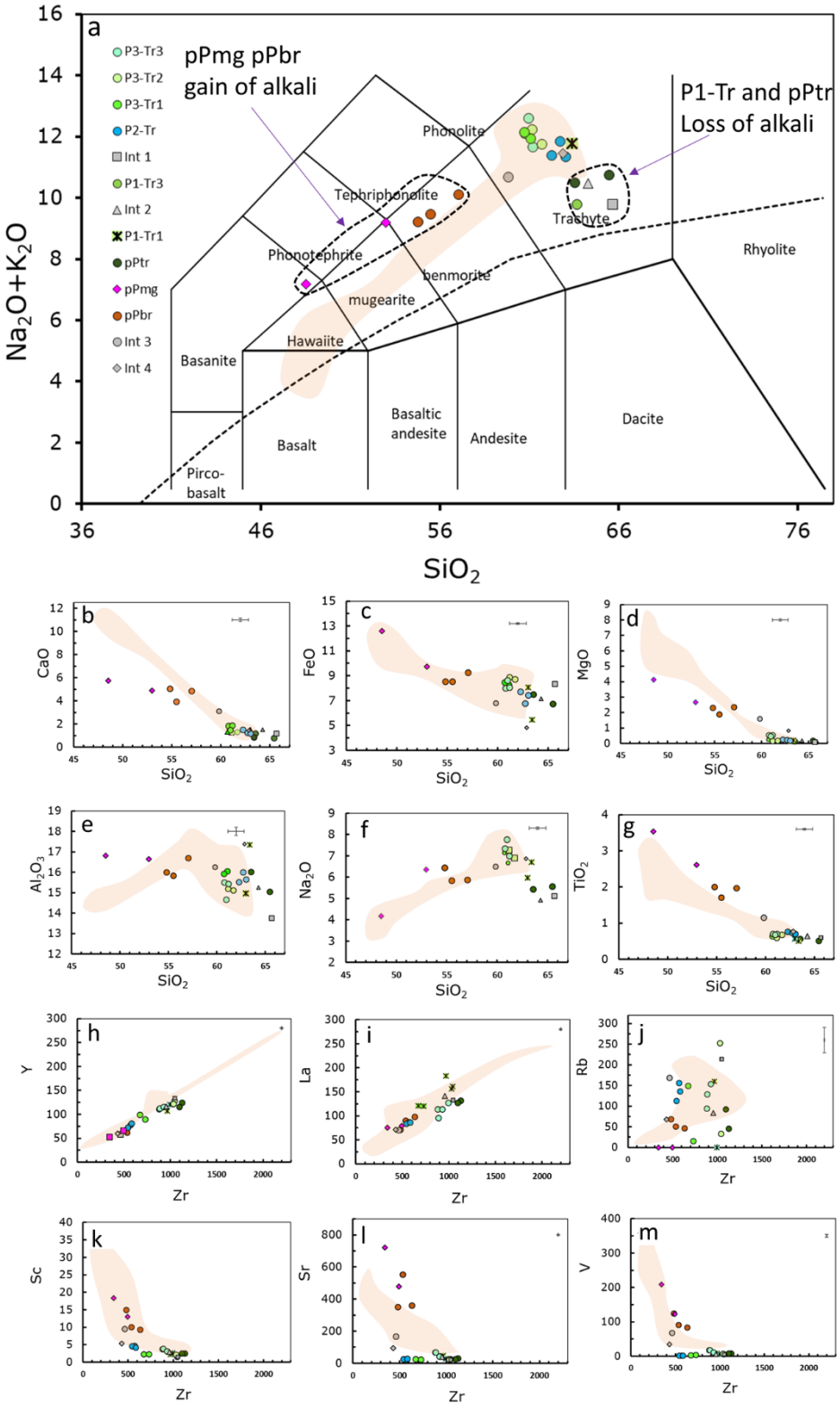

*Fig. 7: a) Borehole samples plotted on a Total Alkali-Silica diagram compared to surface samples (Shaded). *pre-paka mugearite (pPmg), pre -paka benmoreite (pPbr), pre-paka trachyte (pPtr) and Phase 1 trachyte(P1-Tr) b) CaO versus SiO_2 c) FeO versus SiO_2 d) MgO versus SiO_2 e) Al_2O_3 versus SiO_2 f) Na_2O versus SiO_2 g)TiO_2 versus SiO_2 h) Y versus Zr i) La versus Zr j) Rb versus Zr k) Sc versus Zr l) Sr versus Zr m) V versus Zr.*

4.0 Results

4.1 Hydrothermal alteration

Alteration minerals are classified according to deposition and occurrence (Table 1). They include depositions in open space (vesicles/veins) or as alteration products of primary rock constituents, as shown in photomicrographs under transmitted light (Figs. 8a-c) and back-scattered electron images (Figs. 8d-f). The occurrence and abundance of hydrothermal alteration in comparison with loss on ignition (LOI), resistivity and depth are illustrated in Fig. 9. We find that increased degree of alteration with depth correlates with higher values of LOI. The LOI varies from 1-3.7 % with the highest values at ~1300 m and lowest above 380 m. Between 1500-2260 m the LOI is slightly lower or between 2.1-2.7% and may be explained by less water in the higher temperature alteration minerals.

Table 1: Classification of hydrothermal alteration mineralogy in well PK-01

Alteration minerals	Vesicles	Veins and vugs	Interstitial glass	Primary mineral alteration
Smectite	X			
Mordenite	X			
Illite	X	X	X	X
Chorite	X			
Calcite	X	X	X	X
Quartz	X	X		
Chalcedony	X	X		
Albite				X
Epidote	X	X		
Actinolite	X			X
Chalcopyrite	X	X	X	
Pyrite	X	X	X	
Apatite				X

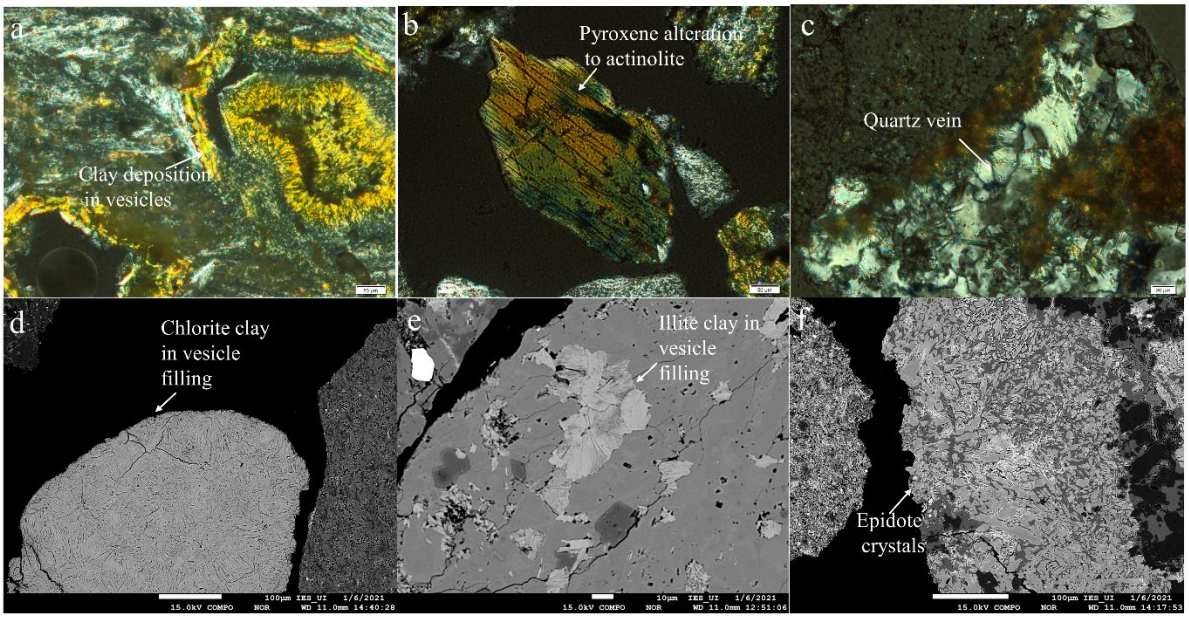

Fig. 8. Photomicrographs under transmitted polarised light of a) Coarse-grained light-yellow clay alteration at 1002-1004 m deposited in a vesicle or as mineral replacement b) pyroxene partially altered to actinolite at high temperature zone at 2400-2402 m and c) Vein deposition of quartz at 678-680 m. Back-scattered electron images of d) Chlorite vesicle deposition at 1178-11780m. e) Illite at 2252-2254 m. f) Epidote at 2252-2254m.

The main alteration minerals identified in PK-01 well cuttings include clays/phyllosilicates (smectite, chlorite, mixed clay and illite,), calc-silicates (epidote, mordenite, albite, actinolite), silica polymorphs (quartz, chalcedony) and non-silicates (pyrite, chalcopyrite, calcite) (Fig. 9). Kaolinite occurs as surface alteration. At shallow levels (0-700 m), low to medium degree alteration is observed where a smectite-mordenite-calcite-pyrite-oxides-chalcedony phase assemblage can be distinguished with abundant pyrite between 500-600 m. The intensity of alteration increases below the water table (800 m) where the primary textures of the rocks are almost completely obscured, with feldspars altered to albite and the occurrence of illite and chlorite. Due to major circulation losses below 1400 m depth, drill cuttings are scarce from that interval and thus less petrological information is available. However, in four of the six narrow sample intervals below 1600 m, the proportion of both fresh and altered syenite intrusions increases (Fig. 9). The alteration mineral assemblage here includes chlorite-epidote-actinolite with pyrite and chalcopyrite. The first appearance of actinolite was logged below 1400 m. There is an unusual presence of smectite in the high-temperature depth zone between 2200-2400 m. Based on the distribution of key temperature-dependent minerals, three main hydrothermal alteration zones were identified in the well, including mordenite-smectite, chlorite-illite and actinolite-epidote at 0-700 m, 700-1450 m and 1450-2550 m, respectively. Their deposition characteristics have been divided into the four different types described below.

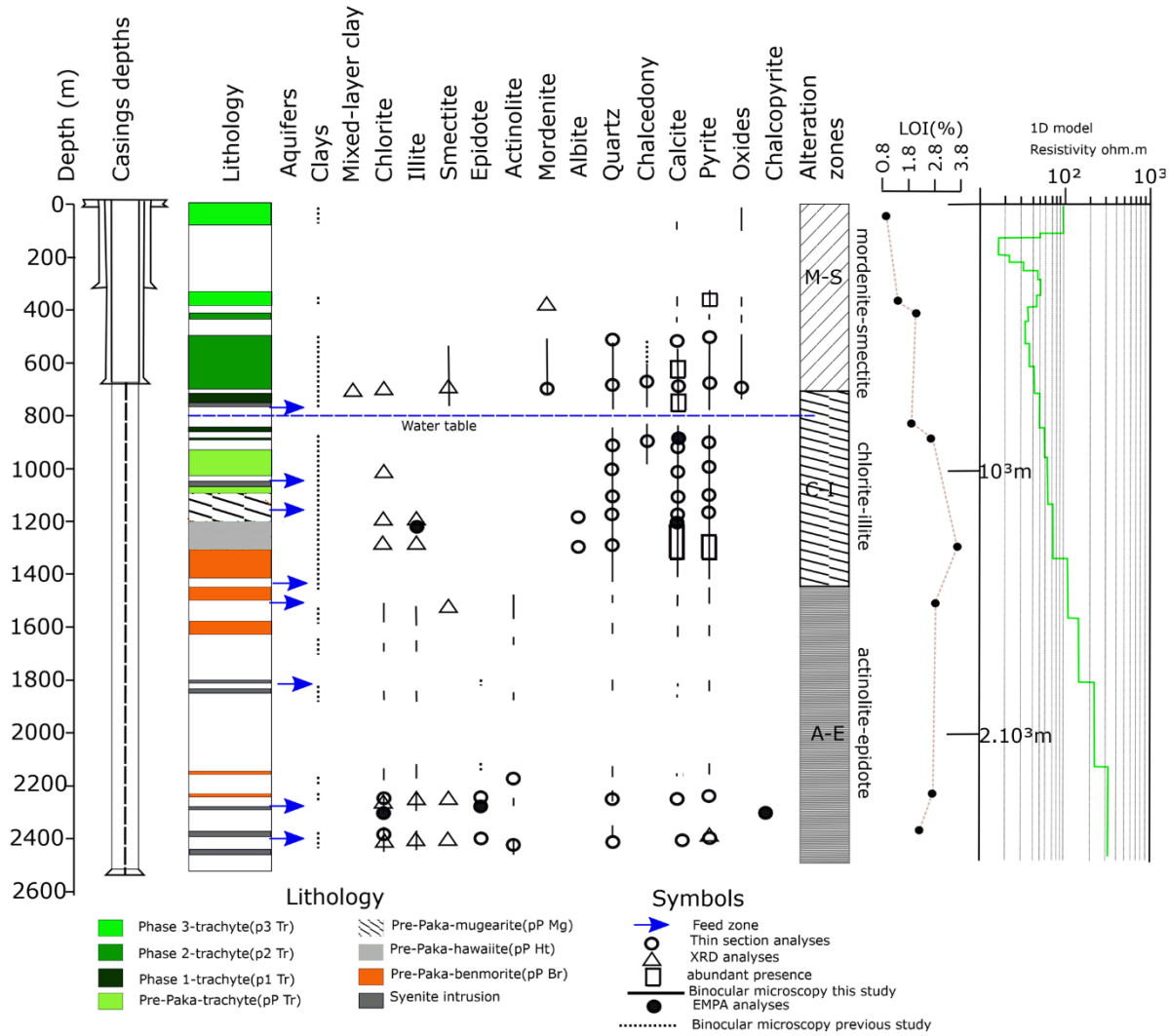

Fig. 9: Raman spectroscopic results from samples at 1388-1390 m and 2552-2554 m a) The characteristic Raman shift of calcite at 1085 cm^{-1}. b) The CO_2 spectral peaks at 1285 and 1388 cm^{-1}, the pronounced peak at 1355 cm^{-1} is the host quartz. c) Characteristic spectra of low-salinity aqueous fluid (3100-3700 cm^{-1}) in the liquid phase.

Clay alteration

Clays are alteration products of interstitial glass and primary minerals, as well as open space/vesicle fillings. They vary from fine-grained clays at shallow depths to coarse-grained at greater depths. Under transmitted crossed-polarized light, the colour changes from brownish yellow to bright yellow with increased depths. Clays were observed at more than 600 m depth as fine-grained brownish interstitial glass alteration. Coarse-grained vesicle clay depositions start appearing at 900 m whereas they change to a bright yellow colour at 1100 m under plane polarised light. Illite occurs as highly birefringent and coarse-grained crystal aggregates from 1100 m to the bottom of the well. X-ray diffractometry identifies clay minerals as smectite, illite, mixed-layer clay and chlorite (Table 2). Smectite occurs at shallow depths (above 600 m), while chlorite and illite occur below 600 m and 1100 m, respectively, to the bottom of the well, contemporaneously with quartz, epidote, actinolite and albite (Fig. 9). Mordenite at 380-400 m was identified by its XRD signature and its fibrous nature in thin section.

Table 2: Distribution of XRD results with depth (m).

From	To	Zeolite	Smectite	Illite	Chlorite	LOI (%)
48	50					1.0
380	382					1.4
388	400	X				-
428	430					2.1
650	652				X	-
678	680		X		X	-
840	842					1.9
908	910					2.7
1002	1004			X	X	-
1178	1180			X	X	-
1280	1282			X	X	-
1318	1320					3.7
1520	1522		X	X	X	2.8
2252	2254		X	X	X	2.7
2400	2402		X	X	X	2.1

Open space depositions

Direct deposition in vesicles and veins of hydrothermal alteration minerals is an important form of alteration in the Paka hydrothermal system. At shallow depths open space deposition occurs as fine-grained clays (smectites and chlorite), calcite, quartz, chalcedony, epidote and actinolite. At greater depths, the highly birefringent, coarse-grained, high-temperature clays (illite) tend to fill open spaces. Platy calcite occurs in open vugs at 904-910 m, 1066-1112 m and 1204-1210 m, while calcite veins were ubiquitous at 1810-1818 m and 2248-2260 m. The calcite size varies from 25-200 µm. Pyrite and chalcopyrite are also seen as open space deposition. Relatively large (100-200 µm) pyrite crystals were observed throughout the borehole, but are abundant at between 200-400 m and 1200-1400 m. Chalcopyrite also occurs as open space deposition at 2252-2254 m, confirmed by EMPA analyses (Table S4).

Quartz and chalcedony occur as open space mineralization in the form of vein and vesicle deposition. Quartz occurs contemporaneously with chalcedony from 400 m depth, but at 1000 m depth chalcedony disappears. Quartz varies in size from 5000 µm to 50 µm. At > 1400 m depth, actinolite is deposited as vesicle fillings.

Interstitial glass alteration

Glass is highly susceptible to alteration and begins altering at 500 m and perhaps shallower. At relatively shallow depths (<800 m) the glass is altered to fine-grained clays (smectite) and oxides (haematite and leucoxene). The fine-grained clays change to coarse-grained clays ± calcite at greater depths.

Primary mineral replacement

Petrographic observations show that primary minerals remain relatively fresh until 600 m depth. Below 600 m depth primary feldspars and pyroxene are progressively altered to clays (illite, chlorite) and calcite. At 1250 m depth albitization of plagioclase is evident and with increasing depth the feldspars are further altered to chlorite + illite ± albite ± calcite. Haematite and goethite tend to form at shallow depths, above 800 m (water table). At greater depths (~1800 m) within the intrusive syenite, clinopyroxene is altered to actinolite.

4.2 Fluid inclusions

Fluid inclusions can help establish past geothermal reservoir physiochemical conditions at the time when the fluid was trapped in a mineral grain (Roedder, 1984; Simmons & Browne, 1997). This information is obtained through microthermometry and Raman spectroscopy. From fluid inclusions of carefully selected hydrothermal alteration minerals, one can measure the homogenization (T_h) and ice-melting temperatures (T_m), representing hydrothermal fluid temperatures and salinity, respectively (Franzson et al., 2002). Raman spectroscopy determines the chemistry of trapped liquid, solid and gas phases in fluid inclusions, and hence provides direct information about hydrothermal fluid chemistry. Quartz and calcite crystals at 1390 and 2550 m depths were selected for fluid inclusion (FI) analyses. The fluid inclusions included primary inclusions in growth zones and secondary inclusions along healed fractures (Fig. S3), characterised by liquid and vapour phases with the occasional presence of a solid phase (Fig. 10). The < 2 µm cubic-like solid phases are calcite based on high birefringence observed under petrographic microscope and the characteristic Raman spectral vibrational peaks at 1085 and 1435 cm^{-1}. Theas peaks are consistent with vibrations $\upsilon 1$ and $\upsilon 3$ of calcite, and thus could be distinguished from aragonite as the υ_2 at 854 cm^{-1} was absent (Frezzotti et al., 2012). Fluid inclusion homogenization (T_h) and melting (T_m) temperatures are summarised in Table 3. A total of 124 fluid inclusions were analysed of which forty-five (45) were from 1390 m, and of these, 12 are hosted by calcite. From 2550 m, 79 fluid inclusions were measured including 26 in calcite. The fluid inclusion sizes ranged from 10-40 µm. All fluid inclusions homogenised to the liquid phase ($LV \rightarrow L$), but at that T_h the solid phases did not dissolve.

Table 3: Fluid inclusion microthermometry results.

1390 m depth				2550 m depth			
Mineral host	Fluid inclusion type	Th range(°C)	Tm_ice range(°C)	Mineral host	Fluid inclusion type	Th range(°C)	Tm_ice range(°C)
Quartz	LV	211(1)	0/-0.1	Quartz	LV	219(1)	
	LV	223(1)			LV	224(1)	
	LV	228(6)			LV	230(2)	
	LV	230(3)			LV	236(1)	
	LV	237(2)			LV	221(1)	
	LV	243(8)	0/-0.1		LV	229(1)	
	LV	245(1)	0/-0.1		LV	219(1)	
	LV	249(4)			LV	227(1)	
	LV	251(2)			LV	224(3)	0/-0.1
	LV	257(1)			LV	226(1)	
	LV	262(3)			LV	224(2)	0/-0.1
	LV	267(1)	0/-0.1		LV	225(2)	
					LV	200(1)	
					LV	217(1)	
					LV	210(3)	
					LV	215(3)	0/-0.1
					LV	232(1)	
					LV	239(1)	
					LV	245(1)	
					LV	250(3)	
					LV	252(2)	
					LV	255(1)	
					LV	260(3)	
					LV	263(1)	
					LV	265(1)	
					LV	271(3)	
					LV	260(1)	
Calcite	LV	264(1)		Calcite	LV	209(1)	
	LV	272(1)			LV	220(1)	
	LV	278(2)			LV	233(2)	
	LV	262(1)			LV	237(1)	
	LV	268(1)			LV	252(2)	
	LV	270(2)			LV	223(2)	
	LV	273(1)			LV	233(5)	
	LV	274(1)			LV	246(2)	
	LV	276(1)			LV	264(2)	
	LV	286(1)			LV	236(3)	
					LV	250(5)	

Samples from 1390 m show decoupled correlation in T_h from quartz- and calcite-hosted FIs. Fluid inclusion T_h in calcite varies from 262 °C to 286 °C (n=12) with a mean of 271 °C. T_h of inclusions in quartz varies from 211°C to 267°C (n=33) clustering bimodally at 230 and ~240 °C. At 2550 m. Cacite T_h ranges from 209 °C to 264 °C (n=26), clustering bimodally at 230 °C and 250 °C, while quartz T_h ranges from 200 °C to 271 °C (n=56), bimodally clustering at 225 °C and 255 °C. The ice-melting temperatures (T_m) range between 0 to -0.1°C.

Raman spectroscopy is a vibrational spectroscopy method which provides detailed information about chemical structure, phase and polymorphy, crystallinity and molecular interactions. Molecular vibrations related to covalent bonds give a characteristic spectrum for each phase present (Bodnar & Frezzotti, 2020; Frezzotti et al., 2012). Raman spectroscopic analysis was carried out on four quartz-hosted fluid inclusions from 1390 m and three from the 2550 m. The solid phase in the fluid inclusion was determined to be calcite (Fig. 10a). The vapour phase showed characteristic peaks at 1285 and 1388 cm^{-1} (Fig. 10b) indicating CO_2 presence. The liquid phase, on the other hand, had a broad humped band between 3100-3700 cm^{-1} (Fig. 10c) suggesting low-salinity fluid. Solid, liquid and gas phases have similar characteristics at both depths.

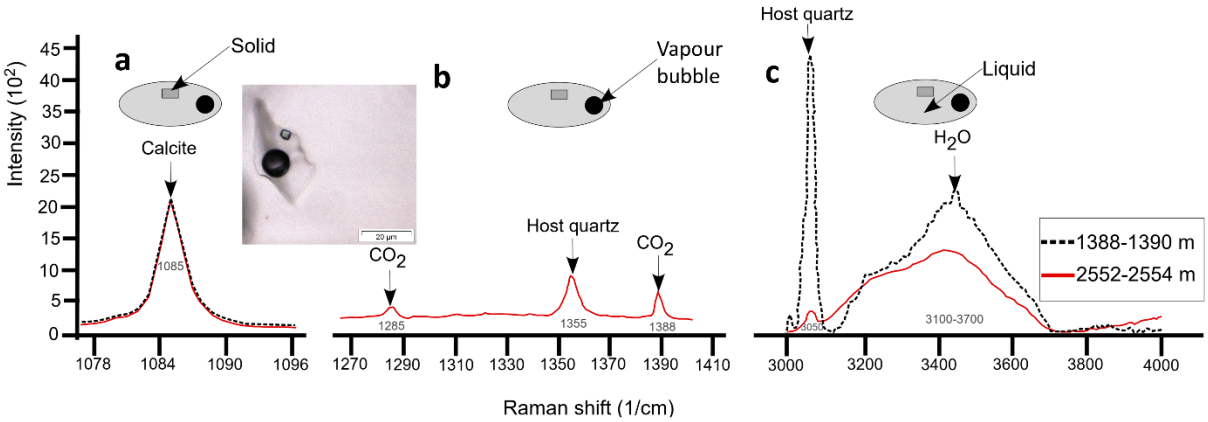

Fig.10: Distribution of hydrothermal alteration minerals and zones in relation to rock type and depths in well PK-01 including loss on ignition (LOI %) and 1D resistivity model.

4.3 Epidote, pyrite and chlorite mineral chemistry

EMPA analyses were carried out to examine the chemical variability of pyrite, epidote and chlorite at three different depth ranges, i.e., 910, 1180 and 2254 m (Tables S3-S5). The results show that iron sulphide at 910 m and 1180 m depths is stoichiometrically pyrite with sulphur of 51.4 to 54.3 wt.% and Fe content of 44.9-45.9 wt.% with variably low values (<0.03wt.%) of Co, Ni and Cu. At a deeper level (2254 m) iron sulphides become sulphur deficient with 37.8-38.5 wt.% S and 58.4-58.8 wt.% Fe consistent with a composition formula Fe(1-x)S (pyrrhotite) where x is~ 0.1(Table S3). Chalcopyrite occurs at 2254 m depth with 34.4 wt.% S, 29.2 wt. % Fe and 32.6 wt.% Cu. The Ni concentrations were less than 0.02 wt.%, whereas the Co was 0.002 wt.%. Epidote from 2254 m consists of 36.3-39.5 wt.% SiO_2, 19.7-25 wt.% Al_2O_3, 10.8-17 wt.% FeO and 21.2-23.6 wt.% CaO. The

compositional range of chlorite from 910,1180 and 2254 m is 34.7-38.36 wt.% SiO_2, 25.5-28.8 wt.% FeO, 10.2-15.1 wt.% Al_2O_3 and 6.3-9.8 wt.% MgO.

5.0 Discussion

We compare reservoir temperatures from well PK01 calculated temperatures based on measured temperature profiles, and alterations mineralogy aimed at exploring the evolution of Paka geothermal system. We integrate available surface data to demarcate the resource extent and possible suitable areas for well sites.

5.1 Hydrothermal alteration in PK-01

Henley and Ellis (1983) described hydrothermal alteration as a general term embracing changes in mineralogy, texture and chemistry of rocks. The changes occur due to chemical transport in disequilibrium thermal conditions facilitated by hydrothermal fluids (Franzson et al., 2008). The intensity of the changes not only depends on temperature, but also on the protolith, permeability and time. The use of hydrothermal alteration mineralogy in evaluating reservoir parameters (e.g.,Reyes, 2000) is very valuable in geothermal conceptual modelling and in assessing reservoir temporal changes within various geothermal reservoirs, e.g., in Iceland (Franzson et al., 2005; Franzson et al., 2002; Fridleifsson, 1991; Marks et al., 2010), the Philippines (Reyes, 2000) and the East African Rift System (Browne, 1978; Lagat et al., 2004).

The onset of hydrothermal alteration in well PK-01 is marked by depletion of Na, Sr and V in trachyte. Basalt and intermediate rocks, on the other hand, are enriched in Al, Ti, Sr and depleted in Ca and Mg. These chemical changes are especially discernible in the deeper rock strata within reservoir depths where trachyte and basalt of Phase 1 and the Pre-Paka trachyte sequence (Section 3.5.1) occur. EMPA analyses have also shown that iron sulphide minerals are mainly pyrite with minor pyrrhotite and chalcopyrite at depth. The presence of pyrite indicates environment of sufficient sulphur while pyrite may indicate rapid cooling and high sulphur fugacity.

Studies have shown that, even though the protolith has an effect on the hydrothermal alteration, temperature, permeability and fluid chemistry appear to have the most significant effects (e.g.,Browne, 1978; Franzson et al., 2002; Li et al., 2011; Reyes, 2000). This, therefore, means that hydrothermal alteration can provide important information regarding reservoir temperatures, permeability and fluid chemistry of a system (e.g., Franzson et al., 2005), and becomes even more useful when data from several wells and the surface can be integrated progressively developing a 3D conceptual model (Browne, 1970).

5.2 Insights into Paka reservoir conditions

Surface exploration data, including resistivity, soil gas surveys and geothermometric calculations from fumaroles and thermal springs, are important data for the initial assessment of reservoir temperatures (Arnórsson, 1985; Arnórsson et al., 1983; Cumming, 2016; Fournier & Potter, 1982; Fournier, 1977; Fournier, 1992). However, direct temperature and reservoir condition information is obtained from drilled wells. Integration of all available surface data (e.g., volcanic history, tectonics, resistivity, gravity and fumarole data) (Kipngok & Nyamongo, 2013; Lichoro et al., 2017; Mibei et al., 2021a) and well data (hydrothermal alteration, measured temperature profiles and well discharge) from well PK-01 is applied here to obtain temperature information about the Paka geothermal reservoir conditions. Gas geothermometry indicate subsurface temperatures of 250-320°C. Quartz and Na/K geothermometers on the other hand indicate 226-296°C (Kipngok & Nyamongo, 2013)

(Table 4), the lower value of 226 °C was obtained from the Na/K geothermometer probably indicating its slow response to secondary processes (Giggenbach, 1988). When gas geothermometers (Table 4) are compared, the CO_2 gas geothermometer indicate higher average reservoir temperatures (320 °C), probably recording deeper magmatic temperatures or higher concentration of CO_2 from active shallow magma bodies (3.7-5 km) beneath Paka (Biggs & Annen, 2019; Biggs et al., 2016; Mibei et al., 2021b). The silica temperature of stabilized discharge from PK-01 based on quartz solubility varies from 250-275 °C (section 3.5) and hence within the range of surface fumarolic estimates.

Table 4: Reservoir temperature from gas and solute geothermometers, mineral thermometers and measured temperatures.

Fumarole Gas Geothermometers(Kipngok & Nyamongo, 2013)					
Fumarole No.	$T_{CO2(a)}$	T_{H2S}	$T_{CO2/H2}$	T_{H2-CO2}	Average
PK-1	320 °C	218 °C	300 °C	347 °C	296
PK-2	391 °C	220 °C	-	-	306
PK-3	277 °C	-	267 °C	229 °C	258
PK-4	276 °C	-	293 °C	278 °C	282
PK-5	-	233 °C	-	-	233
PK-6	353 °C	-	282 °C	353 °C	329
PK-7	372 °C	223 °C	-	-	298
PK-8	-	233 °C	-	-	233
PK-9	288 °C	-	273 °C	252 °C	271
PK-10	-	251 °C	-	242 °C	247
Mean	*320 °C*	*252 °C*	*267 °C*	*251 °C*	
Fumarole solute Geothermometers(Kipngok & Nyamongo, 2013)			Well discharge solute Geothermometers(Ochieng, 2013)		
	Fournier and Potter equation	Giggenbach equation	Fournier and Potter equation	Giggenbach equation	
Quartz	301± 11 °C	296±9°C	250-275 °C	250-275 °C	
Na/K	226± 26 °C	241±25°C			
Hydrothermal alteration temperatures(This study)					
Depth(m)		alteration minerals	Fluid inclusion		
0-700	smectite-mordenite-quartz	180 °C	quartz	calcite	
700-1450	chlorite-illite	220 °C	211-267 °C@1390	262-286 °C@1390	
1450-2550	epidote-actinolite	250° C	200-271 °C@2550	209-264 °C@2550	
Measured temperature (GDC, 2020)					
Depth(m)					
0-700	130 °C				
700-1450	180 °C				
1450-2550	244 °C				

The formation temperature in well PK-01 (Fig. 11) is extrapolated from the most stabilised measured temperature profile using the Horner method with an error of ±8°C (Peters & Nelson, 2012). The calculated formation temperature in the well increases steadily from 85-170°C between 0-800 m. At 900-1000 m depth, the boiling point curve for pure water intersects the calculated temperature profile (Fig. 11), indicating a boiling zone at that depth. This is where steam is flashed and rises buoyantly contemporaneously with condensation and cooling. This enhances alteration at medium to low temperatures, forming the clay cap

alteration above 900 m. The clay cap is coincident with the conductive layer (5-30 Ωm) above the water table as indicated by the 1D resistivity Occam model (Section 3.5), and is characterised by smectite and mordenite. The reservoir level below 800 m depth (base of clay cap) represents a transition zone into the hotter reservoir where the calculated formation temperature is above 170 °C, this is lower than the 230 °C inferred temperatures for the base of the clay cap in Icelandic geothermal systems (Árnason et al., 2010).

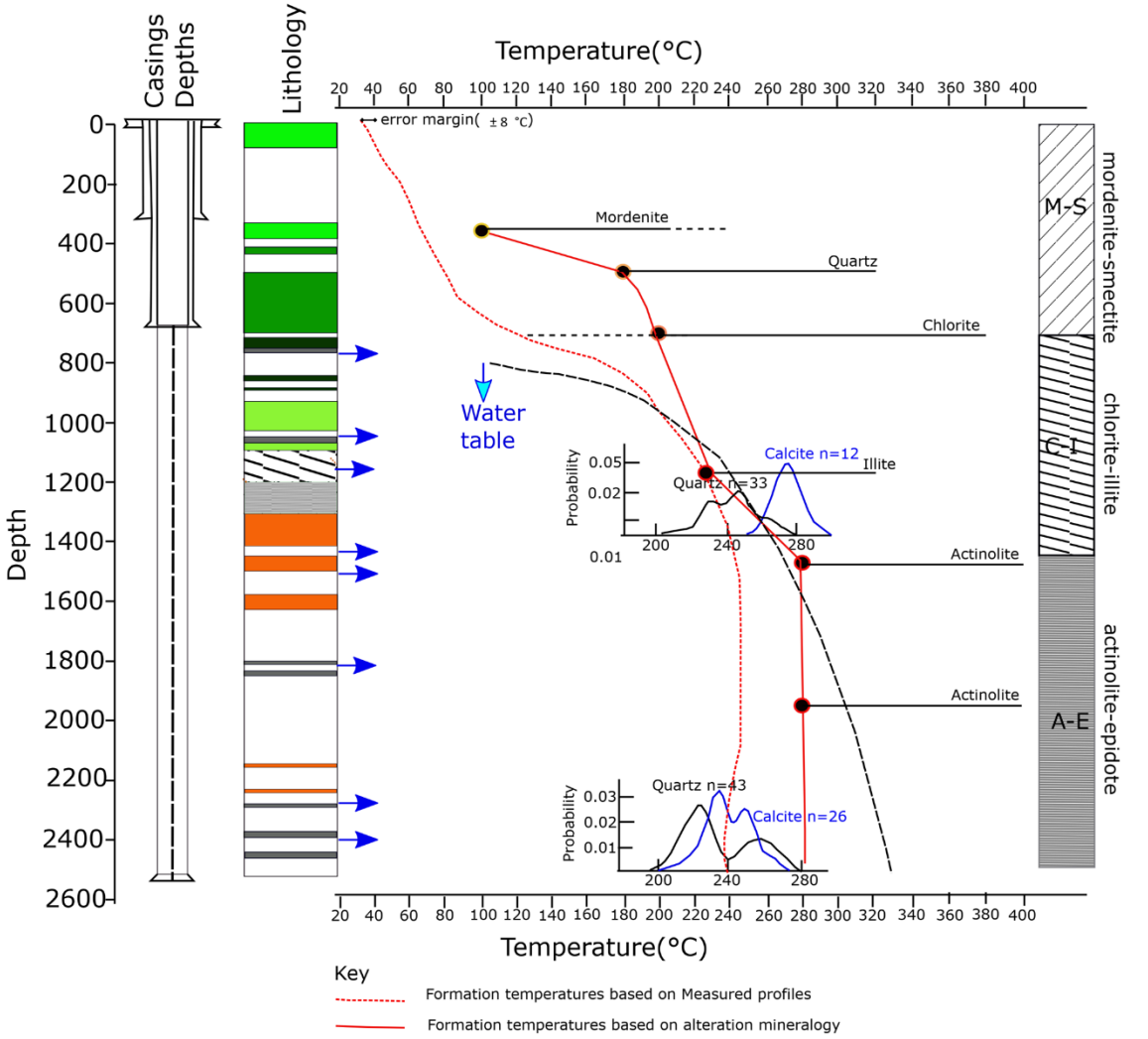

Fig. 11: The correlation of alteration, formation temperature (°C) and fluid inclusion analyses in well PK-01. The black broken line is the boiling point curve.

The appearance of coarse-grained highly birefringent clays (illite, chlorite) indicates transition into temperatures above 220 °C. This transition zone also, and even more importantly, highlights entry into the main reservoir indicated by feed zones at 1050-1150, 1450-1500, 1800 m, 2300 and at 2450 m. This high-temperature reservoir zone is marked by the shift to higher resistivity of >30 Ωm, reflecting the appearance of high-temperature and less hydrous alteration minerals (Lichoro, 2017). Temperature of 245 °C is measured at ~1300 m, while the inferred hydrothermal temperature is at least 280 °C based on the presence of actinolite. It corresponds to the relatively high resistive zone (~40 Ωm).

Resistivity of >100 Ωm below 1600 m is attributed to the presence of syenite intrusion in addition to highly resistive minerals, coincident with a drop in LOI suggesting dehydrated high-temperature alteration minerals. The incidence of smectite at the deeper levels (2200-2400 m) of the well within the high-temperatures zone is not unparalleled, having been observed deep in the high-temperature parts of the Menengai geothermal system (Mibei, 2012) and in Iceland and has been attributed to low permeability (Franzson & Gunnlaugsson, 2020).

5.3 Temporal changes in Paka geothermal reservoir conditions

To evaluate reservoir conditions and evolution of both fluid chemistry and temperatures, we focus on the fluid inclusion samples. Quartz-hosted fluid inclusions are more common than those hosted in calcite. The fluid inclusions are liquid-rich with calcite daughter minerals occassionally present and hence formed in non-boiling conditions. The presence of a calcite phase suggests that the Paka hydrothermal system is CO_2-rich (e.g.,Darimont et al., 1988; Giuliani et al., 1993; Moroz et al., 2001). This is further supported by the Raman shift at 1285 cm^{-1} and 1388 cm^{-1} in the vapour phase of fluid inclusion, indicative of CO_2 gas. No other gas species like SO_2 and H_2S were detected. The ice-melting temperatures (T_m) range between 0 to -0.1°C indicating a low-salinity aqueous fluid. If we compare the current system's well discharge chemistry with the extinct parts of the system, then the Paka reservoir fluid chemistry ($NaHCO_3$) has remained the same and unchanged over time.

In terms of reservoir temperature and its evolution, we compared the fluid inclusion data, measured temperatures and alteration mineralogy. We assume all fluid inclusions trapped a liquid phase made evident by homogenisation to liquid phase (LV→L) (Fall et al., 2009; Roedder, 1984), as opposed to (LV→V), which would be the case if the reservoir fluid were vapour dominated (Hurai et al., 2015). This is indicative of non-boiling conditions hence the pressure effect on homogenization temperature is negligible. The homogenization temperatures are therefore good estimates of trapping temperatures for our inclusions. Correlation of homogenization temperature T_h and the boiling point curve suggests sub-boiling conditions at 2550 m depth indicating a liquid-dominated system. At 1390 m boiling conditions are experienced based on boiling point curve intersection perhaps due to pressure change as fluids raises up in the system to shallower depths.

The Kernel density estimate (KDE) probability plot for fluid inclusion data at 1388-1390 m indicates that the fluid inclusion (T_h) in quartz have peaks at 230 and 240 °C, while calcite gives higher values of 273 °C. The very high homogenisation temperatures of calcite-hosted fluid inclusions (Fig.11) are likely due to stretching of calcite due to its low strength and good cleavage in calcite (Bodnar & Samson, 2003), and thus the homogenisation temperatures may be unreliable. The T_h of quartz-hosted fluid inclusions at 2550 m shows a broad temperature range with two peaks at 225 and 255°C. The bimodal spread of fluid inclusions temperature is associated with variable hydrothermal regimes. At 1390 m the paleo system is in equilibrium with the current system. At 2550 m, however, two systems occurred, on one hand we see as heating and the other we see cooling relative to the current formation temperature perhaps indicating colder fluids channelled to deeper levels via faults and fractures. By Comparing with hydrothermal alteration mineral temperatures (280 °C), we conclude that Paka reservoir has experienced cooling over time at least in the part of the system penetrated by well PK-01.

5.4 The Paka resource suitability model

Resource suitability model is developed by integrating surface exploration data and developing 90% (P90) and 10% (P10) probability models (Cumming, 2016), which are presented in map view. The purpose is to pinpoint the most favourable environment for drilling productive wells which are presented in map view. In our case, P90 is the most suitable presenting an area with the highest probability for successful drilling but spatially smaller area, while P10 has lower probability for productive wells but covers larger area.

Raster and vector data was integrated by QGIS software, where a Boolean integration model using union, intersection and difference modules were used. The integrated surface data sets include faults, fumarole locations, surface manifestations and eruption centres. The 60 °C isotherm from surface temperature measurements and resistivity layers at sea level were used as constraints.

The first stage of the integration involved creating QGIS buffer maps of inferred faults within 200 m, lineaments within 250 m, eruption centres within 300 m and surface manifestations within 200 m. This was overlain by the 30 Ωm iso-resistivity and 60 °C isotherm (Fig. 12a). These criteria are used on the assumption that areas close to these geological features are suitable for geothermal drilling. The second stage was to employ the intersection overlay vector tool on the buffer maps to further delineate the highly probable areas (Fig.12b). The final stage was to carry out an overlay of maps in QGIS covering areas where all the data sets intersected (P90) and a difference overlay to delineate areas where only two data sets intersected (P10) (Fig.12c). The P90 areas located within the summit area (12 km^2) and a small enclave in the northeast (8 km^2) (Fig. 12c) are proposed as highly suitable area for resource development.

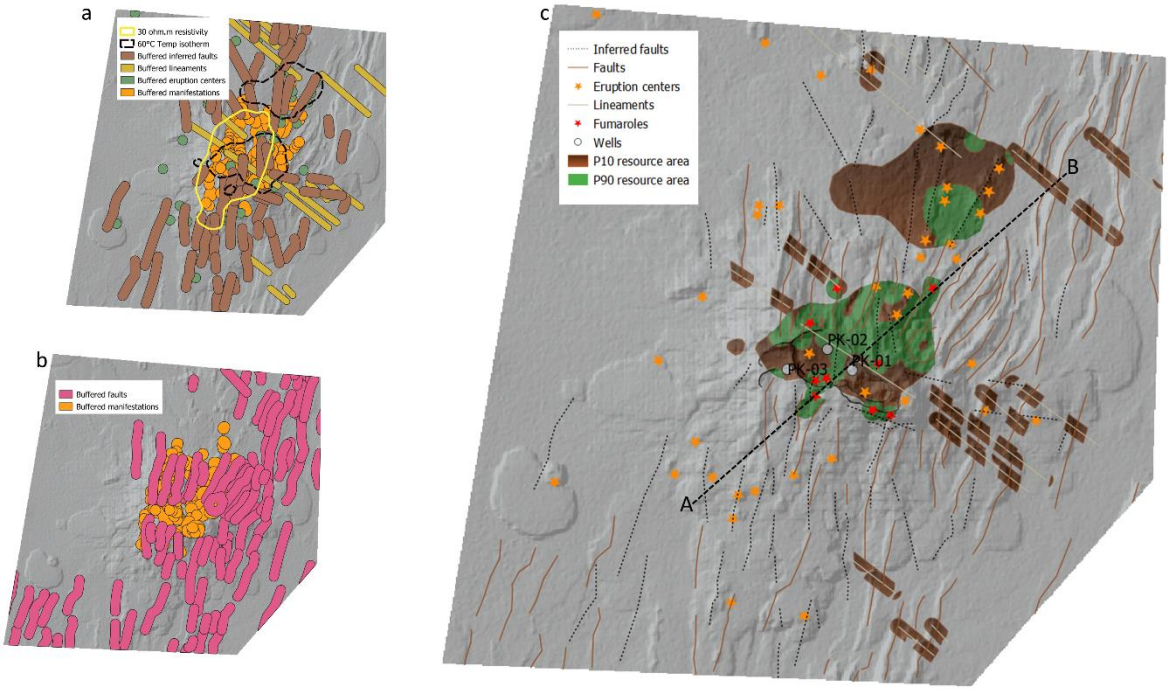

Fig. 12: Geothermal conceptual model in map view based on integrated surface data. a) The map is integrated resistivity data, soil gas contour map, geothermal manifestations and shallow temperature (1m) measurements. b) Faults and geothermal manifestation integrated buffer maps. c) The map-view conceptual model from integrated surface data showing outlines of P10 (dark brown) and P90 (green) potential models.

5.5 Summary of the Paka conceptual model

An update of the reservoir model incorporates subsurface data, mainly well data and resistivity cross-sections along line A-B (Fig.12c).

Our model (Fig. 13) indicates that the formation temperature of 170 °C in the wells coincides with the lower part of the shallow conductive body seen in the resistivity cross-section. PK-01 lithology log data also suggests that the reservoir rocks are trachyte, basalt, mugearite to benmoreite series with extensive loss zones associated with possible faults. The highly resistive zone is marked by the syenite intrusions. The model further suggests that well PK-03 is closer to the up-flow zone than the other two wells. Well PK-02 is projected on the cross-section but its data is not presented as the well has apparently not fully heated up.

To further build the model, we adopted information from previous work, indicating that the heat source is possibly linked to a magma reservoirs at depths between 3.7-5 km (Mibei et al., 2021b). The direct evidence for a magma heat source is the logged syenite intrusive as indicated by well cuttings. The observed inflation-deflation episodes (Biggs et al., 2009; Biggs et al., 2016) are further evidence for an active underlying magma body.

The up-flow in the system is postulated to lie beneath the summit area closer to well PK-03 than PK-01 and around fumaroles 2 or PF-02 (Fig. 13) where fumarole gas and steam

condensate chemistry show high concentrations of fluoride, sulphates and low chloride (Supplementary table S1). The average estimated reservoir temperatures from several gas geothermometers at fumarole PF-02 was 305 °C as indicated in Fig. 11 and is considerably higher compared to the other fumarole estimated temperatures. The area around fumaroles PF-02 and PF-01 has recorded elevated Helium ration suggesting subcontinental lithospheric source further indicating possible up-flow. The fluid out-flow in the area is mainly northwards controlled by sub-vertical NNE and N-S faults (Mibei et al., 2021a). The maximum measured reservoir temperature from the currently available data is 271 °C (Fig. 13), which is lower than the maximum reservoir temperatures of ~340 °C in Olkaria (Ofwona, 2002) and ~400 °C in Menengai (O'Sullivan et al., 2015). The reservoir is a liquid-dominated system discharging $NaHCO_3$-type fluid. This fluid chemistry is similar to that of discharge from wells in Menengai and Olkaria East and Domes, but differs from the Cl-rich Olkaria Central (Karingithi, 2000).

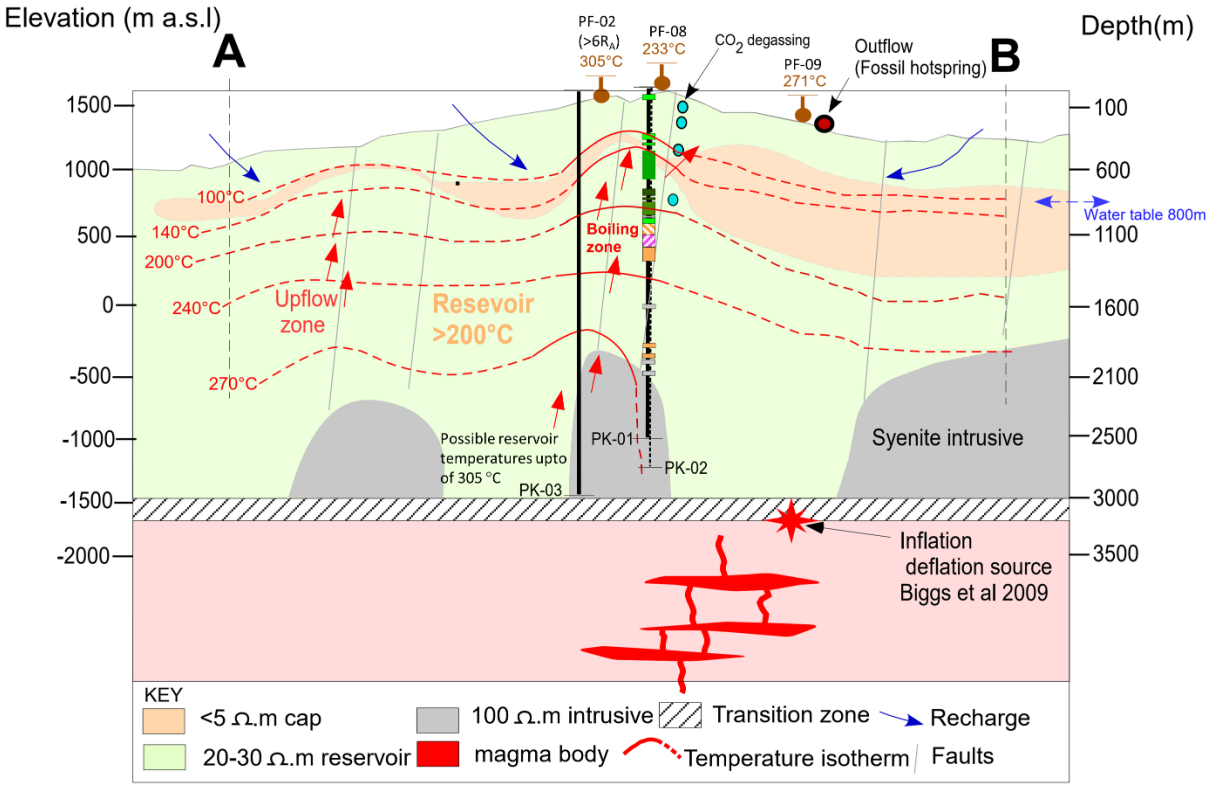

Fig. 13: The geothermal conceptual model cross-section from integrated subsurface and surface data. The reservoir temperatures of 305, 233 and 271 °C are estimated from fumarole PF-02, PF-07 and PF-0 respectively, Helium >6R_A around fumarole 2 . The up-flow is located between well PK-03 and PK-01.

In a regional context, the Paka geothermal system has some similarities but also differences compared to the Menengai and Olkaria systems, the most studied geothermal systems in Kenya. Recharge for geothermal systems within the northern Kenyan rift is of meteoric origin, with a contribution from Lake Baringo through underground discharge towards the north (Darling et al., 1996). The measured borehole pressure profiles from PK-01 (Section 3.5) show that hydrostatic pressure gradient starts at 800 m depth, confirming that the water

table is deeper than observed in the geothermal fields of Menengai, where the average depth is ~300-400 m (Montegrossi et al., 2015), and Olkaria, where it is 400 m (Ofwona, 2002), both of which are located south of Paka. This confirms the long-held belief that the regional hydrological gradient in the rift favours axial fluid flow towards the north and further supporting the concept of underground water flow and recharge of Paka geothermal system from Lake Baringo, through north trending faults systems.

Intrusive formations apparently predominate below 2200 m at Paka resembling the Menengai system but shallower than at Olkaria where an intrusive is intersected at 3000 m (Kandie, 2018). In Menengai the intrusive bodies are associated with anomalously high temperatures (Mibei et al., 2016), unlike Paka where temperature reversals at the bottom of the well (PK-01) occur within the intrusive syenite zone.

6.0 Conclusion

This paper provides insights into the Paka geothermal system from a surface data review and subsurface data analyses mainly from well PK-01. We suggest that the Paka hydrothermal system must be younger than 580 ka using the underlying oldest regional plateau eruptions as a limit. Integrated geoscientific data sets, including resistivity anomalies, soil gas (CO_2 concentrations) and shallow temperature measurements, as well as spatial distribution of geothermal manifestations and faults, provide evidence for the areal extent of the Paka geothermal resource. The reservoir hydrothermal zonation is marked by smectite-mordenite at shallow depths, followed by the chlorite-illite and actinolite-epidote at deeper levels. The transition into the main geothermal reservoir begins at about ~800 m depth and is marked by the chlorite-illite zone. It is estimated that the reservoir temperature in Paka system is ~240-270 °C. The reservoir is a liquid-dominated system of the $NaHCO_3$-type, which has remained stable in terms of chemistry over time. However, subsurface temperature has fluctuated and cooled over time, caused by heat mining and recharge of geothermal fluids. The up-flow of the Paka system is postulated to be located closer to well PK-03 than the other two wells while the out-flow in the area is mainly northwards largely controlled by NNE and N-S faults.

Acknowledgements

The authors would like to thank the Geothermal Development Company Ltd (GDC) for allowing the use of data, and for assistance during several field campaigns. We are grateful to Sigurður Sveinn Jónsson for sample preparation and clay analyses. Thanks are due to Benedikt Steingrímsson for assistance in the interpretation of borehole temperature and pressure profiles and in the estimation of formation temperatures, Associate editor, Dr Rosa Maria Prol-Ledesma and two anonymous reviewers for greatly improving the original manuscript. We also would like to give a special mention to one of the co-authors ‘Charles Lichoro’ who passed away before submission of this manuscript. The project was funded by the Geothermal Development Company Limited of Kenya and the GRÓ–Geothermal Training Programme as part of a Ph.D. fellowship to the first author.

References

Arnórsson, S., Gunnlaugsson, E., & Svavarsson, H. (1983). The chemistry of geothermal waters in Iceland. III. Chemical geothermometry in geothermal investigations. *Geochimica et Cosmochimica Acta, 47*(3), 567-577. doi:https://doi.org/10.1016/0016-7037(83)90278-8

Arnórsson, S. (1985). The use of mixing models and chemical geothermometers for estimating underground temperatures in geothermal systems. *Journal of Volcanology and Geothermal Research, 23*(3-4), 299-335.

Arnórsson, S. (1985). The use of mixing models and chemical geothermometers for estimating underground temperatures in geothermal systems. *Journal of Volcanology and Geothermal Research, 23*(3-4), 299-335.

Arnórsson, S., & Gunnlaugsson, E. (1985). New gas geothermometers for geothermal exploration—calibration and application. *Geochimica et Cosmochimica Acta, 49*(6), 1307-1325.

Arnórsson, S., Gunnlaugsson, E., & Svavarsson, H. (1983). The chemistry of geothermal waters in Iceland. III. Chemical geothermometry in geothermal investigations. *Geochimica et Cosmochimica Acta, 47*(3), 567-577. doi:https://doi.org/10.1016/0016-7037(83)90278-8

Árnason, K., Eysteinsson, H., & Hersir, G. P. (2010). Joint 1D inversion of TEM and MT data and 3D inversion of MT data in the Hengill area, SW Iceland. *Geothermics, 39*(1), 13-34.

Biggs, J., & Annen, C. (2019). The lateral growth and coalesence of magma systems. *Philosophical Transactions of the Royal Society A, 377*(2139), 20180005.

Biggs, J., Anthony, E., & Ebinger, C. (2009). Multiple inflation and deflation events at Kenyan volcanoes, East African Rift. *Geology, 37*, 979-982. doi:10.1130/G30133A.1

Biggs, J., Robertson, E., & Cashman, K. (2016). The lateral extent of volcanic interactions during unrest and eruption. *Nature Geoscience, 9*(4), 308-311.

Bodnar, R. J., & Frezzotti, M. L. (2020). Microscale Chemistry: Raman Analysis of Fluid and Melt Inclusions. *Elements: An International Magazine of Mineralogy, Geochemistry, and Petrology, 16*(2), 93-98.

Bodnar, R. J., & Samson, I. (2003). Reequilibration of fluid inclusions. *Fluid inclusions: Analysis and interpretation, 32*, 213-230.

Browne, P. R. L. (1970). Hydrothermal alteration as an aid in investigating geothermal fields. *Geothermics, 2*, 564-570. doi:https://doi.org/10.1016/0375-6505(70)90057-X

Browne, P. R. L. (1978). Hydrothermal alteration in active geothermal fields. *Annual review of earth and planetary sciences, 6*, 229-250.

Cumming, W. (2016). Geophysics and resource conceptual models in geothermal exploration and development. In *Geothermal power generation* (pp. 33-75): Elsevier.

Darimont, A., Burke, E. A. J., & Touret, J. (1988). Nitrogen-rich metamorphic fluids in Devonian metasediments from Bastogne, Belgium. *Bulletin de minéralogie, 111*(3), 321-330.

Darling, W., Griesshaber, E., Andrews, J., Armannsson, H., & O'nions, R. (1995). The origin of hydrothermal and other gases in the Kenya Rift Valley. *Geochimica et Cosmochimica Acta, 59*(12), 2501-2512.

Darling, W. G., Gizaw, B., & Arusei, M. K. (1996). Lake-groundwater relationships and fluid-rock interaction in the East African Rift Valley: isotopic evidence. *Journal of African Earth Sciences, 22*(4), 423-431. doi:https://doi.org/10.1016/0899-5362(96)00026-7

Fall, A., Rimstidt, J., & Bodnar, R. (2009). The effect of fluid inclusion size on determination of homogenization temperature and density of liquid-rich aqueous inclusions. *American Mineralogist - AMER MINERAL, 94*, 1569-1579. doi:10.2138/am.2009.3186

Fournier, R., & Potter, R. (1982). Revised and expanded silica (quartz) geothermometer. *Bull., Geotherm. Resour. Counc.(Davis, Calif.);(United States), 11*(10).

Fournier, R. O. (1977). Chemical geothermometers and mixing models for geothermal systems. *Geothermics, 5*(1), 41-50. doi:https://doi.org/10.1016/0375-6505(77)90007-4

Fournier, R. O. (1992). Water geothermometers applied to geothermal energy. *Applications of geochemistry in geothermal reservoir development*, 37-69.

Franzson, H., & Gunnlaugsson, E. (2020). *Formation of Clays and Chlorites in the Upper Icelandic Crust.* Paper presented at the World Geothermal Congress Reykjavik, Iceland.

Franzson, H., Kristjánsson, B. R., Gunnarsson, G., Björnsson, G., Hjartarson, A., Steingrímsson, B., . . . Gíslason, G. (2005). *The Hengill-Hellisheiði geothermal field. Development of a conceptual geothermal model.* Paper presented at the Proceedings world geothermal congress.

Franzson, H., Thordarson, S., Björnsson, G., Gudlaugsson, S. T., Richter, B., Fridleifsson, G. O., & Thorhallsson, S. (2002). *Reykjanes high-temperature field, SW-Iceland. Geology and hydrothermal alteration of well RN-10.* Paper presented at the Workshop on Geothermal Reservoir Engineering.

Franzson, H., Zierenberg, R., & Schiffman, P. (2008). Chemical transport in geothermal systems in Iceland: Evidence from hydrothermal alteration. *Journal of Volcanology and Geothermal Research, 173*(3), 217-229. doi:https://doi.org/10.1016/j.jvolgeores.2008.01.027

Frezzotti, M. L., Tecce, F., & Casagli, A. (2012). Raman spectroscopy for fluid inclusion analysis. *Journal of Geochemical Exploration, 112*, 1-20.

Fridleifsson, G. (1991). Hydrothermal systems and associated alteration in Iceland. *Geol Survey Japan Report, 277*, 83-90.

Friese, A. (2015). InSAR, surface movement and dating of Paka volcanic products, Northern Kenya Rift (report). (BGR 05-2343). Retrieved 16.8.2020, from BGR https://www.bgr.bund.de/DE/Themen/GG_Fernerkundung/Downloads/kenia_paka_final_report.pdf?__blob=publicationFile&v=6

GDC. (2020). *Heat up and discharge report of Paka well PW-01*. Retrieved from Unpublished report:

Giggenbach, W., Sheppard, D., Robinson, B., Stewart, M., & Lyon, G. (1994). Geochemical structure and position of the Waiotapu geothermal field, New Zealand. *Geothermics, 23*(5-6), 599-644.

Giggenbach, W. F. (1988). Geothermal solute equilibria. Derivation of Na-K-Mg-Ca geoindicators. *Geochimica et Cosmochimica Acta, 52*(12), 2749-2765. doi:https://doi.org/10.1016/0016-7037(88)90143-3

Giuliani, G., Cheilletz, A., Dubessy, J., & Rodriguez, C. (1993). *Chemical composition of fluid inclusions in Colombian emerald deposits.* Paper presented at the Proceedings of the Eighth Quadrennial IAGOD Symposium.

Henley, R. W., & Ellis, A. J. (1983). Geothermal systems ancient and modern: a geochemical review. *Earth-Science Reviews, 19*(1), 1-50.

Hurai, V., Huraiová, M., Slobodník, M., & Thomas, R. (2015). Chapter 4 - Fluid and Melt Inclusion Microthermometry. In V. Hurai, M. Huraiová, M. Slobodník, & R. Thomas (Eds.), *Geofluids* (pp. 59-115): Elsevier.

Hutchison, W., Biggs, J., Mather, T. A., Pyle, D. M., Lewi, E., Yirgu, G., . . . Fischer, T. P. (2016). Causes of unrest at silicic calderas in the East African Rift: New constraints from InSAR and soil-gas chemistry at Aluto volcano, Ethiopia. *Geochemistry, Geophysics, Geosystems, 17*(8), 3008-3030.

Hutchison, W., Mather, T. A., Pyle, D. M., Biggs, J., & Yirgu, G. (2015). Structural controls on fluid pathways in an active rift system: A case study of the Aluto volcanic complex. *Geosphere, 11*(3), 542-562. doi:10.1130/GES01119.1

Kandie, R. J. (2018). Borehole geology and thermal history of well OW-737, Olkaria geothermal field, Kenya. *Geothermal Training in Iceland, 14, 187, 220*.

Karingithi, C. W. (2000). *Geochemical characteristics of the Greater Olkaria geothermal field, Kenya*: United Nations University.

Kipngok, J., & Nyamongo, J. (2013). Fumarole Gas Geochemistry of Paka Geothermal Prospect, North Rift, Kenya. *GRC Transactions,, Vol. 37*.

Lagat, J., Arnorsson, S., & Franzson, H. (2004). *Geology, hydrothermal alteration and fluid inclusion studies of Olkaria Domes geothermal field, Kenya*: Háskóli Íslands, jarð-og landfræðiskor.

Lagat, J., Wamalwa, A., & Ochieng, L. (2013). *Bogoria-Silali block prospect: Investigations for its geothermal potential*. Retrieved from

Li, Z., Yin, J., Zhu, D., & Datta-Gupta, A. (2011). Using downhole temperature measurement to assist reservoir characterization and optimization. *Journal of Petroleum Science and Engineering, 78*(2), 454-463. doi:https://doi.org/10.1016/j.petrol.2011.06.012

Lichoro, C. M. (2017). Geothermal Characterization of Paka Volcano in Kenya from Resistivity and Gravity.

Lichoro, C. M., Árnason, K., & Cumming, W. (2017). Resistivity imaging of geothermal resources in northern Kenya rift by joint 1D inversion of MT and TEM data. *Geothermics, 68*, 20-32. doi:https://doi.org/10.1016/j.geothermics.2017.02.006

Lichoro, C. M., Árnason, K., & Cumming, W. (2019). Joint interpretation of gravity and resistivity data from the Northern Kenya volcanic rift zone: Structural and geothermal significance. *Geothermics, 77*, 139-150. doi:https://doi.org/10.1016/j.geothermics.2018.09.006

Lopeyok, T. (2019). *Draft borehole Geology of well PW-01*. Retrieved from unpublished report:

Marks, N., Schiffman, P., Zierenberg, R. A., Franzson, H., & Fridleifsson, G. Ó. (2010). Hydrothermal alteration in the Reykjanes geothermal system: Insights from Iceland deep drilling program well RN-17. *Journal of Volcanology and Geothermal Research, 189*(1-2), 172-190.

Mibei, G. (2012). Geology and hydrothermal alteration of Menegai geothermal field. Case study: Wells MW-04 and MW-05. *Geothermal Training in Iceland, Technical Report, 21*, 437-465.

Mibei, G., Bali, E., Geirsson, H., Guðfinnsson, G. H., Harðarson, B. S., & Franzson, H. (2021b). Partial melt generation and evolution of magma reservoir conditions at the Paka volcanic complex in Kenya: Constraints from geochemistry, petrology and geophysics. *Lithos*, 106385.

Mibei, G., Harðarson, B. S., Franzson, H., Bali, E., Geirsson, H., & Guðfinnsson, G. H. (2021a). Eruptive history and volcano-tectonic evolution of Paka volcanic complex in the northern Kenya rift: Insights into the geothermal heat source. *Journal of African Earth Sciences, 173*, 103951. doi:https://doi.org/10.1016/j.jafrearsci.2020.103951

Mibei, G., Mutua, J., Njue, L., & Ndongoli, C. (2016). *Conceptual model of Menengai Geothermal field.* Paper presented at the Proc. ARGeo Conf.

Montegrossi, G., Pasqua, C., Battistelli, A., Mwawongo, G., & Ofwona, C. (2015). *3D natural state model of the Menengai geothermal system, Kenya.* Paper presented at the Proceedings of the World Geothermal Congress.

Moroz, I., Vapnik, Y., Eliezri, I., & Roth, M. (2001). Mineral and fluid inclusion study of emeralds from the Lake Manyara and Sumbawanga deposits, Tanzania. *Journal of African Earth Sciences, 33*(2), 377-390.

Mulusa, G. I. (2015). *Geochemical Study of Fumarolic Condensates from Paka Volcano, Kenya*. Paper presented at the World Geothermal Congress, Melbourne Australia.

Mwawasi, H. M. (2012). Heat Loss Assessment of Selected Kenyan Geothermal Prospects.

O'Sullivan, J., Kipyego, E., Croucher, A., Ofwona, C., & O'Sullivan, M. (2015). *A supercritical model of the Menengai geothermal system.* Paper presented at the Proceedings, World Geothermal Congress.

Ochieng, L. (2019). Well PW-01 Fluid Discharge Chemistry Report. *GDC, Internal report*.

Ofwona, C. O. (2002). *A reservoir study of Olkaria East geothermal system, Kenya*: United Nations University, Geothermal Training Programme.

Opondo, K. (2010). *Radon and Soil Gas Surveys in Paka Geothermal Prospect, Kenya.* Paper presented at the Proceedings World Geothermal Congress.

Peters, K. E., & Nelson, P. H. (2012). Criteria to determine borehole formation temperatures for calibration of basin and petroleum system models. *SEPM Special Publication, 103*, 5-15.

Reyes, A. G. (2000). *Petrology and mineral alteration in hydrothermal systems: From diagenesis to volcanic catastrophes*: United Nations University, Geothermal Training Programme.

Roedder, E. (1984). *Fluid inclusions*: De Gruyter.

Rouwet, D., Tamburello, G., Ricci, T., Sciarra, A., Capecchiacci, F., & Caliro, S. (2020). CO2 and H2S Degassing at Fangaia Mud Pool, Solfatara, Campi Flegrei (Italy): Origin and Dynamics of the Pool Basin. *Minerals, 10*(12), 1051.

Simmons, S. F., & Browne, P. R. (1997). Saline fluid inclusions in sphalerite from the Broadlands-Ohaaki geothermal system; a coincidental trapping of fluids being boiled toward dryness. *Economic Geology, 92*(4), 485-489.

Appendix A: Sample Locations and new stratigraphic names

Table 1 Sample locations (Mibei et al., 2021)

Datum	**Arc 1960**			
Easting	**Northing**	**Age**	**Sample**	**New Proposed names**
186884	101188	8±4		Phase 4-Pyroclastic(P4-Py)
187705	102563	11±4	DN-4	Phase 4-Trachyte 2(P4-Tr2)
190700	103600	81±7	DN-s1	
188500	95000	219±4 ka	DN-2	Phase 2-Trachyte 2(P2-Tr2)
196200	109700	390±6 ka	DN-1	Phase 1-Trachyte 1(P1-Tr1)
Datum	**WGS 84**			
Easting	**Northing**			
190906.6	109337.2	12±3	pk-12	Phase 4-Trachyte 2(P4-Tr2)
188726.09	104848.1	20±5	pk-3	Phase 4-Trachyte 1(P4-Tr1)
185465.91	103352.9	31±17	pk-17	Phase 4-Trachyte 1(P4-Tr1)
181364.74	100300.7	35±10	pk-25	Phase 4-Trachyte 1(P4-Tr1)
188078.6	101687.5	35±5	pk-2-b	Phase 4-Trachyte 1(P4-Tr1)
179151.69	99349.99	39±6	pk-29	Phase 3-Trachyte 3(P4-Tr3)
187155.19	96084.02	71±13	pk-27	Phase 3-Trachyte 2(P4-Tr2)
188109.54	107443.3	80±11	pk-14	Phase 3-Trachyte 2(P4-Tr2)
181885.98	98105.25	126±9	pk-30	Phase 3-Trachyte 1(P4-Tr1)
183622.71	106043.2	139±35	pk-15	Phase 3-Trachyte 1(P4-Tr1)
186937.8	111141.1	145±23	pk-13	Phase 3-Hawaiite(P3-Ht)
184649.35	98087.41	150±6	pk-26	Phase 3-Trachyte 1(P3-Tr1)
170780	102731	160±97	pk-m1	Phase 3-Basalt (P3-Bt)
191724.36	97096.95	205±6	pk-8	Phase 2-Trachyte (P3-Tr)
192546.07	104595.2	234±13	pk-5	Phase 2-Trachyte (P3-Tr)
190790.72	104394.7	238±34	pk-04	Phase 2-Hawaiite(P2-Ht)
182006	98225	247±24	pk-m2	Phase 2-Mugearite (P2-Mg)
194461.01	102517.7	278±13	pk-7	Phase 1-Trachyte 3(P1-Tr3)
180448.06	108016.3	321±13	pk-21	Phase 1-Trachyte 2(P1-Tr2)
189736.48	101538.1	332±17	pk-9	Phase 1-Trachyte 2(P1-Tr2)
192865.34	108076	372±5	pk-11	Phase 1-Trachyte 1(P1-Tr1)
184029.92	109549.8	382±8	pk-18	Phase 1-Trachyte 1(P1-Tr1)
183224.46	103324.4	386±5	pk-16	Phase 1-Trachyte 1(P1-Tr1)
195261.76	104907.2	389±6	pk-6	Phase 1-Trachyte 1(P1-Tr1)
196303.69	110560.7	405±7	pk-10	Pre-paka Trachyte
179068.21	111410.8	415±28	pk-19	Pre-paka Trachyte
177285.68	101713.9	428±12	pk-23	Pre-paka Trachyte
176889.5	101416.6	464±18	pk-24	Pre-Paka Benmorite
176220.72	106349.9	471±13	pk-22	Pre-Paka Benmorite
181086.59	108650.7	582±58	pk-20	Pre-Paka Basalt

Appendix B: Whole rock chemistry

Table 2 Major and trace element chemical composition of surface samples

Major elements

Sample	SiO_2	Al_2O_3	FeO	MnO	MgO	CaO	Na_2O	K_2O	TiO_2	P_2O_5	Σ Norm	Σ Run
PK-M1	48.8	16.8	9.9	0.2	6.8	11.6	3.0	0.8	1.6	0.2	100.0	98.6
PK-20	47.5	14.9	12.3	0.2	6.5	11.1	3.3	0.8	2.9	0.5	100.0	100.7
PK-28a	48.0	14.9	11.3	0.2	8.2	10.1	3.6	1.3	1.6	0.4	100.0	96.0
PK-28c	48.5	14.6	11.1	0.2	7.3	10.2	3.7	1.4	2.1	0.7	100.0	95.5
PK-4	48.5	14.5	13.0	0.2	4.6	9.3	4.4	1.4	3.2	0.7	100.0	103.7
PK-13	49.5	15.0	11.4	0.2	5.2	10.1	4.0	1.3	2.7	0.5	100.0	102.6
PK-22	57.1	17.6	7.5	0.2	2.0	4.1	6.0	3.5	1.3	0.4	100.0	98.9
PK-24	57.6	17.9	6.8	0.3	1.7	4.1	5.7	3.9	1.1	0.4	100.0	96.8
PK-M2	54.1	16.0	9.1	0.2	3.8	6.8	5.6	2.6	1.4	0.2	100.0	100.1
PK-1	52.6	15.6	9.4	0.2	4.9	8.3	4.8	2.1	1.7	0.3	100.0	101.0
DN-1	60.4	14.9	9.4	0.4	0.6	1.9	6.4	4.8	0.8	0.1	100.0	100.5
DN-2	63.3	14.1	8.8	0.3	0.3	1.3	6.3	4.7	0.7	0.0	100.0	97.8
DN-3	60.4	15.0	8.4	0.3	0.8	1.4	7.1	5.6	0.6	0.1	100.0	95.2
DN-4	61.7	16.9	6.5	0.2	0.3	1.4	6.9	5.3	0.6	0.1	100.0	94.4
DN-4EX	61.9	16.2	7.1	0.2	0.4	1.7	6.3	5.2	0.7	0.1	100.0	102.5
DN-5	60.4	16.0	9.1	0.3	0.3	1.7	6.2	5.2	0.6	0.1	100.0	88.8
XE-1	61.1	15.2	8.7	0.3	0.1	1.1	8.1	4.7	0.5	0.0	100.0	99.0
PK-2	62.3	15.3	7.4	0.3	0.4	1.9	6.5	5.0	0.7	0.1	100.0	101.1
PK-3	61.5	16.2	7.2	0.2	0.4	1.7	6.9	5.0	0.7	0.1	100.0	98.5
PK-5	61.5	16.8	6.5	0.2	0.3	1.8	6.7	5.5	0.5	0.0	100.0	101.7
PK-6	61.6	14.6	8.4	0.4	0.2	1.5	7.3	5.0	0.8	0.1	100.0	103.0
PK-7	62.7	14.4	8.6	0.3	0.3	1.3	6.8	4.7	0.7	0.1	100.0	99.1
PK-8	61.4	15.3	8.8	0.3	0.4	1.8	6.2	4.9	0.6	0.1	100.0	97.3
PK-9	62.2	16.9	5.7	0.2	0.4	1.4	6.8	5.4	0.7	0.1	100.0	94.7
PK-10	61.2	14.4	9.1	0.3	0.5	1.8	6.7	4.9	0.9	0.1	100.0	100.2
PK-12	61.9	14.6	8.9	0.3	0.2	1.4	7.3	4.7	0.6	0.0	100.0	98.2
PK-11	59.1	15.0	8.9	0.3	0.6	2.9	7.6	4.7	0.6	0.1	100.0	96.9
PK-14	61.6	15.5	8.1	0.3	0.3	1.4	6.9	5.1	0.6	0.1	100.0	101.5
PK-15	61.7	15.2	8.9	0.3	0.3	1.5	6.3	4.9	0.6	0.1	100.0	97.9
PK-16	61.5	15.1	8.5	0.3	0.5	1.7	6.4	5.0	0.8	0.1	100.0	98.8
PK-17a	61.9	15.3	7.5	0.3	0.3	1.7	6.9	5.2	0.8	0.1	100.0	99.2
PK-18	60.4	15.3	9.6	0.4	0.5	2.1	6.2	4.6	0.6	0.1	100.0	97.2
PK-19	63.1	14.1	8.9	0.4	0.3	1.5	6.3	4.6	0.7	0.0	100.0	100.8
PK-21	61.0	15.3	8.1	0.3	0.5	1.8	6.8	5.0	0.9	0.1	100.0	98.2
PK-23	62.3	15.8	7.4	0.2	0.2	0.7	7.3	5.3	0.6	0.0	100.0	97.2
PK-25a	61.7	15.8	7.9	0.3	0.1	1.2	7.0	5.2	0.6	0.1	100.0	100.6
PK-26	62.5	14.6	8.5	0.3	0.3	1.7	6.5	4.7	0.6	0.0	100.0	100.2
PK-27	60.6	15.4	8.6	0.3	0.1	1.3	8.1	4.8	0.5	0.0	100.0	99.9
PK-29	61.5	15.1	8.3	0.3	0.2	1.2	7.6	5.0	0.6	0.1	100.0	100.7
PK-30	60.8	15.3	7.9	0.3	0.3	2.7	6.9	5.0	0.7	0.1	100.0	95.7

Trace elements- Surface samples contd...

Sample	Ba	Co	Cr	Cu	La	Ni	Rb	Sc	Sr	V	Y	Zn	Zr
PK-M1	585	48	204	79	32	121	1	35	364	239	36	112	116
PK-20	376	62	45	46	24	31	13	36	383	349	35	93	139
PK-28a	831	50	254	55	41	147	16	24	484	203	40	131	168
PK-28c	851	49	231	46	43	109	0	26	497	204	41	129	177
PK-4	660	58	8	29	33	10	13	28	384	277	46	105	209
PK-13	423	56	53	50	25	18	14	34	321	265	41	91	208
PK-22	2363	14	7	22	106	45	41	7	695	34	60	168	355
PK-24	3179	12	6	16	117	29	6	5	777	26	82	161	457
PK-M2	319	31	73	33	55	63	23	19	201	136	64	153	400
PK-1	248	40	87	48	52	36	47	24	263	189	67	104	509
DN-1	253	6	20	36	108	53	208	6	36	2	103	222	760
DN-2	38	4	8	18	103	30	144	4	23	2	108	224	699
DN-3	76	7	12	19	142	39	72	3	40	15	147	224	1059
DN-4	173	4	6	25	75	43	144	3	31	3	84	164	651
DN-4EX	144	5	11	30	76	29	179	4	33	3	88	159	681
DN-5	10	4	8	49	130	108	45	1	59	3	117	233	845
XE-1	28	2	7	22	124	29	103	1	12	4	129	222	1046
PK-2	39	6	1	18	76	4	132	3	18	6	94	133	720
PK-3	163	7	0	20	70	10	69	4	31	5	83	124	625
PK-5	27	3	0	18	111	15	118	2	22	3	79	134	650
PK-6	85	5	3	20	89	19	178	6	15	1	85	188	541
PK-7	69	5	8	23	108	19	210	4	28	3	109	217	738
PK-8	27	4	0	15	140	4	65	1	194	2	145	194	809
PK-9	188	5	0	19	78	11	85	4	16	3	58	116	558
PK-10	175	7	2	17	115	3	107	5	35	7	101	179	745
PK-12	29	4	6	29	128	39	145	2	24	7	145	222	1113
PK-11	168	6	0	20	222	5	103	1	83	11	211	247	1648
PK-14	26	4	4	17	95	19	139	2	15	2	98	185	700
PK-15	45	4	0	12	129	2	135	2	46	2	124	192	787
PK-16	139	7	0	14	116	5	81	4	34	2	110	174	812
PK-17a	243	6	0	20	72	8	196	5	18	1	70	132	509
PK-18	146	6	0	46	243	49	169	2	67	14	260	282	2072
PK-19	57	4	3	15	142	19	151	2	35	5	146	255	957
PK-21	198	7	0	18	98	4	151	5	33	5	92	162	692
PK-23	37	3	14	36	194	53	141	4	13	3	119	228	893
PK-25a	22	3	6	38	98	75	157	2	13	2	106	189	812
PK-26	43	3	6	29	140	36	254	2	40	4	128	221	998
PK-27	36	2	7	16	127	32	129	1	22	4	131	218	1048
PK-29	29	3	7	34	116	29	173	2	17	3	136	215	978
PK-30	49	4	7	19	73	33	166	3	24	1	79	194	573

Table 3 *Major and trace element chemical composition from borehole samples*

Major elements

Sample	SiO_2	Al_2O_3	FeO	MnO	MgO	CaO	Na_2O	K_2O	TiO_2	P_2O_5	Σ Norm	Σ Run
20-22	60.8	15.5	8.0	0.3	0.5	1.9	7.4	4.7	0.7	0.1	100.0	96.3
20-22 dupl.	61.2	15.4	8.1	0.3	0.5	1.9	7.0	4.7	0.7	0.1	100.0	95.4
48-50	61.0	14.7	8.6	0.3	0.5	1.5	7.8	4.8	0.7	0.1	100.0	98.1
358-360A	61.2	15.2	8.9	0.3	0.2	1.3	7.3	5.0	0.6	0.1	100.0	91.6
358-360B	61.7	15.1	8.7	0.3	0.2	1.3	6.9	4.8	0.7	0.1	100.0	96.8
380-382	61.1	16.1	8.3	0.3	0.2	1.3	6.7	5.3	0.7	0.1	100.0	96.3
398-400	60.7	15.9	8.5	0.3	0.2	1.4	7.1	5.0	0.6	0.0	100.0	93.6
428-430	62.3	15.5	7.7	0.3	0.3	1.5	6.3	5.1	0.8	0.1	100.0	100.0
498-500	62.7	16.0	6.8	0.2	0.2	1.2	6.6	5.3	0.7	0.1	100.0	100.3
538-540	63.0	15.7	7.4	0.2	0.2	1.2	6.3	5.0	0.7	0.1	100.0	94.5
678-680	65.7	13.8	8.3	0.3	0.1	1.2	5.1	4.7	0.6	0.1	100.0	96.8
720-722	63.7	14.3	9.4	0.3	0.1	1.6	5.3	4.5	0.6	0.0	100.0	96.0
840-842	63.0	15.0	8.1	0.3	0.1	1.5	6.0	5.3	0.6	0.1	100.0	79.5
908-910	64.3	15.2	7.1	0.3	0.2	1.5	4.9	5.5	0.6	0.1	100.0	90.8
1002-1004	63.4	17.3	5.5	0.2	0.2	0.9	6.7	5.1	0.5	0.1	100.0	92.5
1080-1082	63.5	16.0	7.5	0.3	0.1	1.2	5.4	5.1	0.6	0.1	100.0	86.1
1100-1102	65.4	15.0	6.8	0.3	0.2	0.8	5.6	5.2	0.5	0.1	100.0	93.8
1178-1180	53.0	16.6	9.7	0.2	2.7	4.9	6.4	2.8	2.6	0.8	100.0	79.4
1280-1282	48.5	16.8	12.6	0.2	4.1	5.7	4.2	3.0	3.5	0.9	100.0	89.5
1318-1320	55.5	16.0	8.5	0.2	2.3	5.1	6.4	3.0	2.0	0.7	100.0	90.1
1520-1522	57.0	15.8	8.5	0.2	1.9	3.9	5.8	4.3	1.7	0.4	100.0	95.2
2400-2402	59.8	16.3	6.8	0.2	1.6	3.1	6.5	4.2	1.2	0.2	100.0	101.0
2252-2254	54.8	16.7	9.3	0.2	2.4	4.9	5.9	3.3	2.0	0.4	100.0	97.2
2550-2552	62.9	17.4	4.8	0.1	0.8	1.5	6.9	4.6	0.8	0.2	100.0	90.2

Trace elements -Borehole samples contd....

Sample	Ba	Co	Cr	Cu	La	Ni	Rb	Sc	Sr	V	Y	Zn	Zr
20-22	143.0	7.3	10.0	36.0	113.7	19.2	94.5	3.8	68.2	17.8	111.0	169.4	880.4
20-22 dupl.	142.1	7.9	10.2	36.0	95.4	19.4	129.4	3.9	67.6	18.3	112.7	149.2	886.6
48-50	79.2	6.1	13.0	21.2	113.9	0.0	153.5	3.1	41.6	11.7	116.2	146.3	927.6
358-360A	39.6	3.9	5.1	15.6	161.1	0.0	33.7	1.6	25.1	6.4	128.4	208.7	1042.9
358-360B	38.2	4.8	4.8	19.1	156.1	0.0	252.9	2.1	23.6	7.3	122.1	173.3	1030.7
380-382	43.4	4.2	3.6	17.4	121.1	0.0	149.4	2.3	25.1	3.3	99.4	156.2	672.7
398-400	32.7	4.0	4.3	49.6	120.0	4.4	16.1	2.3	22.4	4.4	89.8	167.7	730.3
428-430	158.1	5.7	4.8	27.2	87.3	22.9	156.6	4.7	21.3	2.5	78.4	120.1	571.7
498-500	188.4	4.8	3.5	43.6	83.5	0.0	113.4	4.6	24.5	2.0	72.5	129.2	542.5
538-540	182.2	4.6	3.3	40.1	86.2	0.0	136.1	4.2	27.4	2.5	81.4	125.8	583.8
678-680	43.4	3.6	3.5	16.9	132.5	0.0	213.9	1.5	21.5	5.2	134.1	178.4	1047.7
720-722	14.2	3.6	12.2	19.7	145.6	0.0	207.3	1.4	25.8	6.5	148.3	195.0	1257.4
840-842	20.0	3.0	5.0	171.5	126.8	0.0	0.0	2.6	27.7	5.5	120.2	174.1	994.6
908-910	54.7	3.6	6.1	14.1	141.1	0.0	83.6	2.9	40.1	6.4	116.7	161.5	956.5
1002-1004	153.2	3.1	3.5	32.7	182.9	0.0	159.7	2.2	47.0	8.0	106.9	131.0	967.9
1080-1082	39.2	3.4	5.4	27.3	132.0	0.0	45.5	2.5	29.2	8.0	124.2	172.5	1126.2
1100-1102	44.1	3.0	5.2	28.1	127.2	3.3	93.0	2.5	26.0	8.0	116.1	165.5	1096.2
1178-1180	1001.1	36.3	6.1	25.4	79.5	1.7	0.0	12.9	479.0	122.7	66.4	122.0	494.5
1280-1282	1618.3	55.3	7.2	53.2	74.9	24.3	0.0	18.4	720.8	208.6	53.0	136.7	342.0
1318-1320	1165.5	26.5	7.8	25.5	90.1	0.0	50.9	10.1	554.5	91.0	69.0	119.4	534.3
1520-1522	859.0	22.8	21.1	23.6	98.1	8.6	47.0	9.3	359.8	83.6	78.8	129.0	633.0
2400-2402	390.3	18.1	30.3	42.9	70.3	25.5	168.9	9.6	166.0	68.6	58.2	92.6	462.8
2252-2254	550.0	33.1	39.8	36.4	71.3	27.2	68.8	15.0	351.1	124.4	62.0	115.5	479.9
2550-2552	207.6	9.9	18.1	21.4	71.2	9.6	68.3	5.4	95.0	34.2	60.1	84.1	431.1

Appendix C: EMPA – Feldspar, olivine, clinopyroxene, oxides, melt inclusions and groundmass glass

Table 4 Mineral chemical composition from surface samples analysed

Feldspar chemistry											
Sample	**SiO_2**	**TiO_2**	**Al_2O_3**	**FeO**	**MnO**	**MgO**	**CaO**	**Na_2O**	**K_2O**	**BaO**	**Total**
pkm2glomero1plag_core	51.8	0.1	30.1	0.7	0.0	0.2	13.1	3.8	0.2	0.0	99.9
pkm2glomero1plag_rim	58.5	0.1	25.7	0.6	0.0	0.1	7.8	6.6	0.7	0.0	100.1
pkm2plag1core	48.5	0.0	32.9	0.4	0.0	0.1	15.8	2.4	0.1	0.0	100.4
pkm2plag1rim1	51.7	0.1	30.5	0.5	0.0	0.1	13.2	3.8	0.2	0.0	100.0
pkm2plag1rim2	58.6	0.2	26.1	0.6	0.0	0.1	7.5	6.7	0.8	0.0	100.4
pkm2plag2core	48.5	0.0	32.4	0.4	0.0	0.1	15.7	2.6	0.1	0.0	99.9
pkm2plag2core2	49.0	0.0	32.7	0.4	0.0	0.1	15.6	2.7	0.1	0.0	100.6
pkm2plag2rim1	51.3	0.1	31.0	0.6	0.0	0.1	13.4	3.7	0.2	0.0	100.4
pkm2plag2rim2	61.0	0.2	24.2	0.8	0.0	0.0	5.5	7.4	1.3	0.0	100.4
pkm2plag3core	48.1	0.0	33.0	0.4	0.0	0.1	16.0	2.2	0.1	0.0	100.0
pkm2plag3core2	48.1	0.1	33.5	0.3	0.0	0.1	16.3	2.2	0.1	0.0	100.6
pkm2plag3rim1	50.8	0.1	31.0	0.5	0.0	0.2	13.9	3.5	0.2	0.0	100.0
pkm2plag3rim2	58.9	0.1	25.3	0.6	0.0	0.0	7.4	6.7	0.8	0.0	99.8
pkm2glom2plag_core	53.3	0.1	29.6	0.6	0.0	0.1	12.0	4.3	0.3	0.0	100.2
pkm2glom2plag_core2	53.7	0.1	29.3	0.6	0.0	0.1	11.9	4.3	0.3	0.0	100.3
pkm2glom2plag_rim	59.8	0.1	25.0	0.7	0.0	0.1	7.0	6.9	0.9	0.1	100.5
pkm2plag4core	49.2	0.0	32.1	0.6	0.0	0.1	15.4	2.6	0.1	0.0	100.1
pkm2plag4core2	48.9	0.1	33.0	0.6	0.0	0.1	15.6	2.4	0.1	0.0	100.7
pkm2plag4rim	59.8	0.1	25.0	0.7	0.0	0.0	6.6	6.6	1.0	0.0	100.0
pkm2glom3plag1core	53.1	0.1	29.7	0.7	0.0	0.1	12.2	4.2	0.3	0.0	100.4
pkm2glom3plag1rim	58.7	0.1	25.4	0.7	0.0	0.0	7.4	6.7	0.8	0.0	99.9
pkm2glom3plag2core	52.5	0.1	29.7	0.7	0.0	0.1	12.2	4.2	0.3	0.0	99.8
pkm2glom3plag2rim	59.2	0.2	25.1	0.6	0.0	0.0	6.7	6.9	0.9	0.0	99.6
pkm2glom4plagcore	51.7	0.1	30.3	0.6	0.0	0.1	12.9	3.8	0.2	0.0	99.8
pkm2glom4plag2core	52.7	0.1	29.6	0.7	0.0	0.1	12.3	4.2	0.3	0.0	100.0
pkm2glom6plag_core	52.7	0.1	29.3	0.6	0.0	0.1	11.9	4.5	0.3	0.0	99.6
pkm2glom7plag1_core	49.7	0.1	31.5	0.5	0.0	0.1	14.7	2.9	0.1	0.0	99.6
pkm2glom7plag1_rim	59.9	0.2	24.2	0.9	0.0	0.1	6.1	7.0	1.4	0.0	99.7
pkm2glom7plag2core1	50.7	0.1	31.4	0.7	0.0	0.1	14.0	3.3	0.2	0.0	100.4
pkm2glom7plag2core2	53.0	0.1	29.9	0.6	0.0	0.1	12.3	4.3	0.2	0.0	100.6
pkm2glom7plag2core3	52.9	0.1	29.6	0.7	0.0	0.1	12.2	4.3	0.3	0.0	100.1
pkm2glom7plag3core	51.5	0.1	30.5	0.6	0.0	0.2	13.3	3.7	0.2	0.0	100.0
pkm2glom7plag3core2	61.5	0.5	21.3	2.3	0.0	0.1	3.4	7.3	3.1	0.1	99.5
pkm2glom8plag1core	52.0	0.1	30.2	0.6	0.0	0.1	13.0	3.9	0.2	0.0	100.0
pkm2glom8plag2core	52.8	0.1	29.8	0.7	0.0	0.1	12.3	3.9	0.2	0.0	100.0
pkm2glom9plag1core	53.4	0.2	29.2	1.0	0.0	0.1	11.7	4.6	0.3	0.0	100.4
pkm2glom9plag2core	53.4	0.1	29.2	0.5	0.0	0.1	11.7	4.6	0.3	0.0	100.0

pkm2glom9plag2rim	59.1	0.1	25.7	0.7	0.0	0.0	7.2	6.9	0.8	0.0	100.6
pkm2glom9plag3core	54.4	0.1	28.9	0.6	0.0	0.1	10.8	4.9	0.4	0.0	100.2
pkm2glom10plag1core	54.4	0.1	29.0	0.7	0.0	0.1	11.2	4.7	0.3	0.0	100.6
pkm2plagX_core	48.4	0.1	33.4	0.4	0.0	0.1	16.1	2.3	0.1	0.0	100.9
pkm2plagX_rim	59.6	0.1	25.4	0.6	0.0	0.0	7.0	6.7	0.9	0.0	100.5
pkm2plag5_core	53.7	0.1	29.1	0.6	0.0	0.1	11.5	4.7	0.3	0.0	100.1
pkm2plag5_core2	52.9	0.1	29.4	0.6	0.0	0.1	12.1	4.2	0.3	0.0	99.7
pkm2plag5_rim	60.4	0.2	24.1	0.7	0.0	0.1	5.7	7.3	1.2	0.0	99.7
pkm3fspar1_core1	66.5	0.0	19.8	0.2	0.0	0.0	0.6	6.4	6.7	0.0	100.3
pkm3fspar1_core2	66.2	0.1	20.2	0.2	0.0	0.0	0.9	7.2	5.7	0.1	100.5
pkm3fspar1_core3	66.7	0.1	19.6	0.3	0.0	0.0	0.4	6.7	6.7	0.1	100.6
pkm3fspar1_rim	66.3	0.1	20.1	0.2	0.0	0.0	0.8	6.8	6.1	0.1	100.4
pkm3fspar2_core	66.9	0.0	19.5	0.2	0.0	0.0	0.3	6.7	7.0	0.0	100.7
pkm3fspar2_core2	66.1	0.0	19.7	0.2	0.0	0.0	0.5	6.9	6.5	0.1	99.9
pkm3fspar2_rim	66.7	0.0	19.1	0.5	0.0	0.0	0.2	7.0	6.7	0.0	100.1
pkm3fspar3_core	66.6	0.0	19.8	0.2	0.0	0.0	0.5	6.9	6.5	0.1	100.8
pkm3fspar3_core	66.2	0.1	19.4	0.2	0.0	0.0	0.4	6.8	6.7	0.0	99.8
pkm3fspar3_rim	66.5	0.1	20.1	0.3	0.0	0.0	0.8	7.4	5.3	0.1	100.6
pkm3fspar4_core	66.7	0.1	19.5	0.2	0.0	0.0	0.4	6.9	6.5	0.1	100.5
pkm3fspar4_core2	66.7	0.0	19.8	0.2	0.0	0.0	0.5	6.9	6.4	0.1	100.6
pkm3fspar4_rim	65.9	0.1	20.2	0.7	0.0	0.0	1.4	7.6	4.6	0.0	100.5
pkm3glomero1fp1core	66.9	0.1	19.4	0.2	0.0	0.0	0.4	6.9	6.4	0.0	100.4
pkm3glomero1fp1core2	66.9	0.1	19.5	0.2	0.0	0.0	0.3	6.7	6.9	0.0	100.6
pkm3glomero1fp1rim	67.2	0.0	19.2	0.5	0.0	0.0	0.2	6.9	6.4	0.0	100.5
pkm3fp4core	67.2	0.0	19.5	0.2	0.0	0.0	0.3	6.6	6.8	0.0	100.7
pkm3fp4core2	66.5	0.0	20.0	0.2	0.0	0.0	0.7	7.0	5.9	0.1	100.5
pkm3fp4rim	66.7	0.1	19.9	0.4	0.0	0.0	0.8	6.9	6.2	0.1	101.0
dn4pl1core	67.0	0.0	19.7	0.2	0.0	0.0	0.5	6.9	6.5	0.1	100.9
dn4pl1core2	66.2	0.1	20.5	0.2	0.0	0.0	1.1	7.3	5.3	0.1	100.8
dn4pl1rim	66.2	0.0	19.5	0.2	0.0	0.0	0.4	6.9	6.4	0.1	99.7
dn4glom1fp1core	66.5	0.1	20.1	0.2	0.0	0.0	0.9	7.3	5.7	0.1	100.8
dn4glom1fp1core2	66.6	0.1	19.7	0.2	0.0	0.0	0.5	6.9	6.3	0.1	100.4
dn4glom1fp1core3	66.4	0.0	19.6	0.2	0.0	0.0	0.5	6.6	6.7	0.0	100.0
dn4glom1fp1rim	67.0	0.0	19.4	0.5	0.0	0.0	0.3	7.2	6.4	0.0	100.8
dn4fp2core	65.9	0.1	20.8	0.2	0.0	0.0	1.3	7.2	5.0	0.2	100.7
dn4fp2core2	66.5	0.1	19.7	0.3	0.0	0.0	0.7	7.4	5.6	0.1	100.2
dn4fp2rim	67.0	0.1	19.3	0.5	0.0	0.0	0.3	6.8	6.5	0.0	100.5
dn4fp3core	66.8	0.0	19.8	0.2	0.0	0.0	0.5	7.0	6.2	0.1	100.6
dn4fp3core2	66.5	0.1	19.8	0.2	0.0	0.0	0.5	6.7	6.7	0.0	100.4
dn4fp3rim	66.8	0.1	19.5	0.5	0.0	0.0	0.3	7.0	6.5	0.0	100.6
dn4fp4core1	66.3	0.1	19.5	0.2	0.0	0.0	0.5	6.8	6.3	0.1	99.8
dn4fp4core2	66.5	0.0	20.1	0.2	0.0	0.0	0.8	7.2	5.8	0.0	100.7
dn4fp4rim	67.1	0.1	19.5	0.6	0.0	0.0	0.5	7.2	6.1	0.0	101.0
dn4fp5core	67.1	0.0	19.6	0.2	0.0	0.0	0.4	6.9	6.6	0.0	100.9
dn4fp5core2	67.2	0.0	19.4	0.2	0.0	0.0	0.4	6.9	6.7	0.0	100.9
dn4fp5rim	67.6	0.1	19.5	0.5	0.0	0.0	0.3	6.7	6.5	0.0	101.1

Feldspar mineral chemistry cont…

dn4glomero3fp_core	66.9	0.0	19.3	0.2	0.0	0.0	0.4	7.0	6.4	0.0	100.4
dn4glomero3fp_core	67.4	0.0	19.5	0.3	0.0	0.0	0.3	6.9	6.6	0.0	101.0
dn4glomero3fp_core	66.8	0.0	19.8	0.2	0.0	0.0	0.5	7.0	6.3	0.1	100.8
dn4glomero3fp_rim	66.9	0.1	19.0	0.7	0.0	0.0	0.3	6.9	6.6	0.0	100.5
dn4glomero4fp_core	66.9	0.1	19.7	0.2	0.0	0.0	0.5	6.8	6.3	0.0	100.4
dn4glomero4fp_core	65.8	0.1	20.0	0.2	0.0	0.0	0.9	7.3	5.5	0.1	100.0
dn4glomero4fp_rim	66.9	0.0	19.2	0.5	0.0	0.0	0.4	7.0	6.3	0.0	100.3
dn4glomero5fp_core	66.6	0.1	19.5	0.2	0.0	0.0	0.3	6.8	6.8	0.0	100.3
dn4glomero5fp_core	66.8	0.0	19.8	0.2	0.0	0.0	0.5	6.9	6.4	0.0	100.7
dn4glomero5fp_rim	66.9	0.0	19.5	0.5	0.0	0.0	0.4	7.0	6.3	0.0	100.6
PK-02 feld1	65.9	0.1	19.9	0.2	0.0	0.0	0.8	7.1	5.8	0.0	99.8
PK-02 feld2	66.6	0.0	19.1	0.3	0.0	0.0	0.1	7.0	6.5	0.0	99.5
PK-02 feld3	66.4	0.1	19.6	0.2	0.0	0.0	0.4	6.9	6.5	0.0	100.0
PK-02 feld4	66.5	0.1	18.8	0.9	0.0	0.1	0.2	6.9	6.3	0.0	99.8
PK-02 feld5	65.1	0.1	17.9	1.5	0.0	0.1	0.6	6.7	6.4	0.0	98.5
PK-u7 feld1	66.5	0.0	19.2	0.3	0.0	0.0	0.2	7.1	6.4	0.0	99.7
PK-u7 feld2	66.2	0.0	19.2	0.3	0.0	0.0	0.2	7.1	6.2	0.0	99.3
PK-u7 feld3	66.4	0.0	19.4	0.3	0.0	0.0	0.3	6.8	6.6	0.0	99.8
PK-u7 feld4	66.6	0.0	19.2	0.3	0.0	0.0	0.1	7.1	6.4	0.0	99.8
PK-u7 feld5	66.4	0.0	19.1	0.2	0.0	0.0	0.1	7.0	6.5	0.0	99.3
PK-u7 feld6	66.6	0.0	19.3	0.3	0.0	0.0	0.1	6.7	5.8	0.0	98.9
PK-u7 feld7	66.1	0.0	19.3	0.3	0.0	0.0	0.2	7.0	6.4	0.0	99.2
pk-12-feldcore 1	66.5	0.0	19.3	0.5	0.0	0.0	0.2	8.4	4.6	0.0	99.5
pk-12-feldrim1	66.5	0.0	19.3	0.5	0.0	0.0	0.1	8.0	4.9	0.0	99.4
pk-12-feldrim2	65.7	0.0	19.4	0.6	0.0	0.0	0.3	7.4	5.8	0.0	99.2
pk-12-feldcor2	66.3	0.0	19.0	0.5	0.0	0.0	0.1	7.0	6.3	0.0	99.3
pk-12-feldcor3	66.3	0.0	19.0	0.5	0.0	0.0	0.1	7.2	6.4	0.0	99.5
pk-12-feldrim3	67.2	0.0	19.3	0.5	0.0	0.0	0.1	7.2	6.3	0.0	100.6
pk-12-feldrim4	66.2	0.1	18.7	0.5	0.0	0.0	0.2	7.0	6.7	0.0	99.5
pk-12-feldcor4	66.6	0.0	19.3	0.5	0.0	0.0	0.1	6.6	7.1	0.0	100.1
pk-12-feldcor5	66.3	0.0	19.1	0.4	0.0	0.0	0.1	7.3	5.9	0.0	99.2
pk-12-feldrim5	66.7	0.0	19.3	0.5	0.0	0.0	0.2	7.4	5.8	0.0	99.8
pk-12-feldrim6	66.2	0.0	19.0	0.5	0.0	0.0	0.1	7.3	6.0	0.0	99.2
pk-12-feldcor6	66.1	0.0	19.0	0.6	0.0	0.0	0.1	7.2	6.1	0.0	99.3
pk-12-feldcor7	65.9	0.1	19.3	0.5	0.0	0.0	0.2	7.1	6.4	0.0	99.5
pk-12-feldrim7	65.9	0.0	19.2	0.5	0.0	0.0	0.3	7.4	6.0	0.0	99.3
pk-12-feldcor8	66.1	0.0	19.1	0.5	0.0	0.0	0.1	6.8	6.8	0.0	99.4
pk-12-feldrim8	66.4	0.0	19.3	0.5	0.0	0.0	0.1	7.8	5.7	0.0	99.7
pk-12-feldcor9	66.4	0.0	19.1	0.5	0.0	0.0	0.1	7.3	6.1	0.0	99.5
pk-12-feldrim9	66.0	0.0	19.3	0.5	0.0	0.0	0.2	7.0	6.5	0.0	99.5
pk-12-feldcor10	66.4	0.0	19.2	0.6	0.0	0.0	0.1	6.8	6.6	0.0	99.8
pk-12-feldrim10	65.9	0.1	18.0	1.6	0.0	0.0	0.1	7.3	6.2	0.0	99.1
pk-12-feldrim11	66.2	0.0	18.9	0.6	0.0	0.0	0.1	7.2	6.1	0.0	99.1
pk-12-feldcor11	65.9	0.0	18.9	0.6	0.0	0.0	0.0	7.3	6.3	0.0	99.1
pk-20-feldcor1	50.6	0.1	30.6	0.6	0.0	0.1	13.7	3.6	0.1	0.0	99.4

Feldspar mineral chemistry cont…

pk-20-feldrim1	51.1	0.1	30.6	0.6	0.0	0.1	13.4	3.7	0.2	0.0	99.8
pk-20-feldcor2	49.1	0.1	31.5	0.6	0.0	0.2	14.3	3.0	0.2	0.0	98.9
pk-20-feldrim2	50.7	0.1	30.7	0.7	0.0	0.1	13.2	3.8	0.2	0.0	99.4
pk-20-feldrim3	53.1	0.1	29.0	0.6	0.0	0.1	11.6	4.6	0.3	0.0	99.4
pk-20-feldcor3	51.0	0.1	30.6	0.6	0.0	0.1	13.3	3.6	0.1	0.0	99.5
pk-20-feldcor4	50.9	0.1	30.5	0.7	0.0	0.1	13.7	3.6	0.2	0.0	99.8
pk-20-feldrim4	51.6	0.1	30.2	0.8	0.0	0.1	13.0	3.8	0.2	0.0	99.7
pk-20-feldrim5	52.0	0.1	30.1	0.7	0.0	0.1	12.8	4.1	0.2	0.0	100.2
pk-20-feldcor5	51.0	0.1	30.1	0.8	0.0	0.1	13.1	3.8	0.2	0.0	99.2
pk-20-feldcor6	51.0	0.1	30.7	0.7	0.0	0.2	13.6	3.6	0.2	0.0	99.9
pk-20-feldrim6	51.3	0.1	30.2	0.7	0.0	0.1	13.0	3.9	0.2	0.0	99.6
pk-20-feldrim7	57.8	0.1	26.0	0.6	0.0	0.0	7.6	6.5	0.7	0.1	99.4
pk-20-feldcor7	51.0	0.1	30.5	0.7	0.0	0.1	13.2	3.7	0.2	0.0	99.5
pk-20-feldcor8	48.5	0.1	32.4	0.5	0.0	0.1	15.3	2.7	0.1	0.0	99.7
pk-20-feldrim8	50.6	0.1	30.9	0.6	0.0	0.1	13.9	3.5	0.1	0.0	99.7
pk-20-feldrim9	51.4	0.1	30.2	0.7	0.0	0.1	13.1	3.8	0.2	0.0	99.6
pk-20-feldcor9	51.0	0.1	30.6	0.6	0.0	0.2	13.3	3.5	0.1	0.0	99.5
pk-20-feldcor10	51.1	0.1	30.8	0.7	0.0	0.1	13.5	3.6	0.1	0.0	100.1
pk-20-feldrim10	53.2	0.1	29.4	0.6	0.0	0.1	11.9	4.5	0.2	0.0	100.0
pk-20-feldcor11	50.7	0.1	30.4	0.6	0.0	0.1	13.3	3.6	0.2	0.0	98.9
pk-20-feldrim11	50.9	0.1	30.7	0.8	0.0	0.1	13.5	3.6	0.2	0.0	99.7
pk-24-feld1	64.9	0.2	20.4	0.6	0.0	0.0	1.3	7.3	4.8	0.2	99.7
pk-24-feld2	64.1	0.2	22.3	0.5	0.0	0.0	2.9	7.9	2.3	0.4	100.6
pk-24-feld3	64.0	0.2	21.2	0.4	0.0	0.0	2.0	7.6	3.6	0.5	99.4
pk-24-feld4	63.1	0.2	22.4	0.4	0.0	0.0	3.4	8.2	1.6	0.4	99.6
pk-24-feld5	61.9	0.2	23.4	0.7	0.0	0.0	4.3	8.1	1.0	0.3	100.0
pk-24-feld6	65.4	0.1	20.0	0.4	0.0	0.0	0.8	6.8	6.1	0.2	99.9
pk-24-feld7	65.3	0.1	20.1	0.4	0.0	0.0	1.0	7.2	5.1	0.2	99.5
pk-24-feld8	65.8	0.1	19.6	0.3	0.0	0.0	0.6	6.4	6.9	0.1	99.9
pk-24-feld9	62.2	0.2	23.0	0.6	0.0	0.0	4.2	8.0	1.4	0.4	100.0
pk-24-feld10	65.5	0.1	19.8	0.4	0.0	0.0	0.8	6.9	5.9	0.1	99.5
pk-24-feld11	65.6	0.2	20.0	0.4	0.0	0.0	0.7	7.0	5.9	0.2	99.9
pk-24-feld12	65.3	0.1	19.8	0.4	0.0	0.0	0.8	6.8	5.9	0.2	99.3
Pk4_glom1_plag1_cor1	62.3	0.1	22.1	0.6	0.0	0.0	3.3	7.3	3.2	0.3	99.1
Pk4_glom1_plag1_cor2	63.4	0.1	21.6	0.5	0.0	0.0	2.5	7.7	3.6	0.2	99.7
Pk4_glom1_plag1_cor3	63.8	0.2	21.4	0.5	0.0	0.0	2.5	7.6	3.5	0.1	99.7
Pk4_glom1_plag1_rim1	63.0	0.1	22.4	0.5	0.0	0.0	3.4	7.2	3.8	0.1	100.5
Pk4_glom1_plag1_rim2	54.9	0.2	28.1	1.1	0.0	0.1	10.4	5.0	0.4	0.0	100.2
Pk4_glom1_plag1_rim3	54.9	0.2	28.0	0.9	0.0	0.1	10.3	5.2	0.4	0.1	100.0
Pk4_plag1_cor1	54.5	0.2	28.1	1.1	0.0	0.1	10.8	4.8	0.4	0.0	100.0
Pk4_plag1_cor2	54.9	0.3	27.8	1.0	0.0	0.1	10.2	5.4	0.4	0.0	100.1
Pk4_plag1_rim1	60.3	0.2	25.6	0.6	0.0	0.1	6.7	6.4	1.4	0.1	101.3
Pk13_plag1_cor1	52.9	0.1	29.6	0.8	0.0	0.1	12.0	4.1	0.2	0.0	100.0
Pk4_glom2_plag1_cor1	53.9	0.2	28.6	1.2	0.0	0.1	10.9	4.9	0.4	0.0	100.2
Pk4_glom2_plag1_cor2	54.2	0.2	29.1	1.1	0.0	0.1	11.3	4.5	0.4	0.1	101.0

Feldspar mineral chemistry cont…

Pk4_glom2_plag1_rim1	54.8	0.2	27.6	1.0	0.0	0.1	10.0	5.4	0.4	0.1	99.6
Pk4_glom5_plag1_cor1	55.9	0.2	27.2	0.9	0.0	0.1	9.4	5.7	0.5	0.1	100.0
Pk4_glom5_plag1_rim1	64.0	0.2	21.1	0.6	0.0	0.0	1.9	6.9	5.0	0.6	100.3
Pk4_plag1_cor1	55.6	0.2	27.7	0.9	0.0	0.1	9.8	5.5	0.5	0.1	100.3
Pk4_plag1_cor2	56.3	0.2	27.3	0.9	0.0	0.1	9.3	5.6	0.6	0.1	100.3
Pk4_plag3_cor1	54.2	0.2	28.5	0.8	0.0	0.1	10.8	4.9	0.4	0.0	99.9
Pk4_plag3_rim1	56.0	0.2	27.6	0.6	0.0	0.1	9.5	5.2	0.5	0.1	99.8
Pk4_plag4_cor1	53.7	0.2	28.8	0.9	0.0	0.1	11.3	4.7	0.3	0.0	100.1
Pk4_plag4_rim1	60.2	0.2	24.7	0.6	0.0	0.0	6.0	7.3	1.1	0.2	100.3
Pk4_plag5_cor1	53.7	0.1	28.5	0.9	0.0	0.1	11.2	4.7	0.4	0.0	99.6
Pk4_plag5_cor2	54.3	0.1	28.6	0.8	0.0	0.1	11.1	4.9	0.4	0.1	100.4
Pk4_plag5_rim1	60.0	0.2	24.3	0.6	0.0	0.0	4.8	8.4	1.5	0.2	100.0
Pk4_plag5_rim2	55.5	0.2	27.7	0.8	0.0	0.1	9.7	5.6	0.5	0.1	100.0
Pk4_plag6_cor1	54.0	0.2	28.7	0.8	0.0	0.1	11.3	4.7	0.3	0.0	100.1
Pk4_plag6_cor2	53.4	0.2	29.1	0.9	0.0	0.1	11.4	4.6	0.3	0.1	100.1
Pk4_plag6_rim1	55.4	0.2	28.1	0.9	0.0	0.1	10.0	5.4	0.5	0.0	100.5
Pk4_plag7_rim1	54.4	0.2	28.2	1.1	0.0	0.1	10.6	5.0	0.4	0.1	100.1
Pk13_plag1_cor1	52.5	0.1	29.5	0.8	0.0	0.1	12.1	4.2	0.2	0.0	99.6
Pk13_plag1_rim1	53.3	0.1	29.2	0.9	0.0	0.1	11.7	4.5	0.3	0.0	100.2
Pk13_plag2_cor1	53.7	0.1	28.9	0.6	0.0	0.1	11.3	4.6	0.3	0.0	99.9
Pk13_plag2_cor2	53.3	0.1	29.3	0.6	0.0	0.1	11.7	4.6	0.3	0.0	100.1
Pk13_plag2_rim1	51.6	0.1	29.9	0.7	0.0	0.1	12.7	3.9	0.2	0.0	99.3
Pk13_plag2_rim2	53.6	0.1	28.8	0.8	0.0	0.1	11.4	4.6	0.4	0.0	99.7
Pk13_plag3_cor1	53.1	0.1	29.4	0.7	0.0	0.1	11.9	4.4	0.3	0.0	100.1
Pk13_plag3_rim1	53.7	0.2	28.7	0.9	0.0	0.1	11.4	4.7	0.3	0.0	100.0
Pk13_glom1_plag1_cor1	53.1	0.1	29.1	0.7	0.0	0.1	11.9	4.4	0.3	0.0	99.7
Pk13_glom1_plag1_cor2	53.7	0.2	28.7	0.7	0.0	0.1	11.5	4.6	0.3	0.0	99.8
Pk13_glom1_plag1_rim1	53.2	0.1	29.2	0.7	0.0	0.1	11.8	4.4	0.2	0.0	99.8
Pk13_glom1_plag1_rim2	53.0	0.1	28.8	0.8	0.0	0.1	12.2	4.2	0.2	0.0	99.4
Pk13_plag4_cor1	52.6	0.1	29.4	0.6	0.0	0.1	12.2	4.2	0.2	0.0	99.5
Pk13_plag4_rim1	52.6	0.1	29.7	0.8	0.0	0.1	12.4	4.2	0.2	0.0	100.2
Pk13_plag5_rim1	52.7	0.1	29.8	0.6	0.0	0.1	12.2	4.3	0.3	0.0	100.2
Pk13_plag5_rim2	54.7	0.2	28.0	0.7	0.0	0.1	10.6	4.9	0.4	0.0	99.7
Pk13_plag6_cor1	52.6	0.1	29.8	0.6	0.0	0.1	12.5	4.2	0.2	0.0	100.2
Pk13_plag6_rim1	52.9	0.1	29.3	0.8	0.0	0.1	12.1	4.4	0.2	0.0	99.9
Pk13_akfeld1_cor1	57.5	0.1	26.4	0.3	0.0	0.0	8.0	6.2	0.6	0.1	99.2
Pk13_akfeld1_cor2	58.2	0.1	26.4	0.3	0.0	0.0	7.8	6.4	0.6	0.1	100.0
Pk13_akfeld1_rim1	53.4	0.1	28.5	0.6	0.0	0.1	11.2	4.8	0.3	0.0	99.1
Pk13_akfeld2_cor1	53.2	0.1	29.1	0.7	0.0	0.1	11.7	4.4	0.3	0.0	99.5
Pk13_akfeld2_cor2	53.2	0.1	29.3	0.7	0.0	0.1	11.6	4.5	0.2	0.0	99.8
Pk13_akfeld2_rim1	52.8	0.1	29.5	0.8	0.0	0.1	12.0	4.3	0.3	0.0	99.9
Pk13_glom3_akfeld1_cor1	56.5	0.1	27.3	0.4	0.0	0.0	9.3	5.5	0.5	0.1	99.9
Pk13_glom3_akfeld1_rim1	53.6	0.1	29.1	0.6	0.0	0.1	11.5	4.7	0.3	0.1	100.0
Pk13_glom4_akfeld1_cor1	53.6	0.1	29.3	0.7	0.0	0.1	11.5	4.5	0.3	0.0	100.2
Pk13_akfeld3_cor1	52.9	0.1	29.7	0.6	0.0	0.1	12.3	4.2	0.2	0.0	100.1

Feldspar mineral chemistry cont…

Pk13_akfeld3_rim1	52.9	0.1	29.5	0.7	0.0	0.1	11.9	4.3	0.3	0.0	99.8
Pk28_akfeld1_cor1	53.1	0.1	29.5	0.5	0.0	0.1	12.2	4.3	0.3	0.0	100.1
Pk28_akfeld1_cor2	53.0	0.1	29.4	0.5	0.0	0.1	11.8	4.5	0.3	0.0	99.7
Pk28_akfeld1_rim1	52.9	0.2	29.4	0.6	0.0	0.1	11.9	4.4	0.3	0.0	99.7
Pk28_akfeld1_rim2	52.9	0.1	29.7	0.6	0.0	0.1	12.0	4.3	0.3	0.0	100.1
Pk28_akfeld1_rim3	52.9	0.1	29.5	0.6	0.0	0.1	11.9	4.4	0.3	0.0	99.7
Pk28_glom1_akfeld1_cor1	51.1	0.1	30.7	0.7	0.0	0.2	13.5	3.7	0.2	0.0	100.2
Pk28_glom1_akfeld1_cor2	50.8	0.1	30.9	0.7	0.0	0.2	13.5	3.5	0.2	0.0	99.9
Pk28_glom1_akfeld1_rim1	50.4	0.1	30.9	0.7	0.0	0.1	13.9	3.3	0.2	0.0	99.7
Pk28_glom1_akfeld1_rim2	50.9	0.1	30.7	0.6	0.0	0.1	13.6	3.6	0.2	0.0	99.9
Pk28_akfeld2_cor1	48.0	0.1	33.3	0.5	0.0	0.1	16.1	2.1	0.1	0.0	100.2
Pk28_akfeld2_cor2	47.6	0.1	33.0	0.4	0.0	0.1	16.1	2.1	0.1	0.0	99.5
Pk28_akfeld2_rim1	53.7	0.2	28.8	0.8	0.0	0.1	11.3	4.7	0.4	0.1	99.9
Pk28_akfeld2_rim2	56.9	0.3	26.3	1.0	0.0	0.1	8.6	5.9	0.6	0.1	99.8
Pk28_akfeld3_cor1	47.3	0.0	33.6	0.5	0.0	0.1	16.6	2.0	0.1	0.0	100.2
Pk28_akfeld3_cor2	47.4	0.1	33.3	0.5	0.0	0.1	16.4	1.9	0.1	0.0	99.8
Pk28_akfeld3_rim1	47.2	0.1	33.2	0.7	0.0	0.1	16.3	2.0	0.1	0.0	99.7
Pk28_akfeld3_rim2	47.6	0.1	32.9	0.7	0.0	0.1	16.2	2.3	0.1	0.0	99.9
Pk28_akfeld4_cor1	54.1	0.1	28.9	0.6	0.0	0.1	11.1	4.5	0.3	0.0	99.7
Pk28_akfeld4_cor2	50.9	0.1	30.5	0.6	0.0	0.1	13.4	3.7	0.2	0.0	99.4
Pk28_akfeld4_rim1	51.7	0.1	30.4	0.6	0.0	0.1	13.0	3.8	0.2	0.1	99.9
Pk28_akfeld4_rim2	52.2	0.1	29.8	0.7	0.0	0.1	12.3	4.1	0.3	0.1	99.5
Pk28_akfeld5_cor1	49.1	0.1	32.0	0.5	0.0	0.1	14.7	2.7	0.1	0.0	99.3
Pk28_akfeld5_cor2	48.6	0.0	32.4	0.5	0.0	0.1	15.3	2.6	0.1	0.0	99.7
Pk28_akfeld5_rim1	48.2	0.1	32.7	0.5	0.0	0.1	15.5	2.4	0.1	0.0	99.6
Pk28_akfeld5_rim2	52.4	0.1	30.1	0.6	0.0	0.1	12.6	3.9	0.3	0.0	100.2
Pk28_glom2_plag1-cor1	51.1	0.1	30.8	0.7	0.0	0.1	13.6	3.4	0.2	0.0	100.1
Pk28_glom2_plag1-cor2	51.1	0.1	30.8	0.7	0.0	0.1	13.5	3.6	0.2	0.0	100.2
Pk28_glom2_plag1-rim1	52.6	0.1	29.8	0.7	0.0	0.1	12.2	4.1	0.3	0.0	100.0
Pk28_glom2_plag1-rim2	52.9	0.2	29.2	0.7	0.0	0.1	12.2	4.2	0.3	0.0	99.7
Pk28_akfed6-cor1	47.5	0.1	33.4	0.4	0.0	0.1	16.4	2.1	0.1	0.0	100.1
Pk28_akfed6-cor2	47.0	0.1	33.6	0.5	0.0	0.1	16.9	1.8	0.1	0.0	99.9
Pk28_akfed6-rim1	53.3	0.2	29.3	0.7	0.0	0.1	11.8	4.5	0.3	0.0	100.2
Pk28_akfed6-rim2	53.3	0.2	29.4	0.6	0.0	0.1	12.0	4.4	0.3	0.0	100.3
Pk28_akfed6-rim3	50.4	0.1	31.4	0.6	0.0	0.1	14.3	2.9	0.2	0.0	100.0
Pk28_akfed7-cor1	48.3	0.1	32.8	0.6	0.0	0.1	15.7	2.4	0.1	0.0	100.1
Pk28_akfed7-cor2	48.7	0.1	32.7	0.6	0.0	0.1	15.4	2.5	0.1	0.0	100.1
Pk28_akfed7-cor3	47.9	0.0	33.2	0.6	0.0	0.1	15.9	2.2	0.1	0.0	100.0
Pk28_akfed7-rim1	53.0	0.2	29.1	1.1	0.0	0.4	11.6	4.4	0.3	0.0	99.9
Pk28_akfed7-rim2	52.6	0.1	29.9	0.7	0.0	0.1	12.2	4.1	0.3	0.0	100.1
Pk28_akfed7-rim3	52.7	0.1	29.4	0.7	0.0	0.1	12.3	4.3	0.3	0.0	99.9
Pk28_glom3_akfed1-cor1	52.1	0.1	30.0	0.6	0.0	0.1	12.5	4.1	0.2	0.0	99.7
Pk28_glom3_akfed1-cor2	52.2	0.1	29.9	0.6	0.0	0.1	12.4	4.1	0.3	0.1	99.7
Pk28_glom3_akfed1-rim1	49.6	0.0	31.5	0.6	0.0	0.1	14.6	2.8	0.1	0.0	99.5
Pk28_glom3_akfed1-rim2	49.3	0.1	32.0	0.6	0.0	0.2	14.7	2.8	0.1	0.0	99.7

Feldspar mineral chemistry cont…

Pk18feld1cor	66.4	0.1	19.7	0.2	0.0	0.0	0.5	7.6	5.5	0.1	100.1
Pk18feld1rim	67.3	0.0	19.5	0.3	0.0	0.0	0.2	7.2	6.1	0.0	100.7
Pk18feld2cor	66.7	0.0	19.3	0.3	0.0	0.0	0.3	7.4	5.5	0.0	99.6
Pk18feld2rim	67.0	0.0	19.3	0.4	0.0	0.0	0.2	7.5	6.5	0.0	100.9
Pk18feld3cor	66.5	0.0	19.6	0.3	0.0	0.0	0.4	7.4	6.0	0.1	100.3
Pk18feld3rim	66.5	0.1	19.3	0.3	0.0	0.0	0.2	7.3	6.2	0.0	99.9
Pk18feld4cor	66.9	0.0	19.6	0.4	0.0	0.0	0.2	7.4	6.1	0.0	100.6
Pk18feld4rim	66.9	0.0	19.2	0.4	0.0	0.0	0.2	7.3	6.1	0.0	100.2
Pk18feld5cor	66.5	0.1	19.9	0.2	0.0	0.0	0.6	7.7	5.2	0.1	100.2
Pk18feld5rim	67.2	0.0	19.5	0.3	0.0	0.0	0.2	7.4	6.1	0.0	100.7
Pk18feld6cor	66.6	0.1	20.0	0.2	0.0	0.0	0.6	7.5	5.4	0.1	100.5
Pk18feld6rim	66.6	0.0	19.4	0.3	0.0	0.0	0.3	6.5	5.9	0.0	99.0
Pk18feld7cor	66.1	0.0	20.2	0.2	0.0	0.0	0.8	7.7	4.7	0.2	100.0
Pk18feld7rim	65.7	0.1	20.0	0.2	0.0	0.0	0.9	8.1	4.5	0.2	99.6
Pk18feld8cor	66.2	0.0	20.0	0.2	0.0	0.0	0.6	7.8	5.1	0.2	100.1
Pk18feld8rim	66.9	0.0	19.5	0.3	0.0	0.0	0.2	7.5	6.2	0.0	100.7
Pk18feld9core	67.3	0.0	19.2	0.2	0.0	0.0	0.1	7.1	6.8	0.0	100.7
Pk18feld9rim	66.9	0.0	19.4	0.3	0.0	0.0	0.2	7.3	6.1	0.0	100.3
Pk18feld10core	67.3	0.0	19.3	0.3	0.0	0.0	0.2	7.3	6.2	0.0	100.6
Pk18feld10rim	67.8	0.0	19.8	0.3	0.0	0.0	0.2	7.3	6.3	0.0	101.9
Pk18feld11core	66.2	0.0	20.3	0.2	0.0	0.0	0.9	7.9	4.6	0.2	100.2
Pk18feld11rim	66.8	0.1	19.9	0.2	0.0	0.0	0.5	7.3	5.9	0.1	100.7
Pk18feld11cor	66.5	0.1	19.5	0.2	0.0	0.0	0.3	7.1	6.4	0.0	100.1
Pk18feld11rim	67.1	0.1	19.7	0.2	0.0	0.0	0.3	7.1	6.3	0.0	100.9
Pk18feld12cor	65.8	0.0	20.5	0.2	0.0	0.0	1.3	7.9	3.9	0.2	99.8
Pk18feld12rim	66.4	0.1	20.2	0.2	0.0	0.0	0.9	8.3	4.2	0.2	100.5
Pk18feld13rim	66.9	0.0	19.5	0.3	0.0	0.0	0.3	7.3	6.1	0.0	100.4
Pk18feld13core	67.0	0.1	19.4	0.2	0.0	0.0	0.1	7.4	6.3	0.0	100.5
Pk18feld14core	66.2	0.0	20.1	0.3	0.0	0.0	0.7	7.6	4.9	0.2	100.1
Pk18feld14rim	66.6	0.0	19.7	0.3	0.0	0.0	0.5	7.6	5.6	0.2	100.5
Pk18feld15cor	67.2	0.0	19.3	0.3	0.0	0.0	0.2	7.4	6.1	0.0	100.5
Pk18feld15rim	66.6	0.0	19.0	0.5	0.0	0.0	0.2	7.6	6.0	0.0	100.0
Pk13feld1cor	50.9	0.1	31.0	0.6	0.0	0.2	14.0	3.5	0.1	0.0	100.2
Pk13feld1rim	49.1	0.0	32.3	0.6	0.0	0.1	15.2	2.7	0.1	0.0	100.1
Pk13feld2cor	50.8	0.1	31.0	0.5	0.0	0.2	13.8	3.5	0.1	0.0	100.0
Pk13feld2rim	51.5	0.1	31.1	0.6	0.0	0.2	13.5	3.6	0.1	0.0	100.6
Pk13feld3cor	55.4	0.1	28.1	0.5	0.0	0.1	10.0	5.4	0.4	0.0	100.0
Pk13feld3rim	55.1	0.1	28.5	0.5	0.0	0.1	10.1	5.0	0.4	0.0	99.8
Pk13feld4cor	56.4	0.1	27.9	0.4	0.0	0.1	9.5	5.4	0.5	0.0	100.4
Pk13feld4rim	55.8	0.1	28.1	0.5	0.0	0.1	9.9	5.5	0.4	0.0	100.5
Pk13feld5core	52.5	0.1	30.3	0.4	0.0	0.1	12.7	4.0	0.2	0.1	100.4
Pk13feld5rim	54.0	0.1	29.6	0.5	0.0	0.1	11.5	4.8	0.3	0.1	100.9
Pk13feld6rim	55.7	0.1	28.3	0.5	0.0	0.1	10.2	5.4	0.4	0.0	100.6
Pk13feld6cor	56.2	0.1	28.0	0.5	0.0	0.1	9.5	5.5	0.5	0.0	100.3
Pk13feld7cor	52.9	0.1	29.7	0.7	0.0	0.1	12.0	4.2	0.2	0.0	100.1

Feldspar mineral chemistry cont…

Pk13feld7rim	52.7	0.1	29.5	0.8	0.0	0.1	11.9	4.3	0.2	0.0	99.7
Pk13feld8cor	53.0	0.1	29.5	0.8	0.0	0.1	12.2	4.4	0.2	0.0	100.5
Pk13feld8rim	53.1	0.1	29.6	0.9	0.0	0.1	12.1	4.3	0.3	0.0	100.6
Pk13feld9cor	53.8	0.1	29.2	0.8	0.0	0.1	11.5	4.7	0.3	0.0	100.5
Pk13feld9rim	52.3	0.1	30.0	0.7	0.0	0.1	12.9	4.0	0.2	0.0	100.4
Pk13feld10cor	54.0	0.1	29.3	0.4	0.0	0.1	11.1	5.0	0.3	0.0	100.2
Pk13feld10rim	53.6	0.1	29.7	0.3	0.0	0.0	11.7	4.5	0.3	0.0	100.4
Pk13feld11cor	52.3	0.1	29.9	0.8	0.0	0.1	12.3	4.2	0.2	0.0	100.0
Pk13feld11rim	52.5	0.1	29.5	0.8	0.0	0.1	12.1	4.3	0.2	0.0	99.7
Pk13feld12cor	52.7	0.1	30.0	0.8	0.0	0.1	12.2	4.2	0.2	0.0	100.4
Pk13feld12rim	52.8	0.1	29.9	0.8	0.0	0.1	12.2	4.3	0.2	0.0	100.5
Pk13feld13cor	54.2	0.1	28.9	0.6	0.0	0.1	11.3	4.9	0.3	0.0	100.4
Pk13feld13rim	53.9	0.1	29.0	0.7	0.0	0.1	11.2	4.8	0.3	0.0	100.2
Pk13feld14cor	50.3	0.1	32.0	0.5	0.0	0.2	14.5	2.9	0.1	0.0	100.5
Pk13feld14rim	50.2	0.1	31.6	0.7	0.0	0.2	14.5	3.1	0.1	0.0	100.3
Pk13feld15cor	49.7	0.1	31.9	0.5	0.0	0.1	15.0	2.8	0.1	0.0	100.1
Pk13feld15rim	49.9	0.1	31.8	0.6	0.0	0.2	14.5	2.8	0.1	0.0	99.8
Pk13feld16cor	53.4	0.1	29.6	0.6	0.0	0.1	11.8	4.5	0.3	0.0	100.3
Pk13feld16rim	53.4	0.1	29.3	0.8	0.0	0.1	11.8	4.5	0.3	0.0	100.3
Pk13feld17cor	52.4	0.1	29.7	0.7	0.0	0.1	12.6	4.1	0.2	0.0	99.9
Pk13feld17rim	53.6	0.1	29.1	0.9	0.0	0.1	11.5	4.6	0.3	0.0	100.2
Pk13feld18cor	53.1	0.1	29.5	0.7	0.0	0.1	12.1	4.5	0.2	0.0	100.4
Pk13feld18rim	52.8	0.1	29.8	0.8	0.0	0.1	12.2	4.2	0.2	0.0	100.3
Pk13feld19cor	53.6	0.1	29.4	0.7	0.0	0.1	12.0	4.5	0.3	0.0	100.6
Pk13feld19rim	52.6	0.1	30.2	0.7	0.0	0.1	12.1	4.2	0.2	0.0	100.2
Pk13feld20cor	52.9	0.1	29.9	0.6	0.0	0.1	12.2	4.2	0.2	0.0	100.3
Pk13feld20rim	52.9	0.1	30.0	0.8	0.0	0.1	12.5	4.2	0.2	0.0	100.9
Pk28feld1cor	53.4	0.1	29.7	0.8	0.0	0.1	11.9	4.4	0.3	0.0	100.7
Pk28feld1rim	53.8	0.2	30.0	0.8	0.0	0.1	11.8	4.4	0.3	0.1	101.5
Pk28feld2cor	55.5	0.2	28.5	0.8	0.0	0.1	10.0	5.0	0.5	0.1	100.7
Pk28feld2rim	54.6	0.2	29.3	0.9	0.0	0.1	11.1	4.5	0.4	0.1	101.3
Pk28feld3cor	53.3	0.2	29.7	0.8	0.0	0.1	11.8	4.1	0.4	0.0	100.5
Pk28feld3rim	57.1	0.3	26.4	1.2	0.0	0.1	8.4	6.0	0.7	0.1	100.3
Pk28feld4cor	53.8	0.2	29.0	1.0	0.0	0.1	11.4	4.6	0.4	0.1	100.6
Pk28feld4rim	53.4	0.2	29.3	1.1	0.0	0.1	11.5	4.5	0.4	0.1	100.6
Pk28feld5cor	54.0	0.2	28.8	0.7	0.0	0.1	11.2	4.7	0.4	0.0	100.0
Pk28feld5rim	54.8	0.2	28.8	0.6	0.0	0.1	10.7	5.1	0.5	0.0	100.8
Pk28feld6cor	53.0	0.1	29.4	0.7	0.0	0.1	12.0	4.4	0.3	0.1	100.0
Pk28feld6rim	52.7	0.1	29.5	0.6	0.0	0.1	12.0	4.3	0.3	0.0	99.6
Pk28feld7cor	53.2	0.1	29.7	0.8	0.0	0.1	12.0	4.4	0.3	0.1	100.6
Pk28feld7rim	53.1	0.1	29.8	0.7	0.0	0.1	12.1	4.1	0.3	0.1	100.5
Pk28feld8cor	47.4	0.0	33.5	0.5	0.0	0.1	16.5	1.8	0.1	0.0	99.9
Pk28feld8rim	47.3	0.0	33.5	0.5	0.0	0.1	16.4	1.9	0.1	0.0	99.9
Pk28feld9cor	53.4	0.1	29.6	0.5	0.0	0.1	11.7	4.4	0.3	0.1	100.2
Pk28feld9rim	53.7	0.1	29.1	0.6	0.0	0.1	11.7	4.6	0.3	0.0	100.3

Feldspar mineral chemistry cont…

Pk28feld10cor	51.6	0.1	30.8	0.6	0.0	0.1	13.1	3.7	0.2	0.0	100.3
Pk28feld10rim	51.2	0.1	30.7	0.7	0.0	0.1	13.4	3.7	0.2	0.0	100.0
Pk28feld11cor	48.4	0.0	32.7	0.5	0.0	0.1	15.6	2.5	0.1	0.0	99.9
Pk28feld11rim	47.3	0.1	33.5	0.5	0.0	0.1	16.8	1.9	0.1	0.0	100.3
Pk28feld12cor	53.6	0.1	29.3	0.6	0.0	0.1	11.6	4.6	0.3	0.0	100.3
Pk28feld12rim	50.7	0.1	31.0	0.6	0.0	0.1	14.1	3.2	0.2	0.0	99.9
Pk28feld13cor	51.1	0.1	31.0	0.6	0.0	0.1	13.4	3.5	0.2	0.0	100.0
Pk28feld13rim	51.0	0.1	30.5	0.6	0.0	0.1	13.3	3.6	0.2	0.0	99.4
Pk28feld14cor	48.0	0.0	33.0	0.6	0.0	0.1	15.9	2.2	0.1	0.0	99.9
Pk28feld14rim	49.1	0.1	32.4	0.6	0.0	0.1	15.2	2.7	0.1	0.0	100.2
Pk28feld15cor	50.1	0.1	31.8	0.5	0.0	0.1	14.5	3.0	0.2	0.1	100.4
Pk28feld15rim	47.8	0.0	33.3	0.6	0.0	0.1	16.2	2.2	0.1	0.0	100.3
Pk28feld16cor	50.1	0.1	31.8	0.6	0.0	0.1	14.1	3.1	0.2	0.0	100.0
Pk28feld16rim	48.4	0.1	33.2	0.6	0.0	0.1	15.7	2.3	0.1	0.0	100.6
Pk28feld17cor	52.9	0.1	29.8	0.7	0.0	0.1	12.4	4.2	0.3	0.0	100.6
Pk28feld17rim	52.8	0.2	29.6	0.8	0.0	0.2	12.1	4.3	0.3	0.1	100.4
Pk28feld18cor	52.4	0.1	30.4	0.7	0.0	0.1	12.9	4.1	0.2	0.1	101.1
Pk28feld18rim	52.0	0.1	30.3	0.6	0.0	0.1	12.8	3.8	0.2	0.0	100.0
Pk28feld19cor	53.8	0.2	29.1	0.7	0.0	0.1	11.2	4.1	0.4	0.0	99.6
Pk28feld19rim	53.6	0.2	29.2	0.9	0.0	0.1	11.3	4.5	0.4	0.1	100.2
Pk28feld20cor	53.1	0.1	29.5	0.6	0.0	0.1	11.9	4.4	0.3	0.0	100.0
Pk28feld20rim	53.6	0.1	29.5	0.6	0.0	0.1	11.8	4.6	0.3	0.0	100.6
Pk28feld21cor	49.3	0.1	32.5	0.7	0.0	0.1	15.1	2.7	0.1	0.1	100.7
Pk28feld21rim	49.3	0.1	32.5	0.7	0.0	0.1	14.9	2.5	0.1	0.0	100.3
Pk28feld22cor	53.2	0.2	29.7	0.9	0.0	0.1	11.6	4.3	0.3	0.1	100.3
Pk28feld22rim	54.2	0.2	28.5	1.1	0.0	0.1	10.9	4.8	0.5	0.1	100.4
Pk28feld23cor	53.8	0.1	29.4	0.6	0.0	0.1	11.4	4.7	0.3	0.0	100.4
Pk28feld23rim	54.0	0.1	29.2	0.7	0.0	0.1	11.4	4.7	0.3	0.0	100.5
Pk18feld1_1cor	66.4	0.1	19.9	0.2	0.0	0.0	0.6	7.3	5.4	0.1	100.0
Pk18feld1_1rim	65.9	0.1	20.2	0.2	0.0	0.0	1.0	7.8	4.5	0.2	99.9
Pk18feld1_2cor	66.5	0.0	19.3	0.2	0.0	0.0	0.3	7.1	6.5	0.0	100.0
Pk18feld1_2rim	67.1	0.0	19.6	0.2	0.0	0.0	0.4	7.2	6.3	0.0	100.8
Pk18feld1_3cor	66.1	0.1	20.2	0.2	0.0	0.0	1.0	8.0	4.5	0.2	100.4
Pk18feld1_3rim	66.1	0.1	20.6	0.3	0.0	0.0	1.1	8.1	4.3	0.2	100.8
Pk18feld1_4cor	66.7	0.0	19.3	0.3	0.0	0.0	0.1	7.1	6.6	0.0	100.1
Pk18feld1_4rim	66.8	0.0	19.2	0.3	0.0	0.0	0.2	7.3	6.2	0.0	99.9
Pk18feld1_5cor	66.6	0.0	19.6	0.2	0.0	0.0	0.3	7.3	6.1	0.1	100.2
Pk18feld1_5rim	67.2	0.0	19.9	0.3	0.0	0.0	0.5	7.7	5.4	0.1	101.2
Pk18feld1_6cor	66.9	0.0	20.0	0.2	0.0	0.0	0.5	7.6	5.4	0.1	100.7
Pk18feld1_6rim	67.0	0.0	19.3	0.3	0.0	0.0	0.2	7.5	5.8	0.0	100.2
Pk18feld1_7cor	67.2	0.0	19.0	0.4	0.0	0.0	0.0	7.2	6.6	0.0	100.5
Pk18feld1_7rim	67.1	0.0	19.2	0.4	0.0	0.0	0.0	6.4	7.6	0.0	100.8
pk30feld1cor	66.6	0.1	19.7	0.4	0.0	0.0	0.4	7.0	6.5	0.1	100.8
pk30feld1rim	66.0	0.1	19.9	0.4	0.0	0.0	0.7	7.0	6.2	0.0	100.3
pk30feld2cor	66.7	0.0	19.6	0.3	0.0	0.0	0.3	6.9	6.7	0.0	100.5

Feldspar mineral chemistry cont…

pk30feld2rim	66.7	0.0	19.6	0.2	0.0	0.0	0.4	6.9	7.1	0.0	100.9
pk30feld3cor	66.2	0.1	19.6	0.2	0.0	0.0	0.5	7.1	6.4	0.1	100.3
pk30feld3rim	65.7	0.1	20.1	0.3	0.0	0.0	0.9	7.1	5.9	0.1	100.2
pk30feld4cor	66.1	0.1	20.1	0.4	0.0	0.0	0.8	7.2	5.9	0.0	100.7
pk30feld4rim	66.7	0.1	19.6	0.4	0.0	0.0	0.4	6.8	6.8	0.0	100.8
pk30feld5cor	67.7	0.1	20.2	0.2	0.0	0.0	0.5	6.7	6.4	0.0	101.9
pk30feld5rim	66.3	0.1	19.7	0.3	0.0	0.0	0.5	6.9	6.5	0.1	100.2
pk30feld6cor	66.5	0.1	19.4	0.2	0.0	0.0	0.3	6.8	7.1	0.0	100.4
pk30feld6rim	66.4	0.0	19.3	0.2	0.0	0.0	0.3	6.9	6.8	0.0	100.0
pk30feld7cor	66.1	0.1	19.5	0.2	0.0	0.0	0.4	7.2	6.3	0.0	100.0
pk30feld7rim	66.5	0.1	19.6	0.2	0.0	0.0	0.5	7.0	6.8	0.0	100.5
pk30feld8rim	66.5	0.0	19.3	0.3	0.0	0.0	0.2	7.1	6.8	0.0	100.2
pk30feld8cor	67.0	0.0	19.5	0.3	0.0	0.0	0.2	7.0	6.8	0.0	100.7
pk30feld9cor	62.1	0.1	18.5	0.2	0.0	0.0	0.5	7.1	6.4	0.1	95.0
pk30feld9rim	65.8	0.0	19.6	0.2	0.0	0.0	0.7	7.0	6.4	0.1	99.9
pk30feld10cor	66.5	0.0	19.2	0.2	0.0	0.0	0.3	6.6	7.3	0.0	100.2
pk30feld10rim	66.5	0.1	19.3	0.2	0.0	0.0	0.3	6.6	7.0	0.0	100.1
pk30feld11cor	65.7	0.1	20.0	0.2	0.0	0.0	0.9	6.7	5.9	0.0	99.6
pk30feld11rim	66.1	0.1	19.6	0.3	0.0	0.0	0.5	7.0	6.6	0.0	100.2
pk30feld12cor	66.0	0.0	20.1	0.2	0.0	0.0	0.9	7.3	5.7	0.0	100.2
pk30feld12rim	66.4	0.0	19.6	0.2	0.0	0.0	0.4	6.8	6.8	0.0	100.3
pk30feld13cor	67.2	0.0	19.5	0.2	0.0	0.0	0.2	6.9	6.9	0.0	101.0
pk30feld13rim	66.6	0.1	19.5	0.2	0.0	0.0	0.4	7.0	6.8	0.0	100.6
pk30feld14cor	67.1	0.1	19.9	0.2	0.0	0.0	0.5	6.8	6.7	0.1	101.3
pk30feld14rim	66.2	0.1	19.6	0.2	0.0	0.0	0.4	7.1	6.7	0.0	100.3
pk30feld15cor	66.2	0.1	20.3	0.2	0.0	0.0	0.8	6.1	5.8	0.1	99.5
pk30feld15rim	66.3	0.1	20.0	0.2	0.0	0.0	0.7	6.9	6.3	0.1	100.5
pk30feld16cor	66.1	0.1	19.7	0.2	0.0	0.0	0.6	6.9	6.5	0.1	100.0
pk30feld16rim	65.8	0.1	19.9	0.2	0.0	0.0	0.6	6.9	6.4	0.1	100.0
pk30feld17cor	66.3	0.0	19.4	0.3	0.0	0.0	0.3	6.6	7.2	0.0	100.0
pk30feld17rim	65.9	0.1	19.8	0.2	0.0	0.0	0.6	7.1	6.6	0.0	100.2
pk30feld18rim	66.2	0.0	19.6	0.2	0.0	0.0	0.3	6.9	7.0	0.1	100.3
pk30feld18cor	66.3	0.0	19.8	0.2	0.0	0.0	0.5	6.8	6.7	0.0	100.4
pk30feld19cor	65.7	0.1	19.9	0.7	0.0	0.0	1.0	7.1	5.8	0.0	100.2
pk30feld19rim	66.7	0.1	19.7	0.4	0.0	0.0	0.5	7.0	6.6	0.1	101.0
pk30feld20cor	65.4	0.0	19.6	0.2	0.0	0.0	0.7	6.6	6.4	0.0	99.1
pk30feld20rim	66.1	0.0	19.8	0.2	0.0	0.0	0.5	6.7	6.8	0.0	100.1
pk30feld21rim	66.1	0.0	19.7	0.2	0.0	0.0	0.5	7.0	6.7	0.0	100.1
pk30feld21cor	66.3	0.0	19.7	0.2	0.0	0.0	0.3	6.7	7.1	0.0	100.5
pk30feld22cor	66.4	0.1	19.7	0.2	0.0	0.0	0.5	7.2	6.3	0.0	100.4
pk30feld22rim	66.2	0.1	19.5	0.2	0.0	0.0	0.4	7.0	6.6	0.0	100.0
pk30feld23rim	66.2	0.0	19.6	0.2	0.0	0.0	0.5	7.1	6.4	0.0	100.0
pk30feld23cor	66.1	0.1	19.5	0.2	0.0	0.0	0.4	7.2	6.4	0.0	100.0
pk30feld24cor	66.5	0.0	19.6	0.2	0.0	0.0	0.3	7.1	6.9	0.0	100.6
pk30feld24rim	66.5	0.0	19.4	0.2	0.0	0.0	0.3	6.8	7.0	0.0	100.3

Feldspar mineral chemistry cont…

pk30feld25rim	66.5	0.1	19.7	0.2	0.0	0.0	0.5	7.0	6.5	0.1	100.6
pk30feld25cor	66.1	0.1	19.8	0.2	0.0	0.0	0.6	6.7	6.4	0.1	100.1

Olivine mineral chemistry										
Sample	**SiO_2**	**TiO_2**	**Al_2O_3**	**FeO**	**MnO**	**MgO**	**CaO**	**Cr_2O_3**	**NiO**	**Total**
pkm2glomero1ol1core1	39.1	0.0	0.0	16.8	0.2	43.1	0.3	0.0	0.1	99.8
pkm2glomero1ol1rim1	36.6	0.0	0.0	30.9	0.7	32.1	0.3	0.0	0.1	100.9
pkm2glomero1ol1rim2	37.5	0.0	0.0	28.1	0.6	34.0	0.3	0.0	0.1	100.7
pkm2glomero1ol1core2	39.1	0.0	0.0	16.8	0.3	43.3	0.3	0.0	0.1	99.9
pkm2glomero1ol2core1	39.2	0.0	0.0	17.3	0.3	42.7	0.3	0.0	0.1	100.0
pkm2glomero1ol2rim1	37.2	0.0	0.0	29.0	0.6	33.2	0.3	0.0	0.1	100.5
pkm2ol1core1	39.0	0.0	0.0	17.7	0.3	42.3	0.3	0.1	0.1	99.9
pkm2ol1rim2	36.4	0.1	0.0	31.6	0.7	31.3	0.3	0.0	0.1	100.6
pkm2ol1cor1	39.0	0.0	0.0	18.2	0.3	42.1	0.3	0.0	0.1	100.1
pkm2ol2cor1	39.0	0.0	0.1	17.7	0.3	42.7	0.3	0.0	0.1	100.2
pkm2ol2rim1	36.1	0.0	0.0	33.2	0.8	30.4	0.4	0.0	0.1	100.9
pkm2glom4ol1cor1	38.7	0.0	0.0	19.2	0.3	41.3	0.4	0.0	0.1	100.1
pkm2glom4ol1rim1	36.2	0.1	0.1	34.2	0.9	29.1	0.4	0.0	0.0	100.9
pkm2ol3core1	38.4	0.0	0.0	20.3	0.4	40.8	0.3	0.0	0.1	100.4
pkm2ol3rim1	36.8	0.1	0.0	29.4	0.7	33.3	0.3	0.0	0.1	100.6
pkm2ol4cor1	37.7	0.1	0.0	24.8	0.4	37.2	0.3	0.0	0.1	100.6
pkm2 glom5ol1core1	38.7	0.0	0.0	20.0	0.3	40.9	0.4	0.0	0.1	100.4
pkm2 glom5ol1core2	39.0	0.0	0.1	17.7	0.3	42.7	0.3	0.0	0.1	100.3
pkm2 glom5ol1rim1	36.1	0.1	0.0	33.6	0.8	29.8	0.4	0.0	0.0	100.8
pkm2 glom5ol1rim2	37.2	0.1	0.0	27.6	0.6	34.4	0.3	0.0	0.1	100.3
pkm2 glom5ol2cor1	39.1	0.0	0.0	17.4	0.3	42.9	0.3	0.0	0.1	100.2
pkm2 glom6ol1core1	38.5	0.0	0.0	20.1	0.4	40.9	0.3	0.0	0.1	100.4
pkm2 glom6ol1rim1	38.0	0.0	0.0	23.9	0.5	38.1	0.3	0.0	0.1	100.8
pkm2 glom7ol1cor1	39.1	0.0	0.0	17.6	0.3	42.8	0.3	0.0	0.1	100.4
pkm2 glom7ol1cor2	39.2	0.0	0.1	17.7	0.3	42.9	0.3	0.1	0.1	100.6
pkm2 glom7ol1rim1	37.0	0.0	0.0	28.2	0.6	34.2	0.3	0.0	0.0	100.5
pkm2 glom7ol2rim1	35.9	0.1	0.0	33.9	0.9	29.5	0.4	0.0	0.1	100.7
pkm2 ol4cor1	36.5	0.0	0.0	32.5	0.8	30.2	0.3	0.0	0.0	100.6
pkm2 ol4rim1	36.1	0.0	0.0	34.2	0.8	29.1	0.4	0.0	0.0	100.6
pkm2 ol5cor1	39.0	0.0	0.1	18.9	0.3	41.4	0.3	0.0	0.1	100.2
pkm2 ol5rim1	36.8	0.1	0.0	31.9	0.8	31.0	0.4	0.0	0.1	100.9
pkm2 ol6cor1	37.8	0.0	0.1	26.0	0.4	36.2	0.3	0.0	0.0	100.8
pk4_glom2_ol1_cor1	36.4	0.1	0.1	32.4	0.5	30.7	0.4	0.0	0.0	100.6
pk4_glom2_ol1_cor2	36.3	0.1	0.1	32.1	0.6	30.8	0.4	0.0	0.0	100.2
pk13_ol1_rim1	37.5	0.1	0.0	27.1	0.5	34.9	0.4	0.0	0.1	100.5
pk13_ol1_rim2	37.6	0.1	0.0	28.2	0.4	34.1	0.4	0.0	0.0	100.9
pk13_ol3_cor1	38.4	0.0	0.0	22.5	0.4	38.7	0.3	0.0	0.1	100.4
pk13_ol3_rim1	37.2	0.1	0.0	27.9	0.5	34.5	0.4	0.0	0.0	100.6
pk13_ol3_rim2	36.7	0.1	0.0	30.4	0.5	32.3	0.4	0.0	0.1	100.5
pk13_ol4_cor1	38.0	0.0	0.0	23.7	0.4	38.3	0.3	0.0	0.0	100.9
pk13_ol4_cor2	38.4	0.0	0.0	23.6	0.4	38.1	0.3	0.0	0.1	100.9
pk13_ol4_rim1	38.1	0.1	0.0	23.6	0.4	38.2	0.3	0.0	0.1	100.8
pk13_ol5_cor1	38.3	0.1	0.0	22.8	0.4	38.8	0.4	0.0	0.1	100.7
pk13_ol5_rim2	37.0	0.1	0.1	29.0	0.5	33.3	0.4	0.0	0.0	100.3
pk13_ol6_cor1	37.6	0.0	0.0	25.5	0.4	36.7	0.4	0.0	0.0	100.5
pk13_ol6_rim2	36.4	0.1	0.0	30.4	0.5	32.4	0.5	0.0	0.0	100.2
pk13_ol6_rim3	36.6	0.1	0.0	32.6	0.5	30.1	0.5	0.0	0.0	100.4
pk13_ol6_2_cor1	37.8	0.1	0.0	23.9	0.4	37.7	0.4	0.0	0.0	100.3

Olivine mineral chemistry contd…

pk13_ol6_2_cor2	37.6	0.1	0.0	24.0	0.4	37.8	0.4	0.0	0.1	100.3
pk13_ol6_2_rim1	36.3	0.1	0.1	30.0	0.5	32.6	0.4	0.0	0.1	100.0
pk13_ol6_2_rim2	35.8	0.1	0.1	36.4	0.6	27.3	0.5	0.0	0.0	100.8
pk13_ol6_2_rim3	36.0	0.2	0.0	36.2	0.6	27.3	0.5	0.0	0.0	100.9
pk13_glom2_ol1_cor1	37.6	0.1	0.0	23.9	0.4	37.4	0.4	0.0	0.0	99.9
pk13_glom2_ol1_cor2	37.6	0.1	0.0	24.0	0.4	37.4	0.3	0.0	0.0	99.8
pk13_glom2_ol1_cor3	37.4	0.0	0.0	25.1	0.4	36.9	0.4	0.0	0.0	100.2
pk13_glom2_ol1_rim1	35.9	0.1	0.0	35.8	0.6	27.9	0.5	0.0	0.0	100.8
pk13_ol7_cor1	37.4	0.1	0.0	25.5	0.4	36.5	0.3	0.0	0.0	100.3
pk13_ol7_rim1	37.3	0.1	0.0	27.4	0.4	35.2	0.4	0.0	0.0	100.9
pk13_ol7_rim2	37.3	0.1	0.0	27.4	0.4	34.7	0.4	0.0	0.0	100.3
pk28_ol1_cor1	38.7	0.0	0.0	19.9	0.3	40.9	0.3	0.0	0.1	100.3
pk28_ol1_cor2	38.8	0.0	0.0	20.1	0.3	41.0	0.3	0.0	0.1	100.6
pk28_ol1_rim1	38.7	0.0	0.0	20.0	0.3	41.3	0.3	0.0	0.1	100.7
pk28_ol1_rim2	38.6	0.0	0.0	19.8	0.3	41.3	0.3	0.0	0.1	100.4
pk28_ol1_rim3	38.5	0.0	0.0	21.6	0.4	39.7	0.3	0.0	0.1	100.6
pk28_ol2_cor1	38.6	0.0	0.0	20.4	0.3	40.6	0.3	0.0	0.1	100.4
pk28_ol2_cor2	38.6	0.0	0.1	20.2	0.3	40.9	0.3	0.0	0.1	100.4
pk28_ol2_rim1	39.0	0.0	0.0	20.0	0.3	40.8	0.3	0.0	0.1	100.7
pk28_ol2_rim2	38.7	0.0	0.0	19.9	0.3	41.3	0.3	0.0	0.1	100.7
pk28_ol3_cor1	39.1	0.0	0.0	17.7	0.3	42.7	0.3	0.0	0.1	100.2
pk28_ol3_rim1	39.4	0.0	0.0	15.8	0.3	44.4	0.3	0.0	0.1	100.4
pk28_ol3_rim2	39.6	0.0	0.0	16.2	0.3	43.7	0.3	0.0	0.1	100.3
pk28_ol3_cor2	39.1	0.0	0.0	18.0	0.3	42.5	0.3	0.0	0.1	100.5
pk28_ol5_cor2	38.8	0.0	0.0	20.3	0.3	40.8	0.3	0.0	0.1	100.7
pk28_ol5_rim1	39.2	0.0	0.0	18.8	0.3	41.6	0.2	0.0	0.2	100.5
pk28_ol5_rim2	39.5	0.0	0.0	17.8	0.3	42.2	0.3	0.1	0.2	100.3
pk28_ol6_cor1	39.1	0.0	0.0	19.5	0.4	41.0	0.3	0.0	0.1	100.3
pk28_ol6_cor2	39.0	0.0	0.0	19.5	0.3	41.1	0.3	0.0	0.1	100.4
pk28_ol6_rim1	38.8	0.0	0.0	18.8	0.3	41.8	0.3	0.0	0.1	100.3
pk28_ol6_rim2	39.0	0.0	0.1	18.9	0.3	41.6	0.3	0.0	0.2	100.3
pk28_ol7_cor1	39.2	0.0	0.0	17.7	0.3	42.8	0.3	0.0	0.1	100.4
pk28_ol7_rim1	38.1	0.0	0.0	22.8	0.4	38.7	0.3	0.0	0.1	100.5
pk28_ol8_cor1	38.9	0.0	0.0	20.3	0.3	40.8	0.3	0.0	0.1	100.7
pk28_ol8_rim1	38.7	0.0	0.0	22.1	0.4	39.1	0.3	0.0	0.1	100.7
pk28_ol9_cor1	39.4	0.0	0.0	18.4	0.3	42.2	0.3	0.0	0.1	100.9
pk28_ol9_rim1	38.8	0.0	0.0	19.7	0.4	41.1	0.3	0.0	0.1	100.3
pk28_ol10_cor1	38.9	0.0	0.0	19.6	0.3	41.1	0.3	0.0	0.1	100.3
pk28_ol10_rim1	38.8	0.0	0.0	22.4	0.4	38.3	0.3	0.0	0.1	100.5
pk30ol1cor	31.1	0.1	0.0	59.5	3.2	5.7	1.1	0.0	0.0	100.7
pk30ol1rim	30.6	0.1	0.1	59.4	3.3	5.8	1.0	0.0	0.0	100.3
pk30ol1rim1	30.5	0.1	0.1	59.6	3.3	5.7	1.0	0.0	0.0	100.3
pk30ol1rim3	30.8	0.1	0.1	59.5	3.3	5.8	0.8	0.0	0.0	100.3
pk13ol1cor	36.2	0.1	0.0	34.1	0.5	28.5	0.6	0.0	0.0	100.1
pk13ol1rim	35.2	0.1	0.0	40.9	0.7	23.0	0.6	0.0	0.0	100.6
pk13ol2cor	38.6	0.1	0.0	21.8	0.4	38.9	0.4	0.0	0.0	100.2

Olivine mineral chemistry contd..

pk13ol2rim	38.1	0.1	0.0	23.7	0.4	37.8	0.4	0.0	0.1	100.5
pk13ol3cor	38.6	0.0	0.0	21.9	0.3	39.1	0.3	0.0	0.1	100.4
pk13ol3rim	37.4	0.1	0.0	29.1	0.5	33.0	0.4	0.0	0.1	100.5
pk13ol4cor	38.0	0.0	0.0	24.9	0.4	36.8	0.3	0.0	0.1	100.6
pk13ol5cor	38.0	0.0	0.0	22.7	0.3	38.2	0.3	0.0	0.0	99.7
pk13ol5rim	38.0	0.0	0.0	23.8	0.4	37.8	0.3	0.0	0.0	100.4
pk13ol6cor	37.3	0.0	0.0	28.5	0.5	34.1	0.3	0.0	0.0	100.8
pk13ol7cor	38.4	0.0	0.1	22.3	0.4	38.5	0.3	0.0	0.1	100.2
pk13ol7rim	38.2	0.1	0.0	22.5	0.4	38.7	0.3	0.0	0.0	100.2
pk28ol1cor	37.6	0.2	0.0	26.4	0.7	35.1	0.5	0.0	0.0	100.4
pk28ol1rim	37.0	0.2	0.1	26.9	0.7	34.6	0.7	0.0	0.0	100.1
pk28ol2cor	37.3	0.1	0.1	26.1	0.6	35.6	0.4	0.0	0.1	100.3
pk28ol2rim	37.1	0.1	0.1	26.2	0.7	35.5	0.5	0.0	0.0	100.1
pk28ol4cor	37.9	0.0	0.0	18.7	0.3	41.1	0.3	0.0	0.1	98.5
pk28ol4rim	38.3	0.0	0.0	21.5	0.4	39.2	0.3	0.0	0.1	99.8
pk28ol5cor	38.7	0.0	0.0	19.1	0.3	41.2	0.3	0.0	0.1	99.8
pk28ol5rim	38.8	0.0	0.0	20.0	0.3	40.5	0.3	0.0	0.1	100.0
pk28ol6cor	38.8	0.0	0.0	20.2	0.4	40.8	0.3	0.0	0.1	100.6
pk28ol6rim	39.1	0.0	0.0	19.1	0.3	41.1	0.3	0.0	0.1	100.1
pk28ol7cor	39.5	0.0	0.1	15.4	0.3	44.3	0.3	0.0	0.2	100.0
pk28ol7rim	40.2	0.0	0.0	12.1	0.2	46.7	0.3	0.0	0.2	99.7

Clinopyroxene mineral chemistry											
Sample	**SiO2**	**TiO_2**	**Al_2O_3**	**FeO**	**MnO**	**MgO**	**CaO**	**Na_2O**	**Cr_2O_3**	**NiO**	**Total**
pkm2glom2cpx1_core	48.8	1.6	5.0	7.6	0.2	14.0	21.5	0.4	0.5	0.0	99.5
pkm2glom2cpx1_core	47.3	2.5	6.3	8.7	0.2	13.0	20.9	0.4	0.1	0.0	99.5
pkm2glom2cpx1_core	51.6	0.9	2.6	6.6	0.2	15.6	21.5	0.3	0.5	0.0	99.9
pkm2glom2cpx1_rim	49.1	1.4	4.6	6.8	0.1	14.2	21.8	0.4	0.8	0.0	99.3
pkm2glom3cpx1_core	48.8	1.9	5.2	7.9	0.2	13.9	21.0	0.5	0.5	0.0	99.7
pkm2glom3cpx1_core	51.9	0.9	2.5	7.7	0.3	15.5	20.6	0.4	0.3	0.0	100.1
pkm2glom3cpx1_core	50.1	1.2	3.4	9.2	0.3	14.1	20.8	0.5	0.1	0.0	99.6
pkm2glom3cpx1_rim	51.8	1.0	2.7	7.2	0.2	15.7	21.0	0.3	0.3	0.0	100.2
pkm2glom3cpx1_rim	52.0	0.9	2.6	7.2	0.2	15.4	21.3	0.3	0.2	0.0	100.1
pkm2glom3cpx1_rim2	51.0	1.3	2.8	10.6	0.3	13.0	20.7	0.5	0.0	0.0	100.2
pkm2glom3cpx2_core	49.1	1.8	4.7	8.6	0.2	13.6	21.0	0.5	0.4	0.0	99.8
pkm2glom3cpx2_core	51.7	1.0	2.3	8.9	0.3	15.0	20.2	0.3	0.2	0.0	99.9
pkm2glom3cpx2_core	48.9	1.9	5.3	7.9	0.2	13.5	21.0	0.5	0.6	0.0	99.8
pkm2glom3cpx2_rim	51.7	0.9	2.9	7.5	0.2	15.0	21.5	0.3	0.2	0.0	100.3
pkm2glom3cpx2_rim	50.3	1.3	4.2	7.2	0.2	14.2	21.7	0.4	0.5	0.0	100.1
pkm2glom3cpx2_rim	49.2	1.8	5.0	7.3	0.2	13.8	21.7	0.4	0.5	0.0	99.8
pkm2glom3cpx3_core	49.5	1.6	5.0	7.2	0.2	14.1	21.2	0.4	0.6	0.0	99.8
pkm2glom3cpx3_core	49.2	1.7	4.8	8.8	0.2	13.6	20.9	0.5	0.1	0.0	99.8
pkm2glom8cpx1_core	48.8	1.7	4.9	8.1	0.2	13.5	21.3	0.5	0.3	0.0	99.3
pkm2glom8cpx1_core	50.6	1.3	3.7	8.0	0.2	15.0	20.4	0.3	0.2	0.0	99.7
pkm2glom8cpx1_core	46.3	2.9	7.7	9.2	0.2	12.4	20.2	0.6	0.1	0.0	99.5
pkm2glom8cpx1_core	50.9	1.1	3.6	6.8	0.2	15.3	21.2	0.4	0.7	0.0	100.0
pkm2glom8cpx1_rim	50.9	1.2	2.5	11.1	0.3	12.6	20.9	0.5	0.0	0.0	100.1
pkm2glom8cpx2_core	49.0	1.8	5.0	8.0	0.2	13.5	21.4	0.4	0.2	0.0	99.6
pkm2glom8cpx2_core	51.4	1.2	2.8	8.5	0.2	15.5	19.9	0.3	0.2	0.0	100.1
pkm2cpx1_core	49.7	1.7	4.5	8.6	0.2	13.9	20.9	0.4	0.1	0.0	99.9
pkm2cpx1_core	46.8	2.7	6.8	8.1	0.2	12.8	21.3	0.5	0.3	0.0	99.4
pkm2cpx1_rim	49.0	1.6	4.6	7.5	0.2	13.9	21.4	0.4	0.4	0.0	99.1
pkm2glom9_core	50.3	1.5	2.7	10.0	0.3	13.8	20.3	0.4	0.0	0.0	99.1
pkm2glom9_core	49.8	1.6	3.3	9.5	0.2	13.8	21.2	0.4	0.0	0.0	99.8
pkm2glom9_rim	46.6	2.3	6.4	7.8	0.2	13.4	21.2	0.4	0.5	0.0	98.8
pkm2glom9cpx2_core	47.2	2.8	5.6	9.9	0.2	12.2	21.1	0.5	0.0	0.0	99.5
pkm2glom9cpx2_rim	49.1	1.6	4.9	7.1	0.2	14.1	21.7	0.4	0.6	0.0	99.5
pkm2glom10cpx1_core	51.5	1.1	2.5	8.3	0.2	15.0	21.0	0.3	0.1	0.0	99.9
pkm2glom10cpx1_core	50.4	1.2	3.8	7.7	0.2	14.7	20.9	0.4	0.4	0.0	99.7
pkm2cpx3_core	50.9	1.2	2.8	8.1	0.2	15.7	20.2	0.3	0.2	0.0	99.6
pkm2cpx3_core	51.5	0.9	2.6	7.5	0.2	15.9	20.3	0.3	0.3	0.0	99.6
pkm2cpx3_rim	46.5	2.6	6.8	8.6	0.2	13.2	20.9	0.5	0.3	0.0	99.5
pkm2cpx5_core	51.9	0.9	2.8	7.2	0.2	16.5	19.8	0.3	0.5	0.0	100.0
pkm2cpx5_core	50.0	1.6	3.6	9.5	0.2	13.8	20.9	0.4	0.1	0.0	100.2
pkm2cpx5_rim	48.6	2.1	5.3	8.2	0.2	13.5	21.4	0.4	0.2	0.0	99.9
pk3Plag1_cpx1_core	51.5	0.6	0.8	18.4	0.8	8.1	20.8	0.5	0.0	0.0	101.4
pk3Plag1_cpx1_core	51.1	0.6	0.7	18.2	0.8	8.0	20.6	0.5	0.0	0.0	100.5
pk3Plag1_cpx1_rim	50.9	0.6	0.7	18.8	0.8	7.8	20.7	0.5	0.0	0.0	100.9

Clinopyroxene mineral chemistry contd…

pk3Plag1_cpx2_core	51.0	0.6	0.7	18.8	0.8	7.8	21.0	0.6	0.0	0.0	101.2
pk3Plag1_cpx2_core	51.0	0.5	0.8	18.7	0.8	7.8	20.9	0.5	0.0	0.0	101.1
pk3cpx_incl_plag2	51.1	0.6	0.6	20.4	0.9	6.6	20.9	0.5	0.0	0.0	101.5
pk3cpx1_core	50.4	0.6	0.6	22.0	1.0	5.8	20.3	0.6	0.0	0.0	101.3
pk3cpx1_rim	50.9	0.6	0.7	20.3	0.8	6.8	20.6	0.6	0.0	0.0	101.3
pk3cpx2_core	50.5	0.6	0.7	21.6	1.0	5.9	20.2	0.7	0.0	0.0	101.1
pk3cpx2_core	51.0	0.6	0.7	21.2	1.0	6.1	20.6	0.7	0.0	0.0	101.8
pk3cpx2_rim	51.0	0.5	0.7	19.4	0.8	7.3	20.9	0.5	0.0	0.0	101.2
pk3cpx2_rim	51.1	0.5	0.6	19.8	0.9	7.0	21.0	0.6	0.0	0.0	101.5
pk3cpx3_core	49.9	0.5	0.4	25.0	1.0	3.5	20.2	0.9	0.0	0.0	101.4
pk3cpx3_core	50.6	0.5	0.7	20.9	0.8	6.2	20.8	0.6	0.0	0.0	101.1
pk3cpx3_rim	50.6	0.6	0.6	20.0	0.8	6.7	20.8	0.6	0.0	0.0	100.7
pk3glomero1_cpx1_core	50.5	0.6	0.6	21.3	0.9	6.0	20.8	0.6	0.0	0.0	101.3
pk3glomero1_cpx1_core	50.7	0.6	0.6	20.6	0.9	6.7	20.7	0.6	0.0	0.0	101.3
pk3cpx4_core	50.1	0.6	0.6	23.4	1.0	4.5	20.4	0.8	0.0	0.0	101.3
pk3cpx4_core	50.5	0.5	0.6	21.3	0.9	6.0	20.6	0.6	0.0	0.0	101.1
dn4glom1_cpx_incl	50.7	0.6	0.6	20.3	0.9	6.6	20.7	0.5	0.0	0.0	100.9
dn4glom1_cpx_incl2	50.3	0.8	0.9	20.5	0.9	6.5	20.1	0.7	0.0	0.0	100.7
dn4glom2_cpx1core	50.6	0.5	0.5	21.7	1.0	5.5	20.7	0.6	0.0	0.0	101.1
dn4glom2_cpx1rim	50.7	0.5	0.6	19.1	0.9	7.5	20.6	0.9	0.0	0.0	100.7
dn4glom2_cpx2core	50.1	0.9	1.1	21.0	0.9	6.2	20.5	0.7	0.0	0.0	101.3
dn4glom2_cpx2rim	50.3	0.5	0.6	19.3	0.9	7.4	20.6	0.9	0.0	0.0	100.4
dn4cpx1_core	50.7	0.5	0.6	19.0	0.9	7.1	20.5	0.8	0.0	0.0	100.2
dn4cpx1_core	50.2	0.5	0.5	22.2	1.0	5.6	20.5	0.6	0.0	0.0	101.1
dn4cpx2_core	50.4	0.6	0.6	21.2	0.9	6.0	20.7	0.6	0.0	0.0	100.9
dn4cpx2_core	49.9	0.6	0.6	21.0	0.9	6.0	20.5	0.6	0.0	0.0	100.0
dn4cpx2_rim	49.9	0.6	0.7	19.3	0.9	7.0	20.3	0.9	0.0	0.0	99.6
dn4cpx_incl_glom_3	50.1	0.5	0.6	21.5	0.9	5.7	20.7	0.6	0.0	0.0	100.6
dn4cpx_incl2_glom_3	49.9	0.5	0.6	21.1	0.9	6.0	20.4	0.6	0.0	0.0	100.0
dn4cpx_incl3_glom_3	50.0	0.5	0.6	21.3	0.9	5.8	20.7	0.6	0.0	0.0	100.3
dn4cpx_incl4_glom_3	50.4	0.5	0.5	21.5	0.9	5.7	20.8	0.7	0.0	0.0	101.1
dn4cpx_incl4_glom_3	50.6	0.6	0.7	19.8	0.9	7.0	20.3	0.6	0.0	0.0	100.4
dn4cpx_incl1_glom_4	49.8	0.8	1.0	20.0	0.9	7.0	19.9	0.6	0.0	0.0	100.0
dn4cpx_incl2_glom_4	49.8	1.0	1.1	20.1	0.9	6.9	20.0	0.7	0.0	0.0	100.5
dn4cpx_incl1_glom_5	50.2	0.6	0.6	20.3	0.9	6.6	20.8	0.6	0.0	0.0	100.5
dn4cpx_incl2_glom_5	50.2	0.5	0.6	19.4	0.8	6.8	20.9	0.6	0.0	0.0	100.0
dn4cpx_incl3_glom_5	50.6	0.5	0.6	20.3	0.8	6.6	20.7	0.7	0.0	0.0	100.8
dn4cpx_incl3_glom_5	50.6	0.5	0.6	20.2	0.8	6.5	20.7	0.6	0.0	0.0	100.7
pk4_glom1_cpx1_cor1	49.5	2.0	2.8	11.0	0.3	13.1	20.6	0.3	0.0	0.0	99.7
pk4_glom1_cpx1_cor2	49.8	1.9	2.6	11.2	0.3	13.1	20.5	0.3	0.0	0.0	99.7
pk4_glom1_cpx1_rim1	46.3	3.7	5.4	11.4	0.2	11.0	20.8	0.6	0.0	0.0	99.4
pk4_glom1_cpx1_rim2	47.4	3.0	4.3	12.4	0.3	10.8	20.9	0.5	0.0	0.0	99.7
pk4_cpx1_cor1	46.5	3.5	5.1	10.3	0.2	11.5	21.5	0.6	0.0	0.0	99.3
pk4_cpx1_cor2	48.9	2.3	3.4	10.9	0.3	12.9	20.3	0.4	0.0	0.0	99.5
pk4_cpx1_rim1	47.7	2.9	4.9	11.0	0.2	11.8	20.9	0.6	0.0	0.0	100.0

Clinopyroxene mineral chemistry contd…

pk4_cpx1_rim2	46.9	3.2	3.9	16.0	0.4	8.3	20.8	0.7	0.0	0.0	100.1
pk4_cpx2_cor1	49.6	1.9	3.2	9.7	0.2	13.0	21.3	0.4	0.0	0.0	99.3
pk4_cpx2_cor2	46.3	3.8	5.3	11.8	0.3	10.9	20.7	0.7	0.0	0.0	99.6
pk4_cpx2_rim1	47.6	3.0	3.7	14.3	0.3	9.7	20.7	0.7	0.0	0.0	100.0
pk4_cpx2_rim2	47.7	3.0	3.7	14.2	0.3	9.6	20.8	0.7	0.0	0.0	100.1
pk4_cpx4_cor1	47.5	2.9	4.7	10.6	0.2	12.0	20.9	0.5	0.0	0.0	99.4
pk4_cpx4_cor2	47.2	3.0	5.1	10.7	0.2	11.6	20.8	0.6	0.1	0.0	99.2
pk4_cpx4_rim1	48.4	3.4	4.4	13.3	0.3	9.4	20.8	0.7	0.0	0.0	100.8
pk4_cpx4_rim2	50.0	3.5	4.6	13.4	0.3	8.6	21.0	0.6	0.0	0.0	102.0
pk4_cpx5_cor1	46.5	3.4	5.0	10.9	0.3	11.6	21.2	0.6	0.0	0.0	99.3
pk4_cpx5_cor2	47.9	2.8	4.3	10.9	0.2	12.0	21.2	0.5	0.0	0.0	99.7
pk4_cpx5_rim1	48.2	2.6	3.7	12.1	0.3	11.1	21.1	0.6	0.0	0.0	99.7
pk4_cpx5_rim2	48.3	2.6	3.5	12.4	0.3	10.8	20.9	0.6	0.0	0.0	99.5
pk4_cpx6_cor1	48.4	2.5	4.0	10.3	0.2	12.2	21.4	0.4	0.0	0.0	99.6
pk4_cpx6_rim1	46.7	3.8	4.6	11.8	0.3	10.6	20.8	0.6	0.0	0.0	99.2
pk4_cpx7_cor1	48.7	2.4	4.0	10.2	0.2	12.6	21.2	0.5	0.0	0.0	99.9
pk4_cpx7_cor2	47.8	2.7	4.5	10.9	0.3	11.9	21.1	0.5	0.0	0.0	99.6
pk4_cpx7_rim1	48.1	2.7	3.9	11.5	0.3	11.8	21.0	0.5	0.0	0.0	99.8
pk4_cpx7_rim2	48.2	2.5	4.2	10.5	0.2	12.5	20.9	0.5	0.0	0.0	99.4
pk4_cpx8_cor1	46.8	3.5	4.9	11.1	0.2	11.5	20.9	0.6	0.0	0.0	99.7
pk4_cpx8_cor2	47.5	3.0	4.4	10.5	0.3	11.9	21.2	0.5	0.0	0.0	99.2
pk4_cpx8_rim1	47.4	3.1	4.2	12.7	0.3	10.6	20.5	0.7	0.0	0.0	99.5
pk4_cpx8_rim2	48.1	2.9	3.8	11.7	0.3	11.0	21.1	0.6	0.0	0.0	99.3
pk13_cpx1_cor1	47.4	2.4	6.1	8.8	0.2	13.2	20.5	0.5	0.1	0.0	99.0
pk13_cpx1_cor2	47.1	2.3	6.1	9.0	0.2	13.3	20.5	0.5	0.1	0.0	99.1
pk13_cpx1_rim1	48.9	1.6	4.9	8.0	0.2	14.1	21.3	0.4	0.2	0.0	99.5
pk13_cpx1_rim2	49.3	1.5	4.7	7.8	0.2	14.2	21.2	0.4	0.2	0.0	99.6
pk13_glom1_cpx1_cor1	48.2	2.1	5.1	8.2	0.2	13.7	21.1	0.5	0.3	0.0	99.3
pk13_glom1_cpx1_cor2	47.0	2.7	6.3	9.0	0.2	12.8	20.9	0.5	0.1	0.0	99.5
pk13_glom1_cpx1_cor3	47.0	2.7	6.5	9.2	0.2	12.8	20.6	0.5	0.1	0.0	99.6
pk13_glom1_cpx1_rim1	51.4	1.1	2.6	7.6	0.2	15.7	20.8	0.4	0.2	0.0	100.0
pk13_glom1_cpx1_rim2	51.0	1.2	2.8	8.2	0.2	15.7	20.1	0.3	0.2	0.0	99.6
pk13_cpx2_cor1	51.9	0.6	1.2	12.5	0.4	11.8	21.3	0.5	0.0	0.0	100.3
pk13_cpx2_cor2	51.8	0.6	1.4	12.7	0.4	11.5	21.1	0.5	0.0	0.0	100.0
pk13_cpx2_cor3	51.7	0.5	1.3	13.8	0.5	10.8	21.5	0.5	0.0	0.0	100.5
pk13_cpx2_rim1	48.9	1.6	5.5	7.9	0.2	14.3	20.6	0.5	0.4	0.0	99.8
pk13_cpx2_rim2	49.0	1.8	5.6	7.7	0.2	14.1	20.7	0.4	0.3	0.0	99.7
pk13_cpx3_cor1	49.5	1.7	4.1	9.3	0.2	13.6	20.6	0.5	0.0	0.0	99.5
pk13_cpx3_cor2	47.5	2.3	5.8	10.2	0.2	12.6	20.7	0.5	0.0	0.0	99.8
pk13_cpx3_rim2	49.7	1.5	4.4	7.8	0.2	14.4	21.1	0.4	0.3	0.0	99.8
pk13_cpx3_rim1	49.5	1.7	4.6	7.7	0.1	14.3	21.2	0.4	0.4	0.0	99.9
pk13_cpx4_cor1	48.7	2.0	5.2	8.0	0.2	13.9	21.0	0.4	0.2	0.0	99.5
pk13_cpx4_cor2	48.1	2.2	5.6	8.2	0.2	13.8	20.9	0.4	0.2	0.0	99.7
pk13_cpx4_rim1	47.6	2.4	5.8	8.5	0.1	13.3	21.0	0.4	0.3	0.0	99.4
pk13_cpx4_rim2	48.5	1.9	5.0	8.0	0.2	14.0	21.1	0.4	0.4	0.0	99.4

Clinopyroxene mineral chemistry contd…

pk13_cpx5_cor1	51.1	1.2	2.9	8.8	0.2	15.8	19.3	0.3	0.2	0.0	99.8
pk13_cpx5_cor2	45.9	2.9	7.1	9.2	0.2	12.9	20.6	0.5	0.3	0.0	99.4
pk13_cpx5_rim1	48.7	1.9	5.3	8.6	0.2	13.9	20.7	0.4	0.3	0.0	100.0
pk13_cpx5_rim2	50.9	1.3	2.8	8.7	0.3	15.5	19.8	0.3	0.1	0.0	99.7
pk13_cpx6_cor1	47.5	2.3	6.1	9.6	0.2	13.2	20.2	0.5	0.1	0.0	99.7
pk13_cpx6_rim1	48.7	1.5	5.4	7.7	0.2	14.3	20.8	0.5	0.4	0.0	99.4
pk13_cpx6_rim2	48.4	1.9	6.0	7.7	0.1	14.1	20.4	0.4	0.5	0.0	99.5
pk13_glom3_cpx1_cor1	51.5	1.0	2.7	7.8	0.2	16.4	19.4	0.3	0.2	0.0	99.5
pk13_glom3_cpx1_cor2	47.5	2.2	5.9	9.0	0.2	13.4	20.0	0.5	0.2	0.0	99.0
pk13_glom3_cpx1_rim1	48.8	1.8	5.1	8.4	0.2	13.6	21.2	0.5	0.1	0.0	99.7
pk13_glom3_cpx1_rim2	49.0	2.2	5.3	9.2	0.2	12.9	21.1	0.5	0.0	0.0	100.3
pk13_cpx7_cor1	51.0	1.0	3.1	8.0	0.2	14.3	21.1	0.5	0.5	0.0	99.7
pk13_cpx7_cor2	51.0	1.0	3.0	8.2	0.2	14.4	21.0	0.5	0.4	0.0	99.7
pk13_cpx7_cor3	51.3	1.0	3.0	8.2	0.2	14.4	21.0	0.5	0.4	0.0	100.1
pk13_cpx7_rim1	50.4	1.7	3.4	8.9	0.2	14.1	21.1	0.5	0.1	0.0	100.2
pk13_cpx7_rim2	50.5	1.4	3.5	8.7	0.2	14.6	20.3	0.4	0.1	0.0	99.9
pk13_glom4_cpx1_cor1	50.0	1.4	4.2	8.7	0.2	14.7	19.6	0.4	0.1	0.0	99.4
pk13_glom4_cpx1_rim1	47.7	2.4	6.0	8.7	0.2	13.4	20.6	0.5	0.1	0.0	99.4
pk13_cpx8_cor1	44.6	3.4	9.1	9.3	0.2	12.0	20.3	0.6	0.0	0.0	99.4
pk13_cpx8_cor2	45.1	3.4	8.5	9.2	0.2	12.2	20.3	0.5	0.1	0.0	99.4
pk13_cpx8_rim1	49.7	1.9	4.5	8.6	0.2	14.1	20.4	0.4	0.1	0.0	99.8
pk13_cpx8_rim2	48.3	1.9	5.8	7.8	0.2	14.1	20.7	0.5	0.4	0.0	99.6
pk13_cpx10_cor1	49.4	1.6	5.3	7.7	0.2	14.1	20.6	0.6	0.3	0.0	99.8
pk13_cpx10_cor2	49.9	1.3	4.7	7.5	0.2	14.7	20.6	0.4	0.3	0.0	99.6
pk13_cpx10_rim1	49.0	1.5	5.4	7.6	0.2	14.2	20.8	0.4	0.3	0.0	99.4
pk13_cpx10_rim2	50.5	1.2	3.6	7.6	0.2	14.9	20.4	0.4	0.3	0.0	99.1
pk28_glom1_cpx1_cor1	47.5	2.0	6.5	6.8	0.1	13.7	21.4	0.3	0.7	0.0	99.1
pk28_glom1_cpx1_cor2	47.7	2.1	6.5	6.7	0.1	13.7	21.5	0.4	0.9	0.0	99.6
pk28_glom1_cpx1_rim2	49.1	1.5	5.6	6.2	0.1	14.2	21.9	0.3	0.9	0.0	100.0
pk28_cpx2_cor1	50.1	1.2	5.0	5.7	0.2	14.9	22.1	0.4	0.3	0.0	99.9
pk28_cpx2_cor2	49.6	1.3	4.8	5.6	0.1	15.1	22.2	0.4	0.3	0.0	99.3
pk28_cpx2_cor3	50.0	1.2	4.9	5.2	0.1	15.0	22.2	0.4	0.3	0.0	99.3
pk28_cpx2_rim1	49.6	1.4	4.9	6.6	0.1	14.4	21.8	0.4	0.7	0.0	99.9
pk28_cpx2_rim2	49.6	1.5	4.9	6.5	0.1	14.3	21.9	0.4	0.7	0.0	99.9
pk28_cpx2_rim3	48.0	1.9	6.0	7.2	0.1	13.9	21.3	0.4	0.3	0.0	99.2
pk28_cpx2_rim4	48.0	2.0	5.8	7.2	0.1	13.8	21.6	0.4	0.4	0.0	99.4
pk28_cpx3_cor1	49.6	1.1	5.2	4.8	0.1	15.4	21.8	0.4	0.8	0.0	99.3
pk28_cpx3_cor2	49.4	1.1	5.3	4.9	0.1	15.4	21.9	0.4	0.8	0.0	99.4
pk28_cpx3_cor3	49.4	1.3	5.9	5.4	0.1	14.7	21.8	0.4	0.8	0.0	99.8
pk28_cpx3_cor4	48.8	1.3	5.9	5.3	0.1	14.8	21.8	0.5	0.8	0.0	99.2
pk28_cpx3_rim1	49.4	1.3	5.7	5.3	0.1	15.0	21.8	0.4	0.8	0.0	99.8
pk28_cpx3_rim2	48.3	1.9	5.7	7.0	0.1	14.0	21.6	0.4	0.4	0.0	99.4
pk28_cpx3_rim3	47.5	2.0	5.8	7.1	0.2	14.0	21.2	0.4	0.4	0.0	98.7
pk28_cpx4_cor1	50.6	0.8	4.1	5.8	0.1	15.3	22.0	0.3	0.2	0.0	99.1

Clinopyroxene mineral chemistry contd…

pk28_cpx4_cor2	49.3	1.7	4.3	7.8	0.2	14.0	21.6	0.5	0.2	0.0	99.5
pk28_cpx4_rim1	49.4	1.5	4.4	7.1	0.2	14.1	21.7	0.5	0.3	0.0	99.2
pk28_cpx4_rim2	50.4	1.1	4.5	5.8	0.1	15.2	21.7	0.4	0.5	0.0	99.7
pk28_glom3_cpx1_cor1	48.3	1.9	6.3	6.8	0.1	13.9	21.6	0.4	0.5	0.0	99.6
pk28_glom3_cpx1_cor2	48.9	1.7	5.6	6.7	0.1	14.3	21.7	0.4	0.3	0.0	99.7
pk28_glom3_cpx1_rim1	48.2	1.7	6.2	6.6	0.1	14.1	21.5	0.4	0.6	0.0	99.5
pk28_glom3_cpx1_rim2	48.8	1.5	5.6	6.3	0.2	14.4	21.9	0.3	0.5	0.0	99.4
pk28_glom3_cpx2_cor1	48.9	1.4	5.5	6.6	0.1	14.3	21.6	0.3	0.6	0.0	99.3
pk28_glom3_cpx2_rim1	51.6	0.8	2.9	5.6	0.1	16.1	21.3	0.3	0.5	0.0	99.2
pk-02cpx2	50.0	0.7	0.8	21.3	0.9	6.1	20.2	0.7	0.0	0.0	100.6
pk-02cpx3	50.0	0.7	0.8	21.4	1.0	6.1	20.2	0.7	0.0	0.0	100.9
pk-02cpx4	49.8	0.7	0.8	21.3	0.9	6.0	20.3	0.6	0.0	0.0	100.5
pk-02cpx5	50.3	0.6	0.6	21.2	0.9	6.3	20.3	0.6	0.0	0.0	100.8
pk-02embayedcpx1	50.1	0.8	0.8	21.3	1.0	6.1	20.0	0.7	0.0	0.0	100.8
pk-02 cpx6	49.2	1.0	1.1	22.4	1.1	5.3	19.3	0.9	0.0	0.0	100.1
pk-02 cpx7	49.3	1.4	0.8	24.4	1.1	3.4	18.1	1.9	0.0	0.0	100.3
pk-02 cpx8	50.5	0.8	1.0	18.8	0.9	7.9	20.1	0.6	0.0	0.0	100.5
pk-02 cpx9	50.0	0.6	0.6	22.9	1.0	4.9	20.4	0.7	0.0	0.0	101.1
pk-02 cpx10	49.8	0.7	0.7	23.3	1.0	4.4	20.1	0.9	0.0	0.0	100.9
pk-02 cpx11	50.0	0.7	0.7	22.4	1.0	5.2	20.3	0.8	0.0	0.0	101.1
pk-02 cpx12	49.8	0.6	0.5	22.5	1.1	5.4	20.1	0.6	0.0	0.0	100.6
pk-02 cpx13	50.2	0.5	0.6	22.2	0.9	5.1	20.7	0.6	0.0	0.0	100.8
pk-u7 cpx1	49.6	0.7	0.5	26.0	1.1	2.9	19.1	1.2	0.0	0.0	101.1
pk-u7 cpx2	49.5	0.8	0.5	25.8	1.1	2.9	19.5	1.1	0.0	0.0	101.1
pk-u7 cpx3	50.4	0.5	0.4	25.6	1.0	2.9	20.1	1.1	0.0	0.0	101.9
pk-u7 cpx4	49.8	0.5	0.5	25.7	1.0	2.8	19.6	1.2	0.0	0.0	100.9
pk-u7 cpx5	49.1	0.8	0.5	27.2	1.1	2.3	18.5	1.4	0.0	0.0	101.0
pk-u7 cpx6	48.9	1.2	0.6	26.4	1.0	2.1	18.8	1.5	0.0	0.0	100.5
pk-u7 cpx7	48.5	1.1	0.6	27.4	1.1	1.9	18.2	1.6	0.0	0.0	100.4
pk-u7 cpx8	49.4	0.6	0.5	26.3	1.0	2.5	19.3	1.5	0.0	0.0	101.0
pk-u7 cpx9	49.4	0.5	0.4	25.2	1.0	3.0	19.7	1.1	0.0	0.0	100.5
pk-u7 cpx rim10	49.1	0.4	0.4	24.9	1.0	3.4	19.9	0.9	0.0	0.0	100.0
pk-u7 cpx cor10	49.1	0.4	0.3	26.1	1.1	2.7	20.2	0.9	0.0	0.0	100.7
pk-u7 cpx cor11	49.4	0.4	0.3	26.1	1.1	2.7	19.9	0.9	0.0	0.0	100.9
pk-u7 cpx rim11	49.3	0.5	0.4	24.9	1.0	3.2	20.2	0.9	0.0	0.0	100.5
pk-u7 cpx rim12	48.7	0.5	0.9	24.3	0.9	3.5	19.5	1.0	0.0	0.0	99.2
pk-u7 cpx cor12	49.4	0.6	0.5	24.5	1.0	3.7	20.1	0.9	0.0	0.0	100.8
pk-u7 cpx cor13	48.8	0.9	0.7	25.9	1.1	3.0	19.2	1.1	0.0	0.0	100.7
pk-u7 cpx rim13	49.1	0.5	0.5	24.9	1.0	3.3	19.8	1.0	0.0	0.0	100.1
pk-u7 cpx cor14	49.4	0.5	0.3	25.8	1.0	3.0	20.2	1.0	0.0	0.0	101.2
pk-u7 cpx rim14	49.3	0.5	0.4	24.7	0.9	3.5	20.4	0.9	0.0	0.0	100.6
pk-2cpx rim21	49.8	0.5	0.5	23.2	1.0	4.5	20.4	0.7	0.0	0.0	100.8
pk-2cpxcor21	48.7	0.8	0.8	24.2	1.0	4.0	19.7	1.0	0.0	0.0	100.3
pk-2cpxrim22	49.9	0.5	0.5	23.5	1.0	4.3	20.3	0.8	0.0	0.0	100.7
pk-2cpxcore22	49.9	0.6	0.5	22.7	0.9	5.0	20.6	0.7	0.0	0.0	100.8

Clinopyroxene mineral chemistry contd…											
pk-2cpx2rim	50.3	0.5	0.6	22.0	1.0	5.5	20.4	0.6	0.0	0.0	101.0
pk-2cpx2core	49.6	0.7	0.7	21.4	0.9	5.9	20.2	0.6	0.0	0.0	100.1
pk-2cpx3core	49.5	0.7	0.8	21.9	1.0	5.6	19.6	0.8	0.0	0.0	100.0
pk-2cpx3rim	49.3	0.6	0.6	22.3	1.0	4.8	20.2	0.8	0.0	0.0	99.6
pk-2cpx6rim	50.0	0.5	0.6	22.8	1.0	4.9	20.6	0.7	0.0	0.0	101.0
pk-2cpx6core	50.5	0.5	0.6	21.2	0.9	5.8	20.6	0.6	0.0	0.0	100.8
pk-2cpx8core	49.7	0.7	0.7	22.5	1.0	5.0	20.4	0.7	0.0	0.0	100.7
pk-2cpx8rim	49.9	0.5	0.6	22.7	1.0	4.9	20.4	0.8	0.0	0.0	100.9
pk-u7 cpx2rim	49.9	0.6	0.4	25.3	1.0	2.8	19.7	1.1	0.0	0.0	100.8
pk-u7 cpx2core	49.5	0.5	0.5	25.5	0.9	2.8	20.0	1.2	0.0	0.0	100.9
pk-u7 cpx3core	49.2	0.8	0.5	26.7	1.1	2.2	19.2	1.3	0.0	0.0	101.1
pk-u7 cpx3rim	49.7	0.5	0.4	25.4	1.0	2.9	19.8	1.1	0.0	0.0	100.7
pk-12 cpx cor1	51.5	0.8	1.6	10.6	0.3	13.0	21.7	0.5	0.0	0.0	100.1
pk-12 cpx rim1	50.1	0.4	0.4	22.7	1.0	4.5	19.8	1.3	0.0	0.0	100.2
pk-12 cpxcor2	51.2	0.9	1.7	11.5	0.4	12.4	21.4	0.6	0.0	0.0	100.0
pk-12 cpxrim2	50.0	0.5	0.5	23.3	0.9	4.4	19.7	1.3	0.0	0.0	100.6
pk-12 cpxcor3	50.3	1.1	1.6	16.4	0.6	8.3	19.3	1.5	0.0	0.0	98.9
pk-12 cpxrim3	50.0	0.6	0.4	24.5	0.9	3.2	18.2	2.4	0.0	0.0	100.0
pk-12 cpxcor4	50.5	1.0	1.3	15.5	0.5	9.1	21.2	0.9	0.0	0.0	100.0
pk-12 cpxrim4	52.9	0.5	4.6	20.2	0.8	1.9	13.2	3.8	0.0	0.0	98.0
pk-12 cpxcor5	48.9	0.9	0.6	26.1	1.1	2.7	19.1	1.3	0.0	0.0	100.6
pk-12 cpxrim5	49.7	1.0	0.8	25.5	0.9	2.3	16.9	2.8	0.0	0.0	99.9
pk-12 cpxcor6	50.2	0.6	0.6	20.1	0.8	6.4	20.8	0.9	0.0	0.0	100.5
pk-12 cpxrim6	48.6	0.6	0.4	25.4	0.9	2.4	19.7	1.4	0.0	0.0	99.5
pk-12 cpxcor7	49.3	0.9	0.7	25.5	1.1	2.8	18.9	1.4	0.0	0.0	100.5
pk-12 cpxrim7	49.7	0.6	0.6	24.6	1.0	2.9	18.0	2.5	0.0	0.0	99.9
pk-12 cpxcor8	51.2	0.5	0.5	18.4	0.8	8.2	20.3	0.7	0.0	0.0	100.6
pk-12 cpxrim8	65.7	0.1	17.1	2.0	0.1	0.1	1.0	6.3	0.0	0.0	92.3
pk-12 cpxcor9	51.7	0.8	1.6	10.5	0.4	12.9	21.7	0.5	0.0	0.0	100.0
pk-12 cpxrim9	51.4	0.6	1.1	14.0	0.6	10.8	21.0	0.6	0.0	0.0	99.9
pk-12 cpxrim10	60.8	0.3	12.7	10.0	0.3	0.9	6.3	5.1	0.0	0.0	96.5
pk-12 cpxcor10	51.4	0.7	1.3	11.5	0.4	12.5	21.4	0.6	0.0	0.0	99.8
pk-20cpxcor1	49.8	1.7	2.7	10.0	0.2	12.6	21.3	0.5	0.0	0.0	98.9
pk-20cpxcor2	48.9	2.2	3.9	10.3	0.2	12.7	20.8	0.5	0.0	0.0	99.4
pk-20cpxrim2	50.8	1.5	2.6	9.3	0.2	13.6	21.4	0.4	0.0	0.0	99.7
pk-20cpxrim1	48.2	2.5	4.6	10.0	0.2	12.7	21.1	0.4	0.0	0.0	99.8
pk-20cpxcor3	39.4	0.0	0.1	20.1	0.3	41.6	0.3	0.0	0.0	0.1	101.9
pk-20cpxrim3	38.6	0.0	0.0	23.5	0.4	38.6	0.4	0.0	0.0	0.1	101.6
pk-20cpxcor4	39.0	0.0	0.1	19.7	0.3	41.7	0.3	0.0	0.0	0.1	101.2
pk-20cpxrim4	38.8	0.1	0.1	20.7	0.3	40.8	0.3	0.0	0.0	0.1	101.2
pk-20cpxrim5	38.5	0.0	0.1	23.3	0.3	39.2	0.3	0.0	0.0	0.1	101.9
pk-20cpxcor5	39.2	0.0	0.1	18.8	0.3	42.7	0.3	0.0	0.0	0.1	101.5
pk-20cpxcor6	50.6	1.3	3.0	7.8	0.2	14.9	21.3	0.3	0.1	0.0	99.4
pk-20cpxrim6	48.0	2.6	4.6	9.7	0.2	12.8	21.5	0.5	0.0	0.0	99.8
pk-20cpxrim7	35.4	0.1	0.0	41.8	0.8	24.2	0.4	0.0	0.0	0.0	102.8
pk-20cpxcor7	37.6	0.0	0.0	28.9	0.5	34.1	0.3	0.0	0.0	0.0	101.6

Clinopyroxene mineral chemistry contd…

pk-20cpxcor8	48.4	1.8	5.1	7.7	0.2	13.7	21.4	0.4	0.3	0.0	99.1
pk-20cpxrim9	48.8	2.1	4.1	9.3	0.2	13.1	21.7	0.5	0.0	0.0	99.8
pk-20cpxcor10	38.6	0.0	0.1	21.1	0.3	40.5	0.3	0.0	0.0	0.1	101.1
pk-20cpxrim10	37.8	0.0	0.0	26.6	0.4	36.5	0.4	0.0	0.0	0.0	101.9
pk-20cpxrim11	39.4	0.0	0.1	21.9	0.3	39.0	0.3	0.0	0.0	0.1	101.1
pk-20cpxcor11	39.0	0.0	0.0	18.7	0.3	42.3	0.3	0.0	0.0	0.1	100.8
pk-24cpxcor1	47.5	3.2	3.2	12.9	0.5	9.5	20.5	1.2	0.0	0.0	98.5
pk-24cpxrim1	36.4	2.4	2.5	12.4	0.5	11.5	20.5	1.4	0.0	0.0	87.6
pk-24cpxrim2	36.2	2.3	2.5	12.4	0.5	11.4	20.6	1.4	0.0	0.0	87.4
pk-24cpxcor2	48.5	2.6	2.7	12.6	0.5	9.9	21.3	1.1	0.0	0.0	99.4
pk-24cpxcor3	49.4	2.0	2.4	12.1	0.5	10.4	21.4	0.9	0.0	0.0	99.1
pk-24cpxrim3	49.9	1.7	2.5	12.3	0.5	10.0	21.1	1.1	0.0	0.0	99.1
pk-24cpxrim4	49.2	2.7	3.7	12.2	0.5	9.7	20.2	1.4	0.0	0.0	99.6
pk-24cpxcor4	51.1	1.3	1.6	12.2	0.5	10.9	21.2	0.9	0.0	0.0	99.5
pk-24cpxcor5	47.5	3.2	3.6	12.7	0.5	9.8	20.9	1.2	0.0	0.0	99.3
pk-24cpxrim5	48.3	3.0	3.9	12.4	0.5	9.9	20.4	1.1	0.0	0.0	99.5
pk-24cpxrim6	49.4	2.2	2.5	11.9	0.5	10.7	21.2	1.1	0.0	0.0	99.4
pk-24cpxcor6	49.1	2.5	2.8	12.6	0.5	10.3	20.6	1.1	0.0	0.0	99.6
pk-24cpxcor7	41.9	2.7	3.4	11.3	0.4	7.9	24.6	1.3	0.0	0.0	93.5
pk-24cpxcor8	0.5	0.0	0.1	0.9	0.1	0.3	53.4	0.1	0.0	0.0	55.4
pk18cpx1cor	50.0	0.5	0.5	22.8	1.1	4.5	19.8	1.1	0.0	0.0	100.4
pk18cpx1rim	50.9	0.3	1.0	21.3	0.9	5.8	18.1	2.6	0.0	0.0	100.8
pk18cpx2cor	50.8	0.5	0.7	20.1	0.9	6.4	20.3	1.0	0.0	0.0	100.7
pk18cpx2rim	50.1	0.6	0.8	22.1	1.0	5.2	19.8	1.3	0.0	0.0	101.0
pk18cpx3core	50.4	0.6	0.7	19.7	0.9	6.9	20.8	0.7	0.0	0.0	100.7
pk18cpx3rim	50.0	0.6	1.0	21.5	0.8	5.2	21.0	1.0	0.0	0.0	101.1
pk18cpx4cor	50.4	0.4	0.6	21.3	0.9	5.7	20.4	1.2	0.0	0.0	100.9
pk18cpx4cor2	50.5	0.4	0.6	21.2	0.9	5.6	20.3	1.1	0.0	0.0	100.7
pk18cpx4rim	50.4	0.4	0.6	21.5	0.9	5.6	20.3	1.1	0.0	0.0	100.9
pk18cpx5cor	50.6	0.4	0.6	21.2	0.9	5.7	20.3	1.2	0.0	0.0	100.9
pk18cpx5rim	50.4	0.4	0.5	21.9	1.0	5.3	20.3	0.9	0.0	0.0	100.6
pk18cpx6cor	50.3	0.5	0.7	20.9	0.9	5.8	20.1	1.2	0.0	0.0	100.3
pk18cpx6rim	50.0	0.5	0.7	21.9	0.9	5.3	20.2	1.2	0.0	0.0	100.8
pk18cpx7cor	50.5	0.4	0.5	22.9	1.0	5.0	20.3	1.0	0.0	0.0	101.6
pk18cpx7rim	50.2	0.7	0.8	22.6	0.9	4.5	19.4	1.4	0.0	0.0	100.6
pk18cpx8cor	50.0	0.6	0.8	21.7	0.9	5.4	20.1	1.3	0.0	0.0	100.8
pk18cpx8rim	50.0	0.7	0.8	22.0	1.0	5.3	19.6	1.4	0.0	0.0	100.7
pk18cpx9cor	50.4	0.4	0.6	23.4	0.9	4.3	19.7	1.5	0.0	0.0	101.1
pk18cpx9rim	49.9	0.6	0.7	22.4	0.9	5.2	19.9	1.3	0.0	0.0	100.9
pk18cpx10cor	49.6	0.9	0.9	22.5	1.0	5.1	19.5	1.3	0.0	0.0	100.9
pk18cpx10rim	50.3	0.4	0.6	21.5	0.9	5.7	20.4	1.1	0.0	0.0	101.0
pk18cpx11cor	49.9	0.6	0.7	22.8	1.0	5.0	19.7	1.3	0.0	0.0	101.0
pk18cpx11rim	50.5	0.4	0.7	21.8	0.9	5.5	20.2	1.3	0.0	0.0	101.2
pk18cpx12core	50.3	0.5	0.8	21.4	0.9	5.7	20.1	1.2	0.0	0.0	100.9
pk18cpx12rim	50.8	0.4	0.6	21.5	0.9	5.7	20.4	1.1	0.0	0.0	101.4

pk18cpx13cor	50.5	0.4	0.7	21.2	0.9	5.8	20.4	1.2	0.0	0.0	101.1
Clinopyroxene mineral chemistry contd…											
pk18cpx13rim	50.3	0.4	0.6	21.6	0.9	5.6	20.2	1.2	0.0	0.0	100.8
pk18cpx14cor	50.2	0.7	0.9	21.5	0.9	5.7	20.2	1.1	0.0	0.0	101.1
pk18cpx14rim	50.3	0.4	0.6	21.5	0.9	5.6	20.3	1.3	0.0	0.0	100.9
pk18cpx15cor	50.3	0.5	0.7	22.1	0.9	5.2	20.0	1.3	0.0	0.0	101.1
pk18cpx15rim	50.3	0.5	0.7	22.0	0.9	5.3	20.0	1.2	0.0	0.0	100.9
pk18cpx16cor	50.4	0.5	0.6	21.5	0.9	5.5	20.3	1.2	0.0	0.0	100.8
pk18cpx16rim	50.4	0.5	0.7	21.3	0.9	5.5	20.2	1.2	0.0	0.0	100.7
pk18cpx17cor	50.1	0.7	0.8	22.2	0.9	5.1	19.7	1.5	0.0	0.0	101.0
pk18cpx17rim	50.7	0.5	0.6	21.7	0.9	5.5	20.1	1.3	0.0	0.0	101.2
pk18cpx18rim	50.5	0.5	0.7	21.4	0.9	5.6	20.1	1.2	0.0	0.0	100.8
pk18cpx18cor	49.8	0.9	1.1	20.8	1.0	6.0	19.6	1.2	0.0	0.0	100.3
pk18cpx19cor	50.7	0.8	1.4	17.5	0.8	8.7	19.8	1.1	0.0	0.0	100.9
pk18cpx19rim	50.4	0.5	1.0	21.8	0.9	5.0	19.2	2.0	0.0	0.0	100.7
pk13cpx1cor	38.4	0.0	0.1	23.1	0.4	39.3	0.3	0.0	0.0	0.0	101.6
pk13cpx1rim	38.4	0.1	0.1	23.0	0.4	39.7	0.3	0.0	0.0	0.0	101.9
pk13cpx2cor	50.9	1.4	3.0	9.0	0.2	14.0	20.9	0.5	0.0	0.0	99.9
pk13cpx2rim	49.4	1.6	5.1	7.4	0.2	14.4	20.8	0.4	0.2	0.0	99.5
pk13cpx3cor	50.9	1.2	3.2	8.9	0.2	15.3	20.0	0.3	0.0	0.0	100.1
pk13cpx3rim	48.1	2.1	5.2	10.4	0.2	12.8	20.7	0.5	0.0	0.0	100.0
pk13cpx4cor	38.5	0.0	0.0	24.1	0.4	39.1	0.3	0.0	0.0	0.0	102.5
pk13cpx4rim	37.9	0.0	0.1	25.8	0.4	36.9	0.3	0.0	0.0	0.0	101.5
pk13cpx5cor	50.0	1.3	4.4	7.5	0.2	14.8	20.7	0.4	0.2	0.0	99.4
pk13cpx5rim	49.2	1.6	5.5	8.2	0.2	14.2	20.4	0.5	0.3	0.0	100.0
pk13cpx6rim	49.0	1.7	5.0	7.8	0.2	14.1	21.2	0.4	0.3	0.0	99.6
pk13cpx6rim	49.2	1.7	5.1	7.8	0.2	14.0	21.4	0.4	0.3	0.0	99.9
pk13cpx6cor	48.1	2.1	5.9	8.1	0.1	13.8	20.7	0.5	0.3	0.0	99.6
pk13cpx7cor	50.8	1.2	3.5	8.7	0.2	16.4	18.8	0.3	0.2	0.0	100.1
pk13cpx7rim	50.2	1.3	4.4	7.4	0.2	14.7	21.1	0.4	0.2	0.0	99.9
pk13cpx8cor	51.7	0.7	1.5	13.2	0.5	11.2	21.2	0.5	0.0	0.0	100.5
pk13cpx8rim	50.3	1.3	4.3	7.6	0.2	14.9	21.0	0.4	0.2	0.0	100.1
pk13cpx8cor	50.1	1.4	4.1	8.8	0.3	13.6	20.8	0.5	0.2	0.0	99.9
pk13cpx8rim	50.2	1.7	3.6	9.0	0.2	13.7	20.8	0.5	0.0	0.0	99.7
pk13cpx9cor	50.5	1.3	3.4	8.8	0.2	13.8	21.2	0.5	0.1	0.0	99.8
pk13cpx9rim	50.7	1.5	3.2	9.2	0.3	13.9	21.1	0.5	0.0	0.0	100.2
pk13cpx10cor	50.6	1.5	3.0	9.4	0.3	14.0	20.6	0.5	0.0	0.0	99.9
pk13cpx10rim	50.4	1.6	3.4	9.2	0.2	13.8	21.0	0.5	0.0	0.0	100.0
pk13cpx11cor	49.0	2.1	4.3	9.7	0.2	13.3	20.7	0.5	0.0	0.0	99.9
pk13cpx11rim	50.7	1.3	3.0	9.3	0.2	13.9	20.8	0.5	0.0	0.0	99.7
pk13cpx12cor	49.0	1.6	5.1	8.3	0.2	13.9	20.6	0.5	0.1	0.0	99.3
pk13cpx12rim	48.8	1.7	5.4	9.0	0.2	13.5	20.6	0.5	0.1	0.0	99.9
pk13cpx13cor	50.2	1.5	3.4	9.9	0.3	13.4	20.9	0.5	0.0	0.0	100.1
pk13cpx13rim	49.5	1.5	5.5	7.7	0.2	14.2	21.2	0.4	0.2	0.0	100.3
pk13cpx14cor	47.6	2.3	6.3	9.5	0.2	12.8	20.6	0.6	0.0	0.0	99.8
pk13cpx14rim	49.2	1.5	5.3	7.6	0.2	14.4	20.8	0.4	0.4	0.0	99.8

pk13cpx15cor	51.3	1.1	2.7	7.8	0.2	15.6	20.5	0.3	0.2	0.0	99.7
pk13cpx15rim	51.1	1.2	3.1	7.9	0.2	15.1	20.7	0.4	0.0	0.0	99.6
Clinopyroxene mineral chemistry contd…											
pk13cpx16cor	47.0	2.5	7.1	8.6	0.2	13.4	**20.3**	**0.5**	**0.2**	**0.0**	**99.7**
pk13cpx16rim	48.4	1.8	5.6	7.7	0.2	14.0	20.8	0.5	0.4	0.0	99.3
pk13cpx17cor	50.8	1.3	3.6	8.6	0.3	15.5	19.6	0.3	0.1	0.0	100.0
pk13cpx17rim	47.2	2.5	5.8	9.0	0.2	13.3	21.0	0.4	0.2	0.0	99.6
pk13cpx18cor	51.2	1.3	2.8	9.1	0.2	15.4	19.8	0.3	0.1	0.0	100.2
pk13cpx18rim	50.7	1.3	3.1	8.9	0.2	15.7	19.3	0.3	0.2	0.0	99.7
pk13cpx19cor	48.2	2.0	6.1	7.9	0.2	13.8	20.9	0.5	0.4	0.0	99.8
pk13cpx19rim	51.7	0.9	2.7	8.6	0.2	16.9	18.2	0.3	0.2	0.0	99.7
pk13cpx20cor	47.3	2.5	6.6	8.1	0.1	13.2	21.1	0.4	0.2	0.0	99.4
pk13cpx20rim	48.3	1.9	5.8	7.8	0.1	13.8	21.0	0.5	0.2	0.0	99.5
pk13cpx21cor	51.5	0.8	1.9	11.1	0.4	12.6	21.4	0.5	0.0	0.0	100.1
pk13cpx21rim	51.3	1.1	2.7	7.8	0.2	15.4	20.9	0.3	0.2	0.0	99.9
pk13cpx22cor	51.5	0.8	1.9	11.3	0.4	12.5	21.3	0.5	0.0	0.0	100.2
pk13cpx22rim	51.2	0.7	1.8	11.7	0.4	12.6	21.1	0.5	0.0	0.0	100.0
pk13cpx23cor	47.6	2.2	7.0	7.8	0.2	13.9	20.3	0.4	0.3	0.0	99.6
pk13cpx23rim	48.7	1.8	5.6	7.7	0.2	14.2	20.7	0.4	0.4	0.0	99.7
pk13cpx24cor	51.6	1.1	2.7	8.3	0.2	15.9	19.8	0.3	0.2	0.0	100.1
pk13cpx24rim	47.6	2.5	5.9	8.5	0.2	13.3	21.0	0.4	0.2	0.0	99.6
pk13cpx25cor	50.7	1.0	3.9	6.9	0.1	14.7	22.1	0.4	0.1	0.0	100.0
pk13cpx25rim	49.6	1.4	4.3	7.8	0.2	13.7	21.8	0.5	0.2	0.0	99.6
pk13cpx26cor	49.1	1.3	5.0	8.2	0.2	14.7	20.2	0.4	0.1	0.0	99.3
pk13cpx26rim	47.8	2.2	5.5	8.4	0.1	13.7	21.2	0.4	0.2	0.0	99.6
pk13cpx27cor	51.5	1.1	2.8	9.0	0.2	16.6	18.5	0.3	0.1	0.0	100.1
pk13cpx27rim	51.4	1.1	2.9	8.1	0.2	15.7	20.2	0.3	0.1	0.0	100.1
pk13cpx28cor	48.8	1.8	5.9	7.5	0.2	14.2	20.7	0.4	0.5	0.0	100.0
pk13cpx28rim	49.0	1.6	5.2	8.3	0.2	13.8	21.3	0.5	0.1	0.0	99.9
pk13cpx29cor	49.5	1.5	5.2	7.7	0.1	14.4	20.9	0.4	0.1	0.0	99.8
pk13cpx29rim	48.5	2.0	5.6	8.2	0.2	13.8	21.1	0.4	0.2	0.0	99.9
pk13cpx30rim	49.9	1.5	4.0	9.5	0.2	13.8	21.0	0.5	0.0	0.0	100.3
pk13cpx30cor	49.9	1.5	3.5	11.0	0.3	12.5	20.9	0.6	0.0	0.0	100.2
pk28cpx1cor	47.9	2.0	6.0	7.5	0.2	13.6	21.7	0.4	0.3	0.0	99.5
pk28cpx1rim	47.1	2.4	6.6	7.7	0.2	13.2	21.3	0.4	0.4	0.0	99.4
pk28cpx2cor	48.1	2.0	5.8	7.4	0.1	14.0	21.2	0.4	0.6	0.0	99.7
pk28cpx2rim	47.8	2.3	5.9	8.2	0.2	13.3	21.5	0.4	0.1	0.0	99.7
pk28cpx3cor	47.9	2.3	5.9	7.8	0.1	13.3	21.5	0.4	0.3	0.0	99.6
pk28cpx3rim	50.5	1.4	3.7	6.7	0.2	15.1	21.3	0.3	0.2	0.0	99.4
pk28cpx4cor	50.2	1.3	4.1	7.0	0.2	14.8	21.6	0.4	0.2	0.0	99.8
pk28cpx4rim	50.2	1.4	4.1	7.3	0.2	14.7	21.5	0.4	0.1	0.0	99.9
pk28cpx5cor	50.2	0.7	5.5	4.5	0.1	15.4	22.0	0.4	0.9	0.0	99.8
pk28cpx5rim	49.3	1.3	5.8	5.6	0.1	14.6	21.4	0.4	0.9	0.0	99.6
pk28cpx6cor	51.2	0.7	4.0	4.7	0.1	15.9	21.8	0.3	0.8	0.0	99.6
pk28cpx6rim	50.9	0.7	4.3	4.6	0.1	15.9	21.9	0.3	0.9	0.0	99.5
pk28cpx7cor	50.9	0.7	4.4	4.8	0.1	15.6	22.0	0.2	0.9	0.0	99.8

pk28cpx7rim	51.2	0.7	4.1	4.8	0.1	15.9	22.2	0.3	0.8	0.0	100.0
pk28cpx8cor	47.2	2.5	6.0	8.5	0.2	13.2	21.0	0.5	0.5	0.0	99.5
pk28cpx8rim	46.7	2.9	6.2	8.5	0.2	12.8	20.9	0.5	0.5	0.0	99.2
Clinopyroxene mineral chemistry contd…											
pk28cpx9cor	37.5	0.1	0.2	27.0	0.6	35.7	0.5	0.0	0.0	0.0	101.6
pk28cpx10cor	37.5	0.1	0.3	28.2	0.7	33.9	0.5	0.1	0.0	0.0	101.3
pk-30cpx1cor	50.0	0.8	0.8	22.3	1.0	5.5	20.3	0.6	0.0	0.0	101.3
pk-30cpx1rim	50.0	0.9	0.8	22.3	1.0	5.3	19.9	0.6	0.0	0.0	100.8
pk-30cpx2rim	49.5	0.9	0.9	22.4	1.0	5.2	19.9	0.7	0.0	0.0	100.4
pk-30cpx2cor	49.2	1.0	1.0	22.9	1.1	5.2	19.5	0.7	0.0	0.0	100.6
pk-30cpx3rim	49.7	0.8	1.0	22.4	1.0	5.5	20.0	0.7	0.0	0.0	101.1
pk-30cpx3cor	46.4	1.1	1.1	22.4	1.0	4.5	21.3	0.8	0.0	0.0	98.6
pk-30cpx4cor	50.2	0.6	0.6	22.9	1.0	5.0	20.1	0.6	0.0	0.0	101.1
pk-30cpx4rim	50.6	0.6	0.6	21.9	0.9	5.5	20.5	0.6	0.0	0.0	101.2
pk-30cpx5rim	50.3	0.6	0.6	22.1	1.0	5.2	20.6	0.6	0.0	0.0	101.0
pk-30cpx5cor	50.6	0.6	0.7	22.8	1.0	5.1	20.6	0.6	0.0	0.0	102.0
pk-30cpx6cor	50.3	0.6	0.6	22.2	0.9	5.6	20.6	0.6	0.0	0.0	101.5
pk-30cpx6rim	50.3	0.6	0.6	22.5	1.0	5.3	20.7	0.6	0.0	0.0	101.6
pk-30cpx7cor	50.7	0.6	0.5	20.7	1.0	6.8	20.5	0.5	0.0	0.0	101.2
pk-30cpx7rim	49.2	1.2	1.2	23.5	1.0	4.9	19.3	0.7	0.0	0.0	101.1
pk-30cpx8cor	49.1	1.2	1.1	23.6	1.1	4.9	19.4	0.7	0.0	0.0	101.1
pk-30cpx8rim	49.6	1.0	0.9	23.5	1.1	4.8	19.6	0.8	0.0	0.0	101.3
pk-30cpx9cor	49.9	0.6	0.6	23.0	0.9	4.9	20.5	0.6	0.0	0.0	101.0
pk-30cpx9rim	49.7	0.7	0.7	24.0	1.1	4.5	20.0	0.7	0.0	0.0	101.4
pk-30cpx10rim	50.2	0.7	0.6	23.1	1.0	4.9	20.3	0.6	0.0	0.0	101.3
pk-30cpx10cor	50.2	0.7	0.6	23.0	1.0	5.0	20.3	0.7	0.0	0.0	101.4
pk-30cpx11cor	50.0	0.8	0.9	23.2	1.0	4.8	20.3	0.7	0.0	0.0	101.8
pk-30cpx11rim	50.4	0.6	0.6	22.5	0.9	5.2	20.6	0.6	0.0	0.0	101.4
pk-30cpx12cor	49.6	0.8	0.7	25.5	1.1	3.1	19.8	0.9	0.0	0.0	101.4
pk-30cpx12rim	50.2	0.6	0.6	22.4	1.0	5.4	20.4	0.6	0.0	0.0	101.2
pk-30cpx13cor	50.2	0.6	0.5	22.7	1.0	5.1	20.1	0.6	0.0	0.0	100.8
pk-30cpx13rim	49.4	0.9	0.8	24.2	1.1	4.6	19.4	0.8	0.0	0.0	101.1
pk-30cpx14cor	50.3	0.7	0.8	22.5	1.0	5.4	20.0	0.7	0.0	0.0	101.3
pk-30cpx14rim	50.5	0.6	0.7	22.1	1.0	5.5	20.3	0.6	0.0	0.0	101.3
pk-30cpx15cor	50.6	0.6	0.6	21.4	0.9	6.1	20.6	0.6	0.0	0.0	101.5
pk-30cpx15rim	50.6	0.6	0.6	22.0	0.9	5.5	20.5	0.6	0.0	0.0	101.4
pk-30cpx16cor	50.7	0.6	0.6	22.3	0.9	5.6	20.5	0.6	0.0	0.0	101.8
pk-30cpx16rim	50.5	0.6	0.6	22.0	1.0	5.8	20.7	0.6	0.0	0.0	101.6
pk-30cpx17cor	50.3	0.7	0.6	22.4	1.0	5.2	20.3	0.6	0.0	0.0	101.0
pk-30cpx17rim	49.8	0.6	0.6	22.1	1.0	5.7	20.4	0.7	0.0	0.0	100.7
pk-30cpx18rim	50.4	0.6	0.6	22.1	0.9	5.5	20.6	0.6	0.0	0.0	101.3
pk-30cpx18cor	48.9	0.7	0.7	23.1	1.0	5.2	19.6	0.8	0.0	0.0	100.0
pk-30cpx19cor	50.2	0.9	0.9	23.5	1.0	4.6	20.0	0.7	0.0	0.0	101.8
pk-30cpx19rim	49.6	0.9	0.9	23.0	1.0	4.8	20.0	0.7	0.0	0.0	100.8
pk-30cpx20cor	49.6	0.7	0.6	26.7	1.1	2.4	19.2	1.1	0.0	0.0	101.4
pk-30cpx20rim	49.9	0.6	0.6	23.4	1.0	4.7	20.2	0.7	0.0	0.0	101.2

pk-30cpx21cor	50.2	0.7	0.8	22.5	1.0	5.3	20.0	0.7	0.0	0.0	101.2
pk-30cpx21rim	50.1	0.8	0.8	22.8	1.0	5.4	19.8	0.6	0.0	0.0	101.2
pk-30cpx22cor	49.9	0.9	1.0	22.2	1.0	5.5	20.1	0.7	0.0	0.0	101.2
pk-30cpx22rim	49.3	1.0	1.0	22.9	1.0	4.9	20.0	0.7	0.0	0.0	100.8
Clinopyroxene mineral chemistry contd…											
pk-30cpx23cor	49.9	0.8	0.9	23.1	0.9	5.0	20.1	0.7	0.0	0.0	101.3
pk-30cpx23rim	50.9	0.6	0.6	21.1	0.9	6.1	20.7	0.6	0.0	0.0	101.6
pk-30cpx24cor	49.7	0.5	0.5	24.9	1.1	3.8	20.2	0.8	0.0	0.0	101.5
pk-30cpx24rim	50.0	0.6	0.6	22.6	1.0	5.3	20.6	0.6	0.0	0.0	101.3
pk-30cpx25cor	50.7	0.5	0.7	21.0	0.9	6.3	20.6	0.6	0.0	0.0	101.3
pk-30cpx25rim	50.3	0.7	0.7	22.3	0.9	5.6	20.3	0.6	0.0	0.0	101.3

Oxides mineral chemistry

Oxides	SiO2	TiO_2	Al_2O_3	FeO	MnO	MgO	V_2O_3	Cr_2O_3	NiO	Total
pk3glom1oxide1	0.1	23.7	0.4	72.1	1.3	0.4	0.1	0.0	0.0	98.1
pkm2glomero1oxide2	0.2	20.4	2.8	68.8	0.7	2.5	0.5	0.2	0.0	96.1
pkm2glomero2oxide2	0.2	20.1	2.6	69.8	0.8	1.6	0.5	0.1	0.0	95.6
pkm2glomero3oxide1	0.3	19.8	2.7	70.0	0.8	1.4	0.4	0.4	0.0	95.9
pkm2glomero6oxide1	0.2	20.1	2.7	69.2	0.7	2.1	0.5	0.1	0.0	95.6
pkm2glomero8oxide1	0.6	19.6	2.7	69.3	0.8	1.3	0.4	0.1	0.0	94.8
pk3pl4oxide1	0.1	22.0	0.3	74.1	1.2	0.2	0.1	0.0	0.0	98.0
pk3ol2oxide1	0.1	22.3	0.5	73.5	1.3	0.4	0.1	0.0	0.0	98.3
dn4pl1oxide1	0.1	21.1	0.7	73.9	1.3	0.6	0.0	0.0	0.0	97.9
dn4glom1oxide1	0.1	21.3	0.7	73.3	1.3	0.6	0.1	0.0	0.0	97.3
dn4glom2oxide1	0.1	20.7	0.7	73.9	1.2	0.6	0.1	0.0	0.0	97.4
dn4glom2oxide2	0.1	20.3	0.7	73.8	1.2	0.6	0.1	0.0	0.0	96.8
dn4glom2oxide3	0.2	18.1	0.5	74.3	1.2	0.2	0.0	0.0	0.0	94.6
dn4glom2oxide4	0.1	20.2	0.7	73.8	1.2	0.6	0.1	0.0	0.0	96.6
dn4glom2oxide5	0.2	20.1	0.8	73.5	1.2	0.5	0.1	0.0	0.0	96.3
dn4glom3oxide1	0.1	24.0	0.6	71.5	1.4	0.6	0.1	0.0	0.0	98.3
dn4glom3oxide2	0.1	21.9	0.7	73.0	1.3	0.6	0.1	0.0	0.0	97.7
dn4glom3oxide3	0.1	21.4	0.7	73.8	1.2	0.6	0.1	0.0	0.0	97.9
dn4glom4oxide1	0.1	27.2	0.8	69.3	1.4	0.7	0.1	0.0	0.0	99.6
dn4glom5oxide1	0.2	20.5	0.8	74.1	1.2	0.7	0.1	0.0	0.0	97.5
dn4glom5oxide2	0.1	20.5	0.8	74.1	1.2	0.6	0.1	0.0	0.0	97.4
dn4glom5oxide3	0.1	20.4	0.7	73.2	1.2	0.6	0.0	0.0	0.0	96.4
pk3pl4oxide2	0.1	21.9	0.3	73.9	1.2	0.2	0.1	0.0	0.0	97.6
pk3pl4oxide3	0.1	23.0	0.5	71.4	0.8	0.1	0.1	0.0	0.0	96.0
pk3pl4oxide4	0.1	24.2	0.4	68.9	0.6	0.2	0.1	0.0	0.0	94.5
pk3py4oxide1	0.1	21.8	0.4	73.6	1.3	0.2	0.1	0.0	0.0	97.6
pk3py4oxide2	0.2	22.2	0.5	73.2	1.3	0.3	0.1	0.0	0.0	97.8
pk3py4oxide3	0.1	22.1	0.4	73.6	1.3	0.2	0.1	0.0	0.0	97.9
pk3py4oxide4	0.1	22.0	0.3	73.5	1.3	0.2	0.1	0.0	0.0	97.5
pk3_glom1_oxide1_cor1	0.1	28.2	1.8	66.6	0.7	1.3	0.7	0.0	0.0	99.4
pk3_glom1_oxide1_cor2	0.1	28.8	1.8	66.0	0.8	1.2	0.6	0.0	0.0	99.3
pk3_glom1_oxide1_cor3	0.1	28.2	1.7	65.6	0.7	1.2	0.7	0.0	0.0	98.3
pk3_glom1_oxide1_rim1	0.1	28.1	1.8	66.3	0.7	1.2	0.7	0.0	0.0	98.8
pk3_glom1_oxide1_rim2	0.1	28.8	1.8	66.3	0.8	1.1	0.5	0.0	0.0	99.4
pk4_glom4_oxide1_cor1	0.1	30.1	1.6	65.2	0.8	1.4	0.5	0.1	0.0	99.6
pk4_glom4_oxide1_cor2	0.1	30.0	1.6	65.1	0.8	1.5	0.6	0.1	0.0	99.7
pk4_glom4_oxide1_rim1	0.1	30.1	1.5	64.6	0.8	1.4	0.5	0.0	0.0	99.1
pk4_glom4_oxide1_rim2	0.1	30.3	1.5	64.8	0.8	1.5	0.5	0.0	0.0	99.5
pk4_glom4_ol_oxide1_cor1	0.1	30.3	1.0	65.0	0.8	1.4	0.6	0.0	0.0	99.1
pk4_glom4_ol_oxide1_cor2	0.1	30.5	1.0	64.9	0.8	1.4	0.5	0.0	0.0	99.2
pk4_glom4_ol_oxide1_rim1	0.1	30.3	0.7	65.0	0.8	1.3	0.5	0.0	0.0	98.7
pk4_glom4_ol_oxide1_rim2	0.1	30.8	0.9	65.1	0.8	1.3	0.5	0.0	0.0	99.5
pk4_ol_oxide2_cor1	0.1	30.2	1.3	65.7	0.8	1.2	0.5	0.0	0.0	99.8
pk4_ol_oxide2_cor2	0.1	29.4	1.6	65.2	0.8	1.3	0.7	0.0	0.0	99.1

Oxides mineral chemistry contd...

pk4_ol_oxide2_rim1	0.1	30.0	1.2	65.4	0.8	1.2	0.5	0.0	0.0	99.1
pk4_ol_oxide2_rim2	0.1	29.8	0.8	66.0	0.8	1.1	0.4	0.0	0.0	99.0
pk4_glom5_cpx_oxide1_cor1	0.1	29.5	1.5	64.7	0.8	1.4	0.4	0.0	0.0	98.4
pk4_glom5_cpx_oxide1_rim1	0.1	29.3	1.3	65.0	0.8	1.4	0.4	0.0	0.0	98.3
pk4_oxide2_cor1	0.1	29.7	1.0	63.7	0.8	1.5	0.5	0.0	0.0	97.4
pk4_oxide2_rim1	0.6	29.3	1.0	64.3	0.8	1.3	0.5	0.0	0.0	97.9
pk4_cpx_oxide2_cor1	0.1	29.0	2.0	65.0	0.7	1.5	0.8	0.1	0.0	99.2
pk4_cpx_oxide2_cor2	0.1	29.8	1.3	66.0	0.8	1.1	0.5	0.0	0.0	99.8
pk4_cpx_oxide2_rim1	0.1	29.3	1.8	64.6	0.7	1.6	0.7	0.0	0.0	98.9
pk4_cpx_oxide2_rim2	0.1	30.2	1.4	66.1	0.8	1.2	0.5	0.0	0.0	100.2
pk13_ol1_Oxide_cor1	0.6	27.5	1.1	65.4	0.7	1.0	0.5	0.0	0.0	97.0
pk13_ol2_Oxide_cor1	0.3	27.2	0.7	67.1	0.8	0.8	0.5	0.0	0.0	97.4
pk13_ol5_Oxide_cor1	0.7	28.4	1.1	65.0	0.7	1.0	0.4	0.0	0.0	97.2
pk13_Glom2_Oxide_cor1	5.8	25.2	3.1	62.1	0.8	0.8	0.3	0.0	0.0	98.3
pk13_cpx5_Oxide_cor1	0.2	26.9	1.2	66.2	0.7	1.1	0.4	0.0	0.0	96.7
pk28_glom3_cpx_Oxide_cor1	0.7	21.1	2.4	63.9	0.8	3.8	0.3	0.1	0.0	93.1
pk28_glom2_plag1_Oxide_cor2	0.2	21.2	3.2	66.0	0.8	3.5	0.3	0.1	0.0	95.4
pk28_cpx2_Oxide_cor1	0.1	20.4	3.3	65.5	0.7	4.8	0.4	0.8	0.0	96.1
pk28_ol3_Oxide_cor1	0.1	12.2	11.1	49.9	0.3	8.5	0.4	16.6	0.2	99.2
pk-02oxide2	0.1	20.2	0.5	74.7	1.2	0.3	0.1	0.0	0.0	97.0
pk-02oxide3	0.1	20.5	0.4	74.8	1.3	0.3	0.1	0.0	0.0	97.5
pk-02oxide4	0.1	21.0	0.5	72.9	1.1	0.2	0.1	0.0	0.0	95.9
pk-02oxide5	0.1	20.9	0.5	72.1	1.2	0.3	0.1	0.0	0.0	95.2
pk-02oxide6	0.1	23.5	0.4	72.2	1.4	0.4	0.1	0.0	0.0	98.1
pk-u7 oxide1	0.1	27.1	0.3	69.8	1.2	0.2	0.1	0.0	0.0	98.8
pk-u7 oxide2	1.3	24.8	0.9	67.9	1.6	0.3	0.3	0.0	0.0	97.2
pk-12-oxid1	0.1	19.9	0.2	73.5	1.3	0.2	0.1	0.0	0.0	95.3
pk-12-oxid2	0.1	18.7	0.3	72.1	1.2	0.2	0.1	0.0	0.0	92.6
pk-12-oxid3	0.1	19.4	0.3	72.8	1.2	0.1	0.1	0.0	0.0	94.0
pk-12-oxid4	0.2	18.8	0.3	69.1	1.0	0.1	0.1	0.0	0.0	89.6
pk-12-oxid5	1.5	16.0	0.4	74.3	1.1	0.1	0.0	0.0	0.0	93.5
pk-12-oxid6	0.8	15.2	0.2	76.0	1.1	0.1	0.1	0.0	0.0	93.4
pk-12-oxid8	0.2	16.0	0.2	76.4	1.1	0.1	0.1	0.0	0.0	94.2
pk-12-oxid9	0.4	15.8	0.3	76.6	1.1	0.1	0.0	0.0	0.0	94.4
pk-20-oxid1	0.1	29.1	2.0	65.4	0.8	1.9	0.6	0.0	0.0	99.8
pk-20-oxid2	0.1	29.6	2.4	64.8	0.7	1.9	0.7	0.0	0.0	100.2
pk-20-oxid3	0.1	29.7	2.0	65.7	0.8	1.5	0.5	0.0	0.0	100.3
pk-20-oxid4	0.1	30.8	1.7	65.5	0.8	1.3	0.6	0.0	0.0	100.8
pk-20-oxid5	0.1	29.6	2.3	64.2	0.7	2.0	0.7	0.0	0.0	99.6
pk-20-oxid6	0.1	29.8	1.6	64.8	0.8	1.4	0.6	0.0	0.0	99.1
pk-20-oxid7	0.1	29.4	1.8	64.6	0.8	1.7	0.6	0.0	0.0	99.1
pk-20-oxid8	0.1	29.8	2.3	65.0	0.8	1.8	0.7	0.1	0.0	100.5
pk-20-oxid9	0.1	29.8	1.8	63.4	0.8	1.5	0.5	0.0	0.0	97.9
pk-20-oxid10	0.1	30.6	1.5	64.7	0.8	1.4	0.5	0.0	0.0	99.5
pk-24-oxid1	0.1	29.3	0.7	61.1	1.2	0.2	0.1	0.0	0.0	92.7
pk-24-oxid2	0.1	28.3	0.7	61.3	1.3	0.4	0.1	0.0	0.0	92.3

Oxides mineral chemistry contd...

pk-24-oxid3	0.9	29.1	0.7	60.6	0.7	0.1	0.2	0.0	0.0	92.3
pk-24-oxid4	0.1	27.7	0.7	64.5	1.1	0.6	0.2	0.0	0.0	94.9
pk-24-oxid5	0.1	27.4	0.7	67.5	1.5	0.5	0.2	0.0	0.0	97.9
pk-24-oxid6	0.1	26.2	0.9	67.6	1.4	0.5	0.1	0.0	0.0	96.9
pk-24-oxid7	0.1	28.6	0.7	61.7	1.6	0.5	0.2	0.0	0.0	93.5
pk-24-oxid8	0.1	26.1	0.9	68.7	1.5	0.5	0.2	0.0	0.0	97.9
pk-24-oxid9	0.1	28.0	1.3	64.6	1.3	0.9	0.2	0.0	0.0	96.5
pk-24-oxid10	0.1	29.2	0.7	63.0	1.3	0.4	0.2	0.0	0.0	94.9
pk30oxd1cor	0.1	30.4	0.6	63.3	1.4	0.6	0.1	0.0	0.0	96.6
pk30oxd1rim	0.1	20.8	0.6	72.4	1.4	0.4	0.1	0.0	0.0	95.8
pk30oxd2cor	0.1	24.0	0.5	70.1	1.5	0.5	0.1	0.0	0.0	96.8
pk30oxd3cor	0.1	26.4	0.6	68.4	1.6	0.5	0.1	0.0	0.0	97.7
pk30oxd4cor	0.1	25.0	0.5	69.1	1.5	0.5	0.1	0.0	0.0	96.8
pk30oxd5cor	0.2	18.9	0.5	74.3	1.3	0.2	0.1	0.0	0.0	95.4
pk30oxd6cor	0.2	19.3	0.4	73.2	1.1	0.1	0.1	0.0	0.0	94.5
pk30oxd7cor	0.2	19.4	0.5	72.9	1.2	0.2	0.1	0.0	0.0	94.5
pk13oxd1cor	0.2	26.1	1.1	65.8	0.8	1.1	0.3	0.0	0.0	95.5
pk13oxd2cor	0.2	25.8	1.2	66.0	0.7	1.1	0.4	0.0	0.0	95.5
pk13oxd3cor	0.3	24.9	1.5	66.0	0.8	1.3	0.4	0.0	0.0	95.3
pk13oxd4cor	0.2	26.2	1.6	65.8	0.8	1.5	0.5	0.0	0.0	96.5
pk13oxd5cor	0.2	26.2	1.8	65.3	0.8	1.6	0.5	0.0	0.0	96.6
pk13oxd6cor	0.1	22.9	3.6	65.9	0.5	3.2	0.9	0.2	0.0	97.3
pk13oxd7cor	0.1	22.5	3.6	66.0	0.5	3.4	0.9	0.2	0.0	97.2
pk28oxd1cor	0.2	19.6	2.5	66.2	0.8	4.1	0.3	0.1	0.0	93.8
pk28oxd3cor	0.2	20.3	2.6	66.3	0.8	4.0	0.3	0.1	0.0	94.6
pk28oxd4cor	0.2	20.2	1.7	66.6	0.9	3.8	0.3	0.1	0.0	93.9
pk28oxd5cor	2.0	20.0	3.7	64.0	0.7	3.6	0.3	0.1	0.0	94.4
pk28oxd6cor	0.3	20.5	2.7	66.6	0.8	3.5	0.4	0.1	0.1	94.8
pk28oxd7cor	0.6	20.4	3.1	65.2	0.8	4.0	0.3	0.1	0.0	94.5

Ol, Plag and Cpx-hosted melt inclusion chemistry - raw data

Sample	SiO_2	TiO_2	Al_2O_3	FeO	MnO	MgO	CaO	Na_2O	K_2O	P_2O_5	SO_3	Cl	Total
pkm2MI1_ol1_2	49.6	2.5	19.2	6.9	0.1	2.7	12.7	4.3	1.1	0.5	0.2	0.0	100.0
pkm2MI1_ol1_1	50.0	2.6	19.7	6.8	0.1	2.5	12.0	4.4	1.2	0.5	0.2	0.0	99.9
pkm2MI1_ol1_3	49.8	2.7	19.0	7.3	0.1	2.5	12.4	4.1	1.1	0.5	0.2	0.0	99.8
pkm2MI2_ol1	51.4	2.5	20.3	5.4	0.1	1.8	10.6	5.2	1.7	0.5	0.2	0.0	99.7
pkm2glomol_Mi1	49.8	2.7	19.7	6.0	0.1	2.0	12.7	4.0	1.1	0.5	0.1	0.0	98.8
pkm2_MI1inplag2	42.9	2.7	5.7	18.0	0.3	15.5	9.8	2.8	0.9	0.3	0.3	0.0	99.1
pkm2_glomero3_embincpx	56.7	1.2	18.8	6.4	0.2	0.3	0.8	9.1	6.4	0.5	0.1	0.1	100.6
pkm2_glom4ol_MI1	54.5	2.8	19.0	4.7	0.1	0.8	4.9	8.3	4.3	0.6	0.1	0.1	100.3
pkm2_glom4ol_MI2	51.3	2.7	20.4	5.7	0.1	1.8	11.3	5.0	1.5	0.5	0.1	0.0	100.3
pkm2_MIinol3	55.3	2.3	17.7	4.9	0.1	0.8	4.3	7.6	5.1	1.1	0.1	0.1	99.5
pkm2_glom7MIol	54.7	0.1	29.0	1.1	0.0	0.2	10.8	4.5	0.4	0.0	0.0	0.0	100.9
pk3_plag1cpxMI1	65.9	0.4	17.0	2.4	0.0	0.0	0.1	6.8	6.7	0.0	0.1	0.1	99.6
pk3_plag1cpxMI1_2	64.5	0.3	16.8	2.3	0.0	0.0	1.2	7.0	6.6	0.8	0.1	0.1	99.8
pk3_plag1cpxMI1_3	66.5	0.3	17.3	2.3	0.0	0.0	0.1	6.5	6.3	0.0	0.1	0.1	99.6
pk3_plag1cpxMI2	66.7	0.4	17.4	2.2	0.0	0.0	0.1	7.3	5.9	0.0	0.1	0.1	100.2
pk3_plag1cpxMI3	66.7	0.1	19.2	1.3	0.0	0.0	0.3	7.3	5.9	0.0	0.0	0.0	100.8
pk3_plag1cpxMI3_2	66.9	0.1	19.0	1.1	0.0	0.0	0.4	8.3	4.8	0.0	0.0	0.0	100.6
pk3_plag3MI1	49.6	1.7	0.7	24.8	0.9	2.5	15.6	4.0	0.0	0.0	0.0	0.0	99.8
pk3_plag3_MI2	50.2	0.9	1.1	19.0	0.8	7.7	20.6	0.7	0.1	0.0	0.0	0.0	101.1
pk3_glom1ol1MI	63.4	0.5	18.0	3.8	0.1	0.1	0.3	9.0	5.8	0.1	0.1	0.2	101.3
pk3_glom1ol1MI2_1	62.8	0.6	17.7	4.3	0.2	0.1	0.1	8.5	5.9	0.1	0.1	0.2	100.6
pk3_glom1ol1MI2_2	62.4	0.6	17.7	4.4	0.1	0.1	0.5	8.9	5.8	0.1	0.1	0.2	101.0
pk3_glom1ol1MI2_3	61.4	0.6	17.0	5.2	0.2	0.3	1.8	8.4	5.6	0.1	0.1	0.2	100.8

Ol, Plag and Cpx-hosted melt inclusion chemistry - raw data contd...													
pk3_glom1plagMI1	51.2	0.6	1.1	27.7	0.4	0.5	6.9	9.9	0.0	0.0	0.0	0.0	98.2
dn4plag1MI1	47.9	1.7	5.3	22.8	1.0	1.3	4.2	7.5	2.1	0.5	0.3	1.0	95.4
dn4plag1MI2	47.3	1.7	5.8	23.0	1.0	1.2	4.1	9.2	2.2	0.4	0.3	0.6	96.7
dn4glom1MI1inplag	45.7	1.7	9.5	22.9	1.0	0.9	4.0	7.9	2.4	0.3	0.4	0.5	97.1
dn4glom1MI1inplag	44.4	1.7	9.0	23.5	0.9	0.8	4.1	8.2	2.2	0.2	0.4	0.5	95.9
dn4glom1MI2inplag	48.8	1.5	5.4	23.9	1.1	0.7	2.5	8.8	2.4	0.4	0.3	0.8	96.4
dn4plag2MI1	0.5	0.0	0.0	0.1	0.0	0.0	52.6	1.5	0.1	30.1	0.0	0.0	85.0
dn4plag2MI2	45.7	1.9	9.6	22.8	0.7	1.5	5.4	8.6	2.4	0.4	0.2	0.3	99.3
dn4plag5MI1_1	47.0	2.1	6.5	23.0	1.0	0.7	3.0	10.8	2.2	0.3	0.3	0.5	97.4
dn4plag5MI1_2	46.1	1.8	6.4	26.4	1.0	1.0	3.7	9.4	2.2	0.3	0.4	0.5	99.2
dn4cpx2MI1	64.8	0.3	16.6	4.7	0.2	0.0	0.3	6.5	5.5	0.1	0.1	0.2	99.4
dn4glomero4ol1MI1_1	60.5	1.1	16.2	6.3	0.2	0.3	1.6	8.8	4.6	0.1	0.1	0.3	100.0
dn4glomero4ol1MI1_2	60.1	1.1	16.2	6.5	0.2	0.3	1.5	8.9	4.6	0.1	0.1	0.3	100.0
dn4glomero4ol1MI1_3	60.3	1.1	16.1	6.4	0.2	0.3	1.5	9.0	4.6	0.1	0.1	0.3	100.0
dn4glomero4ol1MI2	61.8	1.2	17.1	5.5	0.1	0.2	1.1	7.6	5.4	0.2	0.1	0.1	100.3
pk13_ol3_Mi	59.9	0.2	24.7	0.9	0.0	0.1	6.2	7.5	1.2	0.0	0.0	0.0	100.7
pk28_ol1Mi1_1	48.6	2.7	20.1	8.7	0.1	2.1	6.0	6.0	2.2	1.1	0.6	0.1	98.3
pk28_ol1Mi1_2	48.6	2.8	16.0	7.2	0.2	6.0	12.6	3.9	1.3	0.7	0.2	0.0	99.3
pk28_ol1Mi1_3	49.5	2.5	18.1	6.3	0.1	4.3	10.4	4.4	1.7	1.0	0.1	0.1	98.6
pk28_cpx3_MI1_1	48.7	2.5	19.9	11.0	0.1	2.9	4.8	5.9	2.0	0.9	0.4	0.1	99.1
pk28_cpx3_MI1_2	51.7	2.2	20.8	7.5	0.2	2.2	4.4	6.4	2.1	1.1	0.5	0.1	99.2
pk28_cpx3_MI1_3	46.9	2.8	20.2	13.4	0.2	2.7	4.0	6.0	2.0	0.9	0.4	0.1	99.5
pk28_cpx3_MI1_4	51.4	2.2	20.1	7.5	0.2	2.8	5.6	5.3	2.1	1.0	0.5	0.1	98.7
pk28_fp5_MI1_1	41.8	3.6	10.7	14.6	0.3	6.9	6.4	8.1	2.3	0.6	0.3	0.1	95.9

Groundmass chemistry

Groundmass glass	SiO_2	TiO_2	Al_2O_3	FeO	MnO	MgO	CaO	Na_2O	K_2O	P_2O_5	Total
pkm2glomol_gmassgl	55.4	2.2	17.0	7.7	0.2	0.7	1.6	7.4	5.6	0.7	98.4
pkm2_gmassgl1	56.6	1.6	17.1	7.0	0.2	0.6	1.3	9.0	5.7	0.6	99.6
pkm2_gmassgl2	56.8	1.1	17.6	6.8	0.2	0.7	1.5	7.7	5.4	0.5	98.4
pkm2_gmassgl3	56.2	1.8	17.0	6.6	0.2	0.5	1.7	9.7	5.5	0.5	99.6
pkm2_gmassgl4	56.7	1.0	17.4	7.4	0.2	0.4	0.5	9.5	5.7	0.4	99.2
pkm2_glom4ol_gmassgl	53.8	0.1	29.5	1.0	0.0	0.1	11.4	4.8	0.3	0.0	100.9
pk3_plag3_gmassgl	50.4	0.7	0.8	19.3	0.9	7.3	20.9	0.8	0.0	0.0	101.2
pk3_gmassgl2	50.3	0.6	0.8	20.0	1.0	7.0	20.4	1.0	0.0	0.0	101.0
dn4gmassgl1	53.9	0.9	11.7	15.5	0.6	0.5	1.1	9.3	4.1	0.2	97.8
dn4gmassgl2	53.1	1.0	10.8	16.3	0.7	0.7	1.5	8.5	3.9	0.2	96.7
pk-02glass1	50.9	0.0	4.6	20.9	1.2	0.2	1.7	10.4	1.7	0.7	92.2
pk-02glass2	53.4	0.0	4.5	21.8	1.1	0.2	1.7	0.8	1.3	0.5	85.4
pk-02glass3	52.0	0.1	4.5	22.2	1.3	0.2	1.9	9.0	1.9	0.7	93.7
pk-02glass4	54.1	0.1	5.5	21.1	1.1	0.3	1.5	7.5	2.7	0.4	94.3
pk-02glass5	54.6	0.0	4.7	21.4	1.1	0.3	2.2	5.3	2.5	0.5	92.5
pk-02glass6	53.3	0.2	5.2	20.5	1.0	0.2	1.8	9.8	2.2	0.5	94.7
pk-02glass7	49.7	0.9	4.7	19.2	0.8	0.3	1.9	11.3	2.8	0.5	92.0
pk-u7glass1	61.8	0.6	15.1	7.9	0.3	0.1	1.2	8.2	4.8	0.1	100.1
pk-u7glass2	60.9	0.6	15.5	7.9	0.3	0.1	1.0	8.2	4.7	0.0	99.3
pk-u7glass3	61.8	0.6	15.1	7.8	0.3	0.1	1.1	8.2	4.8	0.1	99.7
pk-u7glass4	61.3	0.6	15.2	7.8	0.3	0.2	1.0	8.7	4.8	0.0	99.9
pk-u7glass5	62.0	0.5	15.2	8.2	0.3	0.1	1.2	8.5	4.8	0.1	100.8
pk-u7glass6	61.9	0.5	15.1	7.8	0.3	0.1	0.9	8.8	4.8	0.0	100.3
pk-u7glass7	62.2	0.5	15.3	8.0	0.3	0.1	1.0	8.2	4.8	0.1	100.6
pk-u7glass8	62.2	0.6	15.3	7.5	0.2	0.1	1.0	8.3	4.9	0.1	100.2
pk-2glass21	53.0	0.8	6.3	21.3	1.0	0.4	1.5	9.0	2.6	0.3	96.2

Groundmass chemistry cont...

pk-2glass21	55.0	0.8	6.0	22.6	1.2	0.4	1.7	1.1	2.5	0.4	91.6
pk-2glass21	56.1	0.9	6.0	22.9	1.1	0.3	1.7	0.4	2.2	0.4	92.1
pk-u7-glass11	61.6	0.5	14.8	8.1	0.3	0.1	1.1	8.5	4.9	0.1	99.9
pk-12-glass 1	57.0	6.8	0.5	0.5	17.0	0.9	2.8	0.3	10.8	0.2	96.7
pk-12-glass 2	61.4	11.9	0.2	0.4	8.6	0.2	6.5	0.1	6.0	0.1	95.3
pk-12-glass 3	55.1	5.2	1.1	0.9	19.4	1.1	2.5	0.3	8.6	0.2	94.4
pk-12-glass 4	55.9	5.7	1.0	0.9	18.9	1.1	2.4	0.3	8.3	0.2	94.7
pk-12-glass 5	56.3	6.3	1.0	0.8	17.5	1.1	2.7	0.2	7.4	0.2	93.6
pk-12-glass 6	60.2	8.9	0.2	0.6	11.7	0.3	5.5	0.2	3.4	0.1	90.9
pk-12-glass 7	52.9	4.1	1.0	1.1	20.5	1.2	1.9	0.5	10.1	0.3	93.6
pk-12-glass 8	55.5	5.6	0.5	0.9	18.1	0.9	2.7	0.2	9.8	0.2	94.4
pk-12-glass 9	57.1	5.9	0.6	0.8	18.4	1.1	1.8	0.3	5.7	0.2	91.9
pk-12-glass 10	58.7	10.0	0.6	0.7	13.0	0.5	4.5	0.1	8.8	0.1	97.0
pk-12-glass 11	55.7	5.7	0.7	0.8	18.0	0.9	2.7	0.3	8.8	0.2	93.6
pk-12-glass 12	57.1	5.7	0.6	0.9	18.1	0.9	2.4	0.2	6.8	0.2	92.9
pk-12-glass 13-5 diam beam	57.7	5.8	0.7	0.8	18.8	0.9	2.0	0.2	6.0	0.2	93.2
pk-12-glass 13-5 diam beam	55.9	5.1	0.7	1.0	17.7	1.0	3.1	0.2	11.4	0.1	96.2
pk-12-glass 13	56.7	5.2	0.6	1.0	18.4	1.1	2.4	0.2	7.7	0.1	93.3

Appendix D: EMPA – Pyrite, epidote and chlorite

Table 5 Mineral chemical composition from borehole samples

Pyrite mineral chemistry

Pyrite	S	Fe	Co	Ni	Cu	Total
pk1-910 py 1 pt1	52.1	45.9	0.0	0.0	0.0	98.1
pk1-910 py 1 pt2	52.3	45.7	0.0	0.0	0.0	98.0
pk1-910 py 2 pt1	51.4	45.4	0.0	0.0	0.0	96.8
pk1-910 py 3 pt1	53.6	45.5	0.0	0.0	0.0	99.1
pk1-910 py 4 pt1	52.6	45.5	0.0	0.0	0.0	98.1
pk1-910 py 4 pt2	52.2	45.3	0.0	0.0	0.0	97.5
pk1-910 py 5 pt1	53.2	45.5	0.0	0.0	0.0	98.8
pk1-910 py 6 pt1	53.3	45.7	0.0	0.0	0.0	99.0
pk1-910 py 7 pt1	54.3	45.5	0.0	0.0	0.0	99.8
pk1-1180 py 1 pt1	52.8	45.7	0.0	0.0	0.0	98.4
pk1-1180 py 2 pt1	52.8	45.4	0.0	0.0	0.0	98.2
pk1-1180 py 3 pt3	53.2	45.6	0.0	0.0	0.0	98.8
pk1-1180 py 3 pt4	52.5	44.9	0.1	0.0	0.0	97.5
pk1-1180 py 3 pt5	52.8	45.1	0.0	0.0	0.0	97.9
pk1-2254 py 5pt1	37.8	58.6	0.0	0.0	0.1	96.4
pk1-2254 py 5pt2	37.6	58.4	0.0	0.0	0.1	96.2
pk1-2254 py 5pt3	38.0	58.4	0.0	0.0	0.1	96.4
pk1-2254 py 6pt4	38.5	58.8	0.0	0.0	0.1	97.3

Chalcopyrite mineral chemistry

Sample	S	Fe	Co	Ni	Cu	
pk1-2254 py 4pt3	34.4	29.2	0.0	0.0	32.6	96.2

Epidote mineral chemistry

Sample	SiO_2	TiO_2	Al_2O_3	Fe_2O_3	MnO	MgO	CaO	Na_2O	K_2O	SrO	Total
2254 epi 2point 1	36.3	0.1	23.8	12.3	0.4	0.0	23.6	0.0	0.0	0.1	96.5
2254 epi 2point 2	36.3	0.0	24.0	12.2	0.4	0.0	23.0	0.0	0.1	0.1	96.2
2254 epi 2point 4	37.7	0.1	24.0	12.6	0.6	0.0	22.6	0.0	0.0	0.2	97.8
2254 epi 2point 5	36.7	0.0	22.6	14.2	0.2	0.1	22.0	0.1	0.8	0.2	97.0
2254 epi 2point 7	35.8	0.1	22.6	13.1	0.3	0.1	22.9	0.1	0.6	0.2	95.7
2254 epi 3point 1	37.8	0.1	23.1	13.1	0.5	0.1	22.7	0.0	0.1	0.1	97.5
2254 epi 3point 2	37.3	0.2	20.5	16.9	0.4	0.1	22.6	0.0	0.0	0.1	98.1
2254 epi 3point 3	38.1	0.1	21.6	14.6	0.3	0.1	22.6	0.0	0.5	0.0	97.9
2254 epi 3point 4	37.8	0.2	19.7	17.0	0.2	0.1	22.2	0.0	0.5	0.0	97.7
2254 epi 4point 5	37.9	0.1	23.9	13.2	0.3	0.1	22.5	0.0	0.1	0.1	98.1
2254 epi 4point 1	38.7	0.1	25.0	10.8	0.2	0.1	23.3	0.0	0.0	0.1	98.3
2254 epi 4point 2	37.7	0.0	24.0	13.4	0.2	0.1	22.5	0.0	0.3	0.1	98.3
2254 epi 4point 3	39.5	0.1	24.4	12.3	0.2	0.2	21.2	0.0	1.0	0.1	99.1
2254 epi 4point 4	38.0	0.0	24.2	12.8	0.2	0.1	22.5	0.0	0.3	0.1	98.3
2254 epi 5point 5	37.9	0.2	22.7	14.4	0.2	0.0	23.1	0.0	0.1	0.1	98.7
2254 epi 5point 6	37.5	0.0	22.9	13.3	0.3	0.0	22.7	0.0	0.1	0.1	96.9

Table 6 Mineral chemical composition for chlorite clay from borehole samples

Chlorite clay mineral chemistry

Standards used (Smithsonian)	**SiO_2**	**TiO_2**	**Al_2O_3**	**FeO**	**MnO**	**MgO**	**CaO**	**Na_2O**	**K_2O**	**Total**
ASK86-01 Chl V pt3	67.3	0.1	18.5	2.5	0.0	0.0	0.1	6.6	5.9	101.0
ASK86-01 Chl Mx pt5	65.5	0.0	17.7	2.3	0.1	0.0	0.1	6.0	5.9	97.5
ASK86-01 Micro-Chl Mx pt9	64.5	0.3	18.2	1.5	0.1	0.0	0.1	7.2	6.3	98.1
ASK86-12 Chl V pt10	55.5	0.0	18.4	8.5	0.2	0.7	1.6	0.4	12.5	97.8
ASK86-12 Chl V conc pt11	62.1	1.0	19.9	2.4	0.0	0.6	2.1	8.7	1.4	98.2
Sample										
Pk-01.chl 3 point1	34.7	0.7	15.1	28.8	0.5	6.3	0.1	0.0	9.2	95.5
Pk-01.chl 3 point2	35.1	0.7	15.1	28.9	0.4	6.3	0.2	0.1	9.1	96.0
Pk-01.chl 4 point1	38.1	0.5	10.8	26.2	0.5	9.5	0.3	0.1	8.9	94.9
Pk-01.chl 4 point2	38.6	0.4	10.5	26.5	0.4	9.2	0.2	0.1	8.5	94.5
Pk-01.chl 4 point3	38.1	0.3	10.2	26.2	0.5	9.4	0.5	0.1	8.1	93.4
Pk-01.chl 4 point4	38.4	0.4	10.3	25.8	0.5	9.8	0.4	0.1	8.2	93.9